

**Characterisation and differentiation of kinase  
binding pockets in PKA and Pim1 by small molecule  
fragments using protein crystallography**

Dissertation

zur

Erlangung des Doktorgrades

der Naturwissenschaften

(Dr. rer. nat.)

dem

Fachbereich Pharmazie der

Philipps-Universität Marburg

vorgelegt von

**Christof Siefker**

aus **Osnabrück**

Marburg/Lahn 2018

Vom Fachbereich Pharmazie der Philipps-Universität Marburg als Dissertation

eingereicht am: 13.03.2018

Erstgutachter: **Prof. Dr. G. Klebe**

Zweitgutachter: **Prof. Dr. A. Heine**

Tag der mündlichen Prüfung am: 25.04.2018

Hochschulkennziffer: 1180

Die Untersuchungen zum vorliegenden Thema wurden auf Anregung von Prof. Dr. G. Klebe am Institut für Pharmazeutische Chemie des Fachbereichs Pharmazie der Philipps-Universität Marburg in der Zeit von September2013 bis Juni2017 durchgeführt.



## Table of contents

Table of contents.....	1
Abbreviations.....	5
1. Introduction.....	9
1.1. Protein Kinases.....	10
1.1.1. Signal transduction.....	10
1.1.2. Classification.....	10
1.1.3. Function.....	11
1.1.4. Structure.....	13
1.1.5. The phosphate transfer mechanism.....	14
1.1.6. Substrate specificity.....	16
1.2. The c-AMP dependent protein kinase A (PKA).....	19
1.2.1. Activity regulation.....	19
1.2.2. One protein - ubiquitous occurrence.....	21
1.2.3. Structure of the catalytic subunit.....	23
1.2.4. PKI binding site.....	26
1.3. The Pim1 kinase.....	28
1.3.1. Role and function.....	28
1.3.2. Role in cancer.....	30
1.3.3. Structure.....	31
1.3.4. Consensus peptide.....	33
1.4. Fragment-based drug design (FBDD).....	35
1.4.1. Fragments.....	35
1.4.2. Concept of FBDD.....	36
1.4.3. Fragment libraries.....	37
1.4.3.1. The 361 fragment library.....	38
1.4.3.2. The 96-well plate library.....	40

1.4.4.	Methods for pre-screening.....	41
1.4.5.	The Thermal Shift Assay (TSA).....	42
1.4.6.	Structure determination by protein crystallography.....	44
2.	From thermal shift assay to crystallographic hits – A comparative fragment screening on PKA and Pim1.....	47
2.1.	Introduction.....	48
2.2.	Materials and methods.....	48
2.2.1.	Protein production and crystallisation.....	48
2.2.2.	Thermal shift assay.....	50
2.2.3.	Crystal soaking.....	51
2.2.4.	X-ray data collection, structure solution and refinement process.....	51
2.3.	Results & Discussion.....	52
2.3.1.	TSA analysis.....	52
2.3.2.	Crystallographic screening.....	54
2.3.3.	Crystallographic binders of PKA.....	60
2.3.4.	Crystallographic binders of Pim1.....	69
2.3.5.	Comparison of PKA and Pim1 fragments binders.....	80
2.4.	Summary.....	83
3.	Crystallographic screening of a 96-well-plate fragment library shows a high hit rate for the cAMP-dependent protein kinase A.....	87
3.1.	Introduction.....	88
3.2.	Materials and methods.....	88
3.2.1.	Protein production and crystallisation.....	88
3.2.1.	Crystal soaking.....	89
3.2.2.	X-ray data collection, structure solution and refinement process.....	89
3.3.	Results.....	91
3.3.1.	Categorisation of fragment binding position.....	99
3.3.2.	Diverse benzene derivates in hinge interaction of the ATP-binding pocket.....	108

3.3.3.	Comparison with PDB listed PKA binders .....	115
3.3.4.	The new PKI-free PKA crystals: Characteristics and study effect .....	118
3.4.	Summary .....	123
4.	Identification of novel Pim1 kinase inhibitors using the SCUBIDOO database, fragment docking, and crystallographic screening.....	125
4.1.	Introduction .....	127
4.2.	Materials and methods.....	127
4.2.1.	Protein expression, purification, and crystallisation.....	127
4.2.2.	Thermal shift assay.....	128
4.2.3.	X-ray data collection, structure solution and refinement process.....	129
4.3.	Results and discussion .....	129
4.4.	Status quo & perspective.....	131
5.	Screening the ZINC database against Pim1 kinase via docking results in direct crystallographic hits.....	133
5.1.	Introduction .....	135
5.2.	Material and Methods .....	135
5.2.1.	Docking and ZINC compounds selection .....	135
5.2.2.	Protein expression, purification, and crystallisation.....	136
5.2.3.	Thermal shift assay.....	136
5.2.4.	X-ray data collection, structure solution and refinement process.....	136
5.3.	Results and discussion .....	136
5.4.	Status quo & perspective.....	142
6.	Summary.....	143
7.	Zusammenfassung.....	147
8.	Appendix.....	151
8.1.	Thermal shift data results of the 361 library screen (PKA).....	152
8.2.	Thermal shift data results of the 361 library screen (Pim1) .....	154
8.3.	Crystallographic tables.....	156

---

Table of contents

---

8.4.	Binding mode dossiers.....	170
8.5.	Expression, Aufreinigung und Kristallisation der PKA .....	233
8.6.	Expression, Aufreinigung und Kristallisation der Pim1-Kinase .....	244
9.	References .....	257
11.	Acknowledgement .....	267
12.	Eidesstattliche Erklärung.....	269
13.	Curriculum Vitae.....	270



## Abbreviations

Å	Ångström (1 Å = 10 <sup>-10</sup> m)
Ala	Alanine
Approx.	Approximately
Arg	Arginine
Asp	Aspartic acid
Asn	Asparagine
ATP	Adenosine-tri-phosphate
BisTris	Bis(2-hydroxyethyl)amino-tris(hydroxymethyl)methane
BL	Beamline
c-AMP	cyclic Adenosine-mono-phosphate
clog P	The calculated logarithm of the octanol-water partition coefficient
CPK model	Space-filling-model ( <b>C</b> orey, <b>P</b> auling, <b>K</b> oltun)
CSD	Cambridge Structural Database
Cys	Cysteine
Da	Dalton
DMSO	Dimethylsulfoxide
DTT	1,4-Dithiothreitol
E. coli	Escherichia coli
EDTA	Ethylenediaminetetraacetate
ETP	Endothiapepsin
FBDD	Fragment-based drug design
F <sub>c</sub>	Calculated structure factor amplitudes
F <sub>o</sub>	Observed structure factor amplitudes
g	Gramm
Gln	Glutamine
Gly	Glycine
G-loop	Glycine-rich loop
H-bond	Hydrogen bond
HEPES	2-(4-(2-Hydroxyethyl)-1-piperazinyl)-methane sulfonic acid
His	Histidine
HTS	High throughput screening
ID	Identifier

---

## Abbreviations

---

IL	Interleukin
Ile	Isoleucine
IUBMB	International Union of biochemistry and molecular biology
IPTG	Isopropyl- $\beta$ -D-thiogalactopyranoside
ITC	Isothermal titration calorimetry
K	Kelvin
K <sup>+</sup>	Potassium Ion
L	Litre
Leu	Leucine
Lys	Lysine
m	Meter
M	Molarity (mol / L)
MD	Molecular dynamics
MES	2-(N-Morpholino)ethane sulfonic acid
Met	Methionine
Min	Minute
MPD	2-Methyl-2,4-pentanediol
$\mu$ M	Micromolar
nM	Nanomolar
MR	Molecular replacement
n.an.	Not analyzable
n.s.	Not solvable
NMR	Nuclear magnetic resonance
NTA	Nitrilotriacetic acid
OD <sub>600</sub>	Optical density at 600 nm
ONC	Overnight-culture
Occ.	Occupancy
PCR	Polymerase chain reaction
PDB	Protein Data Bank
PEG	Polyethyleneglycol
pH	The negative decimal logarithm of the hydrogen ion activity
Phe	Phenylalanine
PKA	cAMP-dependent Protein Kinase A
pK <sub>a</sub>	The negative decimal logarithm of the acid dissociation constant

## Abbreviations

---

PKI	Protein kinase Inhibitor
Pro	Proline
Qs	Quantum satis
RNA	Ribonucleic acid
rpm	Rounds per minute
RO3	Rule of three
RO5	Rule of five
RSCC	Real-space correlation coefficient
s / sec	Second
Ser	Serine
SEP	Phosphorylated serine
SDS page	Sodium dodecyl sulfate polyacrylamide gel electrophoresis
SPR	Surface plasmon resonance
$\Delta T_m$	Difference in melting point (Thermal shift)
$T_m$	Melting point
TEMED	Tetramethylethylenediamine
TEV	Tabacco Edge Virus
Thr	Threonine
TLS	Translation/libration/screw-rotation
TPO	Phosphorylated threonine
Tris	2-Amino-2-(hydroxymethyl)-propane-1,3-diol
Trp	Tryptophan
Tyr	Tyrosine
UV	Ultraviolet
V	Volume
V / V	Volume per volume
Val	Valine
W	Watt
°	Degree



# **1. Introduction**

## 1.1. Protein Kinases

### 1.1.1. Signal transduction

Signalling and regulation mechanisms play an important role in complex eukaryotic organisms. In the past, many different mechanisms have been discovered and investigated to understand the complexity of these regulatory processes. The word ‘machinery’ implies that an interplay of many regulatory units is given, that forms the whole signalling pathway (signalling cascade). So far, many signal transduction cascades have been discovered in the human organism, for example in cell migration, proliferation, and differentiation or inflammatory processes.

The initial stimulation of a cascade, depending on the pathway, can start either extracellularly or intracellularly. Nevertheless, the principle of information transfer (Figure 1) is the same in both cases. A signal from the environment, for example a hormone, must first interact with a cellular component (reception). Such a component could be a cell-surface receptor. There, the information from the signal can be further transduced to another component. In most cases, the signal is amplified before a response is initiated. The complete signalling process is also controlled by feedback pathways. Approximately 50% of the 25 largest protein families, which were enciphered by the human genome, are mainly involved in information processing.<sup>1</sup> One of these large protein families is the protein kinase family.

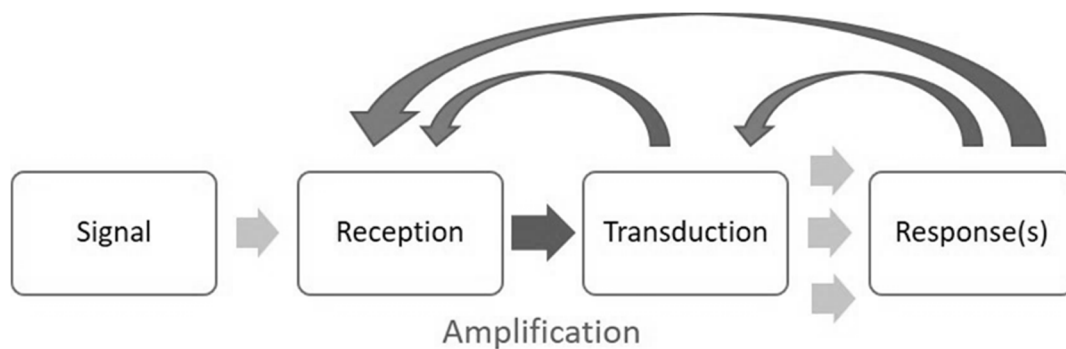


Figure 1: Principles of signal transduction (Adopted from <sup>1</sup>)

### 1.1.2. Classification

Since the discovery that the phosphorylation of proteins takes strong influence on their activity, the interest in the role of protein functional regulation via phosphorylation has steadily increased. Analyses of the human genome discovered a large protein family, which is responsible for the transfer of phosphate groups: The protein kinases. The large number of 518 family members has

been discovered, which comprise 1,7% of all human genes. The family of protein kinases thus belongs to one of the largest groups of genes in eukaryotes. All kinases of the human genome together can be sorted into nine subgroups, shown as a family-tree in Figure 2 (excluding the group “Other”). Apart from these nine groups, there are 40 other kinases, classified as atypical. According to this large number of family members, protein kinases are involved in most signal transduction pathways of eukaryotes including metabolism, transcription, cell cycle progression, cytoskeletal rearrangement, cell movement, apoptosis, differentiation, intercellular communication during development, physiological responses, homeostasis and the functioning of the nervous and immune systems. <sup>2</sup>

Group	Members	Description
<b>AGC</b>	63	Containing PKA, PKG, PKC families
<b>CAMK</b>	74	Calcium/calmodulin-dependent protein kinase
<b>CK1</b>	12	Casein kinase 1
<b>CMGC</b>	61	Containing CDK, MAPK, GSK3, CLK families
<b>RGC</b>	5	Receptor guanylate cyclase group similar to TK group
<b>STE</b>	47	Homologs of yeast Sterile 7, Sterile 11, Sterile 20 kinases
<b>TK</b>	90	Tyrosine kinase
<b>TKL</b>	43	Tyrosine kinase-like
<b>Other</b>	83	Not allocable, diverse

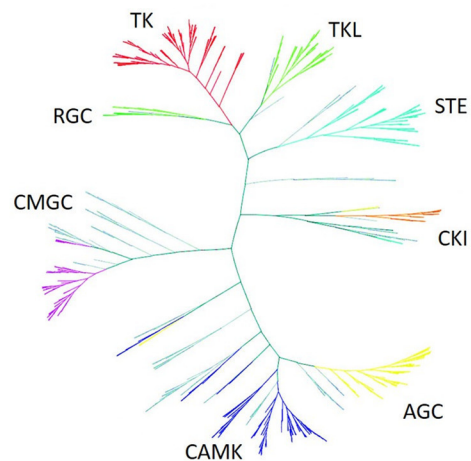


Table 1: All main groups of the human kinome and their description. Adapted from<sup>136</sup>.

Figure 2: Family tree of the human kinome. Adapted from <sup>2</sup>. Group “Other” not shown.

### 1.1.3. Function

With the ability to phosphorylate other proteins, protein kinases modulate the activity of these proteins. To phosphorylate, the  $\gamma$ -phosphate group of an ATP molecule is usually transferred to the alcohol or phenol group of a side chain of a protein target, so that a phosphate ester is formed. It is unlikely that this reaction occurs without enzyme catalysis. In the cytosol of the cell, this reaction is kinetically very slow and unlikely so that a protein kinase is needed as a catalyst. The same applies to the cleavage of the transferred phosphate group. The enzyme family, which catalyzes the hydrolysis of phosphate monoesters, is called phosphatases. With these two protein families, protein phosphorylation and therefore protein activity can be regulated in both directions.

A schematic overview of the activity regulation of proteins via kinases and phosphatases is shown in Figure 3.

Concerning the eight super-families of kinases, used to classify them regarding sequences of the catalytic subunit, the similarity of the sequences, of structured domains beyond the catalytic subunit and the field of their biological operation, kinases can be sorted into three separate classes. The substrate residue, which is phosphorylated by a kinase defines this class. The first class comprises

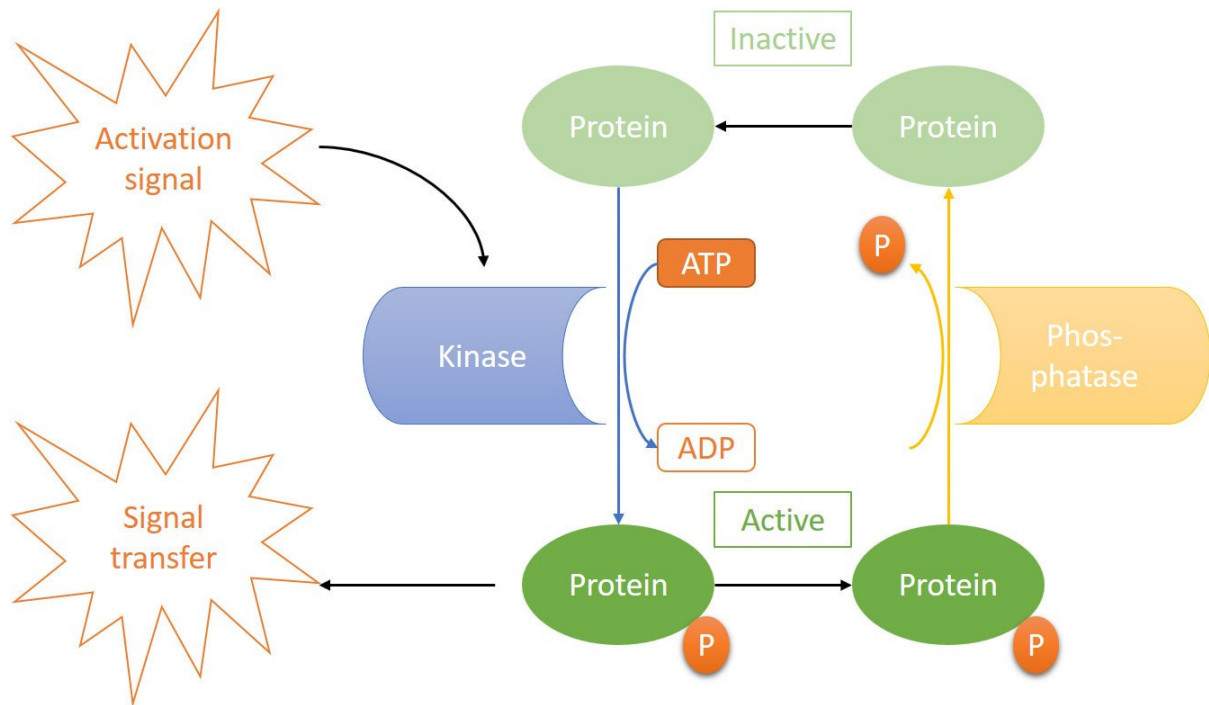


Figure 3: Schematic overview of signalling pathway regulation by protein kinases and phosphatases. Once a kinase is activated by an external signal, it can phosphorylate a target protein. The kinase uses ATP for phosphorylation. The  $\gamma$ -phosphate of ATP is transferred to an alcohol or phenol residue on the protein. The resulting ADP molecule leaves the reaction. This phosphorylation leads to an activity change of the phosphorylated protein. Accordingly, the incoming signal is further transduced. The active state of this signal transfer is then stopped by a phosphatase, which hydrolyses the phosphate ester on the target protein, and again changes the activity of it.

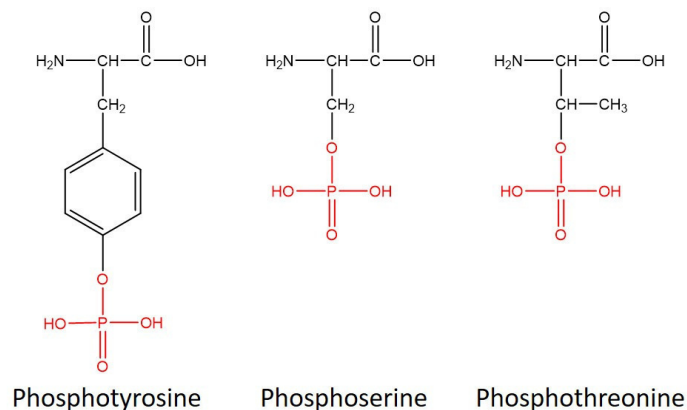


Figure 4: Phosphorylated version of tyrosine, serine, and threonine.



serine/threonine kinases. This class is the most common one and, as the name implies, phosphorylation only occurs at serine and threonine residues of proteins. The second class of tyrosine kinases comprises fewer members than the first one. Kinases that are promiscuously able to phosphorylate all three residues (Figure 4) are less common (third class).

#### 1.1.4. Structure

Although all protein kinases address diverse protein targets in different signal transduction cascades, the structure of their catalytic subunit is almost identical and, therefore, highly conserved. The catalytic subunit of kinases contains approx. between 250 and 300 amino acid residues. Figure 5 shows this conserved spatial fold using the example of the catalytic subunit of cAMP-dependent protein kinase A from *Mus musculus* (PDB 3FJQ). The kinase folds in five antiparallel  $\beta$ -sheets located in the N-terminal (red) domain of the protein. In contrast, the C-terminal part comprises mainly  $\alpha$ -helices (yellow). Here the peptide recognition binding site is located. In the present example, the peptide substrate chain is represented in cyan. PKI is a small peptide inhibitor and usually added to support protein crystallisation. The N and the C-terminal domains are connected through the so-called “hinge region” (blue). This small loop contains the recognition motif for adenosine of ATP. In order to fulfill this recognition, an ATP molecule has to intercalate between the hinge region and the DFG motif, whereby it is also positioned between both terminal domains.

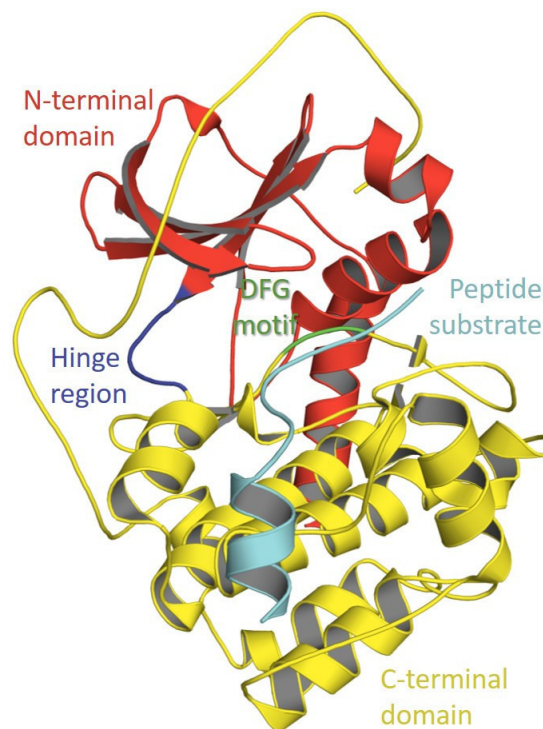


Figure 5: Crystal structure of PKA from mouse with a bound substrate. The tertiary structure is displayed in the cartoon mode. (PDB ID 3FJQ<sup>137</sup>)

The C-terminal part includes this DFG (Asp–Phe–Gly) motif (green), which plays an important role for the stabilisation of ATP in the binding pocket. Mediated through magnesium ions, the aspartic acid of the DFG motif stabilises the electron-rich pyrophosphate chain of ATP in an optimal position for the transfer of the terminal  $\gamma$ -phosphate group. The kinase binding pocket accommodates ATP entirely. Knighton et al. hypothesised that this geometry occurs in all serine/threonine and tyrosine protein kinases as described here using the example of cAMP-dependent PKA. <sup>3</sup> Step-by-step their initial prediction was confirmed by determining more kinase structures. Actually, hundreds of protein domain structures of kinases can be found meanwhile in the protein data bank, which confirms this fundamental folding assumption. <sup>4</sup>

### 1.1.5. The phosphate transfer mechanism

For the phosphorylation of other proteins by kinases, the substrate ATP is indispensable. During the transmission of its  $\gamma$ -phosphate group, the ATP molecule must be stabilised between the N and C-terminal domain connected by the hinge region. An overview of the ATP substrate recognition site in protein kinase A is shown in Figure 6. Adenosine coordinates the hinge region of the protein, and the ribose is placed into the adjacent so-called ribose pocket. The three phosphate groups, attached to the ribose, are oriented towards the solvent-exposed pocket

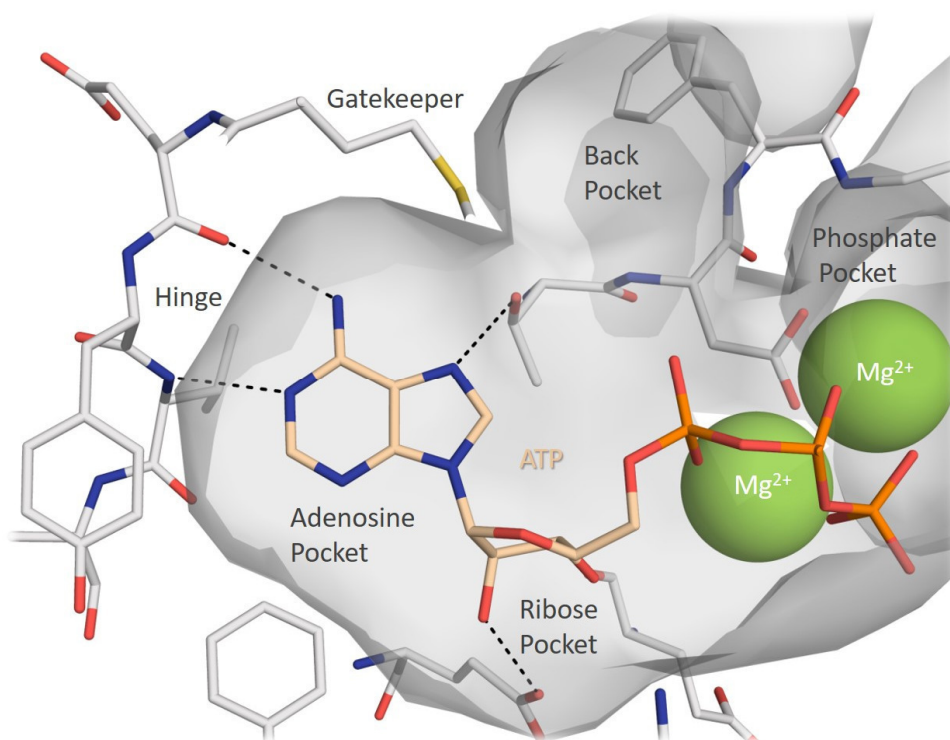


Figure 6: ATP-binding pocket of PKA from mouse with bound ATP. PDB-ID 3X2W. <sup>138</sup> ATP and Protein residues are shown as sticks. Additionally the protein surface is illustrated. Protein carbon atoms are coloured in white, ATP carbon atoms in wheat, oxygen atoms in red, nitrogen atoms in blue, phosphate atoms in orange and sulfur atoms in yellow. The two magnesium ions are presented as green spheres.

opening. The phosphate chain is stabilised by two magnesium ions close to the DFG motif. The aspartic acid in this motif plays an important role in the coordination of magnesium ions to stabilise the phosphates of ATP. The so-called back pocket of the kinase is usually not occupied by ATP. The size of this hydrophobic pocket is restricted by the gatekeeper residue placed next to the hinge region. In Figure 6, a methionine residue takes this role and reduces the space of the back pocket. In contrast, a threonine residue as gatekeeper residue would increase the space next to the ATP-binding pocket. Differences like this can be exploited for finding selective kinase inhibitors.

Since the discovery that the family of protein kinases is responsible for the phosphorylation of other proteins and that they play an important role in regulatory processes of eukaryotic organisms, the interest in detailed information about the phosphorylation processes grew instantly. Many crystal structures have been published, showing tertiary complexes, which include the kinase, part of the protein substrates and ATP or inhibitory analogues. In 2002, the group of S. Taylor published a structure of PKA, where the transition state of the phosphoryl transfer is mimicked. The PKA complexes an ADP molecule in its ATP-binding pocket, so that the missing  $\gamma$ -phosphate leaves a gap between the second messenger and the serine residue on the substrate. This gap was filled with aluminum fluoride, which coordinates in trigonal bipyramidal fashion with the oxygen atoms of the  $\beta$ -phosphate and the serine hydroxy group. It, therefore, gives the first insight into the pathway of the in-line phosphorylation process.<sup>5</sup> Figure 7 shows a schematic overview of the

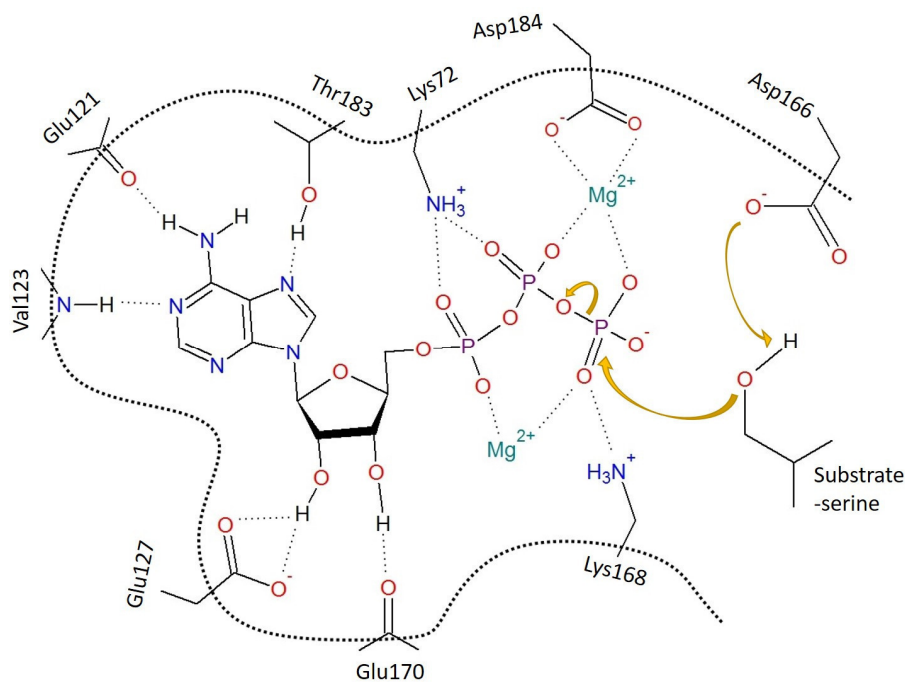


Figure 7: Schematic overview of a phosphorylation process, based on a crystal structure of PKA. The yellow arrows indicate reaction steps during the phosphoryl transfer.

phosphorylation mechanism, based on the example of PKA. The figure demonstrates how an ATP molecule is coordinated in the ATP-binding pocket of PKA. The adenine moiety is close to the hinge region, where the protein residues Glu121 and Val123 are positioned. These residues form hydrogen bonds to the adenine moiety and thus stabilise its binding. Another hydrogen bond is formed to Thr183. The ribose part of ATP additionally forms via its 2' and 3' OH groups two hydrogen bonds to the carboxylate group of Glu127 and to the backbone carbonyl oxygen of Glu170 of PKA. The correct arrangement of the three phosphates is more complex than of the two other substrate moieties. This electron rich phosphate chain is coordinated by two magnesium ions and two protonated amino groups of Lys72 and Lys168, which interact with the phosphate groups. The magnesium ions are in complex with the deprotonated side chain of Asp184 of the DFG motif, indicating its important role and highly conserved position in kinases. When a peptide substrate binds to PKA and one of their serine or threonine residues penetrates into the ATP-binding site of PKA, Asp166 is able to remove a proton from the nearby hydroxy group. This initiates a nucleophilic attack of the oxygen atom on the  $\gamma$ -phosphate phosphorus atom, and the above-described transition state of the reaction is formed. Afterwards, the  $\gamma$ -phosphate is cleaved from the  $\beta$ -phosphate, so that the phosphate transfer is completed.

#### **1.1.6. Substrate specificity**

Although protein kinases show similarities in structure and their catalytic domain, they are able to phosphorylate diverse protein targets in various signal transduction cascades. One significant difference is obvious comparing the family of serine/threonine kinases with the family of tyrosine kinases. Due to the bigger size of a tyrosine residue, the ATP-binding cleft of tyrosine kinases comprises a deeper cleft. It is therefore not surprising that it is easier for a serine/threonine kinase to phosphorylate also tyrosine residues than a tyrosine kinase can overcome the gap to phosphorylate the shorter serine or threonine residues. Although these spatial differences exist, a small number of kinases has found a solution to operate on all three residues efficiently.<sup>6</sup>

The amino acid sequence of the protein target is important for the binding affinity. Even a small change can result in the reduction of affinity. In the mid-1970's, the group of Edwin G. Krebs first performed binding analyses with PKA using peptide sequences of known PKA phosphorylation substrates.<sup>7</sup> They could demonstrate, that the exchange of the phosphorylation site residue serine within the sequence motif LRRASLG to an alanine (LRR AALG) transformed the substrate into an inhibitor. The substrate peptide exhibited a  $K_m$  – value of 16  $\mu$ M, whereas the inhibitory-substrate only scores a  $K_i$  – value of 490  $\mu$ M. This shows that the substrate residue to be phosphorylated is important for the binding affinity to kinases.<sup>8</sup>

Protein kinases are involved in many different signal transduction cascades. Thus, they communicate with a large number of diverse proteins showing diverse recognition motifs. It is not only a serine, threonine or tyrosine residue on the surface of the protein providing the phosphorylation site to a certain kinase. The amino acids adjacent to the phosphorylation position are essential for the substrate recognition so that a certain kinase influences only a particular protein in a cascade.<sup>9 10</sup> For substrate recognition the kinase predominantly interacts with four amino acids

<b>Kinase</b>	<b>Full name</b>	<b>Consensus phosphorylation site</b>	<b>Reference</b>
<b>ABL</b>	Abelson murine leukaemia virus tyrosine kinase	I/V/L-Y-X-X-P/F	11 139
<b>CaMK2</b>	Calmodulin-dependent protein kinase-2	R-X-X-S/T	11 24
<b>CDK</b>	Cyclin-dependent kinase	S/T-P-X-K/R	11 108
<b>CK1</b>	Casein kinase-1	pS-X-X-S/T	11 140
<b>CK2</b>	Casein kinase-2	S/T-D/E-X-E/D	11 141
<b>EGFR</b>	Epidermal growth factor receptor	E-E-E-Y-F	11 142
<b>ERK2</b>	Extracellular-regulated kinase-2	P-X-S/T-P	11 24
<b>GSK3</b>	Glycogen synthase kinase-3	S-X-X-X-pS	11 143
<b>IRK</b>	Insulin receptor tyrosine kinase	Y-M-M-M	11 142
<b>Pim1-3</b>	Proviral integration site kinases 1-3	R-X-R-X-X-S/T	144 47
<b>PKA</b>	Protein kinase A or cAMP-dependent protein kinase	R-R-X-S/T-(Hy)	11 108
<b>PKB/AKT</b>	Protein kinase B	R-X-R-X-X-S/T	145
<b>PKD</b>	Protein kinase D	L/I-X-R-X-X-S/T	144
<b>Src</b>	Rous sarcoma virus tyrosine kinase	E-E-I-Y-E/G-X-F	11 142

Table 2: List of some protein kinases and obtained consensus phosphorylation sites. The sequence of the consensus phosphorylation site is shown in the one-letter-code of amino acids. pS stands for an already phosphorylated serine and (Hy) for a hydrophobic residue. List is adopted from.<sup>146</sup>

near the phosphorylation site. This concerns protein residues N and C-terminal to the residue to be phosphorylated. It has also been demonstrated that kinases and protein targets can interact beyond the phosphorylation sites.<sup>3</sup> A large number of assays have been established to investigate the role of consensus sequences for kinase – protein recognition. Peptide libraries were constructed and tested on several protein kinases to determine such consensus phosphorylation sites.<sup>11 12</sup> Table 2 lists a short overview of consensus peptide sequences that have been observed. The sequence of PKA and Pim1, which are discussed in this thesis, can be found in this list. Nevertheless, it is unclear if a protein that only contains the correct consensus sequence is also phosphorylated by a certain kinase *in vivo*. Additionally, other research projects demonstrated that some phosphorylation sites do not contain such a recognition sequence.<sup>13</sup> Nevertheless, these identified sequences are useful indicators for new phosphorylation sites of putative targets.

That a target protein has a higher affinity than another one can also be explained with additional binding motifs, which are often apart from the catalytic core. Additionally, allosteric binding sites were observed regulating the whole activity of a kinase. For example, the binding of special F-X-F-motifs to the extracellularly-regulated-kinase (ERK) results in an activation effect.<sup>14</sup> The deactivation of kinases via such allosteric binding sites was also observed.<sup>15</sup>

Furthermore, the localisation of the kinase in the cell influences the substrate specificity as well. Kinases can be anchored at different cell compartments (e.g., AKAPs = A-kinase anchoring proteins), which limits the access to protein targets and can, therefore, regulate specificity. Considering that protein kinases are only a part of a cellular system, which contains multiple non-phosphorylation targets at the same time, it could well be that some of them take effect on the kinase by exhibiting a competitive inhibition or an allosteric activation. Several proteins can stay in competition to get phosphorylated by a kinase. Additionally, there are phosphatases which remove the processed phosphorylation. Altogether, it shows the complexity of phosphorylation in signal transduction pathways and the challenge to discover and understand them in detail<sup>4</sup>.

Due to the fact that protein kinases are involved in regulation processes, for example in the cell cycle, metabolism or inflammation, a dysregulation through the abnormal activity of these kinases can lead to diseases such as cancer, diabetes or abnormal inflammation. Thus, protein kinases are interesting drug targets for the development of new pharmaceutical agents<sup>16</sup>.

## 1.2. The c-AMP dependent protein kinase A (PKA)

The PKA is part of the AGC subfamily of kinases. This subfamily consists of 60 members. The human kinome consists of 518 kinases in total. Eponymous for this group are the tree members PKA, PKG, and PKC. Some of the enzymes of this family are already in the focus of investigation as they appear related to diseases such as diabetes or cancer. Nevertheless, there are still many members of this family left with unknown role and function. The catalytic subunit of PKA is one of the best characterised and investigated kinases. At first, PKA was found to regulate the activity of phosphorylase kinase, which is the first purified and characterised kinase, by phosphorylation. Since then, PKA was developed as a model system of a serine/threonine kinase to investigate function, mechanism, regulation, and relevance of protein kinases. Gradually, it became apparent that especially this kinase is involved in many different processes of eukaryotic cells.

### 1.2.1. Activity regulation

The PKA was first named “phosphorylase kinase kinase,” based on the fact, that it was at first discovered to phosphorylate phosphorylase kinase.<sup>7-17</sup> Since Gill and Garren published this discovery, the interest in the role and function of PKA grew. Tao, Salas, and Lipmann were able to separate a PKA holoenzyme from rabbit reticulocytes and further separated its regulatory and catalytic subunits by sucrose density gradient centrifugation, which improved the understanding of the activation mechanism of PKA.<sup>18-19</sup>

There are two types of PKA known (type I and II), which are expressed in human cells. The regulatory subunits are sorted into four subclasses (RI $\alpha$ , RI $\beta$ , RII $\alpha$ , and RII $\beta$ ), where the catalytic subunits show up in three subclasses (C $\alpha$ , C $\beta$ , and C $\gamma$ ). Which isoform is expressed depends upon the cell type. The holoenzyme of PKA is formed by two regulatory subunits and two catalytic subunits and is, therefore, a hetero-tetramer. As long as the PKA remains assembled in this

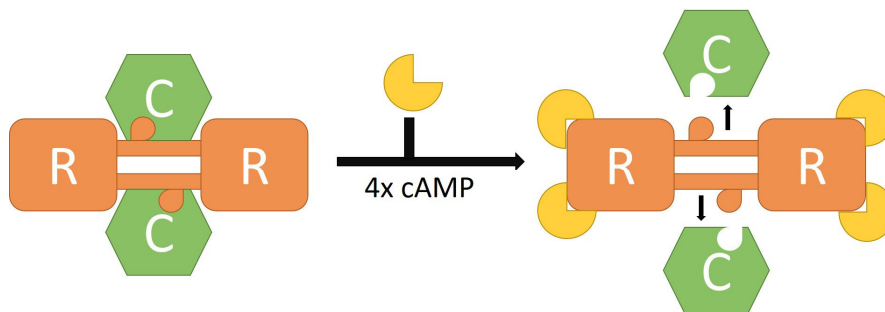


Figure 8: Schematic overview of the activation process of a PKA holoenzyme by cAMP. Regulatory subunits are coloured in orange, catalytic subunits in green and cAMP molecules in yellow. Due to the binding of four cAMP molecules at two regulatory units, the two catalytic units can leave the complex.

complex, it is in an inactive state. The main differences between RI and RII is that RII subunits can be phosphorylated by a catalytic subunit, whereas RI subunits contain an Ala or Gly at their phosphorylation site and are therefore inhibitors of the catalytic subunits. Each R-subunit consists of a linker domain, which includes a substrate identification motif for the catalytic subunit. The RII form exhibits a serine, which can be phosphorylated, where the RI form contains the mentioned Ala or Gly residue at this position. The linker domain connects the dimerisation domain and the two so-called CNB-domains (Cyclic Nucleotide Binding), which are responsible for cAMP-recognition. With two cAMP-binding sites for every R-subunit, four cAMP molecules are essential for the release of the two catalytic subunits from the tetrameric complex. So the dimer complex of the R-subunits remains with the bound cAMP, and two single C-subunits are released. Only after this process, the PKA gains activity to impart an incoming signal. <sup>20</sup>

Other proteins that play an important role in the regulation of PKA are the group of A-Kinase Anchoring Proteins (AKAPs). The name of this protein family is allegorical for its function. These proteins are permanently linked to compartments of the cell and are able to bind regulatory subunits of PKA. Thus, AKAPs can locate PKA molecules in signal pathways. For example, such anchor points could be an AKAP-complex with the cyclic nucleotide-phosphodiesterase, the protein phosphatases or a  $\beta$ -adrenergic receptor. This specific localisation of PKA has an influence on specificity, sensitivity and the time needed for a physiological response. <sup>21</sup>

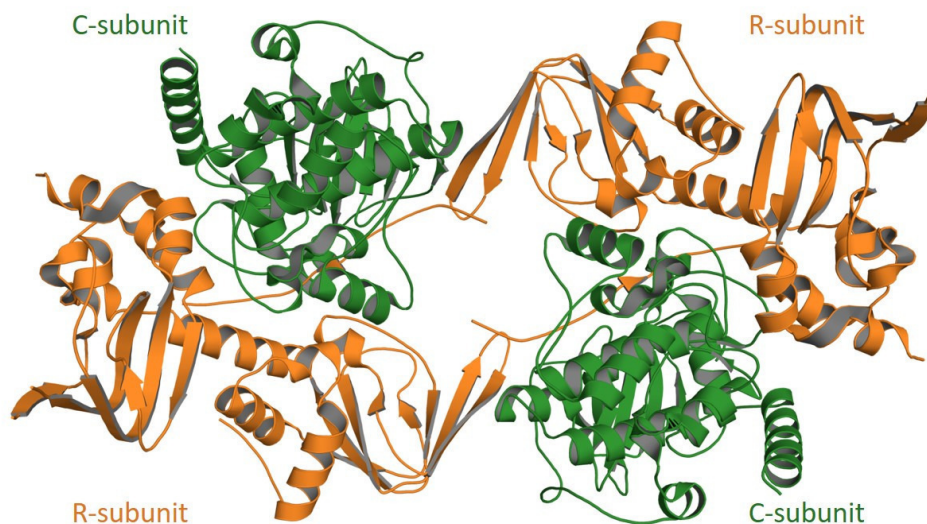


Figure 9: Crystal structure of a PKA holoenzyme (PDB 3TNP) (Taylor et al.2012) displayed in the cartoon motif. The two catalytic subunits are shown in green. The two RII $\beta$  subunits are coloured in orange. The connection sites are located in the middle, displayed as a long orange loop.



### 1.2.2. One protein - ubiquitous occurrence

Protein kinase A is expressed in many diverse mammalian cells, executing a large number of different phosphorylation processes and therefore it is widespread over the whole organism. After PKA activation in a cell by cAMP, there are many target proteins as substrates, which can be phosphorylated by PKA. Thus, dependent upon the cell type, the function of PKA varies. An example of this diversity is cardiac muscle cells of a rat heart, where the contractility is stimulated via a  $\beta$ -adrenergic receptor that leads to an increase of muscle contraction-rate and force. A small collection of diverse PKA action sites is shown in Figure 10. Here, it is especially highlighted that PKA has an effect on several proteins. The example displays the regulation of glycogen synthetase, phosphorylase kinase, troponin I, phospholamban and the sarcolemma p27 protein by PKA. <sup>22</sup> Besides the regulation of cardiovascular functions, it has been shown, that PKA plays a major role in the regulation of steroid biosynthesis, sperm motility, metabolism in adipocytes, exocytic processes (gastric  $H^+$ - secretion, insulin secretion of the pancreas or water reabsorption in renal cells) and immune function (T-cell activation). <sup>23</sup>

The diversity of the phosphorylation targets raise the question of how the enzyme recognises its substrate with the required selectivity. Studies of screening peptide libraries in phosphorylation assays and the determination of crystal structures of catalytic PKA and bound substrate resulted in the consensus sequence R-R-X-S/T-(Hy), where X stands for arbitrary amino acid and (Hy) for an amino acid with a hydrophobic side chain. <sup>24</sup> However, it is not solely the consensus sequence that leads to optimal substrate recognition; it is an interplay of several components. Additionally, there

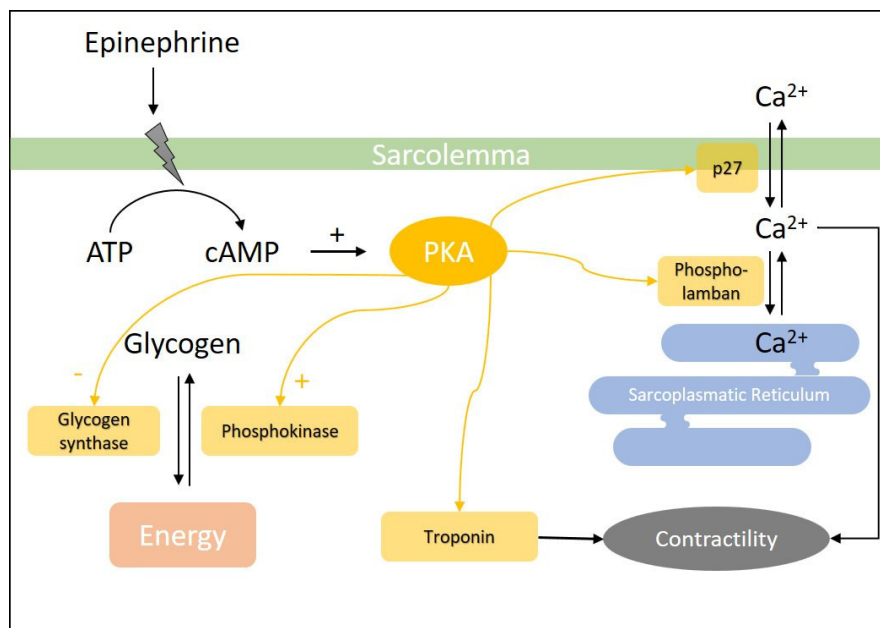


Figure 10: Schematic representation of the role of PKA in cardiac muscle cells of rats. Adopted from <sup>22</sup>

are phosphorylation sites known, which exhibit no consensus sequence. Table 3 lists PKA protein targets. Since PKA can phosphorylate itself, the recognition sequence next to Ser338 is also listed. The table does not only show the diversity of PKA substrates, but it also demonstrates that the phosphorylation can be realised without the presence of the consensus sequence. The exchange of arginine by a lysine seems to be tolerated, similar to a shift of the arginine pair next to the serine phosphorylation site. However, in vitro assays have shown that a change in the consensus sequence leads to a strong downregulation of phosphorylation.<sup>25</sup> Of course, also the concentration of the substrate plays an important role. If only a small amount of PKA is present, a higher affinity by adherence to the consensus sequence is required. PKA is an important player in signal transduction. Protein phosphatases play an important role as an opponent of kinases. They have to recognise a sequence around the phosphorylation site. This demonstrates the complexity of signal transduction and the necessity of the promiscuous PKA as a regulator for many proteins in signal cascades.<sup>22</sup>

PKA substrate	Amino acid sequence around phosphorylation site															
<b>Consensus sequence</b>	-	-	-	-	-	-	-	-	-	R	R	X	S/T	(Hy)	-	
<b>Acetylcholine Receptor <math>\delta</math></b>	P	D	W	Q	N	D	L	K	L	R	R	S	S	S	V	
<b>ATP Citrate Lyase</b>	G	S	T	S	T	P	A	P	S	R	T	A	S	F	S	
<b>Fructose biphosphatase</b>	E	I	Y	N	K	D	K	A	K	S	R	P	S	L	P	
<b>Hormone Sensitive Lipase</b>	H	G	F	W	A	L	T	E	S	M	R	R	S	V	S	
<b>Liver Tyrosine Hydroxylase</b>	A	V	T	S	P	R	S	I	G	R	R	Q	S	L	I	
<b>Muscle Glycogen Synthase</b>	R	N	I	R	A	P	Q	W	P	R	R	A	S	C	T	
<b>Phenylalanine Hydroxylase</b>	V	V	L	G	N	G	V	L	S	R	K	L	S	D	F	
<b>Phospholamban</b>	V	Q	Y	L	T	R	S	A	I	R	R	A	S	T	I	
<b>Phosphorylase Kinase <math>\alpha</math></b>	K	S	E	I	K	Q	V	E	F	R	R	L	S	I	S	
<b>Phosphorylase Kinase <math>\beta</math></b>	V	L	E	R	R	A	R	T	K	R	S	G	S	V	Y	
<b>Pig Liver Pyruvate Kinase</b>				E	G	P	A	G	Y	L	R	R	A	S	L	A
<b>PKA Catalytic Subunit (Ser<sub>338</sub>)</b>	N	F	D	D	Y	E	E	E	E	I	R	V	S	I	N	
<b>PKI - SCP0064</b>				I	A	A	G	R	T	G	R	R	Q	A	I	H
<b>Pro-ANP</b>					G	P	R	S	L	R	R	S	S	C	F	
<b>Protein Phosphatase 1</b>	K	P	G	F	S	P	Q	P	S	R	R	G	S	E	S	
<b>Rabbit Heart Troponin</b>	A	G	E	A	K	P	A	P	A	V	R	R	S	D	R	
<b>Rat Brain CREB</b>	S	Q	K	R	R	E	I	L	S	R	R	P	S	Y	R	
<b>RII subunit of PKA</b>	D	V	P	I	P	G	R	F	D	R	R	V	S	V	C	
<b>S6 Ribosomal Protein</b>	K	R	Q	E	Q	I	A	K	R	R	R	L	S	S	L	

Table 3: Known PKA substrates and their recognition sequence. Also the protein kinase inhibitor peptide PKI is listed, which was used in this thesis to support PKA crystallisation. As an inhibitory peptide it exhibits high affinity towards PKA and an alanine replaced serine, at the phosphorylation site. (Hy) = hydrophobic amino acid.

### 1.2.3. Structure of the catalytic subunit

In contrast to the secondary and tertiary structure of kinases, where all families show similarities (domain arrangement and position), their primary structures show strong differences. These differences are more striking between distinct families. In this thesis, the catalytic subunit of PKA from *Cricetulus griseus* (Chinese hamster; EC 2.7.11.11) is discussed. The protein consists of an amino acid chain of 351 residues. Figure 11 shows the PKA amino acid sequence of *Cricetulus griseus* in comparison to the composition of *homo sapiens*. There are six differences in the sequence, highlighted with bigger letters. Most of these differences are located in the N-terminal  $\alpha$ -helix of the enzyme, also called the N-tail of the enzyme. It is exclusive for PKA and is used for multiple functions like myristoylation motifs or interacting motifs with other proteins (EGFR, CNB, CDK2, AKIP1). The C-tail of the PKA contains the last of the six differences in the sequence. The C-tail is a long loop, highly conserved in the AGC kinase family and consists of interaction motifs with other proteins like SMAD3, SRC or heat shock protein 90. Besides the docking motifs for other proteins, N- and C-tail play a role in the catalytic process as described below. An additional aspect is the phosphorylation sites of PKA. There are three positions, where the catalytic PKA can be phosphorylated by other kinases or by autophosphorylation. Most important is the phosphorylation of Thr197. It is located in domain 8 (activation loop) and essential for the full enzyme activity. The second phosphorylation appears at Ser338 in the C-terminal part. This residue

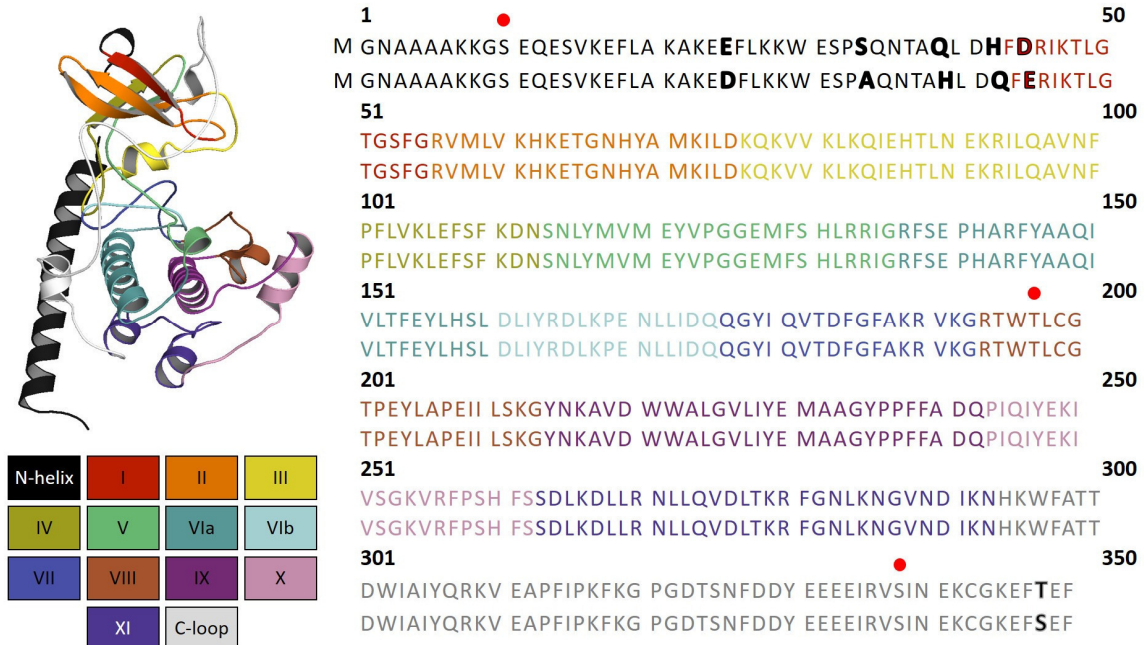


Figure 11: Structure and amino acid sequence of PKA subunit from *cricketulus griseus* (upper row) and from *homo sapiens* (lower row). There are 6 positions in the sequences, which differ from each other. They are highlighted with bigger letters. The colour code refers to the domains, listed in the legend. These domains include all sequence motifs that are highly conserved in protein kinases. Additionally, the PKA has a long  $\alpha$ -helix in the N-terminal part (black) and a long C-terminal loop (gray). Phosphorylatable residues are marked with red dots.

is already available for phosphorylation while the PKA is still in the ribosomal production process. The third position is located in the N-terminal  $\alpha$ -helix (Ser10).<sup>20</sup> The color code represents the respective domains, which include highly conserved sequence motifs of all kinases.<sup>26</sup> Some motifs from serine/threonine kinases are listed in Table 4. The first domain contains the so-called glycine-rich loop or G-loop. The conserved sequence in this domain is Gly-X-Gly-X-X-Gly, and it is located in proximity to the catalytic core. The G-loop is very flexible and supposed to influence ATP-binding. A conserved lysine locates in domain II, which plays an important role for the ATP substrate recognition. The glutamic acid in domain III is also in proximity to this lysine and serves as an anchor point for the lysine by side chain interaction. The subdomain VII contains the most famous motif of protein kinases. The DFG-motif near the catalytic core assists in the arrangement of the ATP molecule in the binding pocket using magnesium ions as mediators. Domain VI contains a sequence, which is also highly conserved in serine/threonine kinases (Asp-Leu-Lys-Pro-Glu-Asn). In tyrosine kinases, the sequence looks a bit different but is also conserved here (Asp-Leu-Arg-Ala-Ala-Asn). The conservation at this position indicates that the recognition of the phosphorylatable hydroxyl group is managed here. Also, a well-known motif is the so-called A-P-E-motif and is located in domain VIII. Similar to domain VI, the main differences between serine/threonine kinases and tyrosine kinases can be observed here. Especially the part preceding the APE motif shows discrepancies: Gly-Thr/Ser-X-X-Tyr/Phe-X-Ala-Pro-Glu for serine/threonine kinases and Pro-Ile/Val-Lys/Arg-Trp-Thr/Met-Ala-Pro-Glu. These discrepancies are an indication of substrate specificity regulation. Additionally, it is important for the kinase activity.<sup>26</sup>

Domain	Conserved sequence/residue	PKA sequence
<b>I</b>	Gly-X-Gly-X-X-Gly	Gly-Thr-Gly-Ser-Phe-Gly
<b>II</b>	Lys	Lys72
<b>III</b>	Glu	Glu91
<b>IV</b>	Hydrophobic residue	Val104
<b>VIb</b>	<b>Asp-Leu-Lys-Pro-Glu-Asn</b>	<b>Asp166-Leu-Lys-Pro-Glu-Asn171</b>
<b>VII</b>	Asp-Phe-Gly	Asp184-Phe185-Gly186
<b>VIII</b>	Ala-Pro-Glu	Ala206-Pro207-Glu208
<b>IX</b>	<b>Asp-X-(ar)-Ser/Ala-X-Gly-Ile/Val</b>	<b>Asp220-Trp-Trp-Ala-Leu-Gly-Val227</b>
<b>XI</b>	X-Arg-X	Arg280

Table 4: Most important and highly conserved sequence motifs of serine/threonine kinases and the corresponding version in PKA. X stands for a various amino acid. (ar) stands for an amino acid with an aromatic side chain.

Another important role in the structure of kinases plays the “gatekeeper” residue. It is located in the ATP-binding pocket and regulates the pocket size by its volume. In PKA the gatekeeper is the large amino acid Met120. Approx. 77% of all human kinases have similarly large gatekeeper residues. In most cases, it is a Met, Leu or Phe residue and belongs to serine/threonine kinases. Therefore, the gatekeeper can play an important role in the design and development of selective and ATP-competitive kinase inhibitors.

Very important factors for the protein stability of PKA are the regulatory and the catalytic spine. These spines are formed by hydrophobic residues and can be seen as a linker enabling the communication between N-terminal and C-terminal part of PKA. The regulatory spine consists of four amino acid side chains including Leu95 and Leu106 from the N-terminal region as well as Tyr106 and Phe185 from the catalytic and regulatory loops of the C-terminal part. Because the catalytic loop is flexible and therefore essential for the enzyme activity, this spine is named ‘regulatory spine.’ This regulation mechanism is generally known as the DFG-in (active) and DFG-out (inactive) state of a kinase, which was first displayed in the crystal structure of Abl kinase in complex with Gleevec (Imatinib).<sup>27</sup> The regulatory spine is anchored to the hydrophobic helix in domain VIa via a conserved aspartate (Asp220). The catalytic spine flanks the opposite side of the catalytic core. Val57 and Ala70 form the spine in the N-terminal part of PKA. The next amino acid is Leu173, which is close to the ATP-binding site. This amino acid has two hydrophobic residues

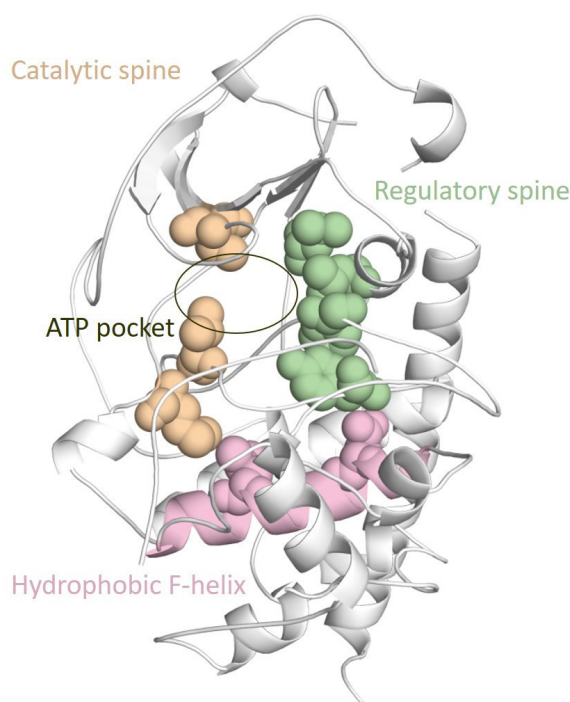


Figure 12: Crystal structure of PKA displayed in cartoon mode. The amino acids, contained in the R- and the C- spine are shown as coloured spheres. The hydrophobic F-helix is also coloured corresponding to its label. The linking amino acids to both spines are highlighted as spheres.

as neighbours (Leu172 and Ile174), which expand the spine in the direction of Met128 in the C-terminal part of PKA. This methionine is the anchor residue to Leu227, the second connection point of the hydrophobic F-helix in domain VIa. Figure 12 displays the gap in this spine between Ala70 and Leu173, which is normally occupied by the adenine moiety of ATP. Since the co-substrate ATP is needed to complete this spine, it is called the catalytic spine. The C-spine is not only a linker of N- and C-terminal part; it is also involved in building the hydrophobic core of the ATP-binding pocket. The hydrophobic helix functions as a connection element between the R- and the C-spine.<sup>28</sup>

#### 1.2.4. PKI binding site

Studies with PKA by testing peptide libraries to identify peptide recognition sequences led to the discovery of a small peptide molecule with high affinity to PKA: The protein kinase inhibitor (PKI). The binding of the peptide led to the first crystal structure of a kinase, which was the catalytic subunit from mouse.<sup>3</sup> The sequence of this peptide is T-T-Y-A-D-F-I-A-S-G-R-T-G-R-R-N-A-I-H-D. This 20 amino acid long polymer chain (5-24) is a segment of the 75 amino acids long peptide

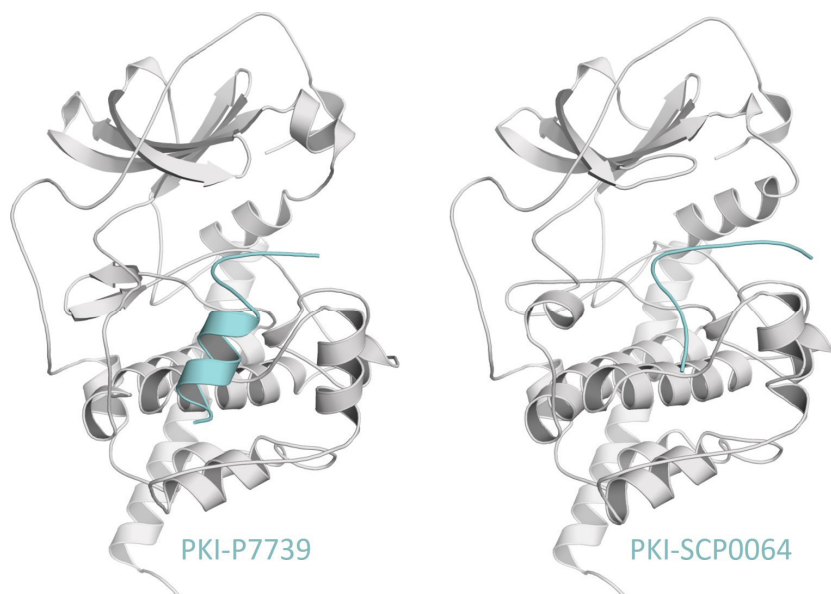


Figure 13: Crystal structures of PKA in complex with consensus peptides, displayed in cartoon mode. The bound peptides are highlighted in cyan.

Type	Sequence
#	5 6 7 8 9 10 11 12 13 14 15 16 17 18 19 20 21 22 23 24 25 26 27 28 29
<b>P7739</b>	T T Y A D F I A S G R T G R R N A I H D
<b>SCP0064</b>	I A A G R T G R R N A I H D I L V A A
<b>General recognition sequence:</b>	- R R X S/T H <sub>y</sub> -

Table 5: Used PKI types for PKA crystallisation. (H<sub>y</sub>) stands for an hydrophobic amino acid.

(UniProt-ID: P61925). Since then, other variations have been established and used for protein crystallisation. Besides the “original” sequence, another version is used in this thesis (type: SCP0064). The superimposition of both sequences is shown in Table 5, where Figure 13 displays their positions in the respective crystal structures. In relation to the original PKI type (P7739), which is usually entirely visible in the electron density in crystal structures, between four and five amino acids of the SCP-type are missing in structures. Both sequences include the typical R-R-X-S/T-(Hy) -motif, which is responsible for major part of the high-affinity binding to PKA. As an inhibitor, the peptides contain an alanine instead of a serine or threonine, which would be the phosphorylated residue. The hydrophobic residue (Hy) is isoleucine for both PKI types. The importance of the arginine pair has already been elucidated. These two peptide residues interact via salt bridges with PKA residues. Arg18 of PKI reaches close to the ATP-binding pocket interacting with Asp328 and Glu127. The second arginine (Arg19) reaches into a small pocket in front of the ATP-binding site. In this pocket, Glu170 and Glu230 form salt bridge interactions to PKI (Figure 14). Both PKI types bind similarly to this part of the protein. The displayed structure contains no bound ATP or substrate analogues. It has been shown that the arginine residue reaches more in the ATP-binding pocket when a bound ATP molecule is present. <sup>4</sup>

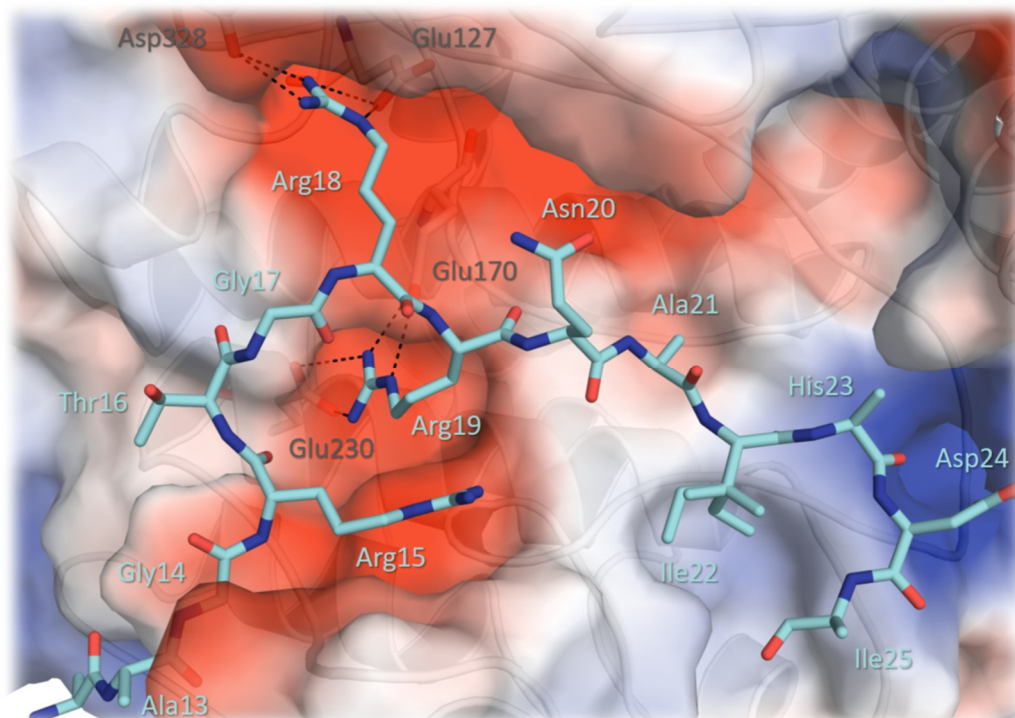


Figure 14: Binding site of PKI (SCP0064). The PKA is shown with its protein surface. The surface is coloured corresponding to its electrostatic potential: negative in red, neutral in white and positive in blue (calculated by PyMol). The PKI peptide is shown as sticks with cyan coloured carbon atoms. The salt bridge interactions of Arg18 and Arg19 with PKA is indicated by black dashed lines.

### 1.3. The Pim1 kinase

Pim1 is an abbreviation and originates from “Proviral integration site for Moloney murine leukaemia virus.” The protein was first discovered during gene experiments for finding new spots of tumourigenesis. There, it was identified as an integration site for the virus. The human Pim1 preferably phosphorylates serine and threonine residues. The enzyme is part of the calcium/calmodulin-regulated kinases (CAMK) family of the human kinome. The human gene encodes two isoforms of Pim1. Isoform 2 contains 91 fewer protein residues than isoform 1. However, it is catalytically active and will be discussed in this thesis.<sup>29</sup> As a result of more profound Pim1 investigations, two more kinases have been observed showing high similarities in sequence and structure to Pim1 (Pim2 and Pim3).<sup>30</sup> Nevertheless, they are not discussed in this thesis.

#### 1.3.1. Role and function

The first protein, which was found interacting with Pim1, was the p100, an activator of the c-Myb transcription factor<sup>31</sup>. Later, another transcription factor was found, involved in T-cell receptor signalling, NFATc<sup>32</sup>. The first hint that Pim1 plays a role in cell progression, came up 1999 with the phosphorylation of phosphatase Cdc25A by Pim1. Cdc25A regulates the G1/S phase of the cell cycle. The effect of increased Cdc25A activity led to a better transition through this cell cycle phase.<sup>33</sup> The G1/S-progression inhibitor p21 was also found to be phosphorylated by Pim1. This resulted in inactivation of the inhibitor that normally inhibits cyclin kinase.<sup>34</sup> Afterwards, it came clear that Pim1 has an influence on cell apoptosis. The phosphorylation and inactivation of the Bad-protein, which advances apoptosis, was demonstrated. This was a major hint for the influence of Pim1 in cell survival<sup>35</sup>. Beside the G1/S phase of the cell cycle, it was also found, that Pim1 is involved in the organisation of the spindle apparatus by phosphorylating the NuMA protein (nuclear mitotic apoptosis protein) during the M-phase.<sup>36</sup> A faster transition to mitosis from the G2 phase was reached by inactivation of C-TAK1 and activation of phosphatase Cdc25C. Here, Pim1 also functions as a regulation factor<sup>37</sup>.

Leaving the field of cell cycle regulation, Pim1 shows to phosphorylate more substrate proteins like the HP-1 (heterochromatin-associated protein 1), the PAP1 or TRAF2/SNX6 (tumour necrosis factor receptor-associated factor 4 (TRAF4)-associated factor 2/sorting nexin 6). HP-1 works as a transcription repressor by disabling chromatin. Phosphorylation by Pim1 leads to an inactivation of HP-1<sup>38</sup>. PAP1 is not only a repressor of transcription, but it is also a regulator of mRNA splicing, whereas TRAF2/SNX6 behaves as an adapter protein in signalling cascades, which are initiated by TNF receptor activation. Pim1 induces the translocation of this peptide from the cytoplasm to the nucleus<sup>39</sup>. SOCS1 and SOCS3 (suppressors of cytokine signalling) are also known substrates of Pim1. Like TRAF2/SNX6 they function as adapter proteins in TNF receptor signal transduction.



They are responsible for negative regulation of Signal Transducer and Activator of Transcription (STATs) or the TNF receptor. <sup>4041</sup> The activation of Pim1 is regulated by the Janus kinase(JAK)/STAT pathway. The primary signal of this pathway can be initiated by several mediators. Already well known is the activation by interleukins, or the tumour necrose factor  $\alpha$  (TNF  $\alpha$ ). An overview of all these interaction partners of Pim1 is shown in Figure 15.

Transcriptional regulation	G1/S progression	G2/M progression	Signal transduction cascades	Apoptosis
<ul style="list-style-type: none"> <li>•HP1 (-)</li> <li>•NFAT (+)</li> <li>•p100 (+)</li> <li>•c-Myb (+)</li> <li>•PAP1</li> </ul>	<ul style="list-style-type: none"> <li>•Cdc25A (+)</li> <li>•p21 (-)</li> </ul>	<ul style="list-style-type: none"> <li>•NuMA (+)</li> <li>•Cdc25c (+)</li> <li>•C-TAK1 (-)</li> </ul>	<ul style="list-style-type: none"> <li>•TRAF2/SNX6 (+)</li> <li>•SOCS1 stabilisation</li> <li>•SOCS3 stabilisation</li> </ul>	<ul style="list-style-type: none"> <li>•PTP-U2S (-)</li> <li>•Bad (-)</li> </ul>

Figure 15: Cell regulatory proteins, which are influenced by Pim1. A (-) means deactivation, (+) stands for activation or acceleration of the protein activity. The proteins are listed in the related area of operations. (Adopted from<sup>29</sup>)

It has been clarified that Pim1 is in contact with many proteins of the cell life cycle regulation. Since these selections have previously been noted <sup>29</sup>, more effects caused by Pim1 have been discovered, showing that Pim1 is involved in a broader field of biological tasks. Also, the

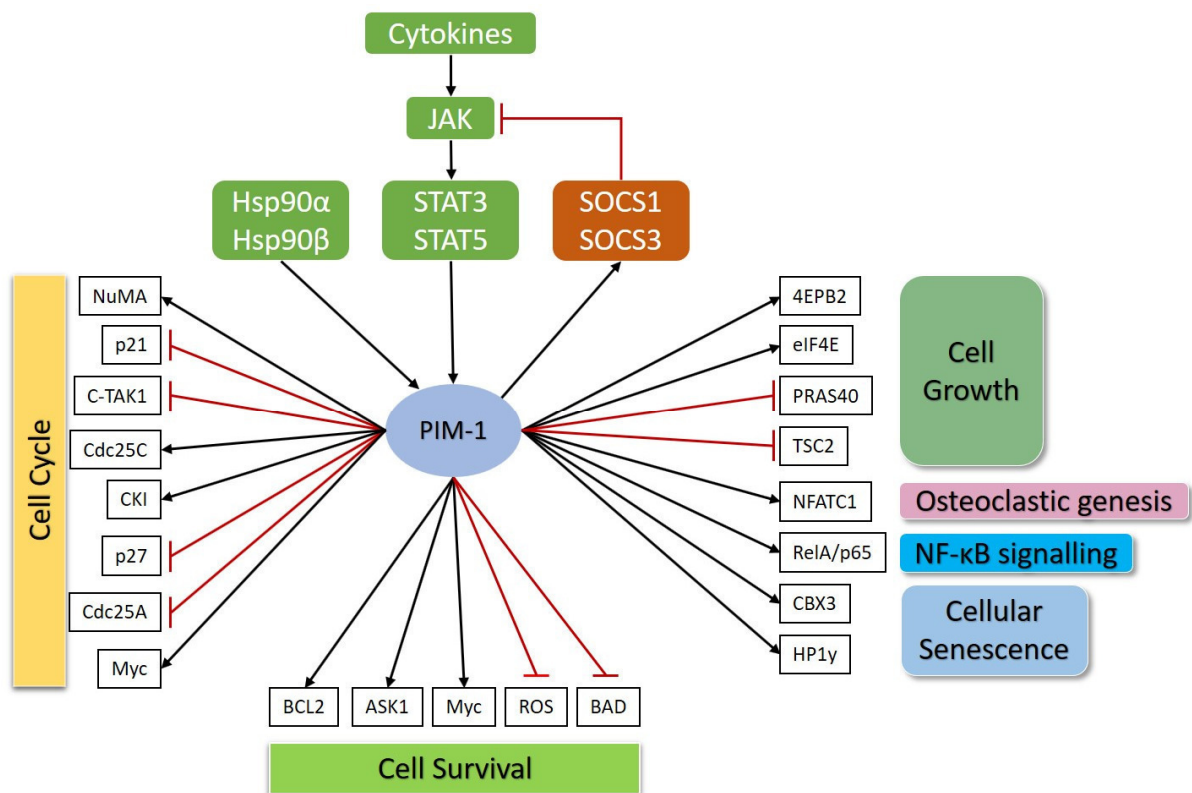


Figure 16: Activation of Pim1 and its regulatory involvement in cell survival, cell cycle, cell growth, Osteoclastic genesis, NF-κB signalling and Cellular senescence. An activating effect is displayed as a black arrow. A deactivating effect is shown as a red line.

understanding of cell regulation processes has improved. An updating review in 2016<sup>42</sup> gave an overview of activation and influence of Pim1. The activation of the JAK pathway is here the most well-described mechanism. Interleukins are initiators of this pathway, and JAK transduces the signal to STATs by phosphorylation, which are able to increase the expression of Pim1 by binding its promoter gene. After expression, Pim1 regulates its own expression by a feedback mechanism. The activity of JAK is reduced by the phosphorylation of SOCS proteins, and this subsequently blocks the STATs activation. It also has been shown that the heat shock proteins  $\alpha$  and  $\beta$  are also correlated with Pim1 expression by stabilizing the protein.<sup>43</sup> The diversity of Pim1 phosphorylation targets is illustrated in Figure 16. The figure also shows the diverse fields of operation where Pim1 is involved. This high involvement in multiple cell regulatory networks has been investigated by several researchers, who suggest that Pim1 functions as a key master in this area.<sup>42</sup>

### 1.3.2. Role in cancer

Since the first association of Pim1 as an oncogene in the 1980s in mouse cells, it has been shown that Pim1 is overexpressed in hematopoietic malignancies and solid cancer cells. Especially in MYC-driven tumourigenesis, Pim1 reduces the cell sensitivity to apoptosis. Pim1 is directly active after its translation. No modification by other proteins is needed, making Pim1 more independent in its activity. Contrarily, the Pim1-encoding mRNA has a short half-life, which exposes the transcription as the main regulation step for its activity. Gradually, the list of malignant human tumour cells associated with an overexpression of Pim1 grew. Table 6 lists reported Pim1-gene-cancer-correlation.<sup>44</sup> Consequently, Pim1 plays an important role in the field of cancer drug research. Understanding the role of Pim1 in detail, the interest in Pim1 also expands in other healthcare domains. It could function as an immunotherapy target, drug resistance target, prostate cancer biomarker or metastatic target.<sup>42</sup>

<b>Haematological malignancies</b>	<b>Malignancies of epithelial origin</b>
○ Mantle cell lymphoma	○ Prostate adenocarcinoma
○ DLBCL	○ Pancreatic ductal carcinoma
○ Primary mediastinal large B cell lymphoma	○ Squamous cell carcinoma of the head and neck
	○ Gastric carcinoma
	○ Oral squamous cell carcinoma

*Table 6: Reported human malignancies, which show an increased expression of Pim1, split in haematological malignancies and malignancies of epithelial origin. (adopted from<sup>44</sup>)*

### 1.3.3. Structure

Two isoforms of human Pim1 are known (IUBMB-ID: EC 2.7.11.1). The first isoform consists of 404 amino acids and has a molecular mass of approx. 45kDa. The second isoform is with 313 residues 22.5% shorter and has a mass above 35kDa. In this thesis, the second isoform of Pim1 is discussed, whereby a single mutation of Arg250 to Gly was conducted. An overview of the amino acid sequence and a Pim1 crystal structure is shown in Figure 17. Similar to all catalytically active kinases the ATP-binding site is located between the N-terminal lobe, which is dominated by  $\beta$ -sheets, and the C-terminal lobe, which is dominated by  $\alpha$ -helices. These two regions are connected by the hinge region. Following the numbering of Pim1 domain sections in Figure 17, the hinge is located between  $\beta$ -sheet five and six. The N-lobe and the C-lobe are not further connected by salt-bridge interactions, which is generally present in other kinases. It has previously been identified that this is a crucial factor for the protein stability and activity.<sup>45</sup> In fact, the Pim1 structure exhibits the typical kinase domains but also contains two additional anti-parallel  $\beta$ -sheets ( $\beta$ H1 and  $\beta$ H2). These  $\beta$ -sheets are located between the third  $\beta$ -sheet and the  $\alpha$ C-helix. In contrast to PKA and other kinases, they are unique structural elements. Similar to PKA, Pim1 contains a glycine-rich loop within the N-lobe (-GGFG-), connecting first and second  $\beta$ -sheet.

Although Pim1 can be phosphorylated, the crystal structure shows no serine or threonine residues with an attached phosphate. This is caused by the treatment of Pim1 with phosphatases during

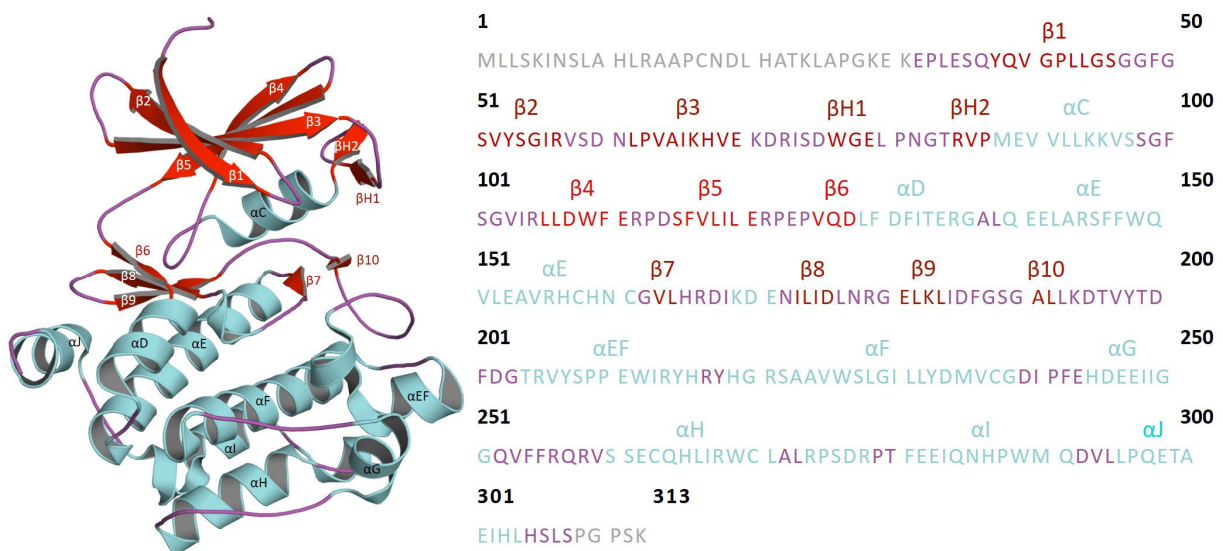


Figure 17: Crystal structure and amino-acid sequence of Pim1. The protein is displayed as cartoon.  $\alpha$ -Helices are coloured in cyan,  $\beta$ -sheets are coloured in red and loop regions are coloured in purple.  $\alpha$ -Helices and  $\beta$ -sheets are named in a consecutive numbering/character system. The gray parts at the N- and the C-terminal part of the protein sequence are not present in the crystal structure (used PDB entry: 1xqz).

protein purification. Consequently, Pim1 is also not phosphorylated in the activation loop (residue 183 – 204). However, Pim1 is even active in its non-phosphorylated state.

One of the first crystal structures of Pim1 contains a bound AMP-PNP molecule (PDB 1XR1) giving information about important protein residues for the ATP recognition (Figure 18). The following amino acids are indicated to be important: Glu121 of the hinge region is the only polar contact formed to the adenosine moiety. The side chain of Lys67 stabilises the phosphate groups of a bound ATP molecule. The side chain of Glu89 supports the positioning of Lys67. The side chain of Asp186 of the DFG motif interacts with the magnesium ions in the proximity of the ATP pyrophosphate unit. Additionally, Asn172 assists the spatial orientation holding one of these magnesium ions.

Pim1 differs from other kinases in the hinge region. As it is well known that this region is crucial for the adenosine recognition, it is surprising that the Pim1 contains only one formed H-bond to a bound ATP molecule. The reason for this restricted interaction motif is Pro123. Due to the presence of this proline, a hydrogen bond donator, which is present in almost all other kinases, is not available for ATP recognition. Another proline (Pro125) is part of the Pim1 hinge and influences its composition. A special feature of this proline is a cis-orientation of the peptide bond,

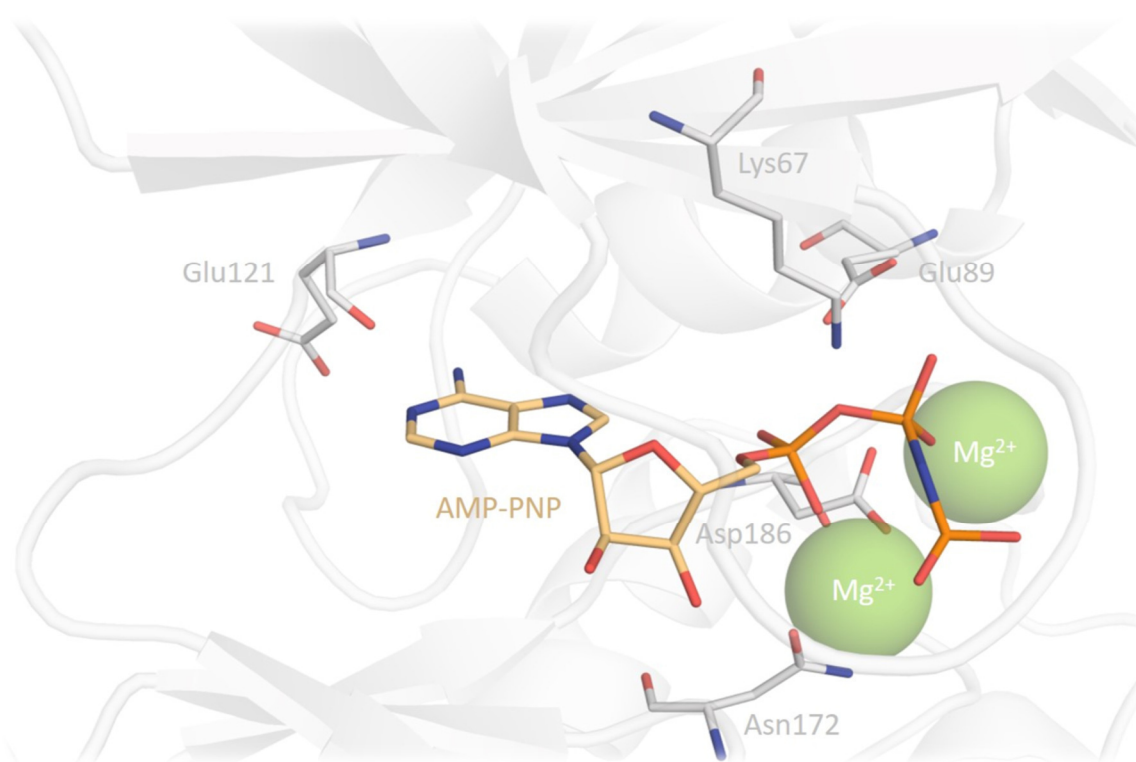


Figure 18: Crystal structure of Pim1 in complex with AMP-PNP (PDB: 1XR1). Highlighted are the protein residues in direct or indirect contact with the ATP derivate AMP-PNP (light orange carbon atoms). The magnesium ions are shown as green spheres.

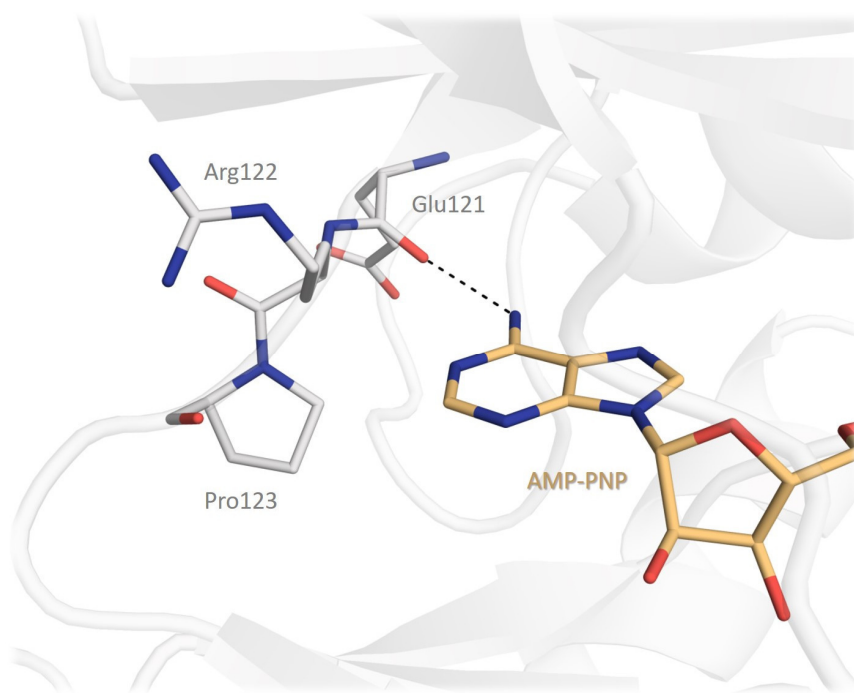


Figure 19: Crystal structure of Pim1 in complex with AMP-PNP (PDB 1XR1). The only hydrogen bond to the adenosine moiety is formed by the Glu121 backbone oxygen, highlighted as a black dashed line.

resulting in a strong bending of the hinge. This bend is also not commonly observed in other kinases. Consequently, the ATP-binding pocket of Pim1 is wider than in other kinases.<sup>15</sup>

#### 1.3.4. Consensus peptide

Similar to PKA, a consensus peptide sequence can bind to Pim1 having a peptide motif mimicking the local environment of the residue to be phosphorylated. This small peptide has a length of 14 amino acids (A-R-K-R-R-R-H-P-S-G-P-P-T-A), a molecular weight of approx. 1,5 kDa and is called PIMTIDE. Similar to the behavior of PKI at PKA, PIMTIDE is used to improve the crystallisation properties of Pim1 by stabilizing Pim1 by its bound state. Although the entire peptide is crystallised with Pim1, not the full sequence is visible in the electron density. Depending on the resolution up to nine amino acids can be assigned to the density. One representative example for the PIMTIDE binding mode is shown in Figure 20. The figure illustrates that PIMTIDE binds with its most likely positive charged residues (Arg, Lys, His) in the region of Pim1, where the surface exposes mostly negatively charged residues. Especially Arg6 of PIMTIDE, which reaches close to the ATP-binding pocket, interacts with three carboxylic acid side chains of the protein. The corresponding amino acids are Asp131, Asp128, and Glu171. Also, Arg4 is involved in strong protein interactions. Its long side chain fits into a small pocket next to the active site surrounded by four interaction partners (Asp239, Asp234, Asp170, and Thr134). The side chain of His7 (PIMTIDE) interacts with the carboxylate group of Glu243. The backbone nitrogen of His7

interacts with the side chain of Glu171. The hydroxy group of Ser9 forms an H-bond to one of the carboxylate oxygen atoms of Asp167. The binding affinity has been determined by ITC experiments described by Bullock et al. It was determined to have a  $K_D$  value of approx. 60 nM.<sup>46</sup> PIMTIDE also fulfills the Pim1 consensus sequence, first reported by Friedmann et al. in 1992. The general sequence is R-X-R-X-X-S/T, where X stands for a convertible amino acid<sup>47</sup>. The equivalent amino acids of PIMTIDE are Arg4, Arg5, Arg6, His7, Pro8, and Ser9. Thus, the role of Arg4, Arg6, and Ser9 is important for the binding of PIMTIDE to Pim1. In relation to the PKA inhibitory peptide PKI, PIMTIDE contains the hydroxy group at Ser9, which could be phosphorylated by Pim1.

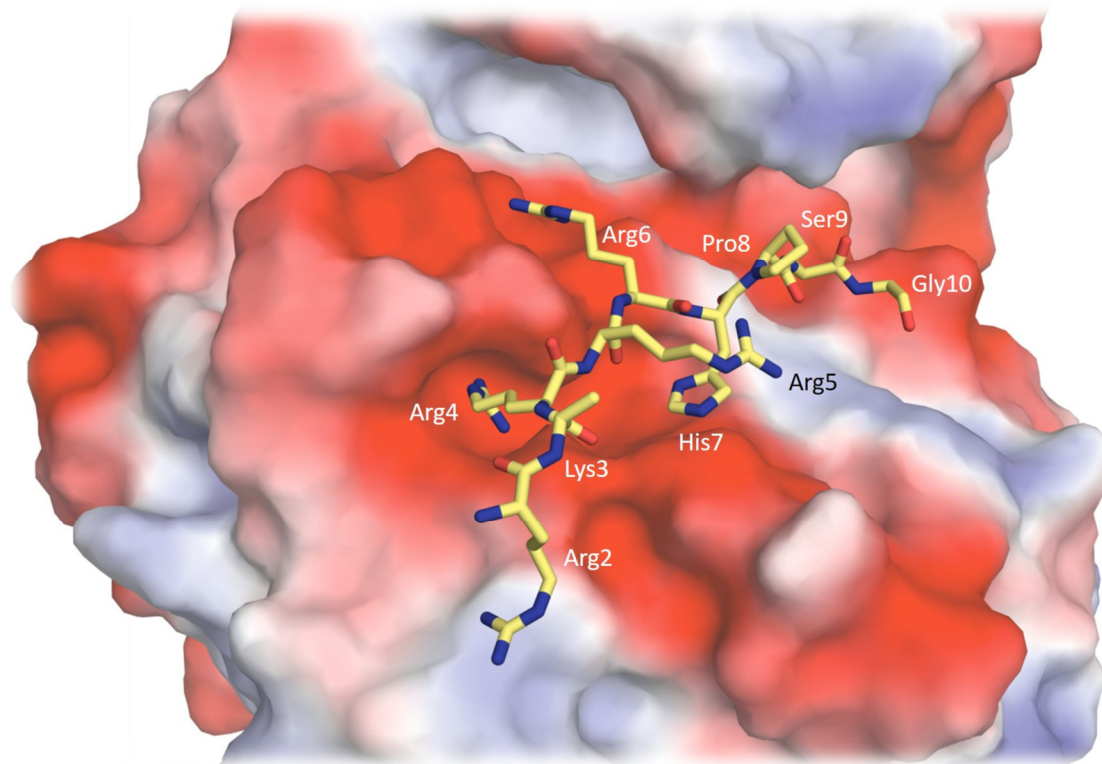


Figure 20: Crystal structure of Pim1 kinase with bound PIMTIDE (PDB 5N4V). The protein surface is coloured corresponding to its electrostatic potential (red = negative, blue = positive, white = neutral). PIMTIDE is displayed as sticks with light yellow coloured carbon atoms. Nitrogen atoms are coloured in blue and oxygen atoms in red.

## 1.4. Fragment-based drug design (FBDD)

The discovery and development of new drugs for the treatment of new and already known diseases is important to improve human quality of life and to enhance the chance of survival of diseases with bad prognoses, such as cancer or infection with multi-resistant germs. In the field of chemical lead discovery, several techniques have been used to identify highly potent candidates suitable for clinical trials. Using the presence of known inhibitors and natural compounds for the optimisation of a high-affinity drug has been successfully demonstrated in the past. The prerequisite to know binder limits the range of imaginable chemical space. Thus, new developments usually end up by providing novel drugs resulting from the same class as the starting ligand. This increases the risk for cross-resistance. A good reason to establish a strategy including a wider chemical space. High-Throughput-Screening (HTS) is commonly used in the pharmaceutical industry for chemical lead discovery. Large libraries with millions of compounds have been established to identify potential hits for a relevant protein target. Assays and crystallographic screenings are used to find novel hits as starting points for a follow-up optimisation leading to an innovative novel lead structure. Fragment-based drug design (FBDD) takes up this idea of screening libraries, but with a different focus on the library design. Instead of creating libraries with millions of compounds that are close to a lead-like molecule, libraries for FBDD need only approx. 1000 entries to simultaneously cover sufficiently the chemical space for drug-like molecules.<sup>48</sup>

### 1.4.1. Fragments

The so-called “rule-of-three” (RO3) was generally used as a first guideline to categorise a molecule as a fragment. These rules are oriented at the Lipinski’s “rule-of-five,” which are used to classify a molecule to be well orally available.<sup>49</sup> These RO3 define a molecule as a fragment when its molecular weight is <300 Da, the number of hydrogen bond donors and acceptors is  $\leq 3$  and the clogP value is  $\leq 3$ . Additionally, the number of rotatable bonds should be  $\leq 3$  and polar surface area  $\leq 60 \text{ \AA}^2$  were assumed to be suitable criteria for building fragment libraries.<sup>50</sup> Today it has been shown that these rules should not be overstated because they limit the variety of chemotypes and leave less room for chemical modification after fragment hit identification. This was demonstrated in a fragment project by colleagues from our research group in 2011.<sup>51</sup>

The great benefit of fragments is their reduced complexity, which leads to a reduced attrition rate in comparison to hits found by normal HTS. Although fragments usually exhibit low affinity to a protein target, they bind more often than compounds with higher complexity. Thus, screens with fragment libraries, sampling a wide range of chemical space, resulting in a higher hit rate than screens with usual HTS libraries, which are up to 100 times larger. The affinity of fragments to

protein targets is expected to be in the mM range. This is obviously caused by the lower number of putative interactions to be formed. In addition, a good solubility of a fragment compound is favorable to increase the probability of protein binding due to the low binding affinity.

Fragments may also have a high ligand efficiency (LE) when they bind to a protein target. This is defined by the free energy of binding ( $-\Delta G$ ) divided by the number of non-hydrogen atoms (HA), see equation (1).

$$LE = -\frac{\Delta G}{HA} \quad (1)$$

Fragments that show an LE value above 0.3 kcal seem to have good chances in the subsequent optimisation process to grow from an mM binder to an nM lead-like molecule.<sup>5248</sup>

### 1.4.2. Concept of FBDD

After setting up a fragment library, the screening of a target protein can directly be started by identifying hits via biophysical methods such as X-ray crystallography or NMR spectroscopy. Furthermore, a less demanding pre-screening can be used to identify putative binders in a fast and time-saving procedure, such as biological function assays or thermal stability assays. Figure 21 shows a schematic overview of the FBDD process. Once fragment hits and their binding positions are found and analyzed, their specific binding motifs give useful information about ligand recognition properties. Thus, fragments can be considered as scouts exploring the binding pockets of proteins. Multiple potent hot spots for protein-ligand interactions can be used as a search technique. Afterwards, the most prospective hits are transferred to an optimisation phase. This phase includes one of the following approaches: fragment growing, fragment merging or fragment linking. A schematic example of fragment linking is displayed in Figure 22. By accurate design, the weak-binding fragments are transformed into binders in the nanomolar range. Promising fragments must be detected via X-ray crystallography experiments or NMR spectroscopy studies before such optimisation can proceed. This thesis primarily focusses on the identification of suitable fragment binders.

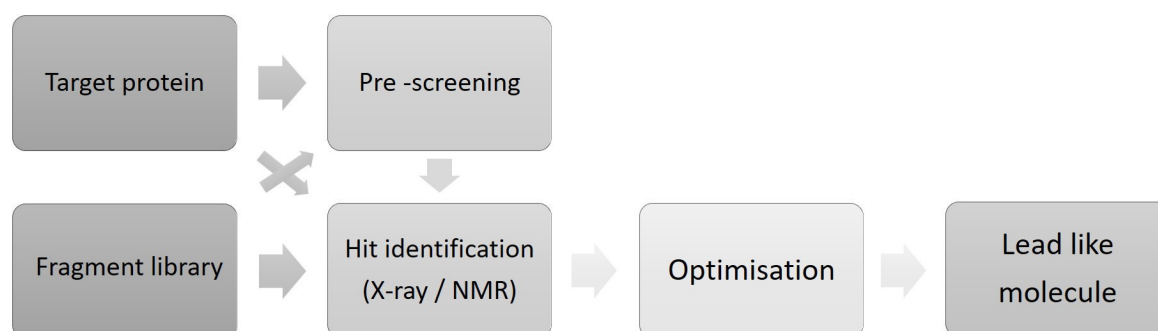


Figure 21: Schematic overview of the FBDD process.



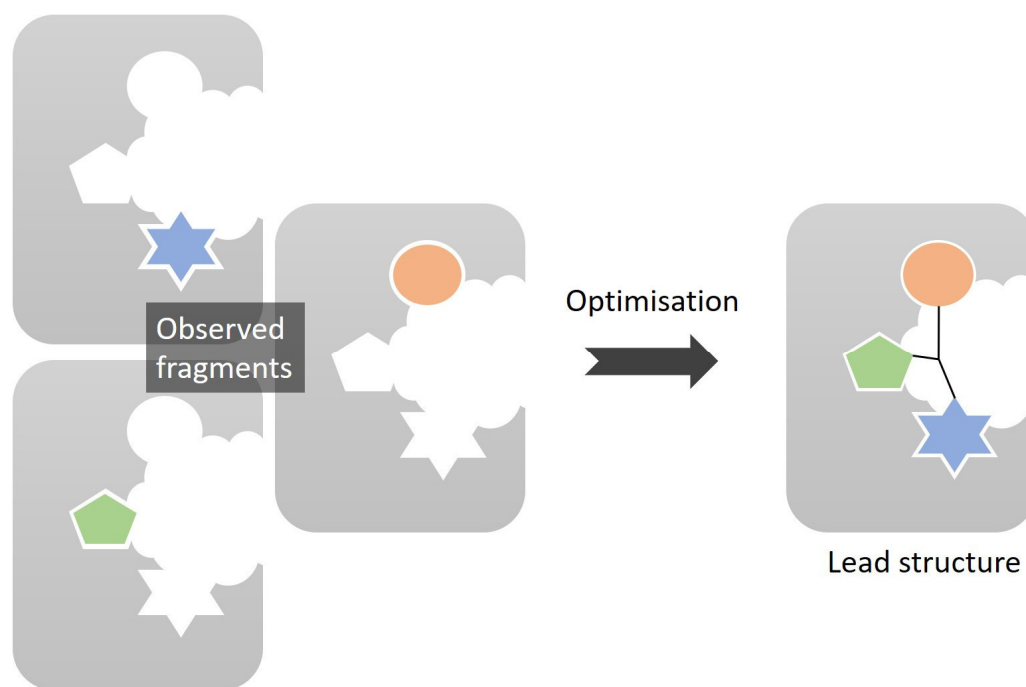


Figure 22: Schematic overview of a fragment optimisation process, using the example of fragment linking. Three fragment molecules bind at three different positions in a protein binding pocket. These fragments are then further linked to form one molecule, which should consequently have a higher affinity to the protein target.

### 1.4.3. Fragment libraries

Since the beginning of FBDD at the end of the 1990's several fragment libraries have been established in academia and industry. Meanwhile, companies offer fragment libraries with thousands of compounds. Nevertheless, while purchasing or building a library, there are several rules and guidelines available for choosing the right fragments. Using the RO3 was a commonly adopted guideline at the beginning of fragment library design. Actually, the use of this concept is still widespread, but beside the RO3 additional factors were found to be important to design a suitable fragment library. The library size is partly dependent on the screening method used for hit identification. Methods with lower detection sensitivity can only discover fragments of higher potency and, consequently, fragments of higher complexity are required for reliable hit identification. However, higher fragment complexity tends to lead to a higher mismatch rate in terms of protein-ligand interactions. Highly reactive chemical groups or those which cause aggregation in solution<sup>53</sup> should obviously be avoided. The optimisation process after fragment hit identification is also important for the library design. Therefore, fragments should contain chemical groups/positions feasible for synthetic fragment growing.<sup>54</sup> The fragment compilation should include fragments with essential pharmacophores, which enhance the probability for successful fragment binding<sup>55</sup>.

### 1.4.3.1. The 361 fragment library

The largest amount of investigated fragment compounds studied in this thesis came from an in-house library with 361 entries. This library was established by Köster et al. in the research group of G. Klebe at the end of the 2000's with commonly available fragments. Databases offered by several compound suppliers were initially screened to find compounds with a number of non-hydrogen atoms  $\leq 20$ , comprising carbon, nitrogen, oxygen, fluorine, chlorine, bromine and phosphorous atoms. Additionally, only entries available in quantities of at least 100 mg were preselected. A further filtering process included the elimination of highly reactive and toxic chemical groups.

In almost all cases the RO3 was not followed strictly. One example is the limitation by molecular weight: Due to the inclusion of heavy atoms such as bromine, some fragments exceeded the RO3-limit of 300 Da to a maximum of 359 Da. Especially the use of such bromine-containing fragments for crystallographic screenings supports the hit identification due to the strong scattering power of bromine atoms. Therefore, the size of the collected fragments is regulated to the number of non-hydrogen atoms (between 8 – 20) and not to the molecular weight. Also in the case of the logP value, a few fragments exceed the cut-off of  $\leq 3$ , the highest logP-value for a molecule of this library is 5.9. Nevertheless, the mean value is 1.58. The number of H-bond acceptors is normally at 3 for the RO3. Similar to the Lipinski's rule of five, where the magic five is multiplied by a factor of two to allow 10 hydrogen acceptors, this factor was also used to set the threshold limit up to six. Only some fragments exceed this limit (up to seven). Thus, the amount of hydrogen-bond acceptors varies between 1 to 7 with a mean value of 3.7. Although the highest value of hydrogen bond donors in one fragment is four, only a few library members exceed the limit of three. The mean value of 1.3 is absolutely in the RO3 range. The upper limit for the total polar surface area (TPSA) augmented from 60 to 80 Å<sup>2</sup>. A few fragments also exceed this limit. As a consequence, the TPSA ranges from 15 to 126 Å<sup>2</sup>. Nevertheless, the average TPSA value remains below the limit of 52 Å<sup>2</sup>. Although the general RO3 guidelines were exceeded by a few specific fragments, the mean values of the library selection broadly fulfill the RO3, excluding the H-bond acceptor rule. A summary of

<b>Parameter</b>	<b>Min</b>	<b>Max</b>	<b>Mean</b>
<b>No. of heavy atoms</b>	8	20	15
<b>MW [Da]</b>	122	359	224
<b>H-bond-donor</b>	0	4	1.3
<b>H-bond-acceptor</b>	1	7	3.7
<b>log P</b>	-1.3	5.4	1.6
<b>free rotatable bonds</b>	0	7	1.7
<b>TPSA [Å<sup>2</sup>]</b>	15	126	52

Table 7: The physicochemical parameters of the 361 fragment library.

these parameters is listed in Table 7. In detail, 141 compounds of the initial 364 library are in the range of the RO3. Consequently, 223 fragments are not in accordance with these rules.

Other aspects were the prevention of similar chemical scaffolds and the requirement of at least one ring system per fragment. Whenever a fragment contains a stereocentre, the compound was usually purchased as a racemic mixture. This concerns 55 library entries in total. The solubility of the compounds was tested experimentally, whereby a value above 1 mM was determined for 76% of the library.<sup>51</sup>

The library contained initially 364 entries. Three compounds were redundantly incorporated in the library but were independently analyzed by several screening assays. This internal validation criterion enabled the chance to detect inconsistencies within the applied assays and allowed testing the reproducibility of assay data.<sup>56</sup>

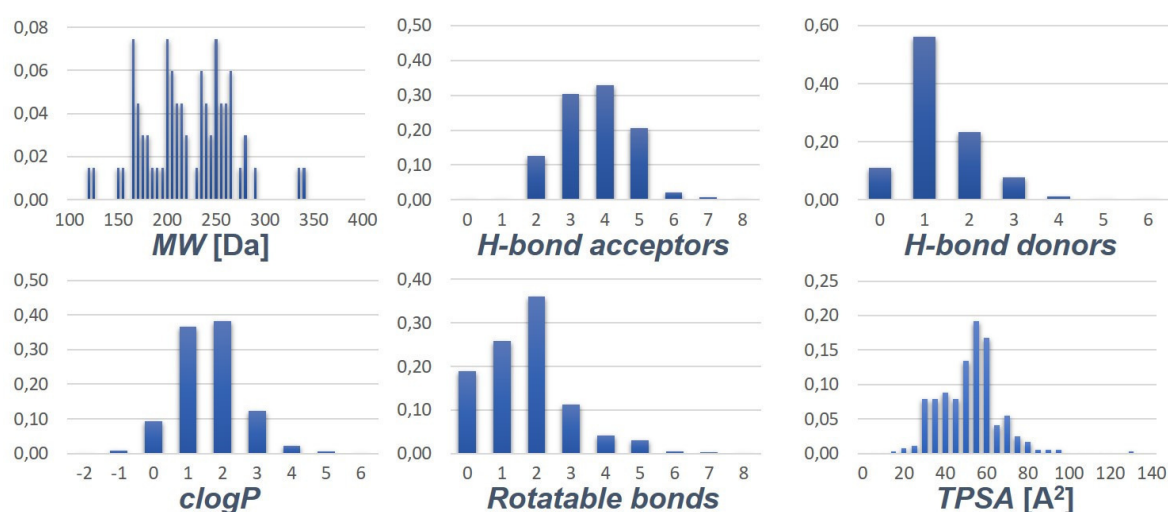


Figure 23: Values for structural and physicochemical properties of the 361 fragment library. The Y-axis represents the relative content of the fragment library, where 1,00 stands for the whole library.

### 1.4.3.2. The 96-well plate library

This library, consisting of 96 entries, is a compilation of fragments resulting from several fragment libraries following the intention to generate a small but broadly applicable library. The composition of the library is intended to provide a high crystallographic hit rate covering diverse chemotypes and being appropriate to several different protein targets using the fragment soaking method. Therefore, knowledge and experience about well-tested libraries are necessary. The above described 361 fragment library was thoroughly tested by several screening methods on the model aspartic protease endothiapepsin resulting in 71 hits identified by crystallographic screening.<sup>56</sup> There were 52 of these 71 hits incorporated into the 96-well plate library building the basic set. To choose the best diversity among these 71 hits, the fragments were clustered and inspected manually so that similar fragments were removed. The second largest part is adopted from a 96-member library, which was established in a collaborative project with the Helmholtz-Zentrum in Berlin and the research group of Prof. G. Klebe.<sup>57</sup> This section includes 36 fragments. Crystallographic hits of several proteins were chosen to complement the new library. Apart from the known protease endothiapepsin, protein crystals of prolidase were used to detect crystallographic screening hits from this library. Five natural-product-like fragments provided by AnalytiCon were chosen to enlarge the chemical space of the library, completing the 96-well plate library. Finally, all compounds of the library were successfully tested in a crystallographic screen with endothiapepsin. This demonstrates their qualification as a general purpose for crystallographic screens. The testing of all fragments against meanwhile more than 10 targets showed that they are all accessible for a crystallographic screening by fragment soaking, which is a convenient criterium for fragment-based drug design.

#### 1.4.4. Methods for pre-screening

Due to their weak binding affinity (usually in the high  $\mu\text{M}$  to  $\text{mM}$  range), it is more difficult to detect fragments than more complex and larger ligands resulting from common HTS. Therefore a method for fragment screening must exhibit a 100-fold higher sensitivity.<sup>55</sup> Several techniques are suitable to detect potential fragment binding, but they are not equal in popularity. The analysis of 165 published fragment screens by Chris Swain in 2013 showed that the five most used detection technologies were nuclear magnetic resonance spectroscopy (NMR), X-ray crystallography, surface plasmon resonance based biosensor technology (SPR), bio-functional assays and thermal shift assay (TSA).<sup>58</sup> These methods differ in the procedure, usage of material and in their sensitivity and specificity. SPR measurements do not need a large amount of protein material and are relatively fast, whereas the structure-related analysis methods such as protein crystallography and protein NMR can consume a lot of protein material and require a fair amount of time. The process of sample preparation and data measuring including the analyses of the results generally takes weeks of effort (Figure 24). A well-chosen method can, therefore, save time and money. Especially when the protein production and purification are done in-house, the amount of time taken to complete the experiment becomes even more important.

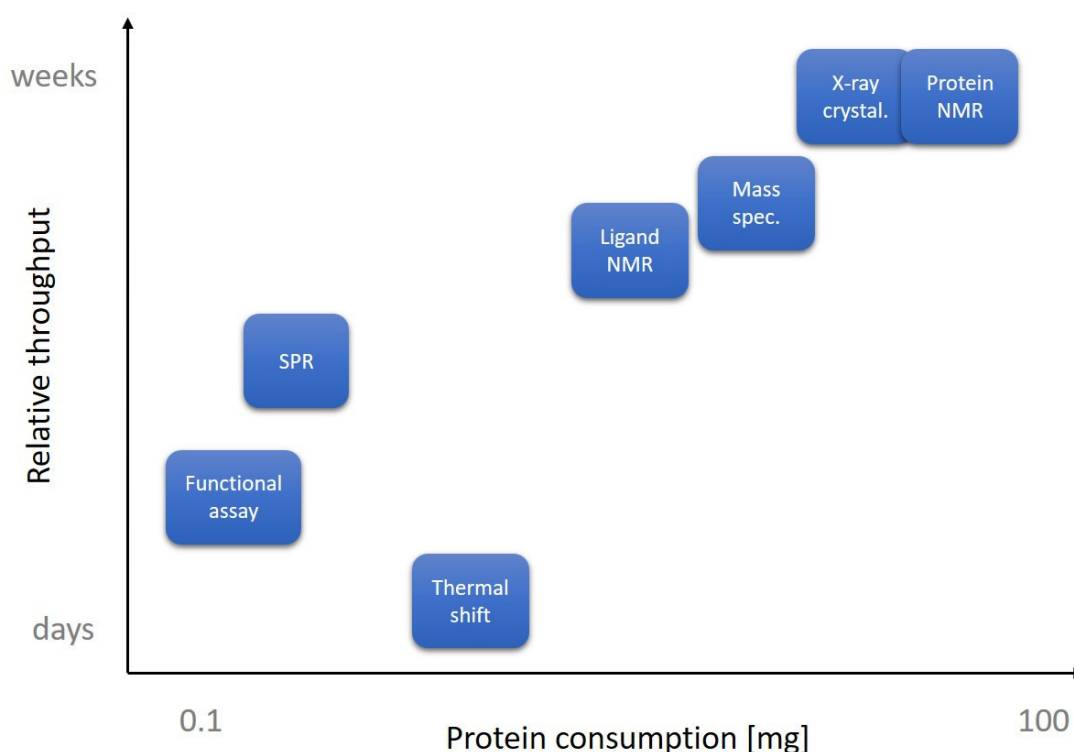


Figure 24: The graph displays the relative throughput time and the average protein consumption required for a fragment detection method. Techniques with high protein consumption are located on the right hand side, techniques with a small consumption are located on the left. Methods, which can be accomplished in a view days are at the lower level, whereas methods which need several weeks can be found on the top of this graph. (This picture is adapted from<sup>58</sup>).

Since the structural information of a bound fragment is absolutely necessary for FBDD, X-ray crystallography or protein NMR is a must but requires major resources to be routinely used without pre-screening methods, when results shall be received in a short period of time. Pre-screening methods should be fast to execute so that a hit list with the most promising candidates of a library can be early screened to obtain first structural insights. Apart from a bio-functional assay, the thermal shift assay is one of the fastest methods with low protein consumption to detect fragments as potential hit candidates. Therefore, this method was chosen as a pre-screening procedure in several sections of this thesis.

#### **1.4.5. The Thermal Shift Assay (TSA)**

The TSA is a fluorescence-based method to identify compound-protein interactions or to screen buffer conditions in order to assess their influence on protein stability. With the aid of the fluorescence dye Sypro orange, which binds to the hydrophobic protein residues exposed during the unfolding process, the protein denaturation process can be detected by changes in the fluorescence intensity.<sup>59</sup>

A real-time PCR device is normally used to perform this method. For the screening of the 361 library, the iCycler5 from Bio-Rad was used. The protein was solved in a buffer solution containing the fluorescence dye Sypro orange and was prepared in a 96-well microtiter plate. In addition to this solution, the wells contained diverse compounds pre-solvated in DMSO stock solutions or pure DMSO as a reference. The prepared and sealed plate was transferred into the real-time PCR instrument to start the measurement. The temperature was increased in a step-wise fashion and with consequent fluorescence control. The starting temperature is important to ensure that the protein did not already start to denature directly at the beginning of a measurement. Therefore, a stabilisation phase prior to denaturation should be performed. Once the temperature reaches the critical point of denaturation, the protein starts unfolding, and the nonpolar amino acid residues buried in the solvent-inaccessible part of the folded protein are exposed. These now-accessible lipophilic parts present new binding positions for a solvated fluorescence dye. Once bound, the dye emits a strong fluorescence signal that is detected by the PCR device. Consequently, the fluorescence level increases until the maximum binding of the dye is reached. By increasing the temperature further, the protein starts to form aggregates and precipitates so that the dye is displaced from its binding sites at the protein surface and therefore returns back to the solution. This is the main explanation why an ongoing decrease in fluorescence intensity is observed after the absorption maximum (Figure 25). The melting point ( $T_M$ ) of the protein is defined as the point of inflection between the lowest and highest fluorescence of the final curve. A determination of

$T_M$  is more easily found by calculating the first derivative of the curve. The derivative shows  $T_M$  as a local minimum.

By comparing the melting points of ligand-free and ligand-added measurements, the impact of ligand binding on protein stability can be calculated. A negative shift of  $T_M$  means destabilisation of the protein and a positive shift, conversely, a stabilisation. This is mainly explained by the following: Destabilizing ligands bind to the unfolded form of the protein, whereas stabilizing ligands bind to the native form.<sup>60</sup>

With respect to its feasibility as a fast pre-screening method, TSA was chosen and by the use of a 96-well-plate in a real-time PCR device and measuring each compound in triplicate, the screening of the 361 library was accomplished within a week. The protein amount needed for each plate is normally below 1 mg. Usually, not more than 10 mg of protein is needed to screen the entire library. Therefore, TSA is an ideal method to identify the most promising protein binders. Subsequently, the resulting list of promising binders is a good starting point for a crystallographic screening.

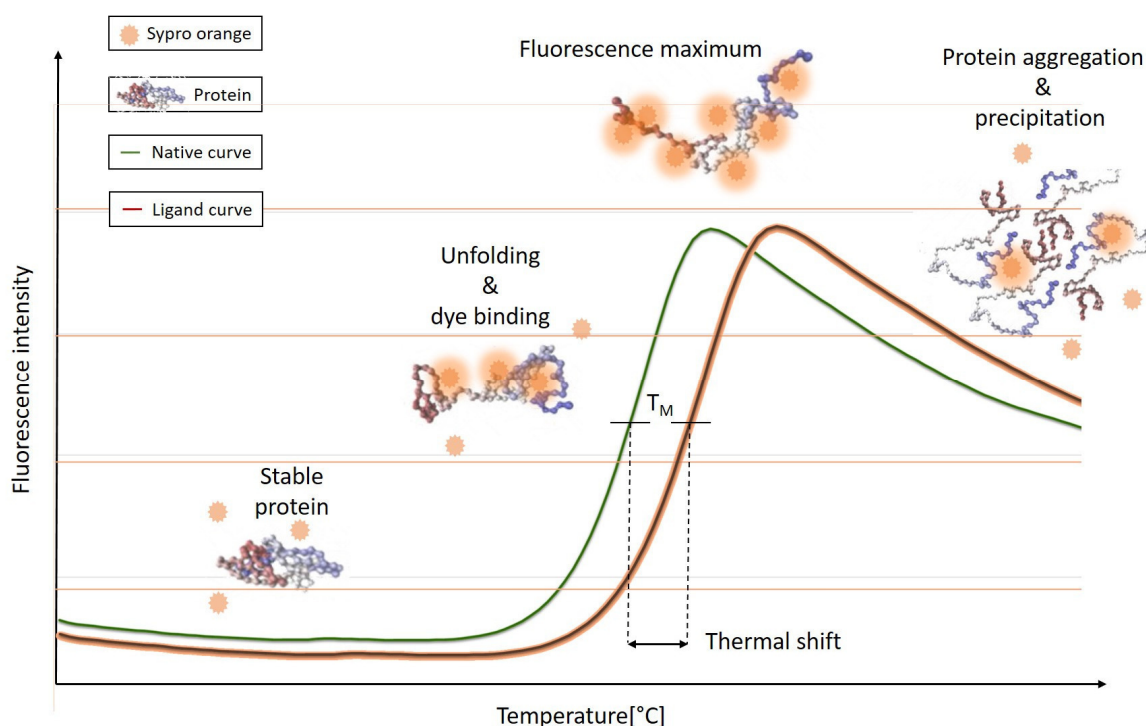


Figure 25: TSA measurement progression. The graph shows two general TSA curves recording the fluorescence intensity versus the temperature. The ligand shows a stabilizing effect on the protein, which is indicated by the shift of  $T_M$  to higher temperature.

#### 1.4.6. Structure determination by protein crystallography

FBDD uses structure-related information to develop a potential drug that ideally matches the drug target. Generally, structure-based drug design results in a more potent drug in 90% of all cases, whereas procedures without structure information only show a success rate of 30%.<sup>61</sup> Ideally, pre-screening methods should be completed fast and give useful indications for protein-ligand interactions. However, methods with high effort and complexity are needed to elucidate structural information. Beside protein-NMR, X-ray crystallography is a commonly used method and the method of choice in this thesis.

As the name protein crystallography implies, this method is based on the utilisation of crystals formed by protein molecules. Purified protein molecules in solution can be forced to arrange in a highly-ordered lattice. This is reached by reducing the protein solubility in buffer solution by continuously rising the precipitant concentration. Thus, small crystal-nuclei form, which can grow into solid protein crystals. Protein crystals can grow in the presence (co-crystallisation) or absence of a ligand molecule. Another method to form a ligand and protein crystal is the method of soaking. Both methods (co-crystallisation and crystals soaking) can be used to prepare crystals for diffracting experiments. Generally, the preparation includes also the protection of protein crystals by a designated cryo-buffer. Afterwards, the protein crystals are flash frozen in liquid nitrogen. The low temperature of approx. 100 K is kept during the measurement preventing the crystals from severe radiation damage. Once exposed to the X-ray beam crystals scatter the beam, so that the resulting diffraction pattern can be detected and subsequently analyzed. Several images of the diffraction pattern using different crystal orientations are combined to form one data set. The X-ray source can be a rotating anode (usually copper) or synchrotron radiation, which is used to produce X-ray beams with much higher intensity resulting in data sets with higher resolution. The higher the resolution of a data set, the higher the content of information. Higher resolutions are especially necessary for the identification of small fragment molecules, which generally show low affinity to proteins. The main synchrotron facility, frequently used for data collection in this thesis was the BESSY II in Berlin.<sup>62</sup> Additionally, the ESRF synchrotron at Grenoble<sup>63</sup> and the ELLETRA at Trieste<sup>64</sup> were used for data collection. Once a data set of a crystal is collected, it is analyzed by specialised software programs to extract the structure information of the sample. Software tools for data processing are for example *HKL2000*<sup>65</sup>, *MOSFLM*<sup>66</sup>, *XDS*<sup>67</sup> or *XDSAPP*<sup>68</sup>. *XDSAPP* was used for all crystal samples in this thesis. Each program uses and analyses the thousands of diffraction spots contained in hundreds of diffraction images of a data set to create a structure factor file. After data processing, the so-called phase problem of X-ray crystallography has to be solved to determine the protein structure. Several techniques have been established to obtain phase



information.<sup>69</sup> Most frequently used techniques are molecular replacement (MR) and single-wavelength anomalous scattering (SAS) experiments. For the usage of MR, an already existing model or a homology model must be available. In this thesis, MR is the only method used for PKA and Pim1 experiments since it is a fast procedure. Subsequently, the sample structure enters a refinement process, where fine adjustments of the protein model, addition of water molecules, buffer contained molecules, and bound ligands are processed. The refinement process is a cycle of manually inspection and model building followed by an automated optimisation of the structure. Widely used software for the automated part is *REFMAC*<sup>70</sup>, *SHELXL*<sup>71</sup> or *PHENIX*<sup>72</sup>. The program *PHENIX* was the software chosen for structure refinement in this thesis. The program *COOT*<sup>73</sup> was chosen for manual model building and visual inspection. It also provides some tools for the validation of the structure model. Specialised software such as *PROCHECK*<sup>74</sup> or *MOLPROBITY* can be used to validate the model-build structure in more detail. With their help still remaining modelling issues can be identified.<sup>75</sup> Finally, the structure is ready for its deposition in the worldwide data bank for protein X-ray structures, the Protein Data Bank.<sup>76</sup> Although the current overview of the process of protein crystallisation and structure determination by X-ray crystallography is rather simplistic, the complexity of the entire process is already obvious. It takes more time, material and costs than other screening methods for hit identification, but it provides the necessary structural information needed for FBDD.

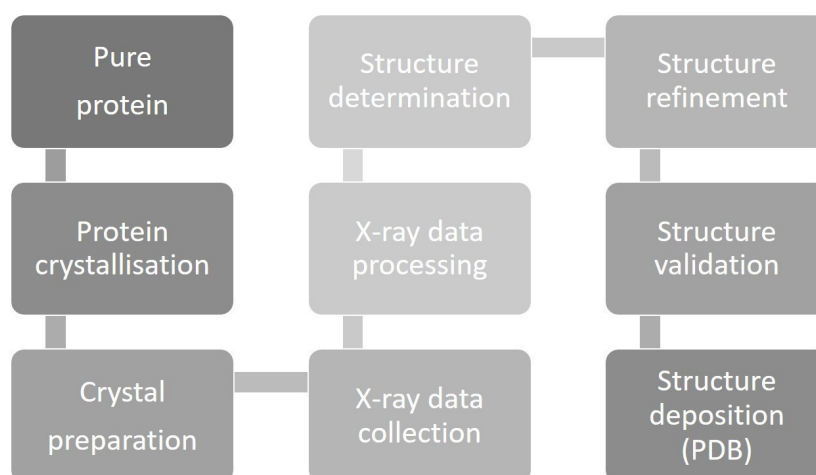


Figure 26: The main steps necessary in FBDD from pure protein to deposited crystal structure.



## **2. From thermal shift assay to crystallographic hits – A comparative fragment screening on PKA and Pim1**

## 2.1. Introduction

The field of fragment-based drug design (FBDD) has grown in the last decades and shows results with potent inhibitors such as the famous BRAF kinase inhibitor Vemurafenib (Zelboraf) developed by Plexxikon and Roche and approved in the US for the treatment of BRAF-mutated metastatic melanoma in 2011.<sup>77</sup> Other companies and groups in academia were able to discover novel ligands using FBDD successfully.<sup>78</sup> FBDD is a useful tool to find and develop highly selective compounds. This is especially important in the field of kinase drug discovery to avoid side effects on similar kinases.<sup>79 80</sup> This project focused on a general purpose fragment library with 361 fragments<sup>51</sup>, which were screened against two different kinases. The screening started with a pre-selection of fragments by using the thermal shift assay (TSA) with a subsequent evaluation of the best fragments via X-ray crystallography. The two kinases, which were investigated in this fragment screen are the cAMP-dependent protein kinase A (PKA) and the oncogenic associated protein kinase Pim1 (Proviral integration Maloney). With PKA a well-investigated kinase ubiquitous in eukaryotic organisms was chosen. It is an ideal example of a model kinase. The Pim1 is different to the PKA a drug target for cancer therapy.<sup>42</sup> Here it will be demonstrated that enrichment of the crystallographic hit rate of ca. 48% for PKA and 85% for Pim1, respectively, was reached using TSA as a pre-screening method. The diverse stabilisation effects of fragments on both proteins in TSA will be discussed, as well as the detected crystallographic binders and the observed convincing correlation between the absolute amount of thermal shift and crystallographic binding mode. Furthermore, it is shown that the observed crystallographic binders complement the pool of known kinase binding motifs. Additionally, three crucial differences in the ATP-binding pocket of PKA and Pim1 are highlighted using the example of the only shared crystallographic hit.

## 2.2. Materials and methods

### 2.2.1. Protein production and crystallisation

For the purification of PKA, the full length of the protein (1-350) from *Cricetulus griseus* (UniProt ID P25321) was previously cloned into the NdeI/BamHI site of pET16bTev (Novagen) with an N-terminal His<sub>7</sub>-tag connected by a tobacco etch virus (TEV) protease cleavage site.<sup>81</sup> This vector was used for a transformation into a BL21 (DE3)/pLysS *Escherichia coli* (*E. coli*) host strain (Agilent Technologies). The protein was recombinantly expressed in ZYM 5025 medium.<sup>82</sup> The expression is induced by adding 1 mM IPTG after 9 hours of cell growth at 310 K. Afterwards, the temperature was reduced to 293 K, and the cells were incubated for approx. 58 hours. The resulting cell-pellet was shock frozen in liquid nitrogen and resolved in a buffer containing 50 mM NaH<sub>2</sub>PO<sub>4</sub>, 500 mM NaCl and 10mM imidazole. After cell disruption and centrifugation, the protein purification was started from the supernatant by conducting a Ni<sup>2+</sup>-NTA (nitrilotriacetic

acid) chromatography (HisTrap HP, GE Healthcare) with subsequent cleavage of the His<sub>7</sub> tag by TEV protease during dialysis over 8 hours. A second Ni<sup>2+</sup>-column was performed subsequently. To reduce the imidazole and salt concentration, the flow-through of this run was buffer-exchanged to 50 mM HEPES, 50 mM NaCl and 5 mM DTT. Utilizing the strong cation-exchange column MonoS (GE Healthcare), different phosphorylation states of PKA were separated by applying a gradient from 50 mM to 200 mM NaCl. The collected fractions of the three phosphorylation states were separately pooled and concentrated in the relevant buffer for TSA or protein crystallisation (see below).

For crystallisation PKA was concentrated to 8-10 mg · mL<sup>-1</sup> and buffered in a solution containing 100 mM MES/BIS-TRIS (pH 6.9), 1.0 mM DTT, 0.1 mM EDTA and 75 mM LiCl. After adding 1.5 mM of the non-ionic detergent MEGA 8 and 0.7 mM of the cAMP-dependent protein kinase inhibitor peptide PKI (IAAGRTGRRQAIHDILVAA; Sigma Aldrich), the crystal growth was induced via microseeding. In case of PKI-free crystals, this peptide inhibitor was omitted. Using the vapour diffusion method crystals grew in 3 µL sitting drops at 277 K. The reservoir solution with 500 µL per well contains 22—24% (v/v) methanol. Protein crystal seeds were obtained a few hours after preparation. Fully grown crystals were ready for data collection after 1-2 weeks. In case of PKI-free PKA crystals, 3 weeks were required until the first crystals grew to a noticeable size.

The expression and purification of Pim1 kinase were similar to the procedure described for PKA. The full-length human Pim1 (isoform 2), previously cloned into the pLIC-SGC vector with an N-terminal His<sub>6</sub>-tag connected to a TEV cleavage site, was transformed into a BL21 (DE3)/pLysS *E. coli* host strain (Agilent Technologies). The expression was performed in ZYM 5025 medium, with an additionally 1 mM IPTG-induced expression after 9 hours of cell grow at 310 K. After 58 hours of further incubation at 293 K the cells were harvested via centrifugation and after flash freezing resuspended in a buffer containing 50 mM HEPES, 500 mM NaCl and 5% (v/v) glycerol. After the cells were lysed, the supernatant was purified after centrifugation by Ni<sup>2+</sup>-NTA chromatography (HisTrap HP, GE Healthcare). In the subsequent dialysis, the His<sub>6</sub>-tag was cleaved by TEV protease, and phosphorylated Pim1 residues were dephosphorylated by λ-protein phosphatase (Sigma Aldrich). The protein was further purified by a second Ni<sup>2+</sup>-NTA run and afterwards rebuffered in a 50 mM HEPES, 50 mM NaCl and 5 mM DTT solution (pH 7,0) for the use of an anion-exchange chromatography column Mono Q (GE Healthcare). The protein was eluted with a gradient from 50 mM to 150 mM NaCl. The collected fractions corresponding to the protein peak were pooled and concentrated in the relevant buffer for TSA and for protein crystallisation (see below).

Pim1 crystallisation was always performed as co-crystallisation with fragments since the reproduction of published crystallisation procedures<sup>83</sup> leading to uncomplexed Pim1 crystals was not successful. Therefore, purified protein was concentrated to approx.  $7.0 \text{ mg} \cdot \text{mL}^{-1}$  in a buffer containing 50 mM HEPES, 250 mM NaCl, 5% (v/v) glycerol and 5 mM DTT. After adding the consensus peptide PIMTIDE (ARKRRRHPSGPPTA-amide) at 1.0 mM concentration, a 1 M fragment stock solution in DMSO was used to adjust the final fragment concentration to 100  $\mu\text{M}$ . The crystals grew in a sitting drop plate via vapour diffusion. One plate was used to test 24 diverse buffer conditions varying the kind of salt ( $\text{Li}_2\text{SO}_4$ ,  $\text{MgCl}_2$ , NaCl, LiCl,  $\text{CaCl}_2$ ,  $\text{MgAc}_2$ ) and the amount of precipitant PEG3350 (6%, 12%, 18% and 24% (w/w), respective). Besides these ingredients, every condition contained BIS-TRIS-Propane 100 mM, 10% ethylene glycol and 0.3% (v/v) DMSO at pH 7.0. The protein solution was mixed in a 1:1 ratio to a total drop volume of 4  $\mu\text{L}$ . Depending on the co-crystallised fragment, first crystals were observed 3-7 days after sealing the plate and crystals of sufficient size and quality for X-ray experiments were usually obtained within 3-4 weeks. Diverse forms of PKA and Pim1 crystals are shown in Figure 27.

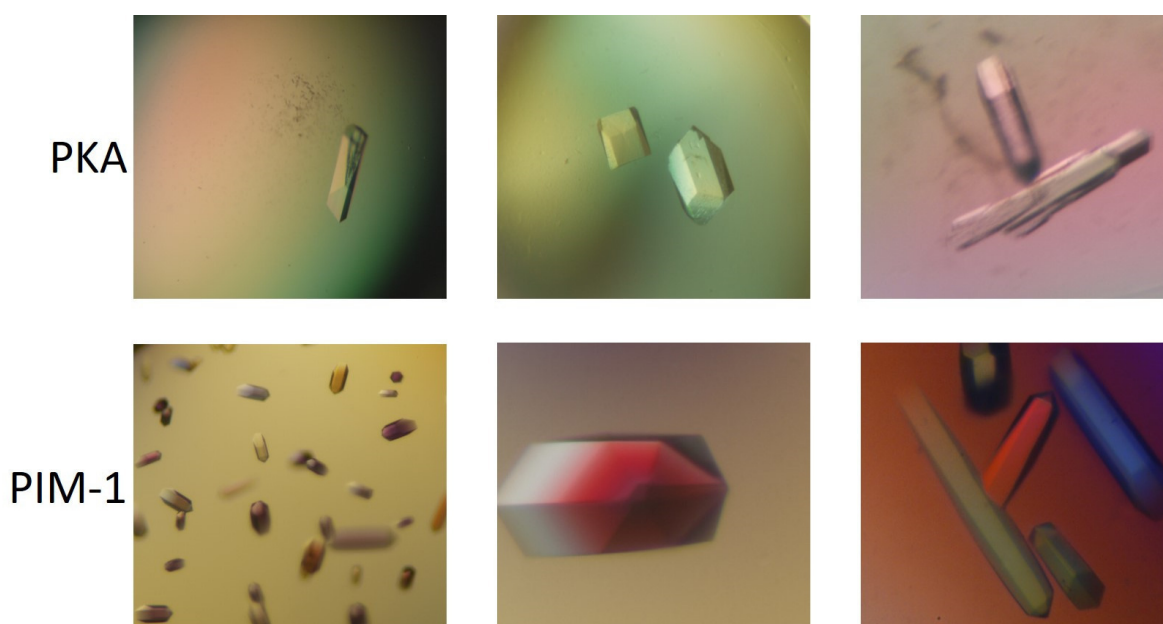


Figure 27: Protein crystals of PKA and Pim1. The shape of the crystals varied for either protein. In addition to long and thin rods, also short and brick-like crystals were obtained. Nevertheless, the Pim1 crystals always showed hexagonal shape.

### 2.2.2. Thermal shift assay

TSA was performed with a real-time PCR Thermo Cycler iQ5 (Biorad) using the fluorescence dye Sypro Orange. After an initial test for obtaining the ideal assay buffer conditions for each protein, the library compounds were measured in triplicates on 96-well plates, so that the median of their melting points could be compared to the value of the native protein. Each plate contained mixtures

for a triplicate measurement of the native protein so that the stabilizing effect of a fragment on the thermal shift could always be compared to that of native protein within the same measurement series. In every well a final volume of 40  $\mu\text{L}$  was pipetted, which contained 38  $\mu\text{L}$  mixture of primary buffer (50 mM HEPES at pH 6.9 for PKA ; 50 mM HEPES at pH 7.0 and 200 mM NaCl for Pim1) and Sypro Orange in a 500:1 ratio, 1  $\mu\text{L}$  of a DMSO-fragment-stock-solution (100 mM) and 1  $\mu\text{L}$  of protein solution. The protein concentration of both protein solutions was set to 7.0 mg  $\cdot$  mL<sup>-1</sup>. For the measurement of the native protein triplet, we used an equal volume of pure DMSO instead of a fragment stock solution.

### 2.2.3. Crystal soaking

As described before, only PKA crystals were used for soaking experiments. For PKA the cryo buffer was used for fragment soaking, which contained a final concentration of 10% (v/v) fragment-stock-solution (1M fragment in DMSO), 30% (v/v) MPD (2-Methyl-2,4-pentanediol) and 60% (v/v) crystallisation solution. The crystals were stepwise transferred into solutions of increasing concentration of MPD (up to 30% (v/v)) to prevent the crystals from being exposed to major osmotic stress. Because longer soaking times had detrimental effects on the crystal integrity and quality, the soaking time was varied between 10-15 minutes. Subsequently, the crystals were mounted in cryo-loops and flash frozen in liquid nitrogen. In contrast to PKA, the Pim1 crystals are protected with a cryo buffer containing 25% (v/v) glycerol and 75% (v/v) crystallisation solution.

### 2.2.4. X-ray data collection, structure solution and refinement process

The frozen crystals from PKA and Pim1 were further tested for diffraction quality using an in-house X-ray source. Crystals showing good diffraction pattern to resolutions better than 2.5 Å during this quality assessment were unmounted, stored in pucks under liquid nitrogen and sent to a synchrotron facility to obtain data sets at a higher resolution. The crystals of this series were measured at different beamlines (BL) at three different synchrotrons, namely BL14.1, BL14.2 and BL14.3 of BESSY II in Berlin <sup>62</sup>, BL ID-23-2 and ID-29 of the European Synchrotron ESRF in Grenoble <sup>63</sup> and BL XRD1 of the synchrotron facility ELETTRA in Trieste. <sup>64</sup>

After data collection, all data sets were processed with the software *XDSAPP*. <sup>68</sup> After processing, the resulting structure factor file was used to determine each structure by molecular replacement using the Software *PHASER MR*. <sup>84</sup> The search model during molecular replacement was PDB entry **4wih** <sup>85</sup> for PKA and PDB entry **3we8** <sup>86</sup> for Pim1. The program *COOT* was used for model building <sup>73</sup> and the program *PHENIX* <sup>72</sup> was used for refinement. The initial refinement step included simulated annealing with default parameters. Further refinement cycles comprised the

coordinate XYZ, occupancy, TLS (Translation-Libration-Screw-rotation) and individual B-factor refinement. Depending upon dataset quality, B-values were calculated via iso- or anisotropic refinement. In some cases, the placement of hydrogen atoms (H-atoms) resulted in an improvement of the R-free value of about 0.5%. The data collection processing statistics for each sample are listed in the crystallographic tables in the appendix of this thesis. The tables also include Ramachandran data generated by the program *PROCHECK*.<sup>74</sup> The molecular graphic figures were made with the program *PyMOL*.<sup>87</sup>

## 2.3. Results & Discussion

### 2.3.1. TSA analysis

Different melting points ( $T_m$ ) were obtained for both proteins:  $T_m = 45.5$  °C for PKA and  $T_m = 36.0$  °C for Pim1. In total 16 fragments could not be measured in TSA due to their reduced solubility in the assay buffer. The remaining fragments were dissolved in the assay buffer up to a final concentration of 2.5 mM. Finally, no fluorescence signals were observed for three compounds in the PKA screen and four compounds in the Pim1 screen. Altogether, this led to 341 analyzed fragments for PKA and 340 for Pim1. The threshold for defining a fragment as a significant hit was differently set for both proteins. This was determined by the individual stability of each protein-fragment solution, as described below. For the PKA a significance level of  $\Delta T_m = 1$  °C was chosen corresponding to the 3.3-fold standard deviation of this screen. Using this threshold, we identified 31 fragments. Using the same threshold with a standard deviation of 0.2 for Pim1 would have resulted in the identification 120 hits corresponding to almost one-third of all tested fragments as hits. Due to the practical limitation, the threshold for  $\Delta T_m$  was set to 3 °C, which still led to 52 TSA hits in the Pim1 screen. Obviously, the thermostabilizing effect of fragment binding on Pim1 seems to be higher compared to PKA. Fragment **F63** showed the highest stabilisation for PKA with  $\Delta T_m = 6.0$  °C, whereas fragment **F225** showed the highest one for Pim1 with  $\Delta T_m = 10.8$  °C. Additionally, 15 fragments with a  $\Delta T_m > 6.0$  °C for Pim1 demonstrate that fragments can stabilise Pim1 under the applied conditions much stronger than PKA. The PKA screen also suggests a larger number of destabilizing fragments than the Pim1 screen (Table 8). The individual  $\Delta T_m$  shifts exerted by the fragments on each kinase are listed in the appendix. All significant positive shifting hits for PKA ( $\Delta T_m \geq 1$  °C) and Pim1 ( $\Delta T_m \geq 3$  °C) are shown, sorted by their  $T_m$  values. The fragments, identified as hits in the TSA screens, were further investigated in the corresponding crystallographic screening.

Comparing all positive shifting hits of PKA and Pim1, there were only 5 fragments or 1.4% of the tested library, which were detected for both proteins (**F196**, **F222**, **F267**, **F304** and **F328**, Figure



29). In Figure 29 the fragments were sorted by their  $\Delta T_m$  shift on PKA. Several fragments showing a significant  $\Delta T_m$  for PKA, do not possess a significant value of Pim1 or even show a negative  $\Delta T_m$ .

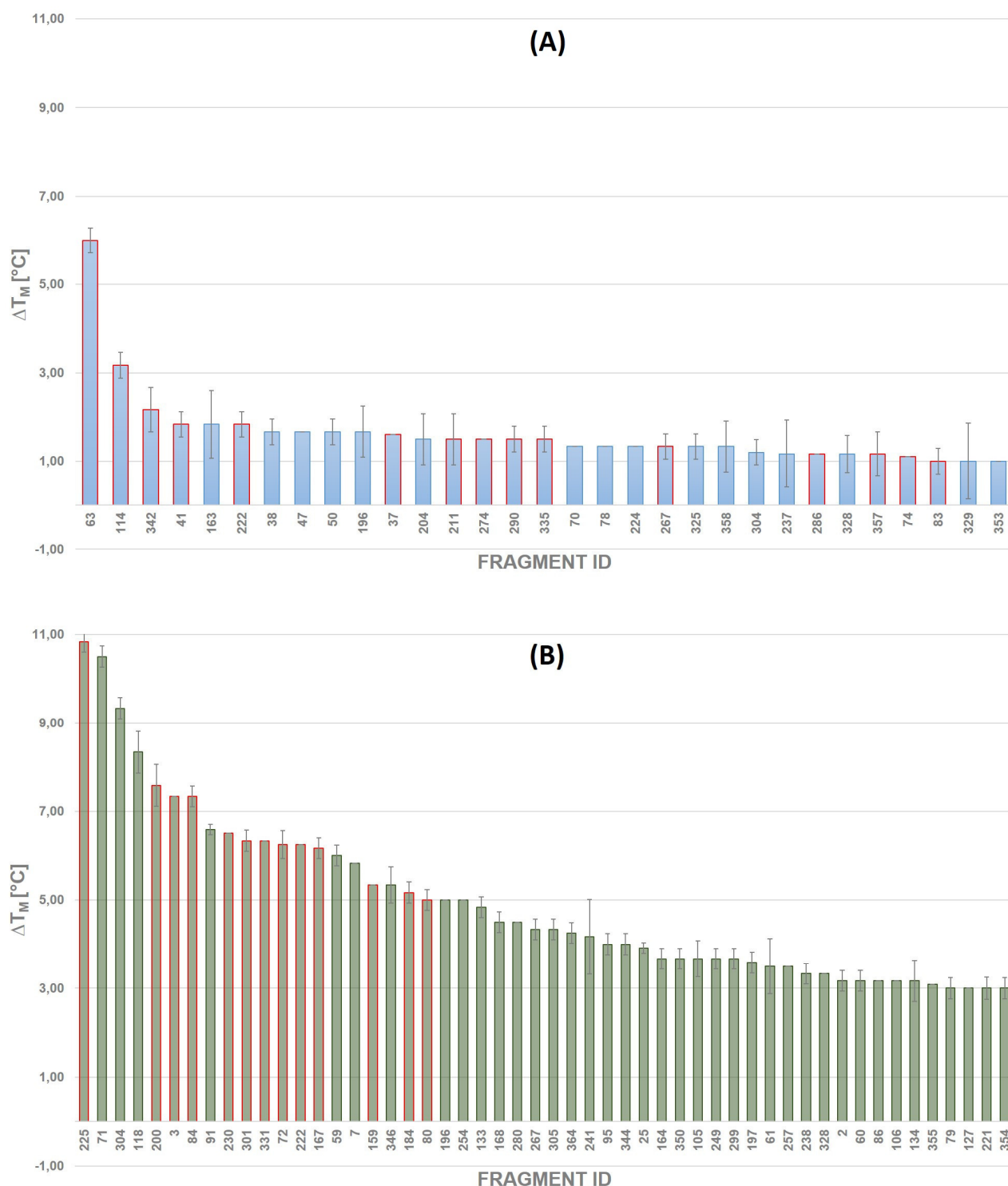


Figure 28: Diagram (A) displays the  $\Delta T_m$  values of 31 fragments within the PKA TSA screen above the applied threshold of ( $T_m \geq 1^\circ\text{C}$ ). Diagram (B) displays the  $\Delta T_m$  values of 52 fragments within the Pim1 TSA screen above the applied threshold of ( $T_m \geq 3^\circ\text{C}$ ). The fragments are labelled by their ID number and ranked according to their strength in thermal stabilisation. The displayed error bar represents the standard deviation of each fragment triplicate. Fragments that are detected as crystallographically hits are marked with a red frame.

There were 26 of 31 significant PKA shifters having no significant  $\Delta T_m$  in the Pim1 screen.

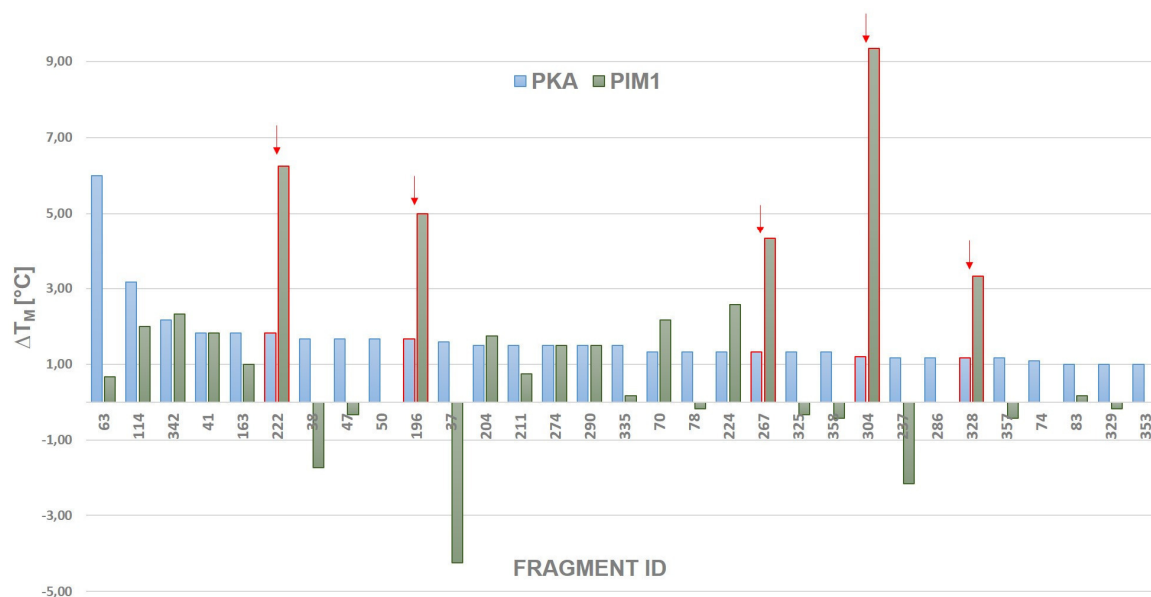


Figure 29: Comparison of fragment shift behavior on PKA and Pim1. The displayed fragment selection are the best 31 positive shifters of the PKA fragment screen (blue). The relevant value of the Pim1 screen is shown in green. Fragments with a significant stabilizing effect on PKA and Pim1 are marked in red.

	PKA	Pim1
<b>General melting point (<math>T_m</math>) [°C]</b>	45,5	36.0
<b>Median standard deviation [°C]</b>	0.3	0.2
<b>Defined threshold of <math>\Delta T_m</math> for hit identification [°C]</b>	1.0	3.0
<b>No. of positive shifting hits</b>	31	52
<b>Maximum <math>\Delta T_m</math> [°C]*</b>	6.0	10.8
<b>No. of negative shifting hits</b>	104	21
<b>Minimum <math>\Delta T_m</math> [°C]*</b>	-7.5	-25.0
<b>No. of analyzed compounds</b>	341	340

Table 8: Resulting values of TSA fragment screen against PKA and Pim1 respectively. \* The highest/lowest  $\Delta T_m$  value within all tested fragments of a screen.

### 2.3.2. Crystallographic screening

Based on the obtained TSA hits, a crystallographic fragment screening for both proteins was conducted. Crystal soaking was used for PKA, whereas co-crystallisation was applied for Pim1 as no crystallisation conditions of native uncomplexed protein crystals were available. In case of Pim1, some of the co-crystallisation attempts yielded crystals of poor diffraction quality or no crystals at all, which reduced the number of measurable crystals. We attribute this to the effect of the large

fragment concentration, which affected the crystallisation conditions. Also, shape and size of the Pim1 crystals were influenced by the presence of certain fragments in the crystallisation solution. Nevertheless, 20 data sets for Pim1 were obtained, of which 15 could be evaluated. The remaining data sets showed poor quality, leading to problems during processing or refinement. The faster fragment soaking method was applied to PKA allowing data collection for every compound identified as hit by TSA. By inspecting the structures after initial refinement cycles, we were able to identify 13 fragments bound to Pim1 and 15 fragments bound to PKA. These hit rates of 48% and 87% (with respect to the collected / evaluable datasets out of the TSA hits) are extremely high for both proteins. In 15 (48%) of the 31 TSA hits, a bound fragment was confirmed by crystallography. The hit rate for Pim1 (with 87%) was even higher (based on 15 evaluable datasets,

PKA			Pim1		
Fragment ID	$\Delta T_m$ [°C]	X-ray hit?	Fragment ID	$\Delta T_m$ [°C]	X-ray hit?
F63	6.0	Yes	F225	10.8	Yes
F114	3.2	Yes	F71	10.5	No
F342	2.2	Yes	F304	9.3	No
F41	1.8	Yes	F118	8.3	n. an.
F222	1.8	Yes	F200	7.6	Yes
F163	1.8	No	F3	7.3	Yes
F38	1.7	No	F84	7.3	Yes
F47	1.7	No	F91	6.6	n. an.
F50	1.7	No	F230	6.5	Yes
F196	1.6	No	F301	6.3	Yes
F37	1.6	Yes	F331	6.3	Yes
F211	1.5	Yes	F72	6.3	Yes
F274	1.5	Yes	F222	6.3	Yes
F290	1.5	Yes	F167	6.2	Yes
F335	1.5	Yes	F59	6.0	n. an.
F204	1.5	No	F7	5.8	n. c.
F267	1.3	Yes	F159	5.3	Yes
F70	1.3	No	F346	5.3	n. an.
F78	1.3	No	F184	5.2	Yes
F224	1.3	No	F80	5.0	Yes
F325	1.3	No	F254	5.0	n. an.
F358	1.3	No	F196	5.0	n. c.
F304	1.2	No	F133	4.8	n. c.
F286	1.2	Yes	F168	4.5	n. c.
F357	1.2	Yes	F280	4.5	n. c.
F237	1.2	No	F267	4.3	n. c.
F328	1.2	No	F305	4.3	n. c.
F74	1.1	Yes	F364	4.3	n. c.
F83	1.0	Yes	F241	4.2	n. c.
F353	1.0	No	F95	4.0	n. c.
F329	1.0	No	F344	4.0	n. c.

Table 9: List of the 31 fragments with the highest  $\Delta T_m$  value in the TSA screen for Pim1 and PKA, respectively. Crystallographically verified binders are labeled. n.an. = Not analysable dataset. N. c. = No measurable crystal.

but this is also a result of the lower amount of diffracting crystals. With respect to the TSA screen of PKA, the five fragments with the highest  $\Delta T_m$  were identified as crystallographic hits. Among the fragments with the highest  $\Delta T_m$  in the TSA screen of Pim1, only two appeared as a crystallographic hit. Most of the observed fragments in the crystallographic screen with PKA are located on the first half of the TSA hit list (F63 – F335, Table 9), indicating that more crystallographic hits are observed for fragments with a  $\Delta T_m \geq 1.50$  °C.

Subsequently, several randomly selected and insignificant or even negative shifters of the PKA TSA screen were tested via X-ray analysis, in order to investigate whether the pre-selection based on TSA was able to enrich the hit rate for a subsequent crystallographic screen. 42 randomly selected fragments of the 361-library were soaked into PKA crystals and identified nine additional binders via X-ray analysis, corresponding to a hit rate of 21%. Remarkably, none of the strong negative shifters resulted in a crystallographic hit, whereas six of the nine additional binders had a small positive shift. The finding indicates that fragments with a stabilizing effect in TSA are more likely crystallographic binders of PKA compared to destabilisers or insignificant shifters. Nonetheless, it has to be mentioned, that the TSA conditions for PKA were closer to the stabilisation optimum of the protein as in the case of Pim1. This may explain the lower stabilisation impact on PKA by fragments and therefore why the additionally detected fragments fell beneath

42 negative & insignificant shifters of PKA					
Fragment ID	$\Delta T_m$ [°C]	X-ray Hit?	Fragment ID	$\Delta T_m$ [°C]	X-ray Hit?
F51	-7.5	No	F162	0.0	No
F164	-3.3	No	F206	0.0	No
F158	-2.0	No	F315	0.0	No
F273	-1.5	No	F4	0.2	No
F131	-1.0	No	F266	0.2	Yes
F291	-1.0	No	F272	0.2	No
F291	-1.0	No	F338	0.2	No
F14	-0.8	No	F54	0.3	No
F159	-0.5	No	F42	0.3	No
F260	-0.5	No	F337	0.3	No
F73	-0.3	No	F35	0.5	No
F103	-0.3	No	F205	0.5	Yes
F171	-0.3	Yes	F207	0.5	No
F189	-0.3	Yes	F236	0.5	No
F255	-0.3	No	F285	0.5	Yes
F261	-0.3	No	F5	0.7	Yes
F17	-0.2	No	F39	0.7	Yes
F81	-0.2	No	F52	0.7	No
F240	-0.2	No	F112	0.7	Yes
F306	-0.2	No	F216	0.7	Yes
F56	0.0	No	F58	0.8	No

Table 10: Fragments with a destabilizing or negative  $\Delta T_m$  in the TSA with PKA tested via crystallographic screening.

the significant level. A hit rate of 21% is still above the generally reported hit rates of 10% for kinases in fragment screenings.<sup>55-88</sup> In sum, 73 fragments of the 361 fragment library were tested crystallographically on PKA with 24 identified hits, which leads to a final hit rate of approx. 33%. A hit rate of approximately 87% for the Pim1 screen is quite surprising, but it may be that the screen is artificially increased by the TSA results. Unfortunately, not all of the TSA hits of the Pim1 screen could be crystallised or resulted in evaluable datasets.

In summary, 24 fragments bound to PKA and 13 bound to Pim1 were identified and the respective complex crystal structures determined. The chemical structures of these binders and their binding modes in the protein structure were compared, to investigate whether there is a correlation between  $T_m$  and crystallographic binding mode. An overview of the chemical structures of all fragments, which were identified in the crystallographic screening, showing a significant  $\Delta T_m$ -value in the PKA TSA screen is given in Figure 30. The additional crystallographic fragment hits with  $\Delta T_m \leq 1$  °C are displayed in Figure 31. All fragments that bound to Pim1 in the crystallographic screen are shown in Figure 32. We compared the chemical composition of bound fragments to obtain some hints whether fragments can be selective, even for two kinases. Focusing on structural elements, which are multiply present in the relevant section. The relevance of these structural elements is further discussed in the crystallographic section. A detailed discussion of the individual binding modes of the bound fragments to PKA and Pim1 is given in the Appendix using the labeling

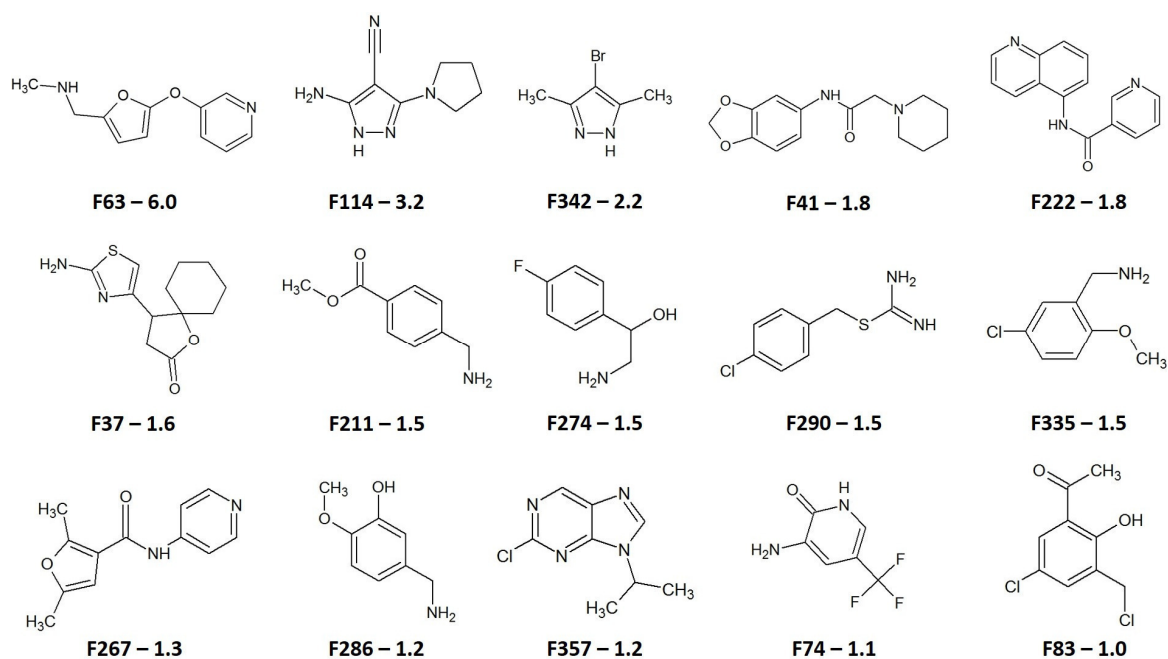


Figure 30: Chemical structure of the crystallographically detected PKA binders with a significant  $\Delta T_m$  in the TSA. The  $\Delta T_m$  value (in °C) of each compound is shown next to the ID number.

assigned to the various candidate fragments of the 361 entry test library. Here, a comparative analysis of the structural elements of PKA binders will be discussed first. A terminal pyridine moiety is part of **F63**, **F222**, **F267**, and **F189**. A central diazole ring is part of fragment **F114** and **F342**. A terminal benzo-dioxane is observed in the structures of fragment **F39** and **F41**. Many fragments contain a benzene ring in the centre with similar substitutions (**F211**, **F83**, **F216**, **F286**,

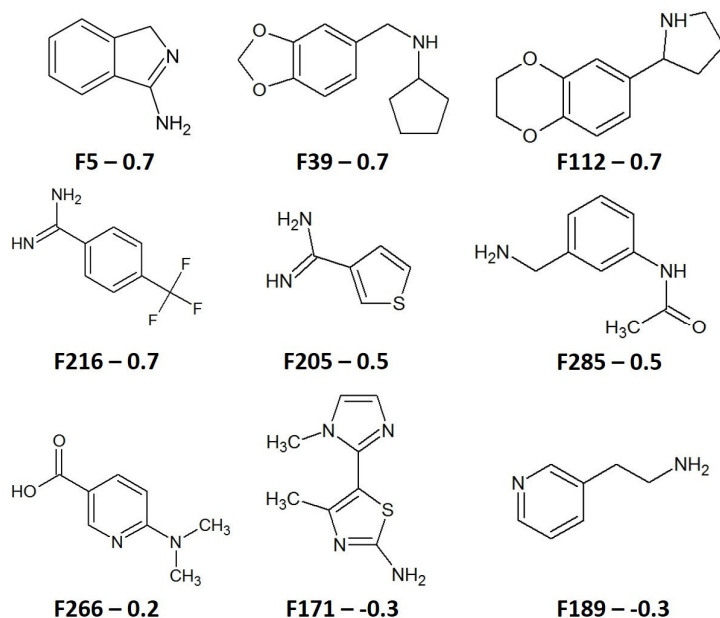


Figure 31: Chemical structure of the crystallographically detected PKA binders without significant  $\Delta T_m$  in the TSA. The  $\Delta T_m$  value (in  $^{\circ}\text{C}$ ) of each compound is shown next to the ID number.

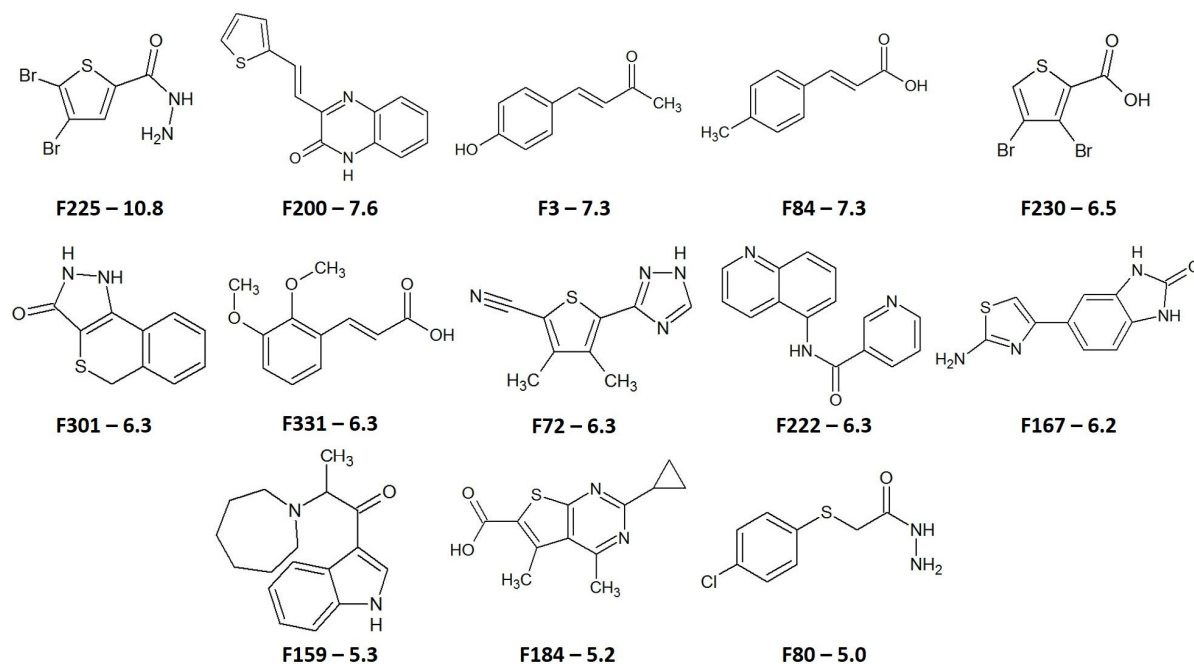


Figure 32: Chemical structure of crystallographic Pim1 binders with a significant  $\Delta T_m$  in the TSA. The  $\Delta T_m$  value (in  $^{\circ}\text{C}$ ) of each compound is shown next to the ID number and visualised as green bars in relation to the strongest signal observed.

**F274, F290, F285, and F335**). In several cases, a halogen atom is attached to such a benzene ring (**F274, F290, F335, F216, and F83**). Two fragments have a methoxy group as substituent (**F286 and F335**). Some fragments with the central benzene ring contain methylamine or an ethylamine group attached to the ring (**F211, F274, F335, and F285**). Thus, the pool of binding fragments exhibits a diverse set of polar and nonpolar interaction properties. Among the Pim1 binders also structural similarities exist. Interestingly, the detected fragments contain cinnamic acid derivatives (**F3, F84, and F331**). This motif has previously been described for Pim1 binders in FBDD research study.<sup>83</sup> Based on this fragment-based approach, the study retrieved Pim2 inhibitors also containing this moiety and showing inhibition on the nanomolar scale.<sup>83</sup> A central thiophene ring with diverse substitutions is also found in three cases (**F225, F230, and F72**). Fragment **F225 and F230** show even several structural similarities. Both are bromine-substituted and contain a carboxylic acid-related moiety in  $\alpha$ -position to the sulfur atom. **F184** also reveals such a moiety, but it also contains a bigger central aromatic portion with an attached pyrimidine ring. A hydrazide motif is present in several fragments (**F225, F301, and F80**). Structural similarity between detected PKA and Pim1 binders is an aromatic scaffold, which was found for every bound fragment. Carboxylate moieties are more frequently discovered in Pim1 binders (**F84, F230, F331, and F184**) than for PKA binders (**F266**). The pyridine moiety appears more frequently in the list of PKA binders (PKA: **F63, F222, F267, F189**; Pim1: **F222**). A hydrazide moiety was only observed for Pim1 binders. Besides the TSA result, which demonstrated different behaviors of PKA and Pim1 of the tested fragments, the diversity in the chemical structures of the crystallographically detected fragments also indicates that a specific chemical motif seems to be more preferred by one kinase than the other. With respect to these structural similarities and differences in both hit lists, the question arises if such a specific motif also dominates a specific binding mode with the protein. A special case for comparing binding poses is fragment **F222** because it is the only compound that was found to be bound to both, Pim1 and PKA. Furthermore, the bound fragments are compared to already known and published inhibitors of PKA and Pim1 and checked for similarities in their binding mode.

### 2.3.3. Crystallographic binders of PKA

Almost all of the 24 crystallographic hits bind to the ATP-binding pocket of PKA. Only **F37** and **F357** were detected at locations on the protein surface. Although not always completely visible in the electron density, some of the ATP pocket binders occupied additional binding positions outside of the ATP pocket.

There are several interacting residues in the ATP-binding pocket of PKA, which play an important role for ATP-binding. Glu121, Tyr122, and Val123 are part of the hinge and involved in recognition of the adenosine moiety. As shown in Figure 6 (Introduction), the adenosine moiety binds close to the backbone of the hinge region and forms a hydrogen bond to the amide nitrogen of Val123 and to the carbonyl oxygen of Glu121. These atoms are hydrogen-bonding partners for 15 out of the 22 fragments. Two further important protein residues for the ATP recognition site belong to the phosphate pocket, where the DFG motif of the kinase is located. In complex with ATP Asp184 stabilises the three phosphate groups in a chelated complex with magnesium ions (Figure 6). Without the magnesium ion, as it is the case under the applied fragment soaking conditions, the negatively charged side chain of Asp184 can function as an anchor for binding positively charged fragment moieties, such as protonated amino groups, by forming a salt bridge. The direct neighbour Thr183 arranges its side chain in the direction of the hinge. It thereby stabilises the ATP adenine moiety by forming a hydrogen bond to one purine nitrogen of adenosine via its hydroxy group. 12 fragments involve the side chain of Thr183 in their binding pose. However, in some cases, the side chain of Thr183 is not or only partly involved in fragment binding. In such cases, the side chain of Thr183 points away from the bound fragment or adopts an alternative orientation. The ribose of ATP is normally oriented towards the opposite side of the pocket, where it forms hydrogen bonds to the side chain of Glu127 and the backbone carbonyl oxygen of Glu170. These amino acids are (five times water-mediated) interaction partners for 12 fragments. All 22 ATP-pocket binders can be classified into 8 different classes. These classes were defined as followed: (I) Fragment interacting directly with Glu121 and/or Val123 of the hinge region; (II) fragments exhibiting a water-mediated contact to Glu121 or Val123 of the hinge region; (III) fragments interacting directly with Thr183 or/and Asp184 of the DFG motif; (IV) fragments showing a water-mediated contact to Thr183 or/and Asp184 of the DFG motif. The classes (I-III), (I-IV), (II-III) and (II-IV) are a combination out of the first four classes. A detailed view of the binding poses of all detected fragments in the ATP-binding pocket is shown in Figure 33. The classification of the 22 fragments proceeds as described below.



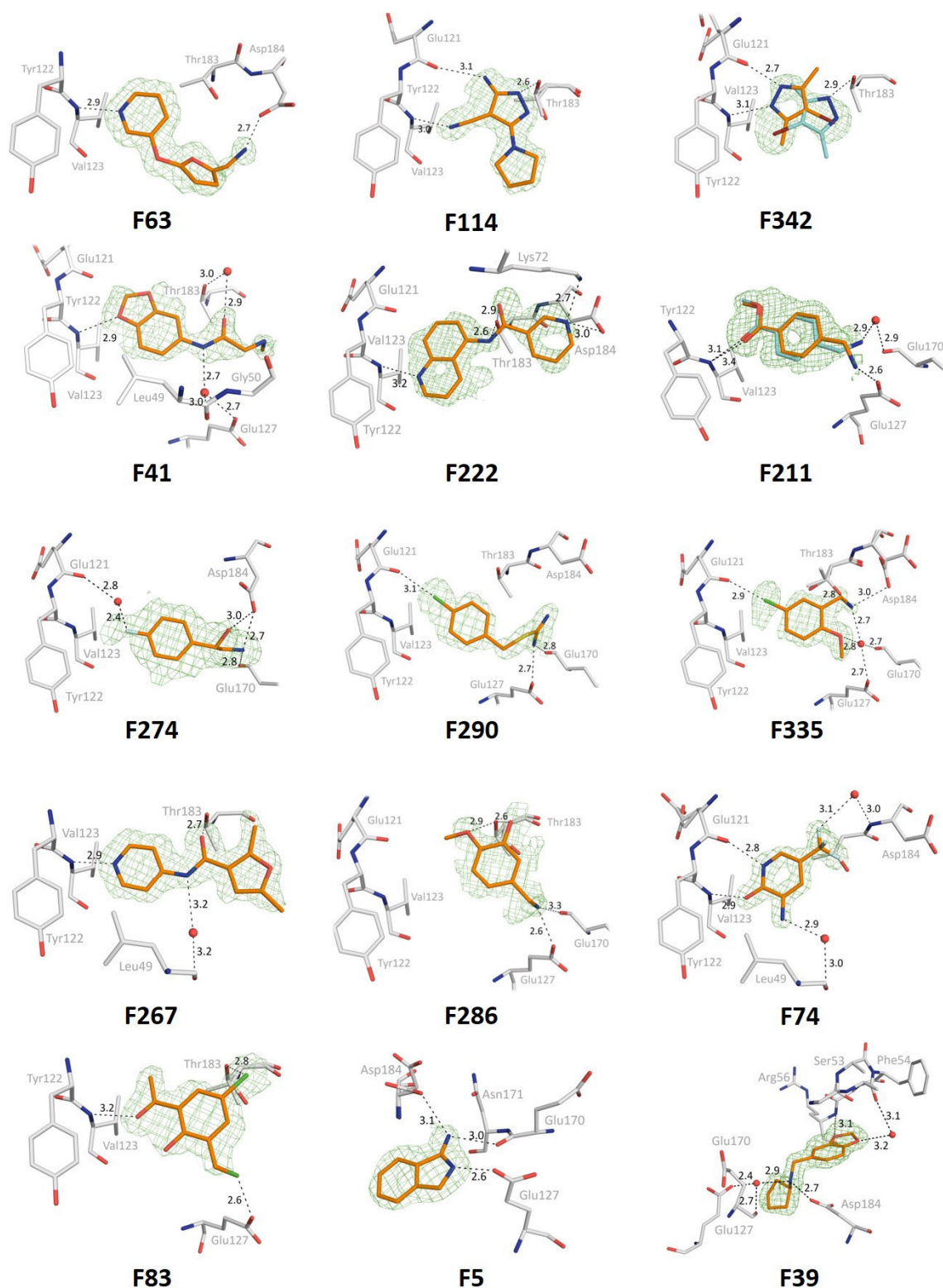


Figure 33: Crystallographically identified fragments bound to the ATP-binding pocket of PKA. The fragments and protein residues are shown as sticks. Fragments carbon atoms are coloured in orange. Protein carbon atoms are coloured in grey. Water molecules are shown as small red spheres. Polar contact interactions are shown as black dashed lines. The unbiased ( $mF_o - D F_c$ ) difference electron density (contoured at  $3\sigma$ ) is displayed in green. Nitrogen atoms are coloured in blue, oxygen atoms in red, chlorine atoms in green, sulfur atoms in yellow and fluorine atoms in light blue. Alternative fragment conformations are shown with cyan carbon atoms. Fragments are listed according to their decreasing TSA value.

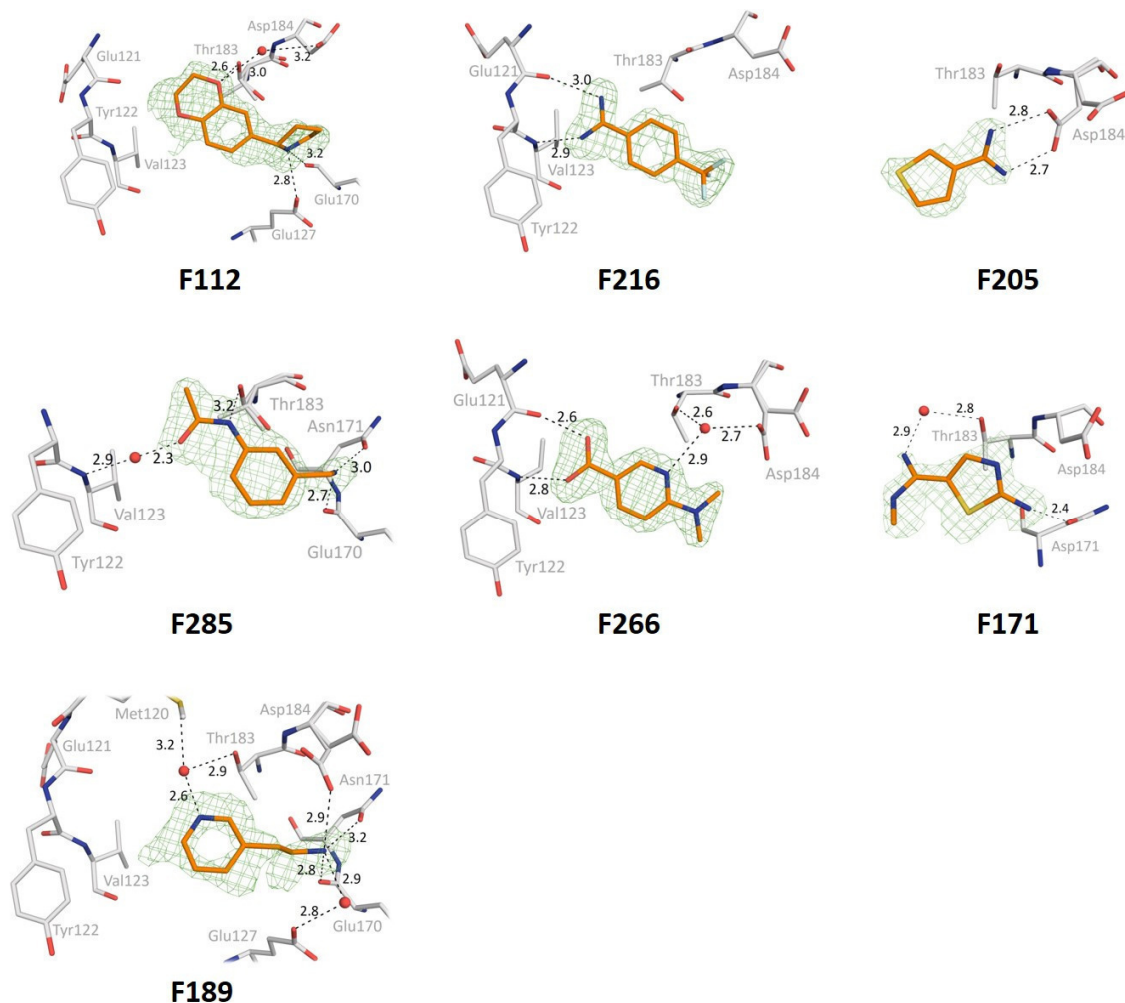


Figure 33 continuation: Found fragments bound to the ATP-binding pocket of PKA. The fragments and protein residues are shown as sticks. Fragments have orange carbon atoms. Protein residues have grey carbon atoms. Water molecules are shown as small red spheres. Polar contact interactions are shown as black dashed lines. The unbiased ( $mF_o - DFC$ ) difference electron density (contoured at  $3\sigma$ ) is displayed in green. Nitrogen atoms are coloured in blue, oxygen atoms in red, sulfur in yellow and fluorine atoms in light blue. Fragments are listed according to their decreasing TSA value.

Class	Fragments	Quantity	Percentage
I	342, 211, 290, 216	4	17.4%
III	342, 286, 5, 39, 205, 189	6	26.1%
IV	112, 171	2	8.7%
I - III	63, 114, 222, 335, 267, 83	6	26.1%
I - IV	41, 74, 266	3	13.0%
II - III	274	1	4.3%
II - IV	285	1	4.3%

Table 11: Distribution of PKA binding fragments in the ATP-binding pocket among 8 defined binding classes. Significant positive shifters are marked in green. Insignificant positive shifters are coloured in black and insignificant negative shifters in red. No fragment was detected exhibiting only a water-mediated contact to the hinge region (class II).

The electron density of **F342** shows two strong anomalous signals for bromine suggesting that the fragment adopts two distinct orientations. After refinement, the occupancy revealed a higher population for the Thr183 bound orientation (60%). The further investigation revealed how the fragments are distributed among the binding classes with respect to their stabilizing effect. Fragments that are classified into class (I-III) or (I) have a high  $\Delta T_m$  value in the TSA screen, which indicates that fragments with a direct hinge interaction exhibit a better stabilizing effect on PKA than those lacking any direct interaction with the hinge. The structures of the 11 crystallographically hits with the highest  $\Delta T_m$  value were aligned and compared to those of the 11 crystallographically hits with the lowest  $\Delta T_m$  value. This comparison reveals, that most of the stronger shifting fragments bind close to the hinge region, whereas a lower number of fragments with weaker  $\Delta T_m$  values bind closer to the ribose pocket. A closer inspection of the binding positions of the fragments with weaker  $\Delta T_m$  values reveals that fragments **F74** and **F83**, which are also significant shifters in the TSA ( $\Delta T_m = 1.1$  and  $1.0$  °C respectively), also interact with protein residues of the hinge region via hydrogen bonds (Glu121 and Val123). This suggests that fragments binding to the hinge region in all cases results in a more likely stronger stabilisation as indicated by TSA. Figure 34 (A) also suggests which structural binding element dominates the hinge binding. In most cases, a heteroatom accepts a hydrogen from the backbone nitrogen of Val123 (**F63**, **F114**, **F342**, **F41**, **F222**, **F211**, **F267**, **F74**, **F83**, **F216**, **F266**) or donates a hydrogen to the backbone carbonyl oxygen of Glu121 (**F114**, **F342**, **F74**, **F216**, **F266**). Fragment F290 and F335 address the backbone carbonyl oxygen of Glu121 with a halogen bond. In the second orientation of **F342** (cyan carbon atoms, Figure 33) the bromine atom is placed in  $3.6$  Å distance to the backbone nitrogen of Val123. Depending on the binding pose of **F342**, the nitrogen atom of the heterocycle interacts either with

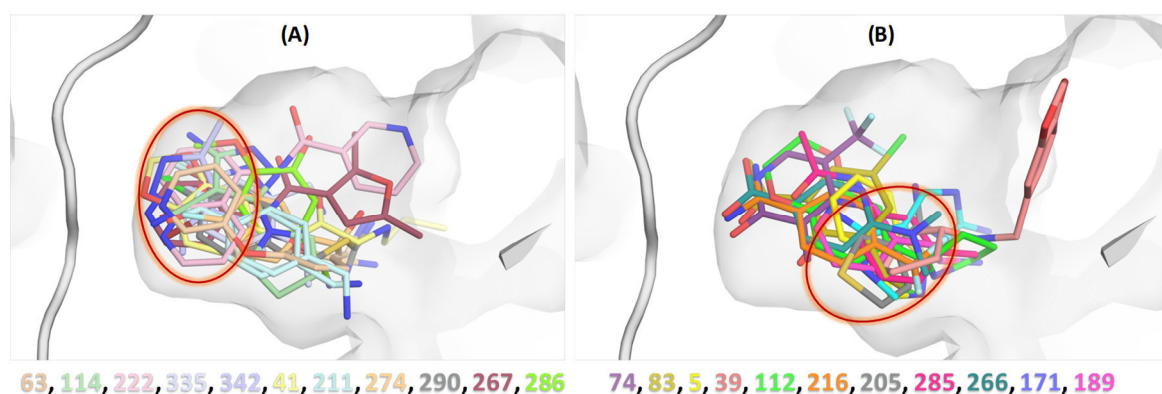


Figure 34: (A) shows the structural alignment of all 11 fragment hits with the highest  $\Delta T_m$  in the TSA. (B) displays the structure alignment of the 11 remaining crystallographic hits. The colour code corresponds to carbon atoms of each fragment. The hinge region is shown in cartoon mode and is coloured in grey. The protein surface forms the ATP-binding pocket, where the fragments are displayed as sticks. The red eclipses encircle the region with highest fragment concentration of each alignment.

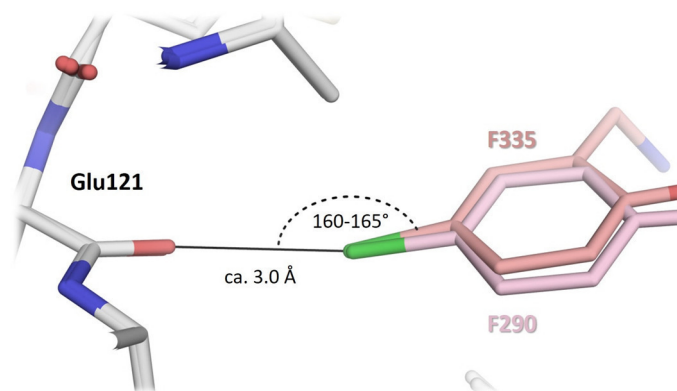


Figure 35: Superimposed structures of PKA in complex with F335 and F290. Protein carbon atoms are coloured in grey. Fragment carbon atoms are coloured corresponding to their labels. Chlorine atoms are coloured in green. Distances between chlorine atom of the fragments and the backbone carbonyl oxygen of Glu121 is shown as black line. The angle between C-Cl-O is indicated by a black dashed curve.

the hinge or with Thr183, in the latter case placing the bromine atom near the hinge. In this orientation, the bromine acts as a hydrogen-bond acceptor.

According to the halogen-bonding theory<sup>89 90</sup>, halogen atoms also show a partial positive charge at the top along the prolonged C-halogen-bond, also called positive cap. This cap on top of chlorine atoms points to the backbone carbonyl oxygen of Glu121 in the case of fragments **F290** and **F335** (Figure 35). Fluorine was only observed acting as an H-bond acceptor according to its

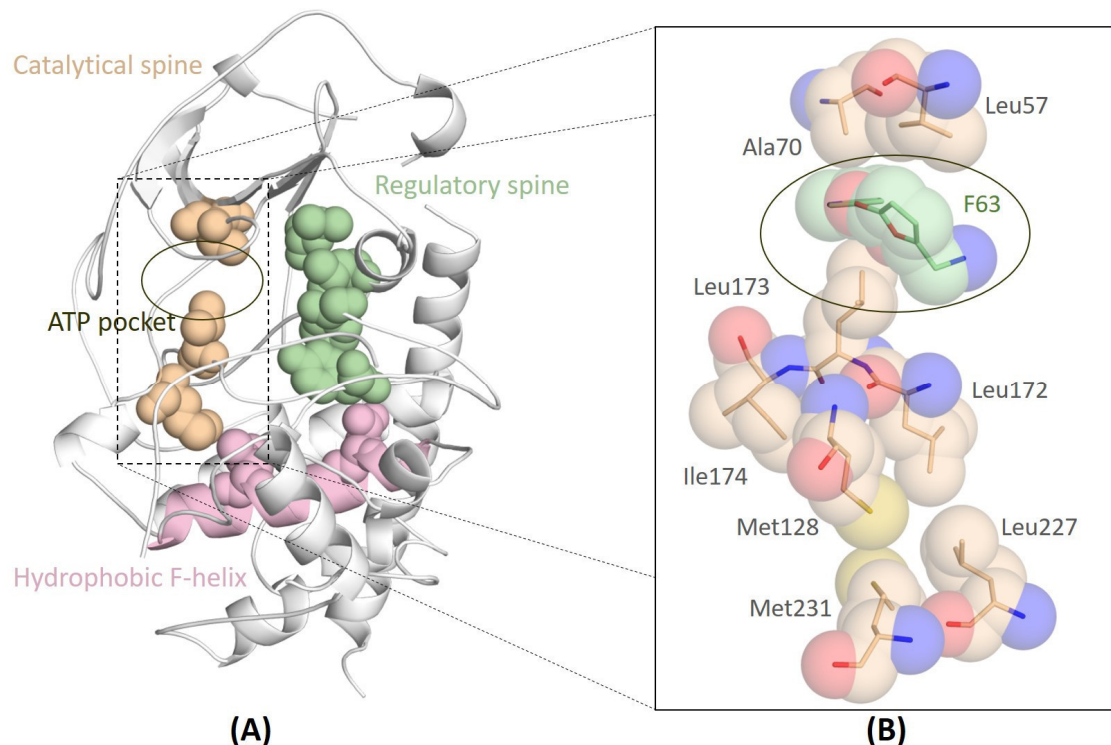


Figure 36 (A) Arrangement of regulatory spine, catalytic spine and hydrophobic F-helix in PKA, which are shown as CPK model. The gap in the catalytic spine is part of the ATP-binding pocket. (B) Amino acid arrangement of the catalytic spine shown as sticks with transparent spheres. The bound F 63 fills the gap between Ala70, Leu57 and Leu173.

high electronegativity. Fragment **F274** uses this feature to form a water-mediated contact to the hinge region. Also fragment **F74** forms a water bridge utilizing one of its fluorine atoms as a hydrogen acceptor, in this case from the backbone nitrogen of Asp184. All of the observed heteroatoms of the fragments binding near the hinge region are attached or embedded into a planar aromatic ring system similar to adenosine. Pyridine (**F63**, **F267**), pyrazole (**F342**) and quinolone moieties (**F222**) bind close to the hinge, but also benzodioxole- (**F41**) and hydroxypyridine-moieties (**F74**). The fragments **F211**, **F290** and **F335** respectively, contain an aromatic benzene ring close to the hinge-interacting heteroatom in similarity to adenosine. When ATP binds to the catalytic pocket, it fills the gap of the catalytic spine of kinases, which defines and stabilises the pocket together with the F-helix and the regulatory spine (Figure 36).<sup>28</sup> The two spines are both anchored on the hydrophobic F-helix and traverse through the N and C lobe of the protein. The only direct connection between the two lobes is the hinge region. Thus, the spines give more stability to PKA. Therefore, A bound ligand that can connect the two parts of the catalytic spine upon binding of a hydrophobic moiety will enhance PKA stability<sup>28</sup>. Figure 36 B shows how **F63** fills the missing element of the catalytic spine, which indicates the strong stabilizing effect of this fragment on PKA unfolding.

Due to the low complexity of fragments, the likelihood of binding to a protein increases in relation to common HTS compounds<sup>91</sup>. In addition to the 22 binders of the ATP-binding pocket, seven fragments were observed at several positions outside the ATP-binding pocket (Figure 37). Two of

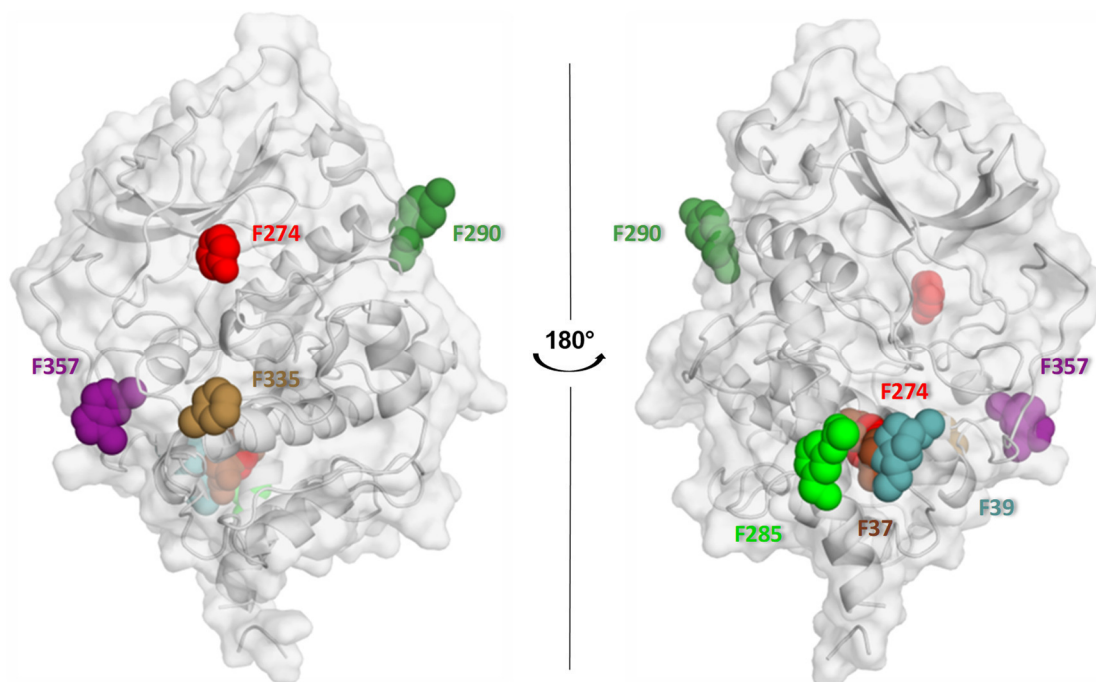


Figure 37: Fragment binding outside the ATP-pocket. The protein is displayed in grey cartoon with transparent surface. Bound fragments are displayed as spheres and are coloured corresponding to their ID names.

these fragments merely bind outside the ATP-pocket. Fragment **F37** binds in a small hydrophobic cleft, which is formed between the long N-terminal  $\alpha$ -helix, the small  $\alpha$ -helix of the C-loop and the central and hydrophobic F-helix. Although the fragment does not bind to the ATP-binding pocket, it stabilised the protein with a  $\Delta T_m$  of 1.6 °C (on rank 11 of the TSA list) (Table 9). This effect can be explained by the formation of two hydrogen bonds. The first one is formed between the amino nitrogen of the compound and the hydroxy group of Ser14. The second one is formed between the fragment's lactone group and the ammonium group of Lys292 of the long C-terminal loop. Thus, **F37** links the N and C terminal parts of PKA. The hydrophobic hexane ring is placed directly in the hydrophobic pocket, which is formed by Phe18, Tyr156, Phe100, Tyr306 and Leu152, where it interacts via van-der-Waals contacts, implying that fragment **F37** can also interact with the central hydrophobic F-helix. Based on the fact that the close fitting to the N-terminal  $\alpha$ -helix stabilises the PKA<sup>28</sup>, the interaction pattern of the molecule fixes this helix in its main position and therefore stabilises the entire PKA molecule. In other structures studied in this series, an MPD molecule is often found in this binding pocket, which coordinates to Glu155 via its hydroxy groups. Although MPD is always present for cryoprotection, **F37** is able to replace this ligand. The second fragment which only binds outside the ATP pocket is **F357**. This fragment binds in a small cleft, which is formed by a part of the C-loop and the  $\alpha$ -helix of domain V. The amino acid side chains of His131, Ile132, Phe138, His142, and Phe314 are surrounding the ligand. Interestingly, the only noticeable protein-ligand interaction is a  $\pi$ -stacking between the purine moiety of the fragment and the side

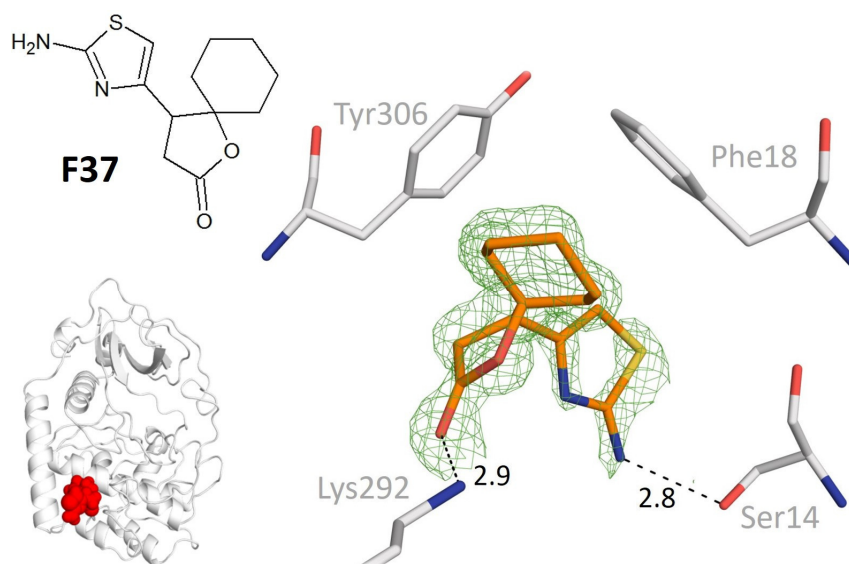


Figure 38: Detailed binding motif of fragment **F37**. Protein and compound are shown as sticks. Protein carbon atoms are shown in white, ligand carbon atoms in orange, oxygen atoms in red, sulfur in yellow and nitrogen atoms in blue. The unbiased ( $mFo - DFC$ ) difference electron density (contoured at  $3\sigma$ ) is displayed in green. Polar contact interactions are shown as black dashed lines. Upper left picture shows the chemical structure of fragment **F37**. Lower left picture shows location of the fragment, which is displayed as red sphere in a cartoon view of the PKA protein.

chain of Phe314 (distance: 3.8 Å). The partly blurred electron density indicates a rather weak binding to the protein resulting in higher residual mobility within the binding pocket. For example, two carbon atoms of the iso-propane moiety could not be assigned due to missing electron density. The refined B-values for the fragment and the aromatic side chain of Phe314 are in the same range. The mean B-values of the interacting side chain (38.9 Å) and the ligand (41.5 Å) are much higher compared to the B-factors of other side chains in this area (e.g., His131: 20.2 Å<sup>2</sup>). It appears that the compound influences the flexibility of the side chain of Phe314. Nevertheless, with respect to the parent purine scaffold, the fragment would be expected to bind in the ATP pocket, but in comparison with adenosine, fragment **F357** does not contain the exocyclic amino group to address the backbone carbonyl oxygen of Glu121 with a hydrogen atom. Additionally, the chlorine atom would clash with the protein if an identical arrangement of the purine moiety would be adopted as found for the adenosine moiety of ATP. In contrast to most of the other detected fragments, there is no direct indication to explain the stabilizing effect of **F357** in the TSA, since it is not binding to the ATP site and it even shows higher residual mobility at its binding position. The five remaining fragments, which were found outside the ATP-binding pocket, were found as a second copy of a fragment also bound at the ATP site. This refers to **F39**, **F290**, **F335**, **F285**, and **F274**, where **F274** is even detected three times in the crystal structure. The binding poses of these fragments are displayed in detail in Figure 40. The second copy of fragment **F290** was identified to form a salt bridge to Asp25 of the peptide inhibitor PKI. The carboxylate group of Asp25, which is most likely deprotonated and negatively charged, interacts with the thiourea moiety of the fragment. One

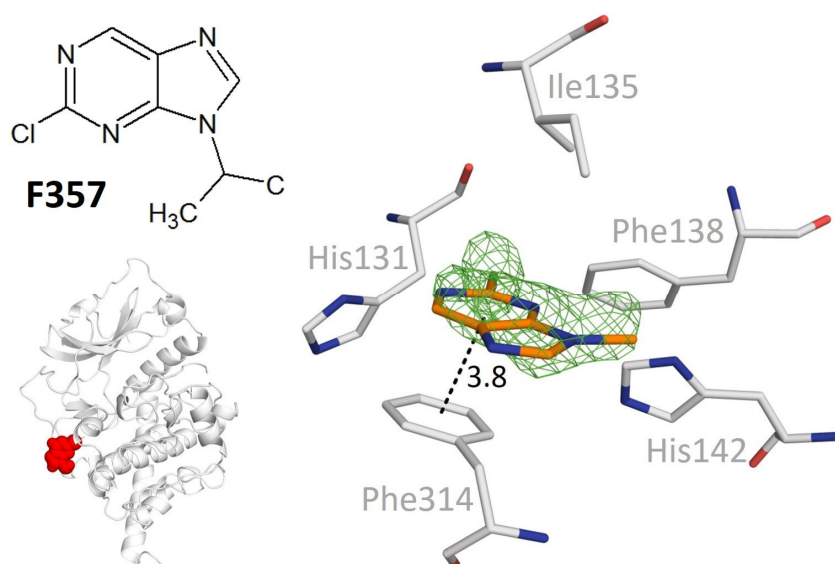


Figure 39: Detailed binding motif of fragment **F357**. Protein and compound are shown as sticks. Protein carbon atoms are shown in white, ligand carbon atoms in orange, oxygen atoms in red and nitrogen atoms in blue. The unbiased ( $mF_o - DF_c$ ) difference electron density (contoured at  $3\sigma$ ) is displayed in green.  $\pi$ - $\pi$ -interaction is shown as black dashed line. Upper left picture shows the chemical structure of fragment **F357**. Lower left picture shows location of the fragment, which is displayed as red sphere in a cartoon view of the PKA protein.

nitrogen atom forms a water-mediated bridge to the phosphorylated Thr197. Due to the fact, that during TSA measurements no PKI was present, this binding is impossible to occur under the applied TSA conditions. For the second bound copy **F335**, not the entire fragment can be attributed to the density. Only the chlorine and the benzene ring were visible. The only contact for a protein-ligand interaction is indicated with the nearby Tyr235, forming an edge-to-face interaction of the aromatic ring systems. The missing part of the fragment is too flexible so that it could not be assigned to the structure. A special case is the second binding pose of fragment **F285** because it is located between two PKA molecules in the crystal lattice. On the one hand, the compound can interact with the amino group of Lys21 via its amide oxygen. On the other hand, the amide nitrogen interacts with the backbone carbonyl oxygen of His260'. Furthermore, the amino nitrogen of the terminal methylene amino group interacts with the backbone carbonyl oxygen of Ser259' of the PKA crystal mate (Figure 40). It is very likely that this binding pose is only possible in the PKA crystal packing. After calculation of the buried surface area of the protein-ligand interface via the PISA-server<sup>92</sup>, we obtained 24,4% burial for fragment **F285** with the contacting lysine and 38.4% burial with the neighbouring PKA. The distribution of the buried areas suggests, that this binding mode is dominated by the histidine and serine residue. The second binding location of **F274** is already suggested by the binding motif of **F37**. The fluorine substituted benzene ring also fills the

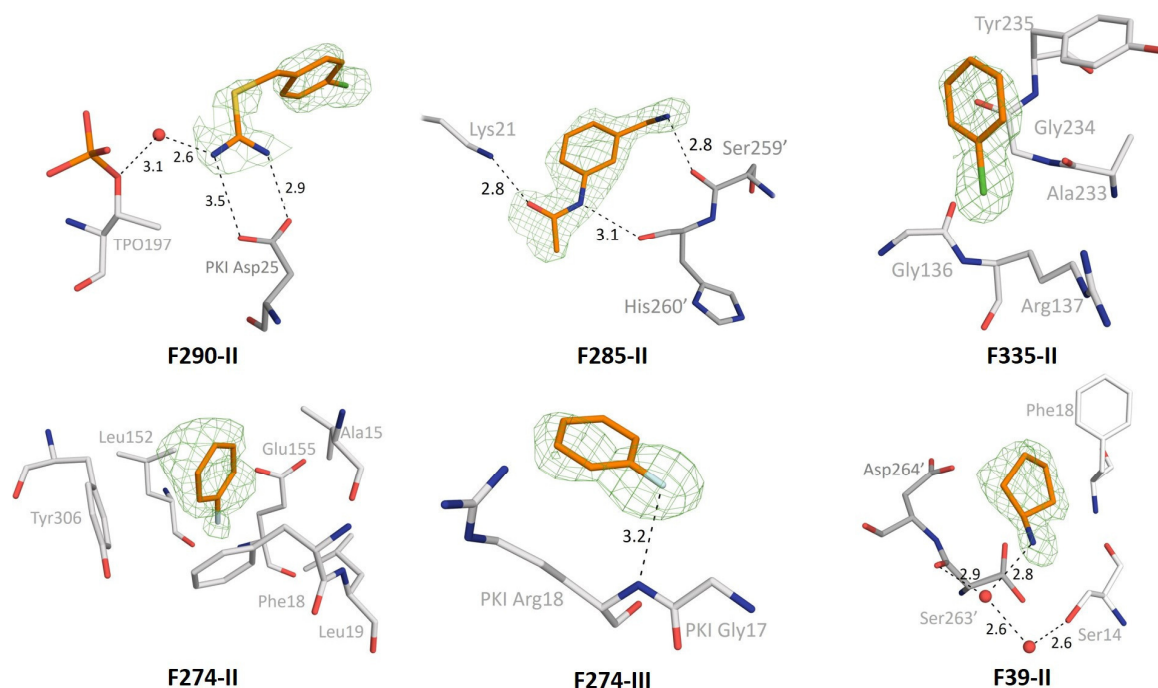


Figure 40: Additional binding modes of fragments apart from the ATP-binding pocket. The fragments and protein residues are shown as sticks. Carbon atoms from fragments are coloured in orange and from protein residues in grey. Water molecules are shown as small red spheres. Polar contact interactions are shown as black dashed lines. The unbiased ( $mF_o - DFC$ ) difference electron density (contoured at  $3\sigma$ ) is displayed in green. Nitrogen atoms are coloured in blue, oxygen atoms in red, chlorine atoms in green, sulfur in yellow and fluorine atoms in light blue.



hydrophobic pocket, whereas **F37** uses its cyclohexyl ring. Because the remaining part of fragment **F274** is scattered over multiple orientations, no well-defined electron density is visible. Therefore, this part could not be assigned. For the third binding pose of **F274**, the only polar interaction is an H-bond between fluorine and the backbone nitrogen of Arg18 belonging to PKI peptide. In this position the fragment interacts with the inhibitor peptide and not with the PKA. Therefore, no effect in TSA could be recorded. The second binding pose of fragment **F39** is close to the binding pocket, where fragment **F37** and **F274** bind. Also in this case, only a part of the compound is visible in the electron density (Figure 40). Solely the cyclopentyl ring and the secondary amino group is indicated by the electron density. The remaining atoms are solvent exposed and too flexible to be modelled. Similar to the second binding pose of **F285**, the second molecule of **F39** is located between two PKA crystal mates in the crystal packing. Again, it is more likely that this binding pose is only caused by the crystalline packing and can therefore be classified as crystallographic artefact. The buried surface area of the protein amounts to 54.9% of the fragment's solvent accessible surface, whereas 32.1% are covered by the nearby symmetry-related PKA molecule.

The crystallographic screen with randomly tested fragments without a significant or a negative  $\Delta T_m$  showed that the TSA also produced “false negatives.” We identified crystallographically five PKA binders with insignificant  $\Delta T_m$  value. One explanation could be a possible fluorescence quenching caused by the fragment during measurements. Another argument might be the previously mentioned additional destabilisation by the fragment binding to the unfolded protein as well. Therefore, it is very likely that more crystallographic hits can be found, once the entire library is tested directly by X-ray crystallography. On the other hand, TSA also produced some “false positive,” which is a widely known issue of TSA<sup>53 93</sup>. There are 16 of all 31 TSA hits in the PKA screening that were not detected in the crystallographic screening. However, it was demonstrated that the TSA pre-screening led to an enrichment of the crystallographic hits so that TSA-based prioritizing results in a higher crystallographic hit rate than an unprioritised strategy going directly on a randomly selected set.

#### **2.3.4. Crystallographic binders of Pim1**

Although in contrast to PKA binders (24) fewer fragments were detected to bind to Pim1 (13), the achieved hit rate was much higher for Pim1 (87%) than for PKA (48%). At first sight, this is most probably related to the lower number of fragments tested on Pim1 crystals. There are 13 out of 15 analyzed datasets with a bound fragment in the ATP-binding pocket of Pim1. None of them had an additional binding pose of a second copy, as observed for some of the PKA fragment binders.

In comparison to the fragments bound to PKA, almost all fragments bound to Pim1 do not interact with the hinge region. Pim1 and PKA differ in their amino acid composition at the hinge region, with the most important replacement concerning Pro123 and Pro125 in Pim1, which are described below. Pro123 leads to the effect that the backbone nitrogen, which is usually available as an H-bond donor in the analyzed PKA complexes, is not available in Pim1. Pro125 causes a flip of the loop directly following the hinge. By this, the hinge region and the ATP-binding pocket are slightly expanded.<sup>94</sup> Another important aspect is the missing of a long C-loop, which is located along the

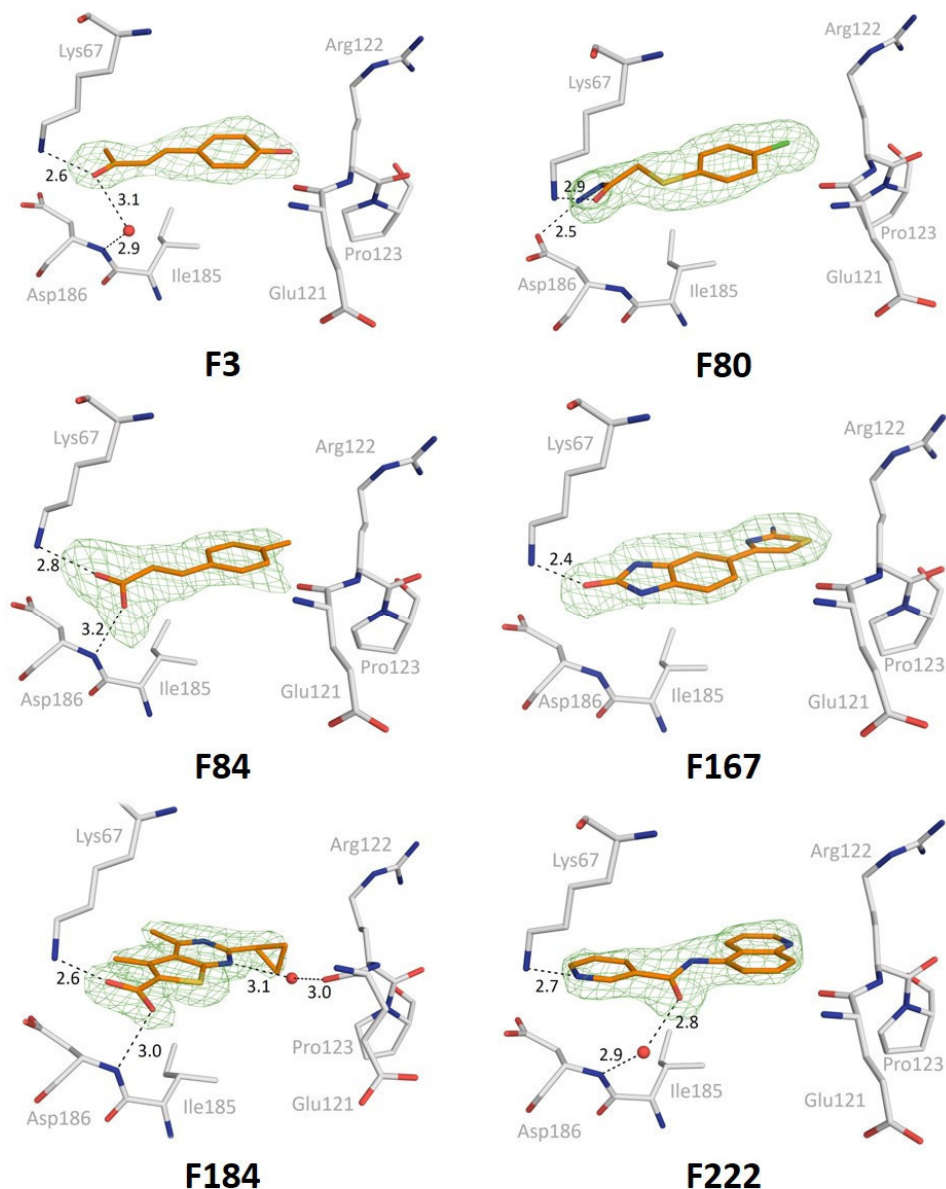


Figure 41: Detected fragments bound to the ATP-binding pocket of Pim1 and interacting with Lys67. The fragments and protein residues are shown as sticks. Carbon atoms from fragments are coloured in orange and from protein residues in grey. Water molecules are shown as small red spheres. Polar contact interactions are shown as black dashed lines. The unbiased ( $mF_o - DFC$ ) difference electron density (contoured at  $3\sigma$ ) is displayed in green. Nitrogen atoms are coloured in blue, oxygen atoms in red, chlorine atoms in green, sulfur atoms in yellow and bromine atoms in brown. Alternative conformations are shown with carbon atoms in cyan.

ATP-binding pocket near the hinge in PKA structures. Phe327 covers the pocket alongside the hinge in PKA, which is missing in Pim1 structures and therefore dilates the ATP pocket (Figure 50 (B)). Interestingly, more fragments were found to bind to Pim1, interacting with Lys67, which is responsible for phosphate stabilisation similarly to Lys72 in PKA. 9 of the 13 detected fragments showed a polar interaction to Lys67 in Pim1 (Figure 41). Those, fragment occupying the ATP-binding pocket, but lacking the Lys67 interaction, are displayed in Figure 42. All observed Pim1 binders share a planar structure in common. These planar portions are surrounded by residues with hydrophobic side chains. Leu44, Val52, and Ala65 expose their side chains to the ATP pocket from the N-terminus. From the C-terminal region, Leu174 and Ile185 approach into the pocket, perpendicular to the hinge – DFG – plane. Additional hydrophobic side chains surrounding the ATP pocket are Ile104, Leu120, and Val126. Obviously, the ATP-binding site of Pim1 has very hydrophobic character and therefore offers reduced possibilities for polar protein-ligand interactions. In 9 of the 13 structures, the side chain of Phe49 of the flexible glycine-rich loop flips over to the ATP binding site, which additionally increases the exposed hydrophobic area of the ATP site. The hinge region provides only the backbone carbonyl oxygen of Glu121 as a possible H-bond acceptor. In the region of the phosphate pocket, the side chain carboxyl group and backbone nitrogen of Asp186 and the terminal amino nitrogen of Lys67 are available to form polar

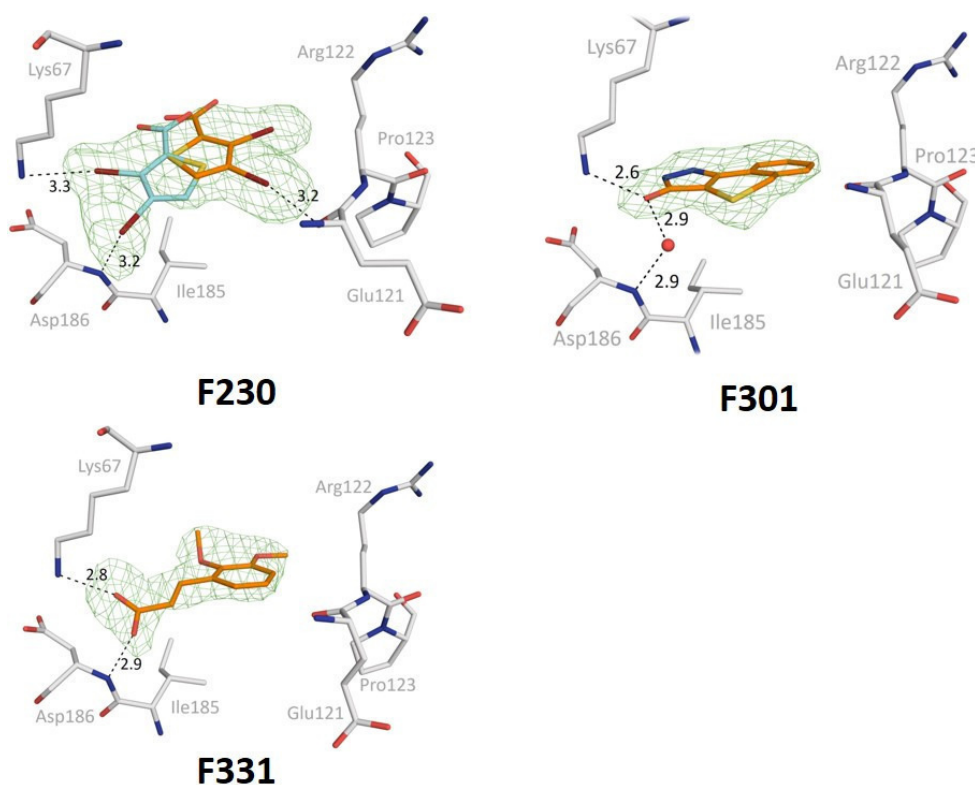


Figure 41 continuation.

interactions. A water molecule was found binding to the backbone nitrogen of Asp186, which can act as an additional polar interaction partner. These structural studies show that approximately 70% of the detected Pim1 fragment binders are interacting with Lys67, ca. 15% with the carboxylic group of Asp186. Another 70% interact directly or water-mediated with the backbone amide group of Asp186 and 23% form a polar interaction to the hinge via the backbone carbonyl oxygen atom of Glu121. Fragments **F225**, **F230** and **F184** belong to the latter group. Whereas **F184** is the only observed fragment in this series that forms a water-mediated contact to the hinge, **F225** and **F230** form a halogen bond interaction utilizing one of their bromine atoms (Distances Br-O: 2.9 and 3.2 Å, respectively). These halogen bonds resemble those of the chlorine-substituted moieties of **F290** and **F335**, which are pointing with their positively charged cap<sup>89</sup> to the carbonyl oxygen of Glu121 in PKA. The position of the halogen atoms is indicated by a strong and clearly defined density spot in the electron density map. Additionally, a strong anomalous scattering signal is detected at these positions. They indicate the location of the halogen atoms. This also explains the higher occupancy of the hinge coordinating orientation of **F230** (occupancy ratio: 68% / 32%). **F225** is the only fragment interacting with the hinge and the DFG loop simultaneously. It can be

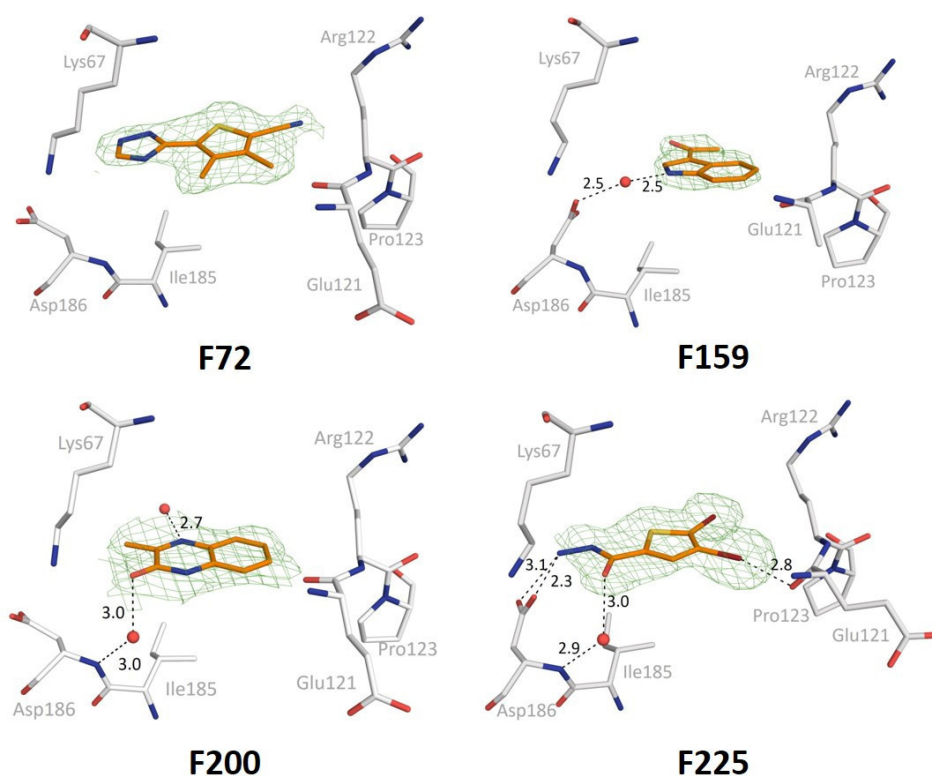


Figure 42: Detected fragments binding to the ATP-binding pocket of Pim1 without interaction to Lys67. The fragments and protein residues are shown as sticks. Carbon atoms from fragments are coloured in orange and from protein residues in grey. Water molecules are shown as small red spheres. Polar contact interactions are shown as black dashed lines. The unbiased ( $mF_o - DFC$ ) difference electron density (contoured at  $3\sigma$ ) is displayed in green. Nitrogen atoms are coloured in blue, oxygen atoms in red, chlorine atoms in green, sulfur in yellow and bromine atoms in brown.

regarded as a bridging molecule between both protein motifs. It is also the best stabilizing fragment for Pim1 according to TSA. This observation is in agreement with the positive shifting of the PKA fragments, which are also bridging the gap between the hinge and DFG loop (Table 11). It seems that especially this binding arrangement has a strong stabilizing effect on kinases. However, the chlorine atom of fragment **F80** does not interact with the hinge as observed for the previously discussed halogen-containing fragments. Its chlorine atom points in the direction of the backbone carbonyl oxygen of Glu124 without interacting with it. If the chlorine atom were attached at meta position to the sulfur atom, it would be able to form a halogen bond to the exposed backbone oxygen atom similar to **F225** (Figure 43). The superimposition of the two fragments (**F80**, **F225**) is moreover interesting because they share a terminal hydrazide group in common, but with deviating attachment length. The aromatic moieties (thiophene and benzene) of both compounds are located at similar positions, but in contrast to **F225** (Figure 32), **F80** contains an additional thioether-methylene bridge part between the aromatic ring and the hydrazide group. The latter, however, interacts with Asp186 in both cases. The structural expansion of the fragments results in a side chain flip of Asp186 to either avoid a clash with the hydrazide group, but also to interact with this group. With a distance of 2.9 Å, **F80** also interacts directly with Lys67 via its hydrazide carbonyl oxygen, whereas the shorter **F225** uses this oxygen to form a water-mediated interaction to the backbone nitrogen of Asp186. The correct placement of the planar aromatic fragment moiety seems to be crucial for the binding in the ATP pocket. All of the discovered fragments, which bind to Pim1 in this series, have such an aromatic moiety placed close to the hinge region. One fragment which has to be highlighted here is **F72** (Figure 42), because it is the only compound lacking any polar interaction to either the hinge, the DFG motif or Lys67. Nevertheless, its thiophene ring is clearly defined by the electron density and adopts almost the same position as the thiophene ring of **F225**. The methyl substituents at **F72** hinders the fragment to place the thiophene ring closer to the hinge region, next to the backbone carbonyl oxygen of Glu121. Fragments with a larger aromatic system, including two or more rings (**F159**, **F200**, **F222**, **F184**, **F167**, **F301**) also place their planar parts in this area. **F159** and **F200** are the only fragments, which could not be modelled completely into the electron density. The indole moiety of **F159** is arranged in a way that the benzene ring points towards the hinge and the indole nitrogen forms a water-mediated contact to the backbone nitrogen of Asp186. In this orientation the terminal azepane ring (s. Figure 32) leaves partially the ATP-binding pocket and remains more solvent exposed. In consequence it is scattered over multiple orientations leading to a missing electron density for this part of the ligand. The same applies to the thiophene ring of **F200** (s. Figure 32). The arrangement of the 1H-quinoxaline-2-one ring system with the benzene ring close to the hinge and the lactone

oxygen forming a water bridge to the backbone nitrogen of Asp186, forces the attached thiophene moiety to a position remote of the ATP pocket. Also here, this part of the fragment could not be assigned, due to missing electron density in this region. Although fragment **F301** has no fully conjugated aromatic system in the central 2-H-thiopyran ring, the almost planar ligand binds with the benzene portion close to the hinge and uses its carbonyl oxygen of the hydrazide unit to form a water bridge to Lys67. The same oxygen interacts with the backbone nitrogen of Asp186 via a water bridge. **F167** does not form an interaction to Asp186, instead it contacts Lys67 via its cyclic urea oxygen. Its benzene ring binds close to the position where **F225** positions its thiophene moiety. Here, the 2-amino-thiazole ring orients towards the solvent-exposed area of the pocket and locates directly between the two hydrophobic side chains of Leu44 and Leu174. The thiazole moiety is almost co-planar to the benzimidazole-2-one portion with a slight twist along the connecting single bond. **F184** forms a water bridge to interact with the backbone carbonyl oxygen of Glu121 via its endocyclic nitrogen atom. By this, fragment **F184** is the only example with a water-mediated interaction to the hinge in this series. Furthermore, this fragment contains a carboxylate group, which is most likely deprotonated and therefore forms a salt bridge to the protonated Lys67. Additionally, one oxygen atom of this carboxylate is placed close to the backbone nitrogen of Asp184, allowing the formation of an H-bond.

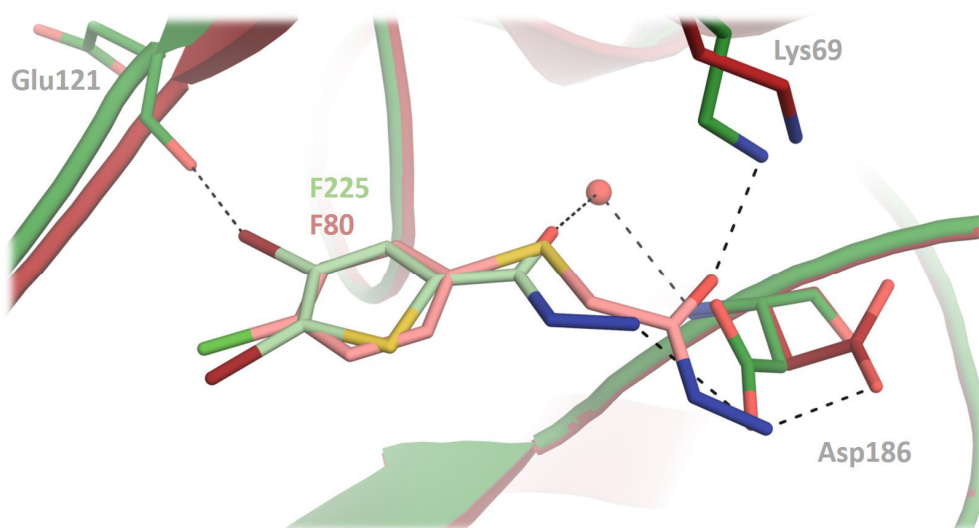


Figure 43: Superimposed Pim1 crystal structures containing fragments F225 and F80. The image shows the binding mode of both fragments in the ATP-binding pocket. Carbon atoms of F225 are coloured in light red. Carbon atoms of F80 are coloured in light green. Water molecules are shown as small red spheres. Polar interactions are shown as black dashed lines. All nitrogen atoms are coloured in blue and oxygen atoms in red.

Remarkable is the binding of the three cinnamic-acid like fragments **F3**, **F84**, and **F331**. In a published study of Schulz et al. in 2011, this substructure was discovered as a potential binder to Pim1.<sup>83</sup> In this study, the authors could obtain a few crystallographic hits from a small 148 fragment library, compiled as an ATP-site motif library and based on Cdk2 docked compounds retrieved from the Available Chemicals Directory (ACD; Symyx Technologies, Sunnyvale, California, USA). They used especially the cinnamic acid-like fragments to compare their binding modes with those found for known Pim2 inhibitors, which also comprise this moiety, showing an  $IC_{50}$  value on the nanomolar scale.<sup>95</sup> The natural product cinnamic acid is produced by the deamination of phenylalanine, and it was already shown by Liu et al. in 1995, that it can induce cytostasis and reverse malignant properties of human tumour cells *in vitro*.<sup>96</sup>

The alignment of the cinnamic acid structures discovered by the crystallographic screening of Schulz et al. with our newly discovered fragments indicates a very similar binding mode (Figure 44). Due to some minor differences in their structures, **F331** and **F3** deviate in their binding mode. The side chain and the keto group of **F3** take a different orientation compared to the chain and the carboxylate group of **F331** or **F84**. Here, **F3** contains a terminal methyl group, which is incompetent to form a hydrogen bond or a salt bridge to the amino group of Lys67 as observed for fragments exhibiting the carboxyl group. In consequence, the binding mode of **F3** is shifted, so that the ketone oxygen functions as H-bond acceptor with the protonated lysine ammonium

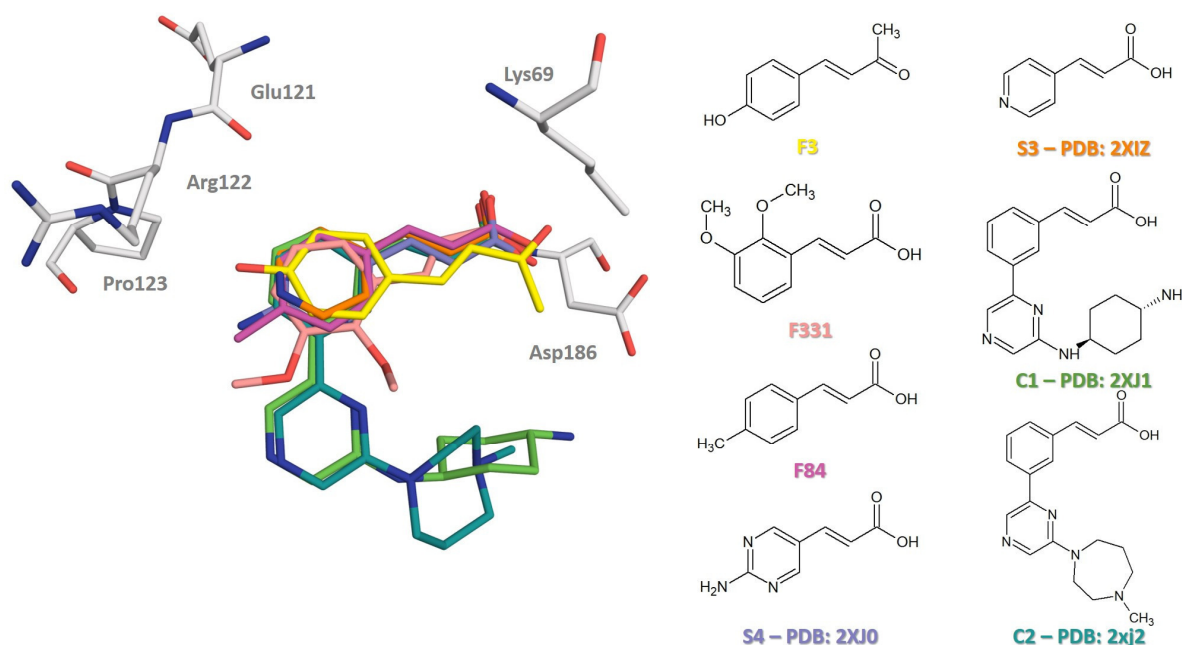


Figure 44: Derivatives of cinnamic acid bound to Pim1. On the left, the structural alignment of all compounds listed on the right side is shown. Carbon atoms from protein are coloured in grey, whereas the carbon atoms of the compounds are colour coded corresponding to the structures on the right. The compounds not contained in this fragment screening are named corresponding to their PDB code.

group. Also, fragment **F331** shows a small shift in the binding mode compared to **F84**. The central methoxy group in ortho position at the benzene ring deviates from the planar aromatic system, making this aromatic portion a non-ideal interaction partner for the protein residues in the hinge region. Therefore, the benzene ring and the attached double bond have to flip over, and the two methoxy groups point towards the pocket opening, where more space is available. Nevertheless, our fragments adopt a binding mode that is very similar to that previously discovered for cinnamic acid derivatives. Especially **F84** matches perfectly with the binding mode of compounds **S3**, **S4**, **C1**, and **C2**. The fragments **S3** and **S4** contain additional nitrogen atoms. Affinity experiments with derivatives of **C2** showed that major changes such as the replacement of the carboxyl by an ester group could cause an affinity reduction by a factor of ca. 200.<sup>95</sup> This difference demonstrates the importance of the carboxylate group of a cinnamic acid moiety for Pim1 binding affinity.



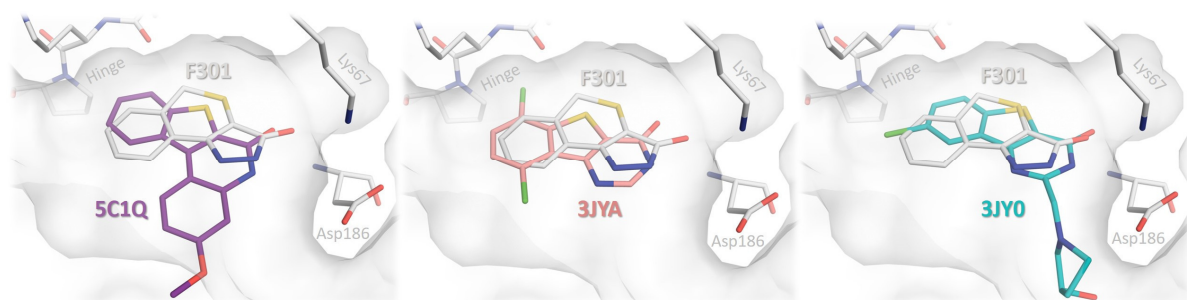


Figure 45: Binding pose of F301 compared to the ligands of PDB entries 5C1Q, 3JYA and 3JY0 respectively. The protein surface is shown in white. All ligands are shown as sticks. Carbon atoms are coloured corresponding their PDB ID label. Fragment F301 carbon atoms are coloured in grey. Oxygen atoms are shown in red, nitrogen atoms in dark blue, sulfur atoms in dark yellow and chlorine atoms in green.

Other fragments of our series also show some structural similarities to known Pim1 inhibitors, which will be discussed in the following. Visual inspection of the published PDB entries with Pim1 inhibitors revealed several entries with the same or similar structural moieties at matching positions. For example, **F301** superimposes with three PDB entries (**SC1Q**, **3JYA** and **3JY0**). Their ligands contain three or more fused aromatic rings, of which the central ring corresponds to a thiophene, and the neighbouring lactam ring, which mimics the cyclic hydrazine of **F301** (Figure 45). In all three images, the ring systems are in a very similar position compared to the one in **F301**. Also, the sulfur atom and the amide group are located in similar positions. A common difference of these ligands compared to **F301** is the five-membered ring in the centre instead of the six-membered ring of **F301**. The amide group is embedded in a neighbouring six-membered ring, which causes small changes in the geometry. In **3JYA** the ligand uses the chlorine atom to interact with the hinge region comparable to fragments **F225** and **F230**. As a second example, **F184** is compared to structures with a carboxylic acid directly attached to a planar five-membered ring. Therefore, the

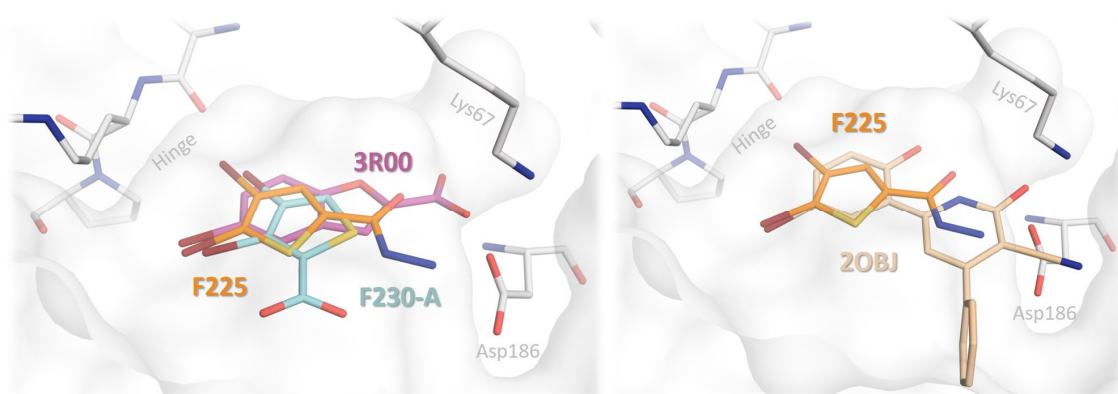


Figure 46: Aligned structures of fragment structures F225 to F230-A and PDB entry 3J00 and PDB entry 2OBI, respectively. The protein surface is shown in white. Ligands are shown as sticks. Carbon atoms are coloured corresponding their labels. Oxygen atoms are shown in red, nitrogen atoms in blue, bromine atoms in brown and sulfur atoms in dark yellow.

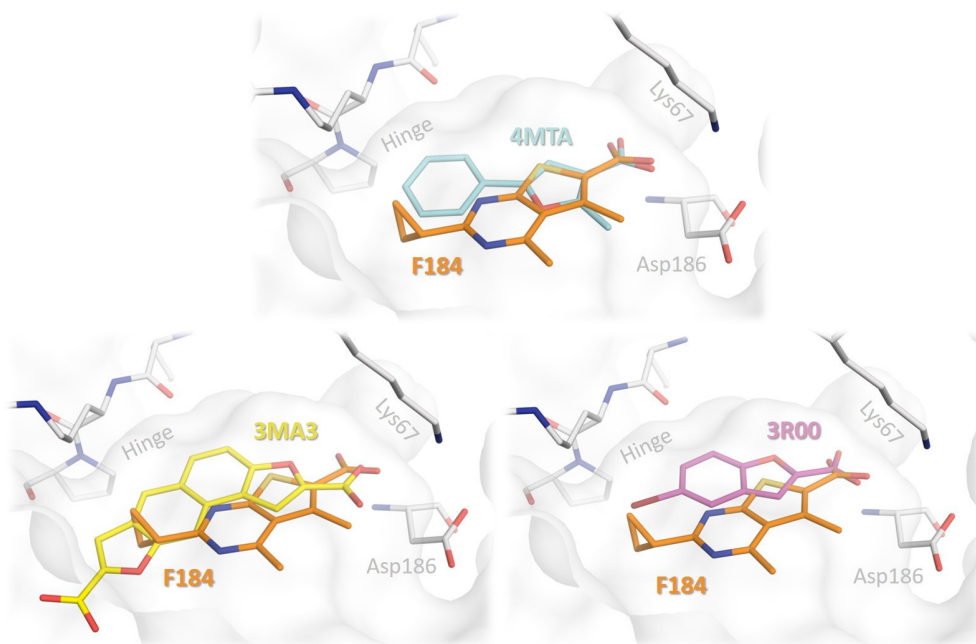


Figure 47: Binding pose of F184 compared to the ligands of PDB entries 3MA3, 4MTA and 3R00 respectively. All ligands and protein residues are shown as sticks. Carbon atoms are coloured corresponding their PDB ID label. Fragment F184 carbon atoms are coloured in orange. Oxygen atoms are shown in red, nitrogen atoms in dark blue and sulfur atoms in dark yellow.

binding modes of structures with PDB-codes **3MA3**, **4MTA** and **3R00** were chosen for the comparison (Figure 47). After superposition of the structures, the carboxylic acids are found nearly in the same position. In their deprotonated state, the carboxylate groups interact with the ammonium group of Lys67 forming a salt bridge, comparable to the cinnamic acid derivatives. A carboxylate group appears to be a structural element of a ligand to interact with Lys67. Only the ligand in **3MA3** is slightly shifted with respect to its carboxylate position. Due to its extended and rigid scaffold, the ligand partly reaches out of the binding pocket. These superimpositions indicate that the region above the pyrimidine ring, which is close to the hinge, favorably accommodates planar and hydrophobic ring systems. All compared structures occupy this region with a benzene ring. **F184** does not fully stay in this position since the steric demand of the cyclo-propyl substituent on one side and the two methyl groups on the other side results in a shift of the scaffold. The bromine of **3R00** is nearly in the same position as the one in **F225** and **F230** (orientation A), shown in Figure 46. A further structure has been reported exhibiting bromine at this position. Structure **2OBJ** is superimposed with the structure of fragment **F225**. It is also shown in Figure 46. Although both compounds do not share many structural similarities, the superimposition shows, that the bromine and the attached thiophene/benzene ring are occupying the same position. A bromine atom, which is pointing towards the hinge backbone similarly to **F225** and **F230**, was not detected in this PDB search. Only the ligand in **3JYA** (Figure 45) shows a similar motif, but containing a chlorine instead of a bromine atom. A fourth example is the cyclic urea group of **F167**, which is

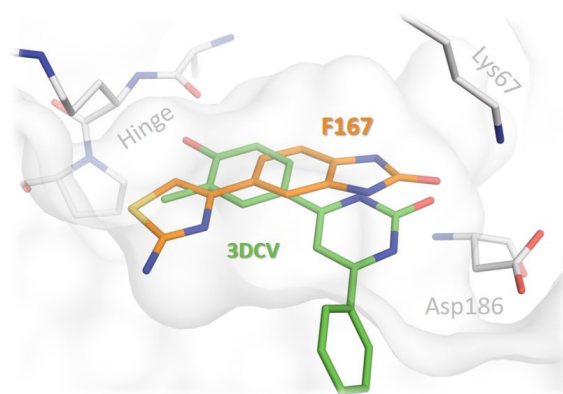


Figure 48: Aligned structures of PDB entry 3DCV with fragment structure F167 show the view in the ATP-binding pocket. Ligands are shown as sticks. Carbon atoms of 3DCV are coloured in green, Fragment F167 carbon atoms are coloured in orange. Oxygen atoms are shown in red, nitrogen atoms in blue and sulfur atoms in dark yellow.

compared to a compound exhibiting an analogous moiety in structure **3DCV** (Figure 48). Besides the urea group, both compounds share no further structural element in common, and both functionalities superimpose only with the carbonyl oxygen. The last example compares the binding mode of fragment **F222** and the compound of PDB ID **4XHK** (Figure 49). The structural element shared in common is a pyridine ring that is attached to the terminal end of **F222** whereas it displays the central part of the ligand in **4XHK** (right side in the figure). Both pyridine rings are in nearly identical binding positions. The nitrogen atom of the pyridine ring should be uncharged so that its lone pair can serve as an H-bond acceptor for Lys67. A  $pK_a$ -value of about 5 is estimated for the pyridine moiety in this environment.<sup>97</sup> The pH of this crystallisation condition for fragment **F222** was 7.0. With the  $\pi$ -conjugated peptide bound, the basic character of this nitrogen atom is further reduced. Accordingly, the pyridine nitrogen should remain deprotonated for the interaction with Lys67. Although the pH value for the crystallisation condition of **4XHK** was 5.5, the pyridine ring must also be deprotonated to establish the H-bond interaction with Lys67. The terminal carboxylate groups of Glu89 and Asp186 fall close to the lysine ammonium group and may also influence the local orientation of protons, so that the pyridine nitrogen can act as an H-bond acceptor of the Lys67 side chain ammonium group. Beside this similar positioning of the pyridine ring, the other planar ring elements of both compounds are also similarly positioned next to the hinge region. The amide oxygens of both compounds are also able to form a water-mediated bridge to the backbone nitrogen of Asp186. As a major difference, the ligand in **4XHK** comprises a flexible pyrrolidine ring, which orients into the ribose pocket without forming any direct contacts to the protein. **F222** does not occupy this region.

The comparison of known structures provides some insights into how structural elements found in our fragment structures could be grown into larger Pim1 inhibitors. In addition, new structural elements were discovered in our fragment binders, which have not been observed previously (PDB up to June 2017) described to interact with Pim1, i.e. the hydrazide groups of **F225** and **F80**, which interact directly with Asp186 or the bromine atom, which points directly to the backbone carbonyl oxygen atom of Glu121 in fragments **F225** and **F230**.

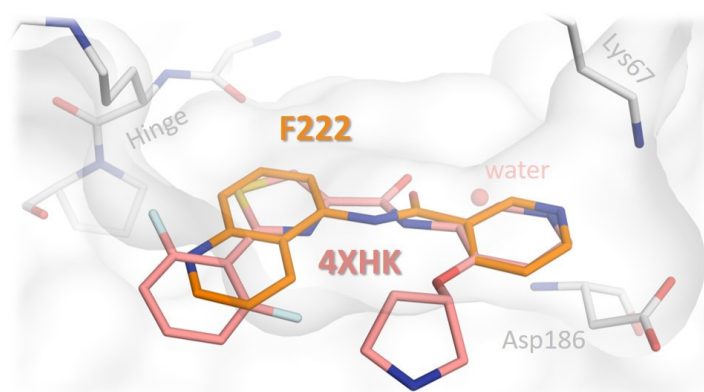


Figure 49: Aligned structures of PDB entry 4XHK with fragment structure F222 show the view in the ATP-binding pocket. Ligands are shown as sticks. Carbon atoms of 4XHK are coloured in purple, Fragment F222 carbon atoms are coloured in orange. Oxygen atoms are shown in red, nitrogen atoms in blue, fluorine atoms in light blue and sulfur atoms in dark yellow.

### 2.3.5. Comparison of PKA and Pim1 fragments binders

The preselection using TSA revealed an overlap of hit lists containing only fragment **F196**, **F222**, **F267**, **F304**, and **F328**. Only two of them were crystallographically confirmed to bind to PKA (**F222** and **F267**), and only one was found in the crystallographic screening as a Pim1 binder (**F222**). In TSA **F222** is a well-stabilizing fragment for both kinases and ranked within the first half of promising hits (Table 9). For PKA it is the 5<sup>th</sup> best stabilizing compound and for Pim1 is on rank 13. The structural alignment of PKA and Pim1 with this bound fragment shows similarities in the binding modes (Figure 50 (B-C)). An overview of the entire protein shows three important differences in their secondary structures (Figure 50 (A)). Firstly, the long PKA  $\alpha$ -helix at the N-tail of the protein, which occurs exclusively for PKA and exhibits structural elements for multiple functions such as the myristylation motif or other motifs for protein-protein interactions (EGFR, CNB, CDK2, AKIP1). The long loop at the C-tail of PKA is also missing in Pim1 and consists of interaction motifs to communicate with other proteins like SMAD3, SRC or heat shock protein 90.<sup>20</sup> The third important structural difference is the two anti-parallel  $\beta$ -sheets between  $\beta$ -sheet-3 and  $\alpha$ -helix-C of Pim1. For the arrangement of the ATP-binding pocket, only the C-tail loop plays an important role. Figure 50 (A) shows that this loop reaches into the ATP-binding pocket close

to the hinge region, where it orients the hydrophobic side chain of Phe327 into the pocket (Figure 50 (B)). This reduces the available space in the pocket and thus the area, where a molecule can enter and leave the pocket. A detailed view onto the ATP-binding pocket (Figure 50 B, C) reveals that the overall binding pose of **F222** is similar in Pim1 and PKA. The pyridine ring, in its deprotonated form, interacts with Lys72 and Lys67, respectively. The quinoline moieties are located near the hinge, where the largest differences are apparent. Compared to PKA, the quinoline moiety is approx. 1.9 Å shifted in Pim1 parallel to the hinge backbone in the direction of the pocket's mouth. In PKA, a similar shift is not possible without replacing the side chain of Phe327. Additionally, the quinoline nitrogen acts as an H-bond acceptor for the backbone nitrogen atom of Val123, which orients its NH functionality into the binding pocket. In Pim1, this interaction cannot occur since a proline is present at the same position as Val123. Proline prevents the formation of such an H-bond at this position and displays a second crucial difference between the ATP-binding pockets of PKA and Pim1. Without this H-bond, the quinoline moiety is slightly shifted. Another difference between PKA and Pim1 (Figure 50 (C)) concerns the amino acid prior to the DFG motif of both proteins. It is a threonine in PKA and an isoleucine in Pim1. Thr183 is flexible and often adopts in two orientations. In the first, the hydroxy group is directed toward the ATP position, and in the second, it is pointing away. An example of these alternative orientations

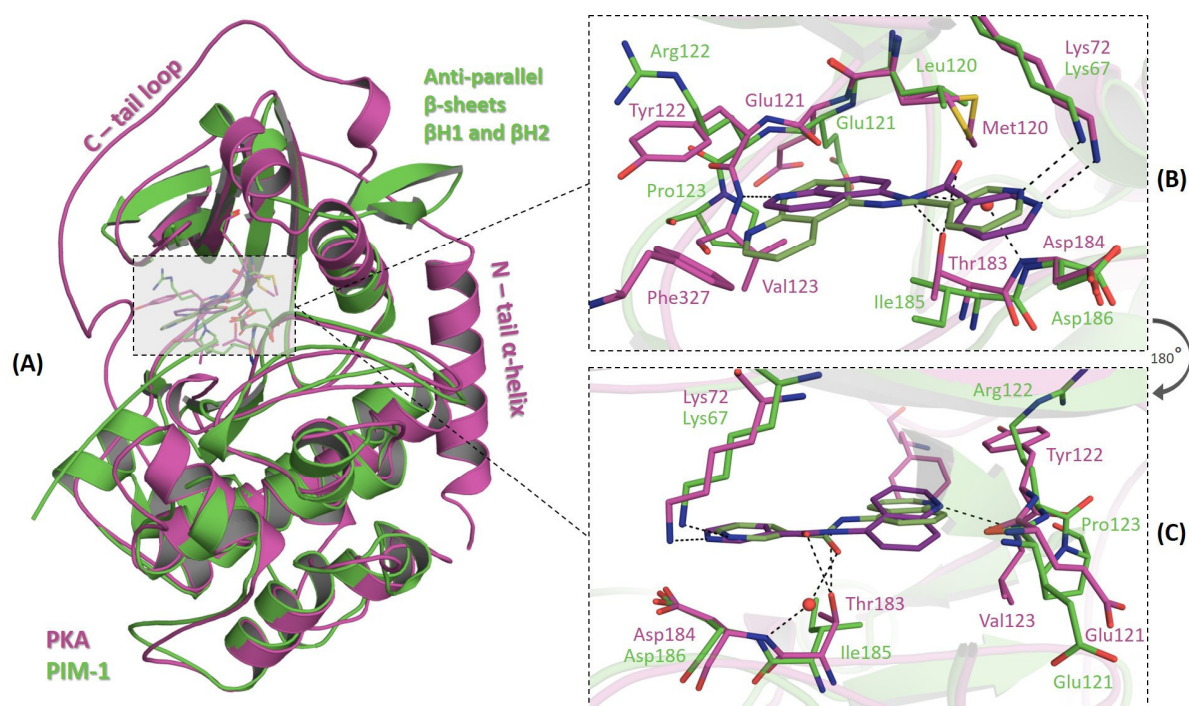


Figure 50: **(A)** Structural alignment of Pim1 and PKA with bound fragment F222. Both proteins are displayed in cartoon representation; PKA in magenta and Pim1 in green. Protein structural elements are labelled in the same colour. The grey box frames across the ATP-binding pocket, accommodating F222 **(B)** Detailed view of the ATP-binding pocket, showing relevant protein side chains as sticks. For the carbon atoms the same colour code is used as in (A). Fragment carbon atoms are displayed in dark green (Pim1) and dark magenta (PKA). Oxygen atoms are shown in red, nitrogen atoms in blue and sulfur atoms in dark yellow. **(C)** 180° rotated view of the (B) image.

can be seen in the structure of **F335** in Figure 33. In the structure of PKA in complex with **F222**, the threonine is pointing towards the amide group of the fragment. With 2.9 and 2.5 Å, the distances to amide carbonyl oxygen and nitrogen are ideal for H-bond interactions. Nevertheless, the angles to form a hydrogen bond are not optimal. The angle between C=O and O is only 66 ° and therefore below a threshold of 90 °.<sup>98</sup> The C-N - O angle of 77° is also too small. An unfavorable positioning of the amide bond in this geometry is also supported by the poorly defined electron density and thus the large B-values. The density is only fragmentarily defined, and the carbonyl oxygen shows the highest B-value of the ligand with 32.0 Å<sup>2</sup>. The lowest B-value of the ligand is 23.3 Å<sup>2</sup> whereas a mean B-value of the protein is 15.0 Å<sup>2</sup>. This correlates with a reduced occupancy of the ligand, which refines to only 85%. This is different for the Pim1-bound molecule of **F222**. The Ile185 of Pim1 points away from the ligand. This creates room for a water molecule that binds to the backbone of Asp186. Thereby it mediates a contact between protein and amide oxygen. The formed H-bonds and angles fall better in the ideal range (distances: 2.9 Å and 2.8 Å; N-O-O angle: 105°). The density is fully defined, and the B-value of the amide oxygen is with 42.2 Å<sup>2</sup> even lower than the mean B-value of the protein (50.7 Å<sup>2</sup>), while the occupancy refines to 100%. This suggests that the fragment is better fixed in the Pim1 complex. However, the comparison of both binding modes illustrates the differences between the ATP-binding pockets of Pim1 and PKA.

The missing H-bond donor functionality at Pro123 in Pim1 is crucial as it increases the hydrophobicity in this already rather hydrophobic binding pocket. 11 of the 22 PKA ATP pocket binders are using the amide nitrogen atom of Val123 to form an H-bond (**F63**, **F114**, **F342**, **F41**, **F222**, **F211**, **F267**, **F74**, **F83**, **F216**, and **F266**). Two water molecules, which usually bind to the hinge region, are displaced upon binding of these fragments. In Pim1, this interaction is not possible. Many fragments binding to PKA also form an H-bond interaction to Thr183, which is also not possible in Pim1 due to the replacement of Thr183 by Ile185. There were 9 out of the 22 fragments found to be in direct contact with the threonine in PKA complexes (**F114**, **F324**, **F222**, **F335**, **F267**, **F286**, **F83**, **F285**, and **F112**). Most fragments in this series binding to Pim1 form instead interactions with Lys67, as shown in Figure 41. Four of these Lys67 binders use a carboxylate group for a salt bridge with the protein residue (**F3**, **F84**, **F184**, and **F331**). The only fragment with a carboxylate group bound to PKA is **F266**, but it does not interact with the Lys72 amino group. Instead, it is in contact with the hinge backbone as mentioned above. The water molecule that normally coordinates to the backbone nitrogen of Asp186 in Pim1 is often used to mediate an interaction between protein and ligand, or it is replaced by the compound's carboxylate group. The presence of Thr183 seems to influence the water architecture in PKA. The visual

inspection of the corresponding PKA structures revealed that no water molecule binds to the backbone nitrogen of Asp184. The third main difference in the ATP-binding pocket is Phe327 of PKA, where Pim1 provides increased space due to the missing C-loop. There are five fragments that would clash with the side chain of Phe327, once a PKA structure is superimposed to the fragment-bound Pim1 complexes (**F184**, **F159**, **F167**, **F331**, and **F222**). In consequence, it appears unlikely that these fragments could adopt a similar binding pose in PKA without displacing the Phe327 side chain. The deviating binding modes of **F222** in both proteins illustrates the influence of this residue. Another difference between fragments bound to PKA and Pim1 is the higher frequency of fragments containing amino groups in PKA structures. Whereas several fragments in PKA contain primary (**F211**, **F274**, **F335**, **F286**, **F285** and **F189**), secondary (**F39**, **F63**, and **F112**) and tertiary amines (**F41**), not a single one is detected in Pim1.

These differences between PKA and Pim1 binders suggests that fragments show selectivity for both proteins. Pre-selection by TSA reduced the number of fragments that were crystallographically screened against both kinases, but even the suggested hits indicate selectivity. A full library screen against both proteins by crystallography would reveal how many fragments of the 361 entry library bind to PKA and Pim1 and would, therefore, allow a more comprehensive mapping. Nevertheless, it was demonstrated that the differences between the PKA and Pim1 ATP-binding pockets take an impact on the selection and binding poses of the discovered fragments.

## 2.4. Summary

A primary aim of this project was the enrichment of crystallographic hits subsequently to TSA as a pre-screening method. In TSA, 31 compounds were identified as most promising binders for PKA, while 52 fragments out of a 361 entry library were found as most promising binders for Pim1. The 31 crystal structures of PKA soaked with the relevant subset of fragments were analyzed and led to 15 crystallographic hits, which corresponds to a hit rate of approx. 48%. Pim1 crystals had to be grown via co-crystallisation. By this approach, 15 diffracting crystals were obtained, in which a fragment was observed for 13 cases. This corresponds to a hit rate of approx. 87%. Other studies following a crystallographic fragment screening without any preselection assay reported hit rates of only 5%, in case of kinases, hit rates of 10% were communicated.<sup>99</sup> The hit rates achieved in the present study are 4.8-8.7 fold higher, which at first suggests that TSA is a reasonable and useful pre-selection method. However, a subsequent analysis based on randomly selected fragments, not applying any preselection protocol, resulted in a hit rate of approx. 21% (9 of 42) for PKA, which is still twofold higher than the reported 10% for kinases. Closer inspection of the nine additional fragments revealed that most of them also had a slight stabilizing effect below the

threshold of  $\Delta T_m = 1.0^\circ\text{C}$  in TSA. Nevertheless, the results also show TSA method missed several of crystallographically identified binders, an aspect always to be considered upon evaluation of TSA results. An explanation for this phenomenon may be that the buffer conditions were too close to the stability optimum of PKA and therefore the effect of a bound fragment shows only minor impact on protein stabilisation. This may also provide an explanation for the higher number of fragment hits discovered in the TSA screen of Pim1, since here, the conditions were not as close to the stability optimum of the protein.

With the current analysis, we wanted to investigate, whether fragments can serve as selective binders for different kinases. Already the TSA pre-screening suggested some differences. The TSA hit list for PKA revealed only five overlapping compounds with the hit list of Pim1, which is a rather low number considering the large test sample of 361 compounds. Only one of them was crystallographically identified to bind to Pim1 and PKA, in a similar but not identical position. A detailed comparison of both ATP-binding pockets indicates three major differences: Pro123 in the hinge region, reducing the hydrogen-donor facilities in Pim1, Phe327 contributed by the PKA C-tail loop, reducing the available space in the ATP pocket and the miscellaneous amino acids prior to the DFG motif (Thr – Ile) creating different binding opportunities. Our comparative investigation indicated 22 compounds that use these deviating interaction spots or access the space set free by the missing Phe327 in Pim1. Additionally to the diverse TSA buffer conditions, these differences in the ATP-binding pocket of PKA and Pim1 also gives an explanation for the low overlap of the TSA hit lists. Nevertheless, it has to be mentioned, that TSA is known for producing “false negatives”<sup>53</sup>, which is confirmed by the observation of 9 randomly selected fragments showing a  $\Delta T_m$  value below the predefined threshold of  $1.0^\circ\text{C}$  in TSA. Thus, it appears likely that the number of fragments binding to PKA and Pim1 would increase if the entire library would be screened directly by crystallography.

In order to evaluate the detected fragments bound to Pim1, a comparison with published Pim1 inhibitors, exhibiting some structural similarities was performed. Pim1 was chosen because of its relevance in cancer drug therapy. An interesting study used cinnamic acid-like fragments as starting points for potent Pim1 inhibitors and they match with three fragments of our series showing similar chemical composition. A further comparison with other Pim1 binders revealed hot spots for small structural elements such as a carboxylate or a pyridine moiety for the interaction with the ammonium group of Lys67 or a bromine atom binding close to a carbonyl oxygen in the hinge region. In addition, our structural study identified new scaffolds and binding motifs for Pim1 binders that may provide novel starting points to be developed in an optimisation process to more



potent inhibitors. Especially **F225** has to be mentioned because it forms a halogen bond to the backbone carbonyl oxygen of Glu121 via its bromine atom and shows an interaction simultaneously to the terminal carboxylate group of Asp186 via its hydrazide group. This pattern may display a new opportunity for Pim1 interactions. All of the identified Pim1 binders are binding near the hinge region and the ammonium group of Lys67. This allows the extensions of these fragments so that interactions with Asn172 or Asp128 can be formed, as demonstrated in the discussed fragment study based on cinnamic acid derivatives. Extensions of fragments that lead to verified selective Pim1 binders exhibit the potential to create potent and also selective inhibitors. The development of such selective inhibitors is important to reduce side effects in drug therapy.



**3. Crystallographic screening of a 96-well-plate fragment library shows a high hit rate for the cAMP-dependent protein kinase A**

### 3.1. Introduction

In the field of fragment-based drug design, a challenging task is the identification of promising binders, which can be further optimised in a structure-based approach to highly potent inhibitors for a given target protein.<sup>100</sup> This approach is frequently applied in pharmaceutical industry, and several compounds have been identified, which have reached the clinical trial phases.<sup>101</sup> The most prominent candidate is the BRAF kinase inhibitor Vemurafenib, also known as Zelboraf, which is administrated to treat late-stage melanoma.<sup>77</sup> Here, we present a 96 compound library, which was assembled from hits already confirmed in protein-fragment crystal structures and which covers a wide range of chemical compounds. A full crystallographic screen of this library against the catalytic subunit of cAMP-dependent protein kinase A (PKA) from *Cricetulus griseus* results in a conspicuously high hit rate of 31.3%. The library was not assembled by using a kinase pre-screening method. PKA is one of the most investigated kinases, and its crystals show diffraction properties to high resolutions<sup>85</sup>, which improves detection of low-affinity binders such as fragments.<sup>102</sup> PKA is generally involved in many signal transduction pathways, such as the  $\beta$ -adrenergic cascade, steroid biosynthesis, metabolism, exocytic processes and immune system regulation.<sup>2322</sup> The ubiquitous presence of PKA makes this kinase a challenge to use as a drug target, although it could play a role in Alzheimer disease<sup>105</sup> or even cancer.<sup>104</sup> However, PKA is an ideal model protein to map its ATP-binding pocket with low-affinity fragment molecules. PKA is usually crystallised together with the peptide inhibitor PKI to improve crystal growth and quality. During this study, a new PKI-free crystal form could be obtained, which yielded even better resolution data. This is an ideal case, because now also the peptide binding cleft is accessible for potential fragment binders. By use of these PKA crystals for X-ray data collection, 30 fragments were detected binding to PKA and were compared to other PKA binders, listed in the PDB. Due to the high number of discovered fragment hits, they will be classified according to their binding position and achieved interaction pattern. Furthermore, the most frequent binding motifs of this series will be discussed.

### 3.2. Materials and methods

#### 3.2.1. Protein production and crystallisation

The protein production and crystallisation were performed as previously described (chapter 2.2.1). The full length of the PKA protein (residues 1-350) from *Cricetulus griseus* (UniProt ID P25321) was transformed into a BL21 (DE3)/pLysS *E. coli* host strain (Agilent Technologies). The recombinant protein expression was processed in ZYM 5025 medium.<sup>82</sup> Protein purification started with a Ni<sup>2+</sup>-NTA chromatography column (HisTrap HP, GE Healthcare) followed by dialysis to cleave off the His<sub>7</sub>-tag using TEV protease and to reduce the imidazole concentration. The 2<sup>nd</sup> Ni<sup>2+</sup>-NTA column was applied to separate undesired protein material from PKA. A final and strong cation-exchange

column MonoS (GE Healthcare) also was used to remove impurities and separated different phosphorylation states of the kinase. These states were separately collected and subsequently prepared for protein crystallisation.

The buffer of the concentrated PKA protein solution ( $8 - 10 \text{ mg} \cdot \text{mL}^{-1}$ ) was replaced by a solution containing 100.0 mM MES/BIS-TRIS (pH 6.9), 1.0 mM DTT, 0.1 mM EDTA and 75 mM LiCl to prepare the crystallisation conditions. This protein solution was added to a sitting drop vapour diffusion plate in  $3 \mu\text{l}$  drops, the concentration of non-ionic detergent MEGA 8 and cAMP-dependent protein kinase inhibitor peptide PKI (IAAGRTGRRQAIHDILVAA; Sigma Aldrich) was adjusted to 1.5 mM (MEGA 8) and 0.7 mM (PKI), respectively. Alternatively, the solution was prepared without PKI. The crystallisation condition contained a 22—24% (v/v) methanol/water mixture. Depending on whether PKI-present or PKI-free conditions were applied, the crystals grew to optimal size in 1-2 weeks or 3 weeks, respectively. Crystal growth was induced by microseeding. Detailed information about these processes can be found in the appendix of this thesis.

### 3.2.1. Crystal soaking

The fragments were soaked into fully grown PKA crystals at  $4^\circ\text{C}$  in a buffer containing 10% (v/v) fragment-stock solution (1M in DMSO), 30% (v/v) MPD and 60% (v/v) crystallisation solution. MPD was added as cryo-protectant. To reduce the amount of mosaicity created by a too harsh transfer, the crystals were transferred into cryo condition by several steps of increasing MPD concentration, thus reducing the influence of severe osmotic shock. The fragment-stock solution was only added to the final cryo condition. The crystals were incubated for 10-15 minutes in this final solution before they were mounted in a cryo-loop and flash frozen in liquid nitrogen.

### 3.2.2. X-ray data collection, structure solution and refinement process

The crystals of this series were measured at the beamlines (BL) at three different synchrotrons, namely BL14.1 and BL14.3 at BESSY II in Berlin <sup>62</sup>, BL ID-23-2 and ID-29 at the European Synchrotron ESRF in Grenoble <sup>63</sup> and BL XRD1 at the synchrotron facility ELETTRA in Trieste. <sup>64</sup>

The software *XDSAPP* <sup>67</sup> was used for processing of the data sets. Structures were determined by molecular replacement using the software *Phaser MR* <sup>84</sup>, and as a search model, the crystal structure **4wih** <sup>85</sup> from the PDB was used. The program *Coot* was applied for model building <sup>73</sup> and *Phenix* for structure refinement. <sup>72</sup> The first refinement cycle included simulated annealing based on default parameters. TLS refinement was carried out in further steps. Depending upon the dataset quality, the individual B-values were calculated via iso- or anisotropic refinement. B-values of water

molecules were always refined isotropically. The occupancy of split orientations and bound ligands was also refined. In some cases, the placement of H-atoms resulted in an improvement of the R-free value. The crystallographic data for each data set are listed in the crystallographic tables in the appendix. The tables also include Ramachandran plots generated by the program *PROCHECK*.<sup>74</sup> The graphic images of the structures were produced with the program *Pymol*.<sup>87</sup>

### 3.3. Results

All 96 fragments were soaked into PKA crystals and analyzed by X-ray diffraction. Since the PKI-free crystals were obtained during this project, where almost half of the screen had already been completed, a subset of 43 fragments was soaked into crystals containing PKI and 53 into PKI-free ones. The resolution of the final data sets varies between 1.07 Å and 2.19 Å with a mean resolution of 1.42 Å. It was conspicuous, that especially the PKI-free PKA crystals revealed a better resolution with a mean value of 1.29 Å, whereas the PKI bound crystals had a mean resolution of 1.55 Å. Through careful visual inspection of the electron density at several refinement stages, a total of 30 fragments was detected in the relevant structure. 15 were detected in PKI-containing and 15 in PKI-free PKA structures. With 30 hits out of 96 compounds, the hit rate reached the remarkable rate of 31%. It has been previously reported<sup>55</sup> that hit rates in unprioritised crystallographic

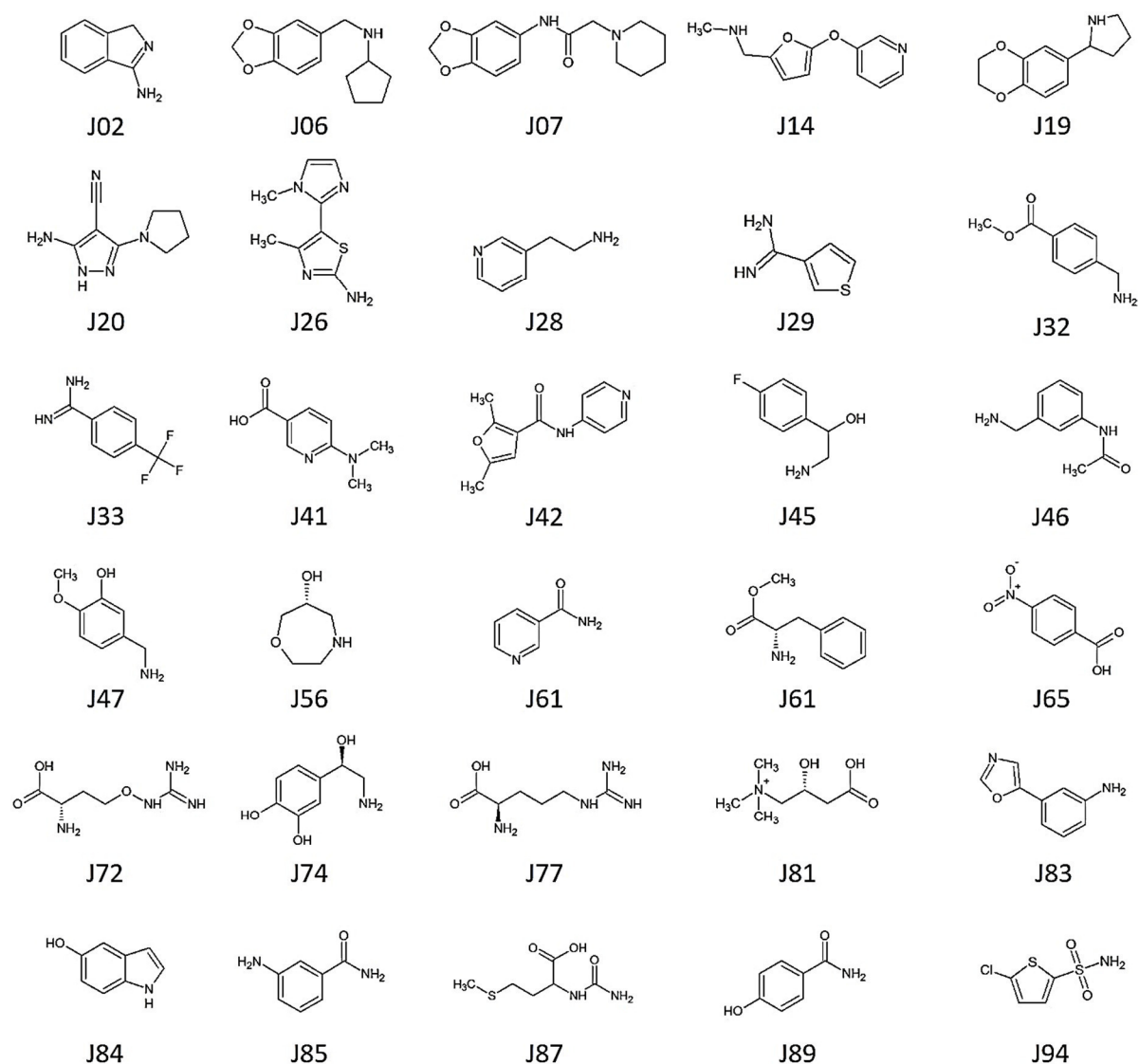


Figure 51: Chemical structure of PKA bound fragments. The fragments are labeled corresponding to their ID.

screening using kinases achieved a mean hit rate of 5%. Considering the short soaking time of fewer than 15 minutes per crystal, this quantity of fragment binders appears surprising as in many cases a soaking time span of one or two days or even extending to one month have been suggested.<sup>105</sup> Nevertheless, for most of the observed fragments the electron density was clearly defined so that the compound could be easily identified and assigned to the protein structure. Most of the fragments were observed to bind in the catalytical centre of the kinase, the ATP-binding pocket. In some cases, a second or third copy of a fragment binds in a remote position. Other fragments were exclusively detected in remote positions. Table 13 lists all detected fragments of the tested 96-well-plate library summarizing where the corresponding electron density was observed in the crystal structure. Six of the 30 identified PKA binders do not occupy the ATP-binding pocket (**J62**, **J72**, **J77**, **J81**, **J87**, and **J94**). Such fragments may be interesting for the development of allosteric binders, assuming they bind to an allosteric pocket and do not result in an artificial binder due to the crystal packing. Therefore, the so-called remote binders will be especially analyzed and discussed. Due to the fact that some fragments bind multiple times to PKA, there are 15 remote binding positions to be discussed. Six compounds, which are already present in the ATP-binding pocket, also occupy a remote binding site additionally (J06, J45, J46, J56, J83, and J85). Two

ID	Occ.	RSCC	ID	Occ.	RSCC
J02	1.00	0.86	J47	0.81	0.70
J06	0.82 / 1.00	0.48 / 0.95	J56	1.00 / 1.00	0.84 / 0.69
J07	0.93	0.88	J61	1.00	0.92
J14	1.00	0.95	J62	1.00	0.98
J19	1.00	0.85	J65	1.00	0.97
J20	1.00	0.95	J72	1.00	0.96
J26	0.70	0.84	J74	1.00	0.98
J28	0.83	0.81	J77	0.65 / 0.35*	0.94 / 0.94
J29	0.69	0.73	J81	1.00	0.96
J32	0.27 / 0.73*	0.90 / 0.90	J83	1.00 x 3	0.93 / 0.93 / 0.98
J33	0.88	0.85	J84	1.00	0.95
J41	1.00	0.98	J85	1.00 / 0.61	0.97 / 0.88
J42	0.91	0.96	J87	1.00	0.93
J45	1.00 x 3	0.93 / 0.71 / 0.90	J89	0.60 / 0.40*	0.98 / 0.98
J46	1.00 / 1.00	0.94 / 0.76	J94	0.74 / 0.74	0.84 / 0.78

Table 12: Occupancies and RSCCs of the 30 fragment hits and their binding positions. \* These fragments have been modelled in two conformations. In both cases the sum of conformation A and B is 1.00.



fragments (**J45** and **J83**) accommodate even three diverse binding positions. In summary, 39 binding poses are indicated by 30 bound fragments. The lowest occupancy is shown by fragment **J29** with 0.69, whereas for 19 fragments the indicated binding position refines to full occupancy. We used the validation criteria of Deller & Rupp to evaluate whether the fragments fit well into the obtained difference electron density.<sup>106</sup> After using this categorizing scheme almost all fragments fall into the first or the second category of density fitting. There are 20 fragments in the first category with a value for the corresponding real-space correlation coefficient (RSCCs) between 1.0 and 0.9, which indicates good density fitting. Furthermore, there are eight fragments found in the second category, which falls into the RSCC range of 0.9 and 0.8. This category is called ‘dubious fitting binders.’ Only two fragments are below the limit of 0.8 and therefore fall into the third category of bad fitting ligands. Keeping in mind that fragments are supposedly weak binders, it is surprising, that 66.6% of the 30 fragments are located in the first category of well-fitting ligands. Table 12 shows the refined occupancy values for each observed binding position and the corresponding RSCCs. 19 fragments show fully occupied positions in their crystal structure, and there are three additional fragments which are scattered over two alternative binding poses in the same region. However, their summed occupancy adds up to 1.00 (**J32**, **J77**, and **J89**). According to its low occupancy, fragment **J29** only achieves a low RSCC of 0.73. The second low RSCC was obtained for **J47** with 0.70. In this case, the occupancy refines to only 81%. Nevertheless, the

ID	ATP-Pocket	Outside ATP-Pocket	ID	ATP-Pocket	Outside ATP-Pocket
<b>J02*</b>	<input checked="" type="checkbox"/>	<input type="checkbox"/>	<b>J47*</b>	<input checked="" type="checkbox"/>	<input type="checkbox"/>
<b>J06*</b>	<input checked="" type="checkbox"/>	<input checked="" type="checkbox"/>	<b>J56</b>	<input checked="" type="checkbox"/>	<input checked="" type="checkbox"/>
<b>J07*</b>	<input checked="" type="checkbox"/>	<input type="checkbox"/>	<b>J61</b>	<input checked="" type="checkbox"/>	<input type="checkbox"/>
<b>J14*</b>	<input checked="" type="checkbox"/>	<input type="checkbox"/>	<b>J62</b>	<input type="checkbox"/>	<input checked="" type="checkbox"/>
<b>J19*</b>	<input checked="" type="checkbox"/>	<input type="checkbox"/>	<b>J65</b>	<input checked="" type="checkbox"/>	<input type="checkbox"/>
<b>J20*</b>	<input checked="" type="checkbox"/>	<input type="checkbox"/>	<b>J72</b>	<input type="checkbox"/>	<input checked="" type="checkbox"/>
<b>J26*</b>	<input checked="" type="checkbox"/>	<input type="checkbox"/>	<b>J74</b>	<input checked="" type="checkbox"/>	<input type="checkbox"/>
<b>J28*</b>	<input checked="" type="checkbox"/>	<input type="checkbox"/>	<b>J77</b>	<input type="checkbox"/>	<input checked="" type="checkbox"/>
<b>J29*</b>	<input checked="" type="checkbox"/>	<input type="checkbox"/>	<b>J81</b>	<input type="checkbox"/>	<input checked="" type="checkbox"/>
<b>J32*</b>	<input checked="" type="checkbox"/>	<input type="checkbox"/>	<b>J83</b>	<input checked="" type="checkbox"/>	<input checked="" type="checkbox"/> <input checked="" type="checkbox"/>
<b>J33</b>	<input checked="" type="checkbox"/>	<input type="checkbox"/>	<b>J84</b>	<input checked="" type="checkbox"/>	<input type="checkbox"/>
<b>J41*</b>	<input checked="" type="checkbox"/>	<input type="checkbox"/>	<b>J85</b>	<input checked="" type="checkbox"/>	<input checked="" type="checkbox"/>
<b>J42*</b>	<input checked="" type="checkbox"/>	<input type="checkbox"/>	<b>J87</b>	<input type="checkbox"/>	<input checked="" type="checkbox"/>
<b>J45*</b>	<input checked="" type="checkbox"/>	<input checked="" type="checkbox"/> <input checked="" type="checkbox"/>	<b>J89</b>	<input checked="" type="checkbox"/>	<input type="checkbox"/>
<b>J46*</b>	<input checked="" type="checkbox"/>	<input checked="" type="checkbox"/>	<b>J94</b>	<input type="checkbox"/>	<input checked="" type="checkbox"/> <input checked="" type="checkbox"/>

Table 13: All fragments of the tested library which could be seen bound to the crystals of PKA. The location where the soaked fragments could be found is marked by a check. If a fragment is checked twice, it means that two different positions could be observed for it in the relevant category. \*PKI-complexed structure.

electron density for both fragments is reasonably well defined and shows the presence of the fragments. The difference electron density of all fragments is shown in figures 52-55. These figures also depict the detailed binding pose of every detected fragment. The binding poses are roughly sorted according to the region where they occupy the protein: The ATP-binding pocket or remotely to the ATP-binding pocket, similarly as listed in Table 13. A more detailed classification of all binders into diverse sub-sets will be presented in the following section. A detailed description of the individual binding modes of the various fragments can be found in the appendix of this thesis. There, the individual fragments are labeled according to the number assigned in the 96 fragment screen (J02 -J95). As some overlap with the test fragments from the 361-entry library is given, some fragment hits in the appendix are assigned to two labels (e.g., J02/F5 or J06/F39).

We analyzed the binding pose of fragment **J32** in PKI-free and PKI-containing structures to evaluate if comparability of the fragment binding poses in the ATP-binding pocket is given. In both crystal structures, J32 adopts the same binding pose interacting with the backbone nitrogen of Val123 and the carboxylic acid of Glu127 (Figure 52). Nevertheless, there is a difference of 0.9 Å in data resolution affecting the level of detail. Therefore, an alternative orientation of the amino group is visible in the PKI-free crystal using a water mediation to contact the backbone carbonyl oxygen of Glu127. This only partly populated interaction pattern could not be observed in the PKI-containing structure. However, this comparative analysis indicates that PKI does not influence fragment binding.

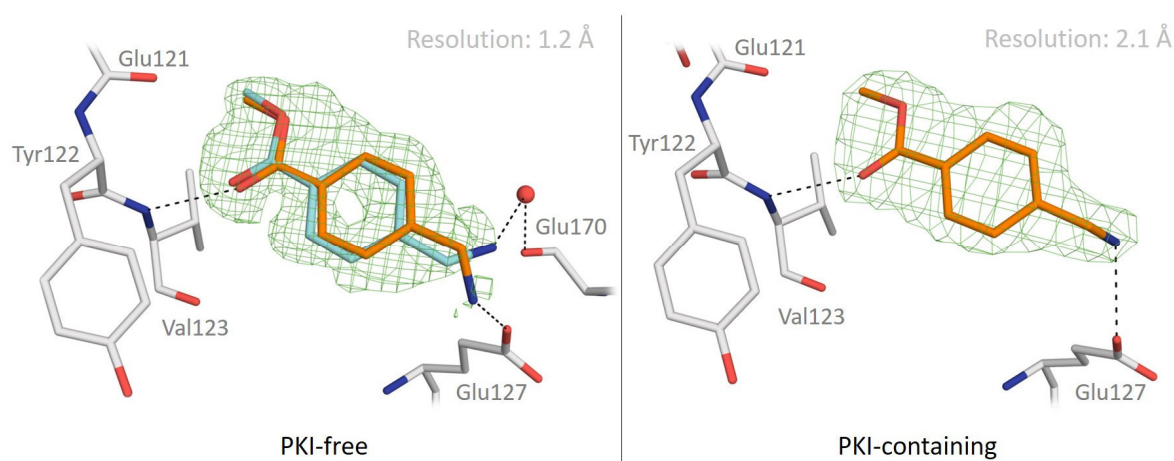


Figure 52: Fragment J32 binds to the PKI-free crystal structure of PKA as well to PKI-containing one in very similar binding pose. Since the resolution of the PKI-free structure (1.2 Å) is significantly higher than for the PKI-containing one (2.1 Å), more details are visible in the electron density of the PKI-free structure. For example the alternative orientation of J32's amino group involving a water-mediated interaction with the backbone carbonyl of Glu127.



Crystallographic screening of a 96-well-plate fragment library shows a high hit rate for the cAMP-dependent protein kinase A

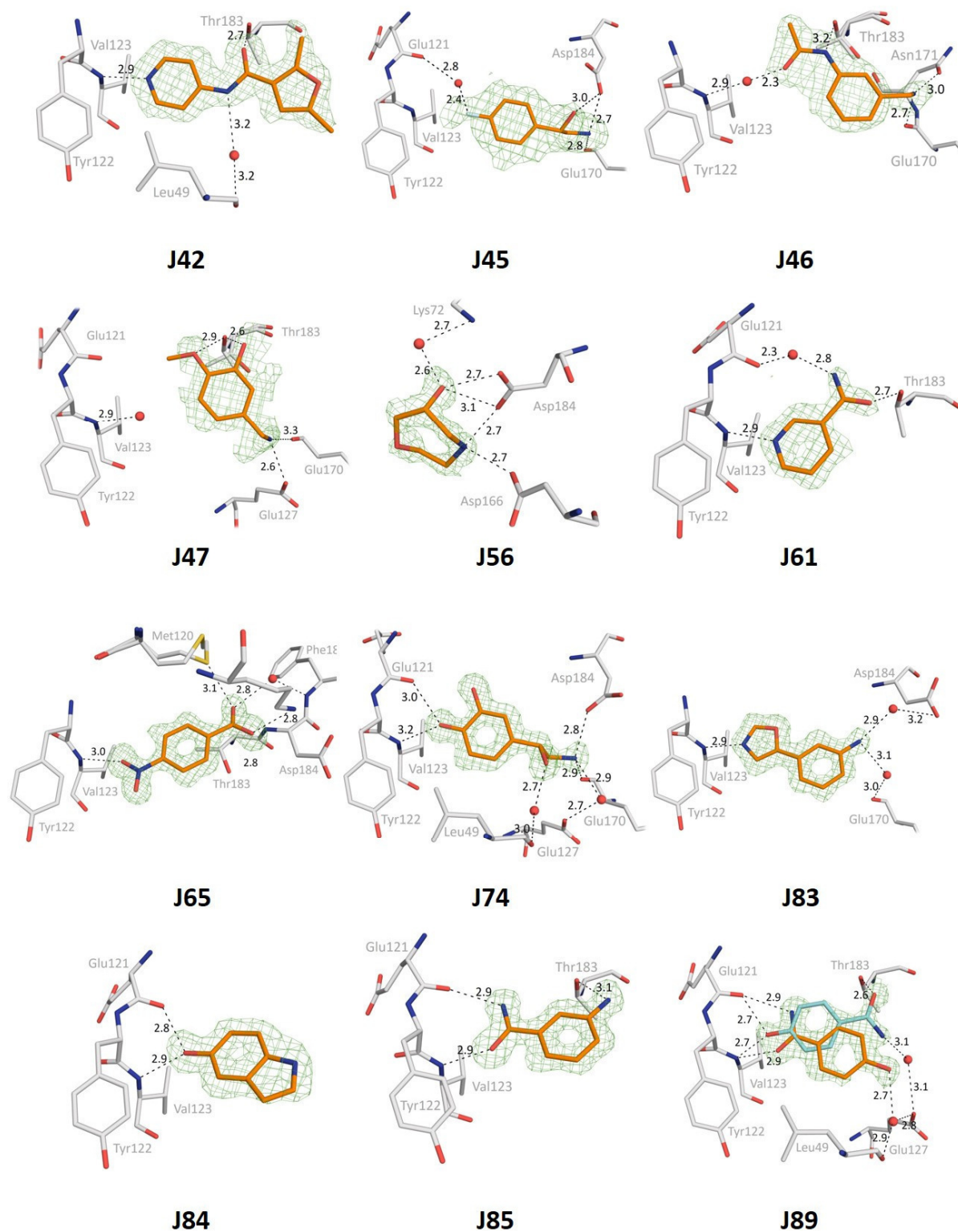


Figure 54: Detected fragments bound to the ATP-binding pocket of PKA. Fragments and protein residues are displayed as sticks. Protein carbon atoms are coloured in grey, fragment carbon atoms in orange or cyan (alternative conformation). Water molecules are shown as small red spheres. Nitrogen atoms are coloured in blue, oxygen atoms in red, sulfur atoms in yellow and fluorine atoms in light blue. Polar contact interactions are shown as black dashed lines. The unbiased ( $mF_o - DF_c$ ) difference electron density (contoured at  $3\sigma$ ) is displayed as green mesh.

Crystallographic screening of a 96-well-plate fragment library shows a high hit rate for the cAMP-dependent protein kinase A

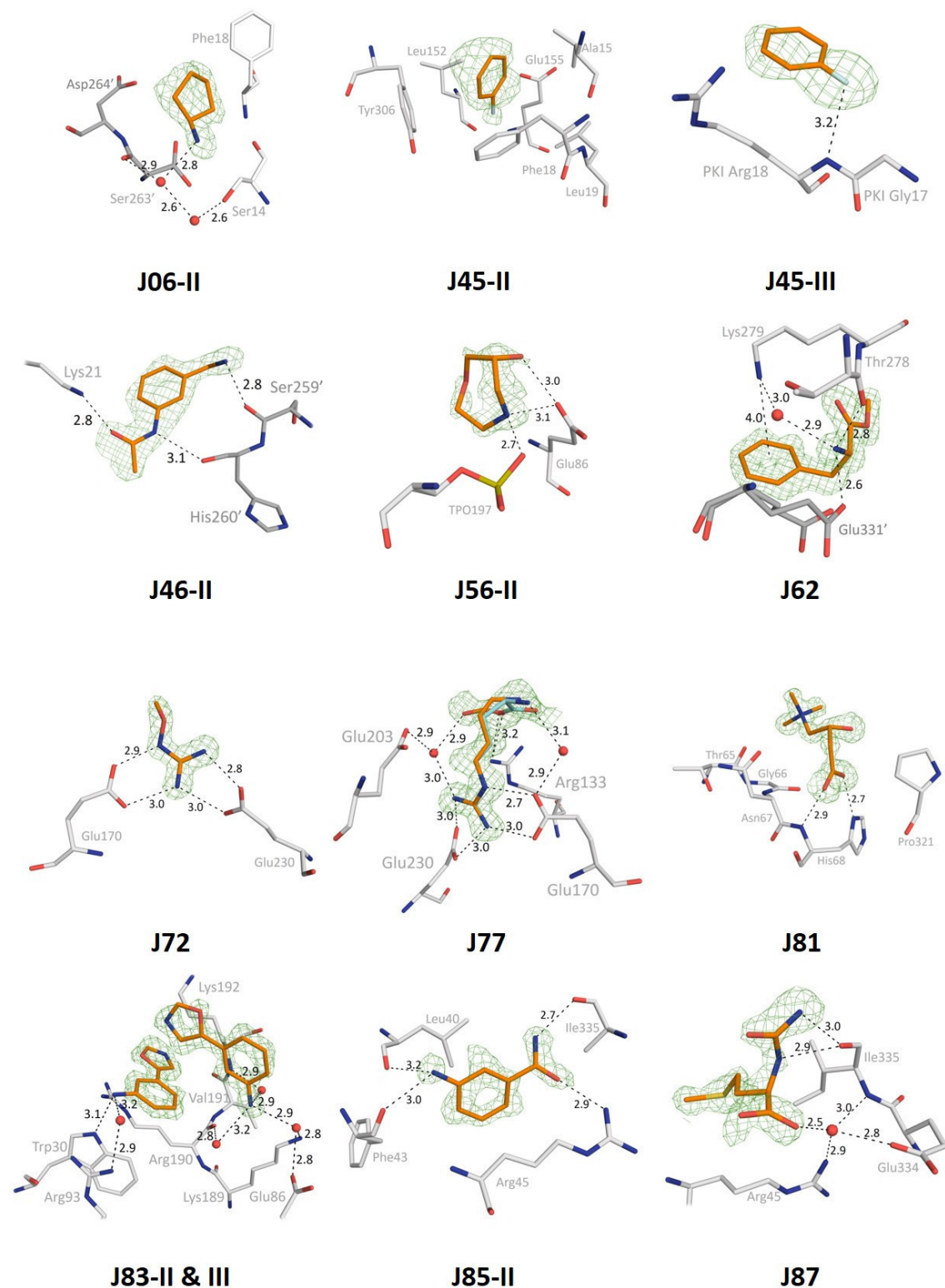


Figure 55: Detected fragments bound outside the ATP-binding pocket of PKA. Fragments and protein residues are displayed as sticks. Protein carbon atoms are coloured in grey, fragment carbon atoms in orange or cyan (alternative conformation). Symmetry-related protein residues have darker grey carbon atoms. Water molecules are shown as small red spheres. Nitrogen atoms are coloured in blue, oxygen atoms in red, sulfur atoms in yellow and fluorine atoms in light blue. Polar contact interactions are shown as black dashed lines. The unbiased ( $mF_o - DFC$ ) difference electron density (contoured at  $3\sigma$ ) is displayed as green mesh.

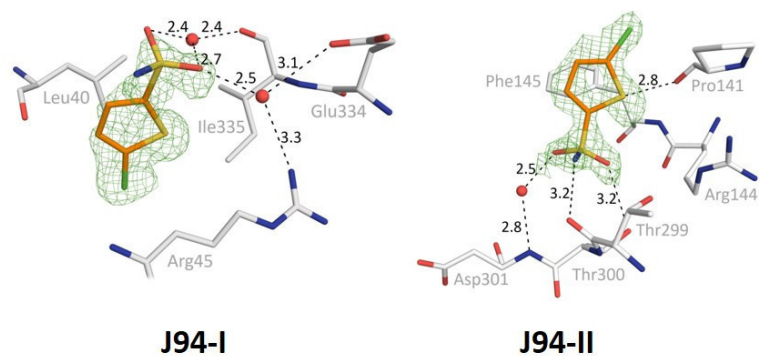


Figure 56: Binding modes of J94 outside the ATP-binding pocket of PKA. Fragments and protein residues are displayed as sticks. Protein carbon atoms are coloured in grey, fragment carbon atoms in orange. Water molecules are shown as small red spheres. Nitrogen atoms are coloured in blue, oxygen atoms in red, sulfur atoms in yellow and chlorine atoms in green. Polar contact interactions are shown as black dashed lines. The unbiased ( $mF_o - DF_c$ ) difference electron density (contoured at  $3\sigma$ ) is displayed as green mesh.

### 3.3.1. Categorisation of fragment binding position

As described above, the fragment binders were roughly sorted into the categories of either ATP-pocket or non-ATP-pocket binders (Table 13 & Figure 57). To further subcategorise, each observed binding motif was analyzed to elucidate where the hot spots of binding are located. The results show that almost all fragments (20 out of 24) in the ATP-binding pocket are in contact with the DFG loop (Thr183 & Asp184). A smaller amount only interacts with the hinge backbone (16

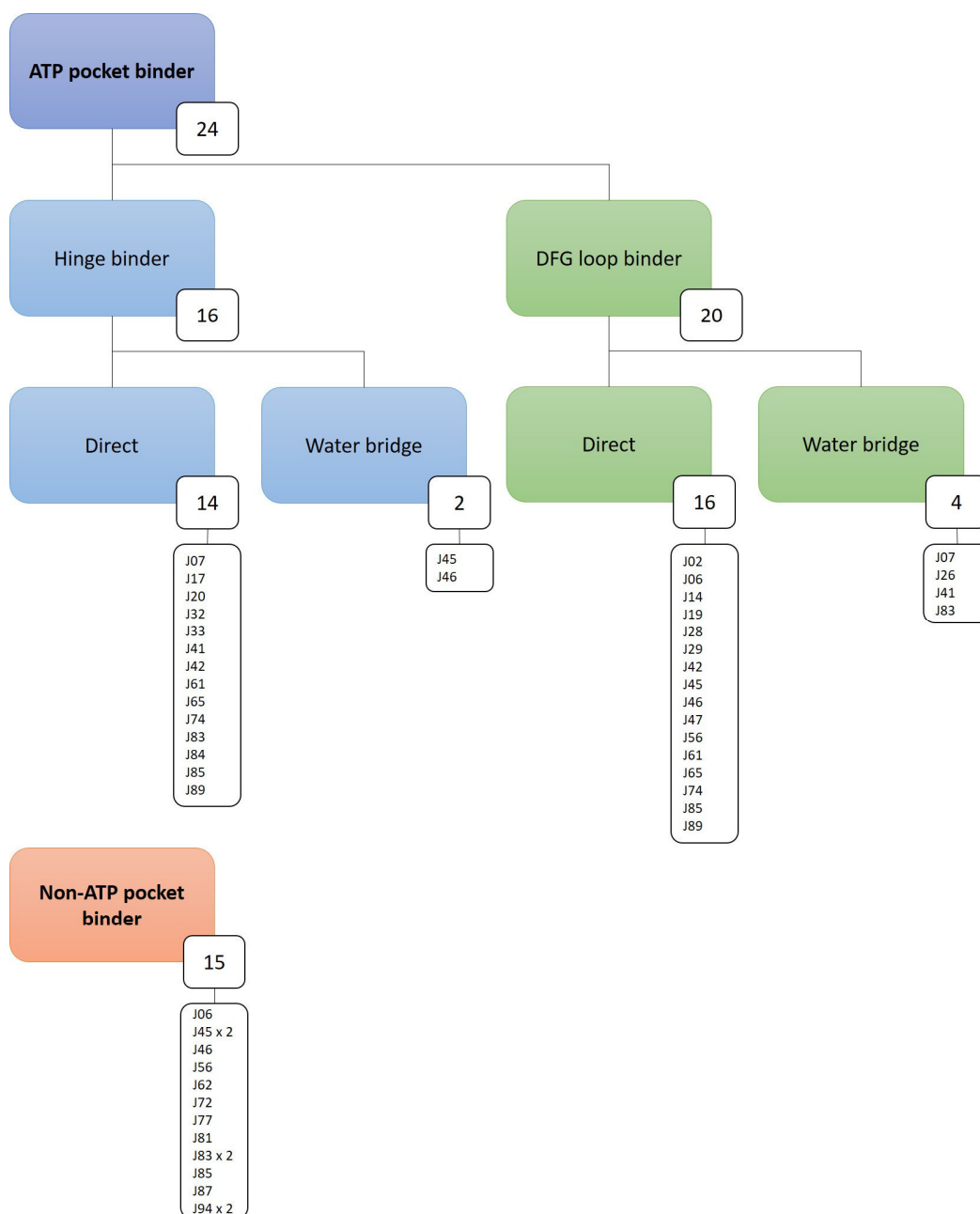


Figure 57: Schematic overview of the categorisation of fragment binding to PKA. The mean filter sorts a fragment into the ATP-pocket binder (blue) or the non-ATP-pocket binder (red). The ATP-pocket binders are further sorted into the subclasses hinge binders (light blue) and/or DFG Loop binders (green). Because a fragment can interact with both parts, 12 of them fall in more than one category. Number and fragment ID is shown for each category.

out of 24) (Glu121 & Val123). Even fewer examples penetrate into the ribose pocket forming an H-bond to the carboxylate group of Glu127 (**J02**, **J19**, **J32**, and **J47**). In several cases, interactions are mediated by a water molecule. According to these observations, the ATP-pocket binders were sorted into four subclasses, as presented in Figure 57. Using this classification scheme, the 24 ATP binders fall into the subcategory “hinge binder” and/or “DFG loop binder.” A fragment is assigned to both subclasses when contacts to both parts are found. Subsequently, a fragment is either classified as “direct interactor” or “water bridge-mediated interactor.”

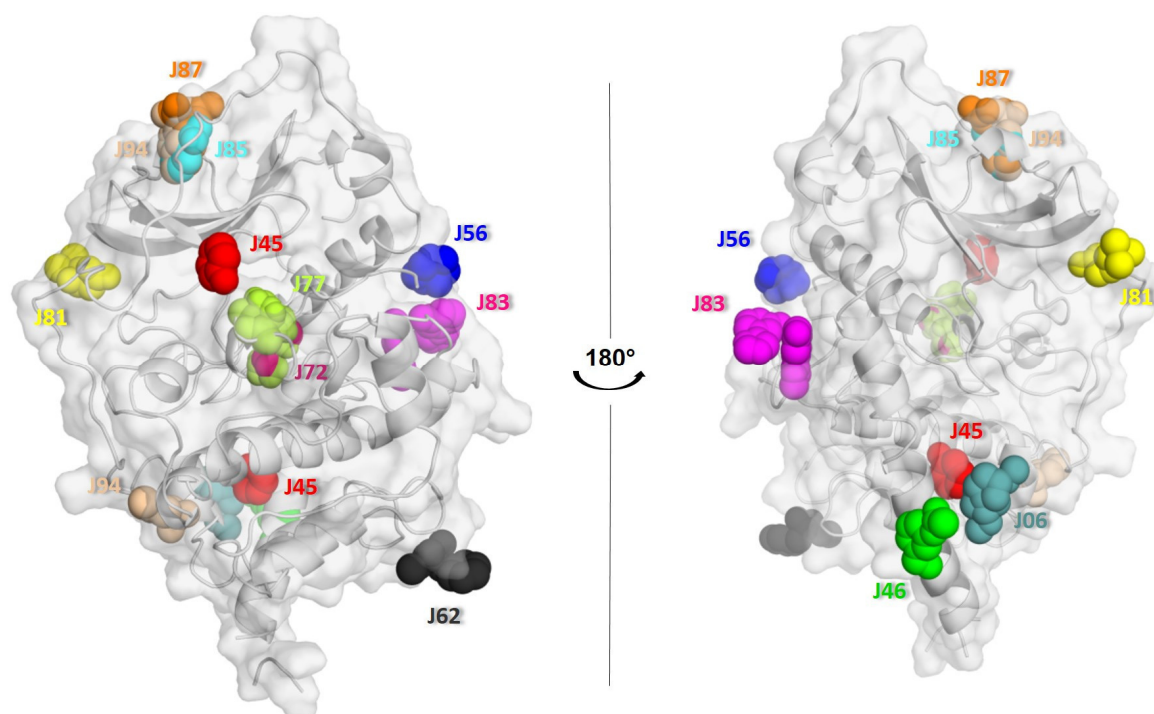


Figure 58: Overview of all PKA binding sites remote of the ATP-binding pocket. The protein is shown in grey and cartoon mode. The protein surface is indicated in light transparency. The fragments are shown as coloured spheres and are labelled in the same colour according to their library ID.

The binding positions of all non-ATP pocket binders are widely scattered across the protein surface. There are a few positions that are occupied more than once suggesting them as remote hot spots. These putative hot spots will be described in more detail. In Figure 58, all binding positions, observed in this series, are displayed to indicate how many diverse binding sites were localised. Of 15 binders in this category, 12 are found at different binding positions; thus, only at two positions, fragments are detected multiple. These hot spots accommodate **J72** and **J77**, in the PKI-binding cleft. It is obvious that the binding of **J72** and **J77** can only be realised in the absence of PKI.<sup>107</sup> The structural comparison of both fragments explains their similar binding. They mimic Arg19 in the PKI binding motif establishing salt bridges to the carboxylate groups of Glu170 and Glu230 (Figure 59 & Figure 60). It is not surprising that the Arg19 site of PKI is accommodated by both



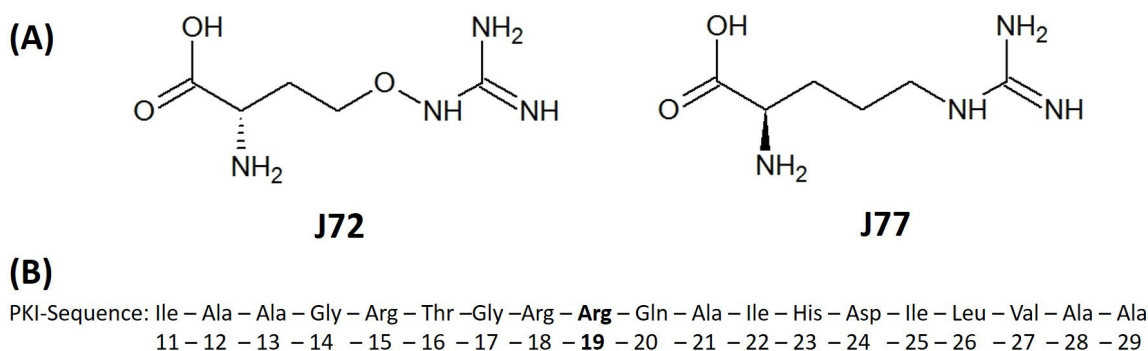


Figure 59: (A) Chemical structure of J72 and J77. (B) Part of the PKI-sequence (type SCP0064 from Sigma Aldrich) in three letter code. The highlighted amino acid Arg19 binds in the same position as the two fragments.

fragments since it has been shown that Arg19 is crucial for the binding affinity of PKI.<sup>108</sup> It is part of the substrate recognition motif for PKA (Arg – Arg – X – S/T – [Hydrophobic AA]). Therefore, this binding hot spot is essential for the construction of a competitive peptide inhibitor. A published example is the inhibitor ARC-670,<sup>109</sup> which binds to the ATP-binding pocket and the peptide-binding site. ARC-670 mimics an adenosine moiety at the hinge and uses arginine residues to address the discussed pocket (PDB entry: **3agm**). It achieves potent binding only in the presence of these arginine-like sidechains.

The second remote binding hot spot is located in the small hydrophobic pocket in the  $\beta$ -sheet region. Three fragments are found in this pocket (**J85-II**, **J87**, and **J94-I**). It is primarily formed by hydrophobic side chain residues. The bottom of this pocket is represented by a methionine side chain with its thioether group (Met71). The rim of the pocket is formed by the amino acids Leu40,

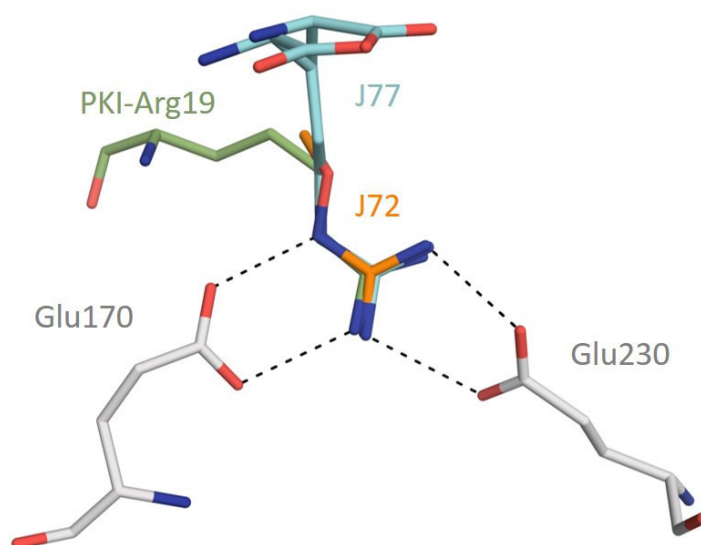


Figure 60: Comparison of PKI-Arg19, J72, and J77 binding. Protein residues and fragments are shown in sticks mode. Oxygen atoms are displayed in red, nitrogen atoms in blue, and protein carbons in grey. The carbon atoms of the three binders are differentiated by colours also used for the compound labels.

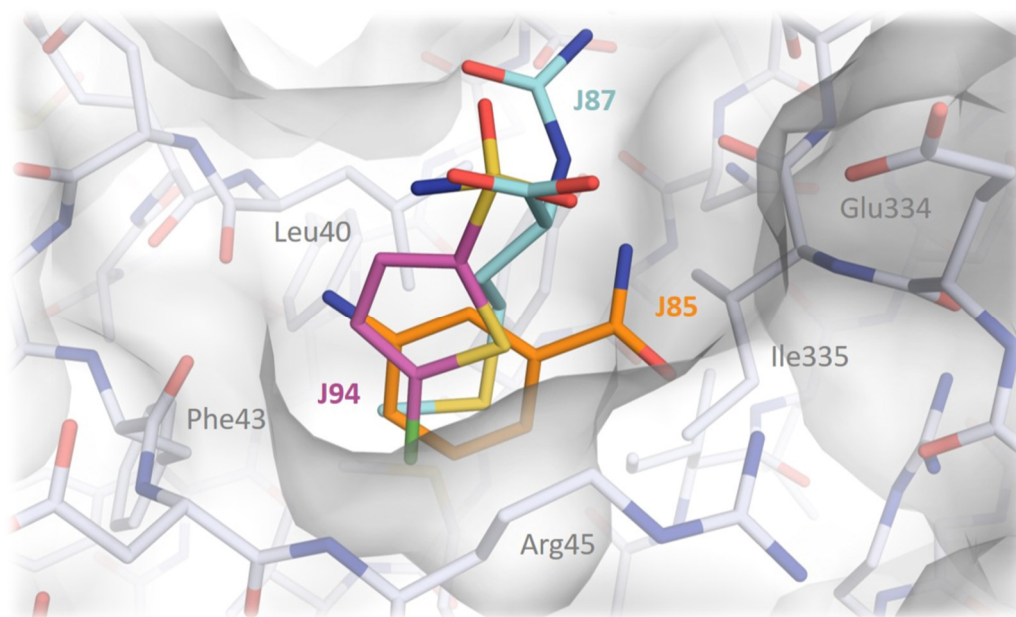


Figure 61: Observed binding pocket in the  $\beta$ -sheet region of PKA. The surrounding amino acids are coloured in grey. Protein atoms are shown as sticks. Additionally, the protein surface is displayed. The bound fragments are differentiated according to the colour of their carbon atoms. Overall, nitrogen atoms are coloured in blue, oxygen atoms in red, sulfur atoms in yellow and chlorine atoms in green.

Phe43, Arg45, Glu334, and Ile335 (Figure 61). Only at the pocket's opening, polar interaction partners are present. All three ligands position a hydrophobic portion into this pocket; in **J85** its benzene ring, in **J87** its thioether group and in **J94** its chloro thiophene ring. The distance between the methionine sulfur to the sulfur atom of **J87** amounts to 4.5 Å. At the edge of the pocket, fragments are interacting with the backbone carbonyl oxygen of Phe43, the hydrophobic part of the side chain of Arg45, the backbone carbonyl oxygen of Ile335 or a water-mediated contact is

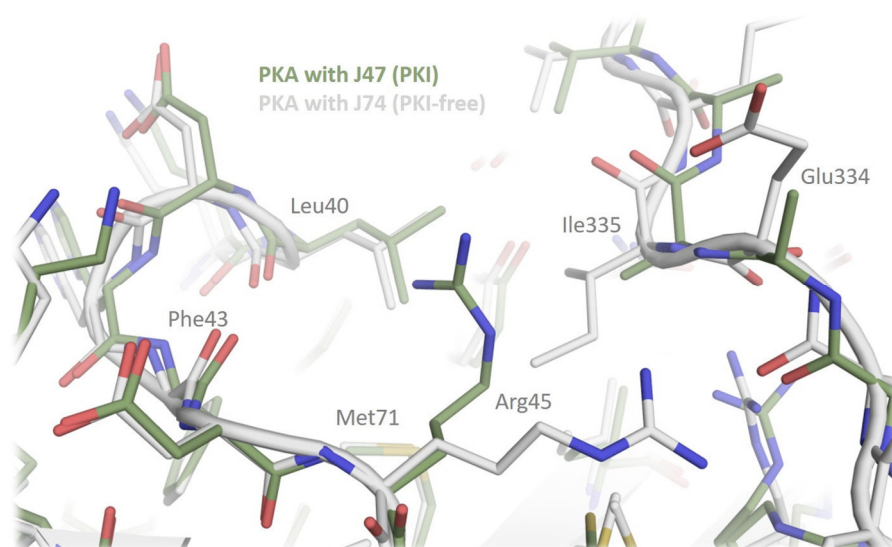


Figure 62: Superimposed structures of PKA in complex with J47 and J74. The displayed section captures the swap of Arg45 from the PKI free (J74) to the PKI-bound structure (J47).

used to the side chain of Glu334 (**J94**). A literature search did not disclose any indication that this hydrophobic pocket has been reported as functionally relevant. The inspection of all PKA structures in the present series revealed that only the PKI free crystals showed this pocket in an accessible state. In PKA crystals structures complexed with PKI, Arg45 is observed to block this pocket by populating another side chain rotamer. To highlight this swap, the structures with **J47** and **J74** are superimposed, a PKI-containing and a PKI-free structure, respectively (Figure 62).

A critical aspect while discussing remote binding sites, is the occurrence of these surface binders in close neighbourhood to a symmetry-related protein molecule. Close crystal packing protein-protein contacts provide artificial binding positions in the solid states. Consequently, they can be classified as false positive protein binders in crystallography. Some of the detected fragments bind adjacent to a symmetry-related molecule which contributes interactions. Therefore, binding of these fragments might be an artefact in comparison to other screening methods. All remote binders were investigated in terms of the calculated buried surface area of the ligand contacting neighbouring protein molecules. Thus, the percentage of the buried surface area with each neighbouring protein molecule will be compared. The analysis was performed with the PDBePISA web server PDBe (v1.52 [20/10/2014]).<sup>92</sup> Subsequently, the binders were categorised into three classes. The first one included all fragment binders with an unambiguous binding mode contacting only one protein molecule. The second category comprises examples where it is difficult to decide whether the fragment would also bind to the protein if it is not arranged in a crystal packing. The third category contains fragment binding modes that most likely only occur in a crystal packing. In the following, the binding modes of the classified binders are individually discussed.

**J06-II** discloses only a part of the fragment **J06**, as indicated by its chemical formula listed in the second column of Table 14. The facts that the ligand has no direct polar interaction with any neighbouring protein molecule, the buried surface of the ligand with the closest PKA mate is only 54.9%, and with the next one 32.1% suggests that likely a crystal packing-induced binding is observed. Therefore this binding mode is assigned to the third class. Nonetheless, fragments with such binding modes between symmetry-related protein molecules may influence the crystallisation process, since they provide additional interaction points between them.

**J45-II** binds partly in the hydrophobic pocket near the long N-terminal  $\alpha$ -helix. Although the rest of the fragment is not well visible for placement, the hydrophobic part fills the pocket, and 96.2% of the ligand surface is covered. The adjacent symmetry-related molecule is too far away to influence the fragment binding. Accordingly, a productive remote binding (class 1) is assigned.

Crystallographic screening of a 96-well-plate fragment library shows a high hit rate for the cAMP-dependent protein kinase A

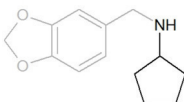
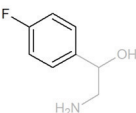
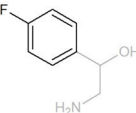
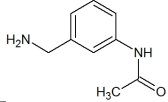
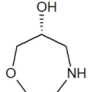
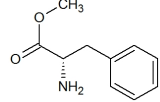
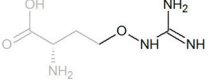
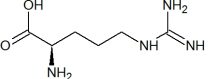
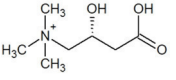
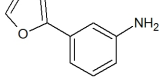
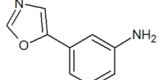
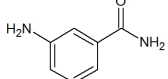
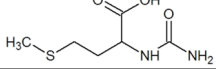
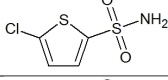
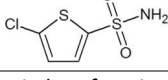
Fragment ID	Analyzed structure	Ligand buried surface by 1 <sup>st</sup> PKA unit[%]	Ligand buried surface by a further PKA unit[%]	Class
J06-II		54.9	32.1	3
J45-II		96.2	-	1
J45-III		25.2 (34.2 by PKI)	40.6	3
J46-II		38.4	24.4	3
J56-II		45.2	27.9	2
J62		31.7	32.4 19.1	3
J72		80.0	-	1
J77		67.4	13.9	1
J81		48.3	12.4 11.1	1
J83-II		62.6	8.3 (18.1 by J83-II)	1
J83-III		29.9	48.5 (18.1 by J83-III)	3
J85-II		84.9	8.1	1
J87		67.1	32.8	2
J94-I		66.4	29.1	1
J94-II		74.9	25.1	2

Table 14: Calculated buried surface interfaces between fragment and protein and between fragment and symmetry protein molecule. For J45-III and for both J83 there are additional entries placed, since J45-II is close to the peptide PKI and both J83 binders are in close contact to each other. The classification of the binding mode into classes 1 to 3 is a result of the percentage interface distribution and the interaction between ligand and the respective PKA molecules. Fragment parts not observed in the electron density are displayed in light grey.

The third binding position of **J45** is close to a neighbouring PKA molecule, and 40.6% of the ligand is contacted by this entry. A fluorine atom is a weak hydrogen bond acceptor, and the remaining part of the phenyl ring comes close to the polar side chain part of Arg19 of PKI. Additionally, the electron density indicates that only weak binding occurs. This categorises the binding pose of **J45** to class 3.

The visual inspection of **J46-II** binding implicates its pose as a crystallographic artefact. The compound is located between two PKA molecules, which both have an interaction interface with the ligand. The first protein molecule covers 38.4%, whereas the second covers 24.4% of the ligand surface. This is consistent with a class 3 classification.

The second pose of **J56** shows up with a weaker electron density as the first one, and a fewer number of polar interactions are observed. 45.2% of the ligand is buried by the closest protein molecule, whereas 27.9% is buried by an adjacent protein molecule. Additionally, the salt bridge interaction occurs with the first protein molecule, so that classification into class 2 seems reasonable.

**J62** is in contact with three protein molecules. The first one forms cation- $\pi$ -interactions and a hydrogen bond to Thr287. It covers 31.7% of the ligand's surface. The two other PKA molecules cover 32.4% and 19.1% respectively. Although the only observed polar interaction is a salt bridge of the amino group to the carboxylate of Glu331', the distribution of buried surface areas suggests an artificial binding position (class 3).

The binding position of **J72** is apparently not artificial since the fragment is located in the PKI binding site of PKA. As the partly visible ligand is deeply bound in the Arg19-binding site of PKI, the fragment is mainly surrounded by PKA residues (80% buried interface) of one crystal mate.

The same applies to **J77**, present at the same binding position. However, the fragment is fully assigned to the density and sticks more out of the pocket, so that a small interface of 13.9% is formed to an adjacent PKA molecule. This interface seems to be rather small compared to that with the closest PKA molecule covering 67.4%. Therefore, this fragment is assigned to the first class.

Analysing the binding mode of **J81** discloses that the compound forms polar interactions only with the closest PKA molecule via its carboxylate group. The positively charged quaternary ammonium group remains solvent exposed, but in close distance to electron-rich backbone carbonyl oxygen atoms. However, there are also contacts to two symmetry-related PKA molecules which bury

12.4% and 11.1% of the fragment-surface, respectively, compared to the 48.3% with the closest PKA molecule. It is therefore assigned to class 1.

At first glance, the arrangement of **J83-II** and **J83-III** is surprising. The fragments are mutually in close contact and share 18.1% of their surfaces in common. **J83-II** has larger contact with the closer PKA molecule covering 62.6% interface surface. **J83-III** is much less covered by this mate (29.9%) but forms larger contact with an adjacent protein molecule (48.5%). The only polar contact to the protein is mediated by a water molecule. It is unlikely that this binding would also occur in solution. Therefore, this pose is sorted into class 3. The issue is different with **J83-II**. Apart from an improved interface, the binding causes the replacement of two water molecules and a side chain shift of Lys192. In other crystal structures of the series, this lysine interacts with Asp241 of a neighbouring PKA molecule via a salt bridge. This salt bridge is disrupted by the fragment accommodation, and the lysine residue is subsequently pushed upwards to come closer to **J83-III** (Figure 63). The binding of **J83-II** seems to be more favoured than the formation of the salt bridge. In solution, the energy cost for repelling the salt bridge is not required, as the salt bridge is formed to a neighbouring PKA molecule in the packing. Obviously, many effects have to come together so that this binding geometry is observed. However, the observed facts suggest that **J83-II** should be assigned to class 1.

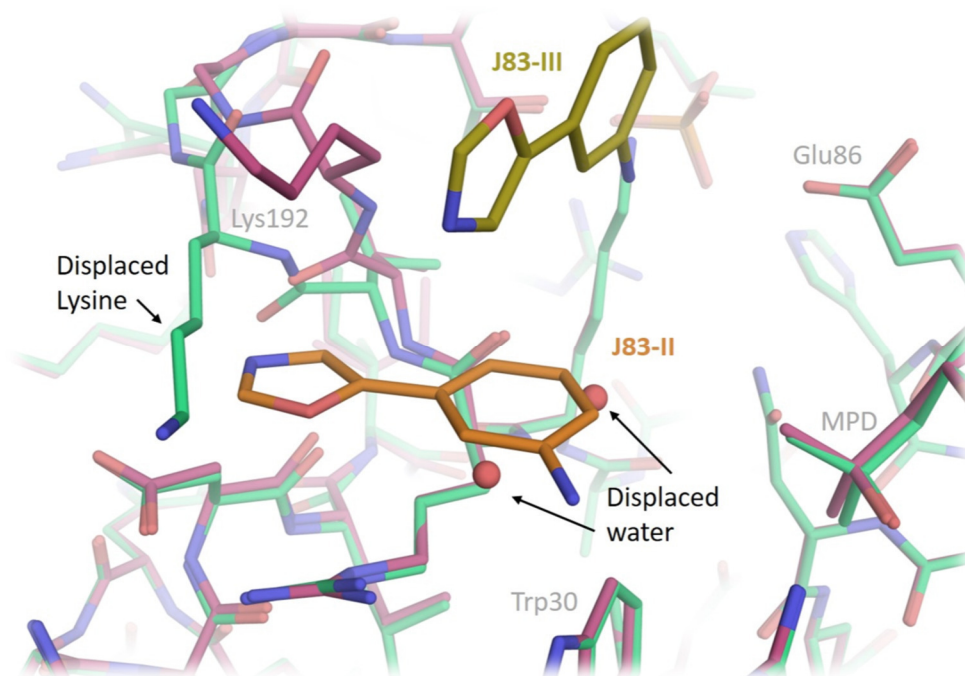


Figure 63: Representation of the binding modes of **J83-II** and **J83-III** in PKA crystal (purple carbon atoms). Superimposed to this structure is the one of **J81**(green carbon atoms), where no ligand has bound at this position. Induced by the binding of **J83-II**, Lys192 moves upwards towards **J83-III**. The two water molecules presented in **J81** are displaced by **J83-II**.

**J85-II** is placed in the hydrophobic pocket of the  $\beta$ -sheet part (Figure 61) and has only minor contact with the neighbouring PKA molecule (8.1%). A major part of the fragment occupies this pocket, and it is buried to 84.9% by the protein surface. The compound is clearly sorted into class 1.

Fragment **J87** binds into the same pocket. It is more extended and has more degrees of freedom for rotations. In contrast to **J85-II**, it is in contact with a PKA symmetry-related packing mate (32.8%) and forms only polar interactions to the latter. Although the majority of contacts is made with the closest PKA molecule (67.1%), the polar interaction to the symmetry-related molecule is obvious, and **J87** is sorted into class 2.

In contrast to **J87**, the binding mode of the first copy of **J94** which accommodates in the same pocket, offers no direct polar interactions with a symmetry-related molecule, although its solvent accessible area is covered to 29.1%. This mainly affects the sulphonamide part. Via water bridges, it interacts with the closest protein molecule. The buried surface of the ligand by the latter PKA molecule is 66.4%. Therefore, **J94-I** is classified as class 1 member.

The second binding mode of **J94** is unique in the series. The compound displaces two water molecules, which are in the first solvation shell of the protein. Remarkably, a DMSO molecule frequently binds in this area (e.g., structure with **J62**) and is displaced by **J94**. Nevertheless, the fragment seems to bind weakly (74% occ. and 0.78 RSCC), which is also reflected by the faint electron density. Most of the ligand surface area is covered by the closest protein molecule with 74.9%. The symmetry-related molecule contributes only 25.1%. Although this distribution looks promising for class 1, overall, assignment to class 2 appears reasonable for **J94-II**.

In summary, considering the amount of buried surface area, water displacements, polar interactions, and the refined occupancies and RSCC values, 7 of all 15 non-ATP-pocket binders are assigned to class 1, 3 to class 2, and 5 fragments as crystallographic packing artefact (class 3). In total, 13.2% of all the found hits are most likely found as hits in crystal packing. At first glance, this number appears high, however, regarding the high number of fragment hits (31.3%) it is of minor importance. Considering that usually hit rates are reported between 3 and 10%<sup>58</sup>, the crystallographic screening is still very efficient, even if some artefacts will be discovered.

### 3.3.2. Diverse benzene derivates in hinge interaction of the ATP-binding pocket

In 2010, phenol was structurally characterised as a hinge binder that also occupies the ribose pocket of PKA (PDB entry: 3nx8)<sup>110</sup>. A third binding position was observed in the hydrophobic pocket of the  $\beta$ -sheet region. At the hinge motif, phenol uses its hydroxy group to form two hydrogen bonds with the backbone nitrogen of Val123 and carbonyl oxygen of Glu121. Several fragments of the 96-series also use these two interaction sites. Interestingly, almost all fragments bound in this area consist of a benzene ring with attached substituents such as amide groups, methoxy groups, amidine groups, or hydroxy groups such as phenol. Variations using a pyridine ring are also observed. The compilation in Figure 64 shows the chemical formulas of the hinge binding fragments with their structural elements within this series.

The PKA hinge region offers one H-bond donor (amide nitrogen of Val123) and one acceptor (backbone carbonyl oxygen of Glu121). With the exception of **J45** and **J46**, which use water molecules as mediators, the studied fragments bind to one or two of these polar interaction partners. 12 of the 14 hinge binders interact directly with the nitrogen, whereas only 6 use the carbonyl oxygen for their interaction. Three fragments bind to the hinge via their phenolic OH group (**J74**, **J84**, and **J89**). The alignment of these structures is shown in Figure 65. All three examples address the backbone carbonyl oxygen of Glu121 with a hydrogen of their hydroxy group and also accept the hydrogen from the backbone nitrogen of Val123. The observed small shift of the benzene ring is most likely caused by further interactions to **J89** and **J74** (Figure 54). **J84** does

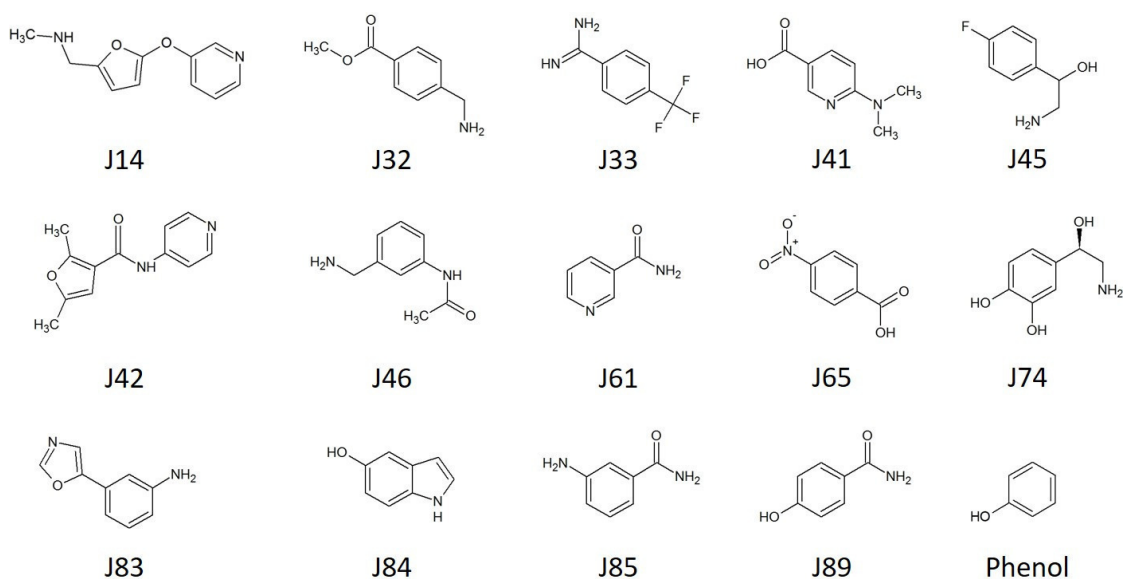


Figure 64: Chemical structures of all PKA hinge binders of the J96 library with a benzene or pyridine ring moiety. Additionally, phenol is listed for comparison.



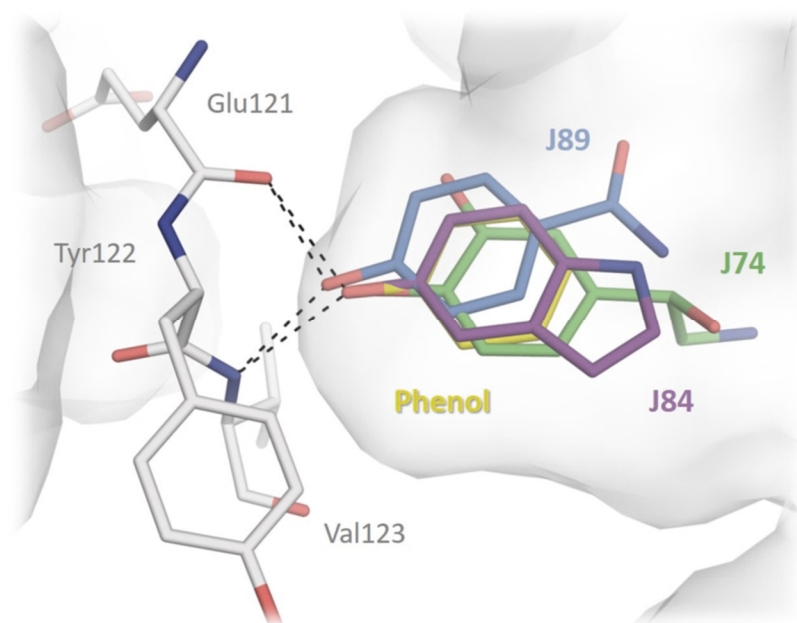


Figure 65: Fragment hinge interaction in the PKA binding pocket of superimposed structures of J74, J84, J89 and phenol (PDB-3NX8). Protein hinge amino acids are shown as sticks, like the bound fragments. The colour code is following the fragment label. For the remaining protein residues, the protein surface is presented.

not experience further interactions and fits perfectly to the same position as the benzene ring of phenol.

**J89** also adopts a second binding pose, where its amide group interacts with the hinge and the hydroxy group orients towards the ribose pocket. This orientation seems to be favoured since the occupancy distribution is 3:2 for the amide group versus the hinge. Another fragment with an

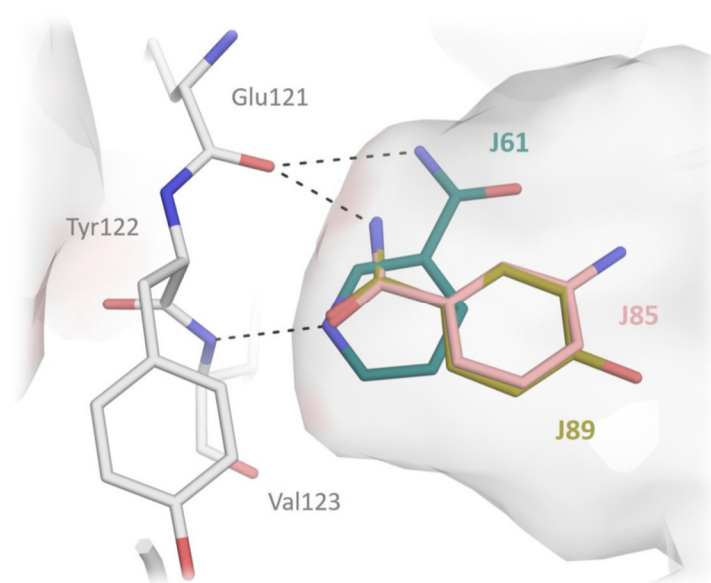
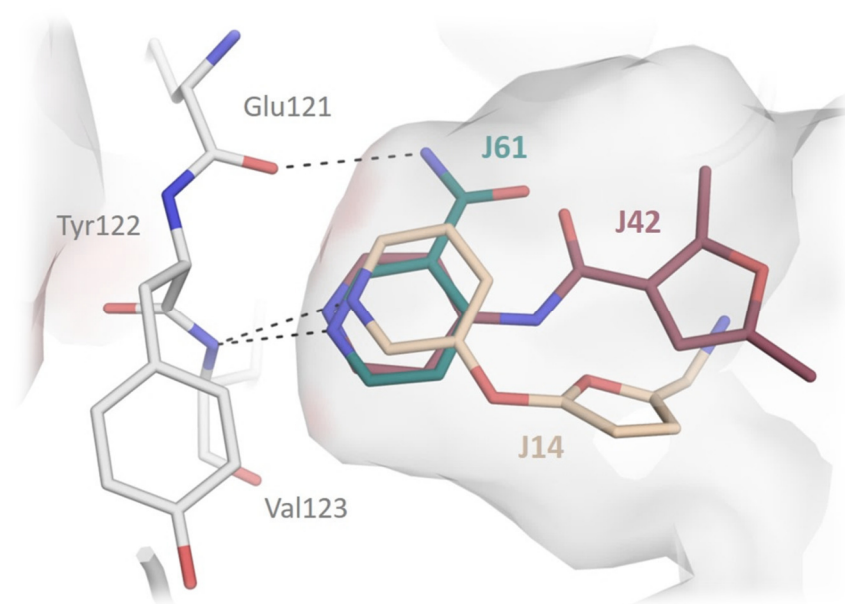


Figure 66: Fragment hinge interaction in the PKA binding pocket of superimposed structures of J61, J85, and J89. Protein hinge amino acids are shown as sticks, like the bound fragments. The colour code is following the fragment labels. For the remaining protein residues, the protein surface is presented.

amide group binds very similarly (**J85**). The only difference is the exocyclic amino group in the meta position to the amide group, whereas **J89** has a hydroxy group in the para position. In both compounds, the amide nitrogen forms an H-bond to the carbonyl oxygen of Glu121, and the oxygen of the fragment's amide group accepts an H-bond from the backbone nitrogen of Val123. The third fragment with such an amide group is **J61**. Instead of using its amide group for the hinge interaction, **J61** uses its pyridine nitrogen as an H-bond acceptor toward the hinge. The carbonyl oxygen atom of Glu121 is furthermore in contact with the amide nitrogen of **J61** via a water bridge (not illustrated in Figure 66 or Figure 67), but the group is rotated by ca. 90 ° and comes in contact with the hydroxy group of Thr183 of the DFG loop.

The discovery of two additional fragments with a binding geometry using their pyridine moiety suggests this ring system as a putative hinge binding element. Fragments **J14** and **J42** have a more complex structure than **J61**, but also involve their pyridine ring into the hinge interaction. They both get close to Asp184 of the DFG loop, where **J14** interacts via a salt bridge. Its pyridine moiety is slightly shifted compared to the other pyridine rings but remains in an H-bond distance (Figure 67). All three compounds orient their planar ring systems identical, put in place by the hydrophobic side chains of Ala70 and Leu173 (not shown). These amino acids are part of the catalytic spine and limit the available space at the hinge.

Another fragment that also contains a pyridine ring is fragment **J41**. This fragment does not bind via its pyridine-type nitrogen to the hinge, but rather via its protonated carboxylic acid group.



*Figure 67: Fragment hinge interaction in the PKA binding pocket of superimposed structures of J14, J42, and J61. Protein hinge amino acids are shown as sticks, like the bound fragments. The colour code is following the fragment labels. For the remaining protein residues the protein surface is presented.*

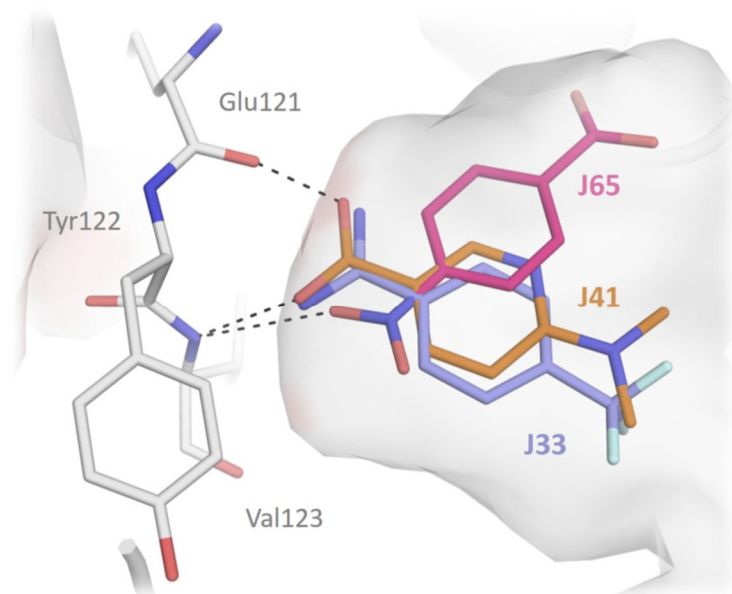


Figure 68: Fragment hinge interaction in the PKA binding pocket of superimposed structures of J33, J41, and J65. Protein hinge amino acids are shown as sticks, like the bound fragments. The colour code is following the fragment labels. For the remaining protein residues, the protein surface is presented.

Adjacent to the pyridine nitrogen a dimethyl-amino group is present in the ortho position, which would create a steric clash when arranged similarly to **J61**, **J42** or **J14**. In addition, the dimethyl-amino group takes an impact on the acidic character of the carboxylic acid group. Carboxylic acid groups have a  $pK_a$  value of approx. 4.8 and benzoic acid even lower with 4.2.<sup>97</sup> Therefore, the fragment would be deprotonated at a pH of 6.9 of the soaking buffer. In a deprotonated state, the carboxylate could not interact with the Glu121 backbone carbonyl oxygen. The dimethyl-amino group reduces the acidic strength via a positive mesomeric effect so that the protonated form is likely present. A reversed situation is observed for **J65**. The nitro group of this compound is located in the para position to the carboxylic acid group. A negative mesomeric effect of the  $NO_2$  group stabilises the negatively charged carboxylate group. Therefore, its  $pK_a$  value should fall below 4.2, explaining the deviating binding mode of **J41**. The fragment is still in contact with the hinge but uses its nitro group to H-bond to the hinge and its carboxylate group to contact Lys72, which is most likely positively charged. The third case of a  $pK_a$  shift is apparent for **J33**. Its benzamidine bears a  $CF_3$ -group in the para position. Usually, a benzamidine has a  $pK_a$  value of ca. 11.5. Thus, the amidino group would be protonated at pH 6.9, and no H-bond to the backbone nitrogen of Val123 is formed. The inductive effect of the  $CF_3$ -group reduces the basic character of the amidino group by the strong electron pulling effect of the fluorine atoms (Figure 68). The compound offers H-bond donor and acceptor in this uncharged state towards the hinge.

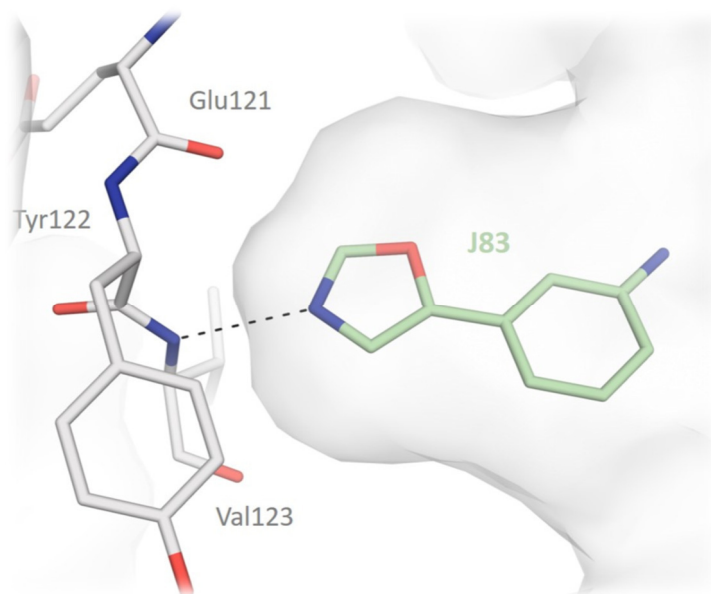


Figure 69: Interaction of J83 at the hinge region. Protein hinge amino acids are shown as sticks, like the bound fragments. Carbon atoms of J83 are coloured in light green. For the remaining protein residues, the protein surface is presented.

In contrast to **J14**, **J42**, and **J61**, one nitrogen atom of **J83** is embedded in an oxazole ring. Similar to a pyridine ring, the free electron pair of the oxazole nitrogen allows an H-bond interaction to the hinge (Figure 69). **J83** is the only compound of the series with an oxazole ring, which was found in the screening campaign.

The phosphate binding pocket and the ribose pocket are located near the hinge region. The amino acids responsible for the formed polar interactions in these pockets are Glu170, Glu127, and

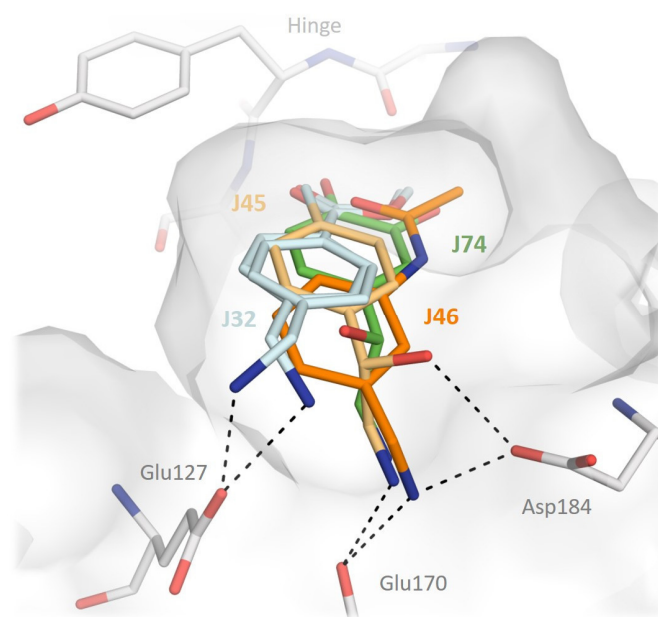


Figure 70: Fragment interaction with Asp184, Glu127, and Glu170 in the PKA binding pocket of superimposed structures of J32, J46, J46, and J74. Protein amino acids in polar interactions are shown as sticks, like the bound fragments. The colour code is following the fragment labels. For the remaining protein residues, the protein surface is presented.

Asp184. Fragments **J32**, **J45**, **J46**, and **J74** all share in common that they comprise a methyl- or ethylamino group attached to a benzene ring. Most probably, these amino groups are basic enough to be protonated and thus positively charged in the bound state, which makes them perfect salt-bridge interaction partners for the side chains of Asp184 and Glu127. **J32** is the only one forming a salt bridge to Glu127. It contacts the hinge via its carboxy ester group in the para position to the amino group at the benzene ring. Only one methyl group links the amino group with the benzene ring. All three other fragments are in direct contact with Asp184. The backbone carbonyl oxygen of Glu170 is also addressed. Similar to **J32**, **J46** has only one methylene group between the amino group and the benzene ring. The ring is further shifted toward the rim of the pocket. Another interesting case is the comparison of **J45** and **J74** with a focus on their stereogenic centre at the hydroxyl group. Whereas **J74** was applied enantiopure in R-configuration, **J45** was used as a racemic mixture. The crystal structure shows the S-configuration exclusively at the hydroxy group. This configuration allows direct contact with Asp184. The R-configuration of **J74** does not allow to interact with Asp184. Instead, a water-mediated interaction with the backbone of Leu49 is established. Other fragments of the series, which do not contact the hinge or possess aromatic ring systems such as a benzene or pyridine ring, orient basic amino groups in this area.

For FBDD it is important to know, which kind of scaffolds are frequently found at specific positions of a binding site. Fragments are probes, reflecting the properties of the site<sup>111</sup> and help to identify hot spots of binding and suggest molecular scaffolds that can address these hot spots. In the series, most of the fragments bind to the ATP pocket next to the hinge, ribose and phosphate pocket. The schematic summary in Figure 71 shows in which area of the ATP pocket functional groups of bound fragments are observed. The largest variety of functional groups is found next to the hinge region with ten different structural elements. Two of them, pyridine and oxazole also occur as part of extended aromatic scaffolds. All of the bound fragments in the ATP pocket exhibit an aromatic portion, which fits perfectly well between the hydrophobic side chain of Ala70 and Leu173. Eight variations of aromatic ring systems were found in the data sample. One compound (**J65**) only interacts with the ammonium group of Lys72 via a carboxylate salt bridge. Such interactions were previously described, specifically for the proto-oncogene Pim1 kinase<sup>83</sup>. The fourth area corresponds to the ribose and phosphate pocket. Several fragments have amino or protonated amidino groups, and they interact with Glu127 or Glu170 in this area.

Fragment **J89** has a hydroxy and an amide group attached to its central benzene ring. In the crystal structure, the fragment binds with two orientations to the hinge (Figure 54). The occupancy was refined to 60% for the amide-to-hinge orientation and 40% for the hydroxy-to-hinge geometry.

The amide group seems to be favoured if thermodynamic equilibrium would only determine the binding pose. **J61** also has an amide group but uses this group to interact with Thr183 and the pyridine nitrogen to interact with the hinge. In spite of their more complex structure, two more fragments use their pyridine ring in the same way (Figure 67).

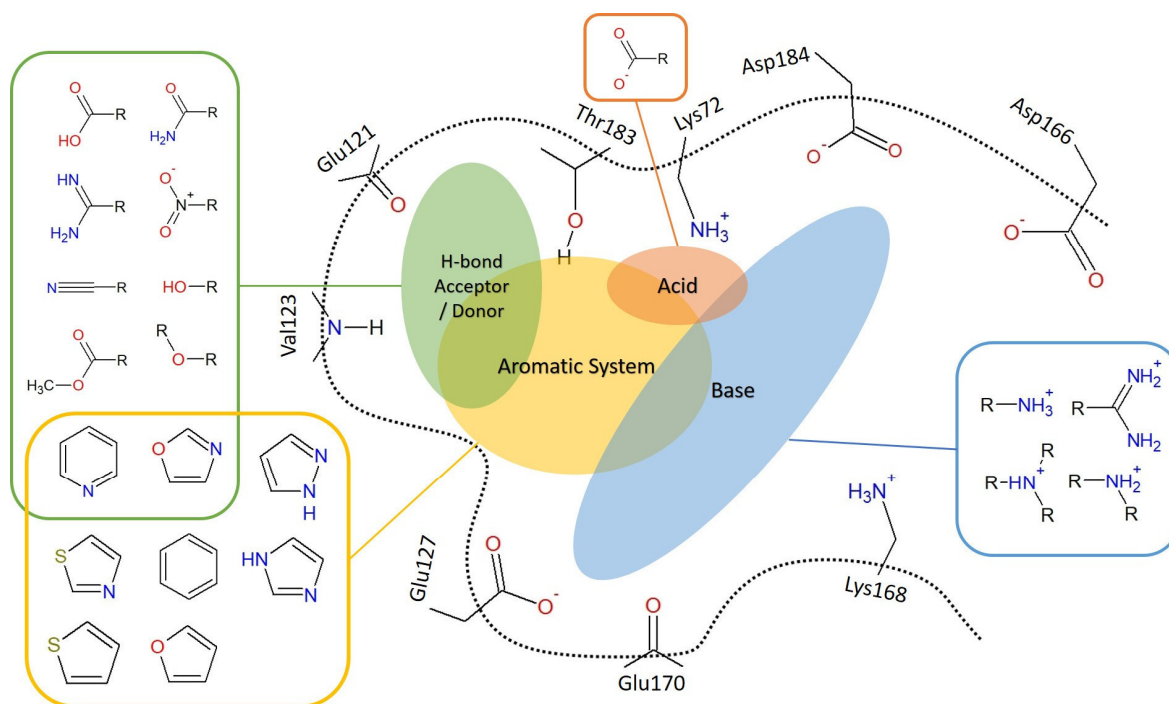


Figure 71: Schematic overview of the PKA ATP-binding pocket. The coloured ellipsoids represent areas where specific functional groups of bound fragments were detected. The relevant functional groups are listed in the boxes with the same colour.

### 3.3.3. Comparison with PDB listed PKA binders

A search in the PDB for entries of the catalytic subunit alpha of cAMP-dependent protein kinase A resulted in 192 entries (status: 07/2017). This included PKA from *Homo sapiens*, *Bos Taurus*, *Mus musculus*, *Oryctolagus cuniculus*, *Rattus norvegicus*, *Sus scrofa*, and *Cricetulus griseus*. As shown in Figure 11 (Introduction) there are only a few changes in the amino acid sequences, remote of the ATP-binding pocket. These 192 PDB entries were examined, and several cases could be found with a bound inhibitor comparable to the detected fragments.

Phenol and pyridine moieties are most frequently present. These groups are similarly arranged towards the hinge as corresponding fragments of our series. A number of examples are listed in Figure 72. The well-known PKA inhibitor Fasudil and analogues were also found frequently. An isoquinoline ring is found uncharged in all examples at a similar position as the pyridine ring in other binders. PDB entry **2f7e** also has an isoquinoline moiety adopting the same binding mode as the Fasudil derivatives, but lacking the sulphonamide. Less frequently found at the hinge were amide functions (PDB: **4c35**) or a benzene ring (PDB: **5bx7** and **2uw6**) without hydrogen bond interactions. Instead of the more frequently found amide function in our series, in the PDB more compounds with a lactam ring interacting with the hinge are detected (**1stc**, **3191**, **4nj1**, **4z83** and **4z84**). This includes the unselective kinase inhibitor staurosporine (**1stc**). Apart from pyridine other heterocycles were discovered as hinge binders: Indazole (**2jds**, **2oh0**), azaindole (**2uvx**, **2v07**, **3mvj**), diazole (**2uw4**, **2uw6**, **2uw7**, **3amb**, **4axa**), triazole (**3ama**), purine (**3bwj**, **3zo1**, **4yxs**), aminothiazole (**3dnd**), and oxadiazole (**3e8c**, **4c36**, **4c37**, **4c38**). Although some fragments in our

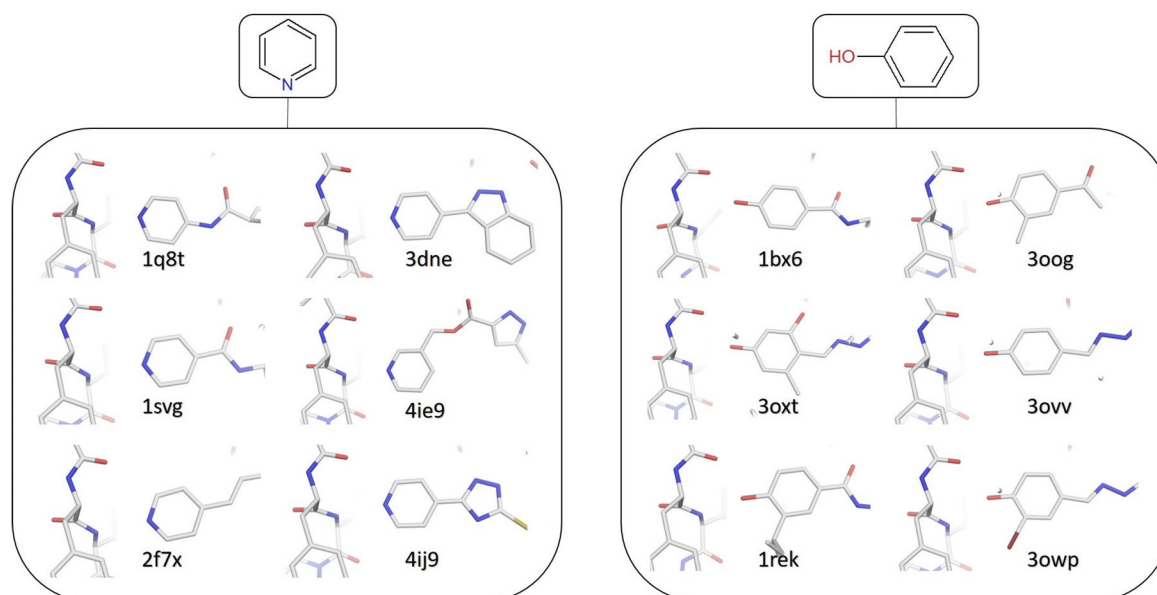


Figure 72: Examples of PKA binding compounds with a phenol or a pyrimidine moiety. Compound and protein residues of the hinge region are shown as sticks. The relevant PDB ID is listed next to the binding ligand.

library contain similar moieties (e.g., diazole or purine) a binding to PKA could not be observed. Instead, new functional groups as binders to the hinge were observed, which are not present in the PDB: Carboxylate group (**J41**), nitro group (**J65**), amidine (**J33**), carboxy-ester (**J32**), or an oxazole ring (**J83**).

In 2007, the group of Gordon Saxty published a study, where they developed a nanomolar inhibitor of protein kinase B using FBDD and a mutated variant of PKA (*Bos taurus*) resulting in a PKA-PKB-chimera protein<sup>112</sup>. These mutations concern four amino acids in the ATP-binding site (V104T, V123A, L172M, and Q181K). Nevertheless, these mutations do not alter the available interaction pattern at the hinge, since the backbone and the carbonyl oxygen of Ala123 orient similarly to Val123. Thr104 and Lys181 were not observed to be involved in protein-ligand interaction. Solely, Met172 orients close to the bound fragment forming van-der-Waals interactions. However, the bound fragments are able to occupy the same space (Figure 73), which allows the comparison of both independent fragment discovery projects. They developed a ligand with an  $IC_{50}$  value of 18 nM starting from a fragment with an  $IC_{50}$  value of 80  $\mu$ M. They followed an optimisation by fragment growing. Some similarities between structural elements found by this study and the present investigation with respect to the binding motifs are observed. An interesting match are fragments **J83** and **L15** of structure **2uw4** (Figure 73 B). The six-membered and five-membered rings adopt nearly an identical binding position. **J28** exhibits larger chemical similarity in part of the ligand, but the hinge interacting motif is missing. Thus a deviating binding pose is adopted. Nevertheless, the structural alignment with **2uw4** shows that both fragments are located close to each other and form polar interactions with Glu170 via their protonated amino group. A third example exhibits a chlorobenzene ring approaching the glycine-rich loop. Fragment **J06** also binds to this region using its benzodioxole ring. As displayed in Figure 74, the two benzene moieties

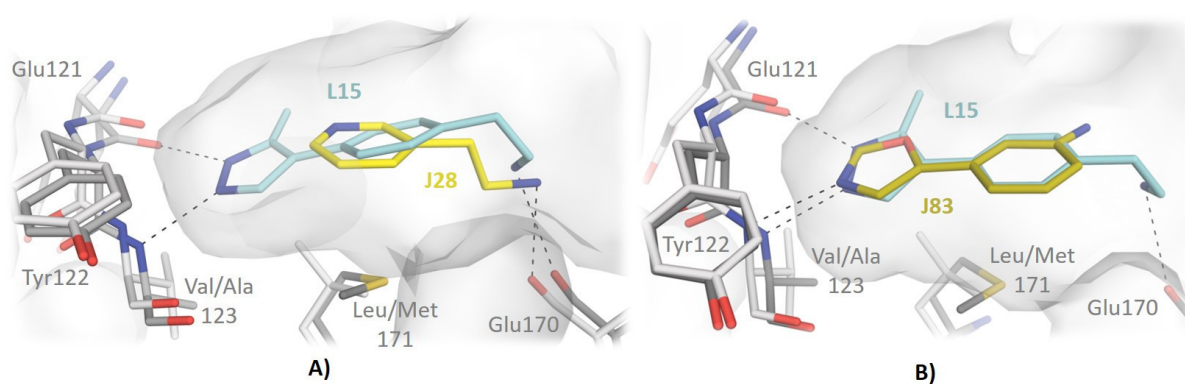


Figure 73: Structure alignment of 2uw4 with the complexes of J28 (A) and J83 (B). 2uw4 contains the complexed fragment L15, which is shown in image (A) and (B). Both images show binding motifs at the hinge region of the ATP-binding site. Protein amino acids in 2uw4 are shown as grey sticks. Protein residues of our series are shown as light grey sticks. The colour of the fragment carbon atoms corresponds the colour of the fragment label. The protein surface is represented in grey.



are quite close together, but the attached amino groups are involved in different interactions, which influences the binding modes. The ligand in **2uw9** uses its protonated ammonium group for a salt bridge with the side chain of Glu127, whereas **J06** forms a salt bridge to Asp184. Apart from **J06**, there is no further fragment in our series that addresses the glycine-rich loop region, which makes this structure a unique case.

All three structures (**J06**, **J28**, and **J83**) were aligned with the ligand of the Saxty series (Figure 75). It demonstrates how well the scaffold of **2uw9** is mimicked by our fragments. Whereas the compound in **2uw9** is the result of fragment growing, a target ligand could be imagined by merging the three fragments into one chemical structure.

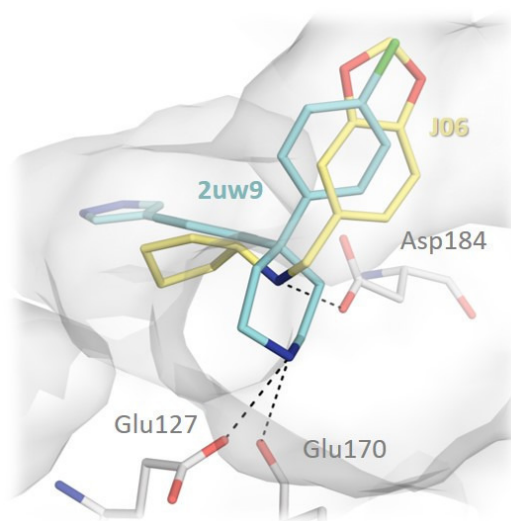


Figure 74: Structure alignment of 2uw9 with the complex of J06. The image shows the binding motifs in the ribose and phosphate pockets of PKA. Protein amino acids in polar interactions are shown as sticks, similarly as the bound fragments. The colours of the carbon atoms of the bound compounds correspond to the labels. The protein surface is represented in grey.

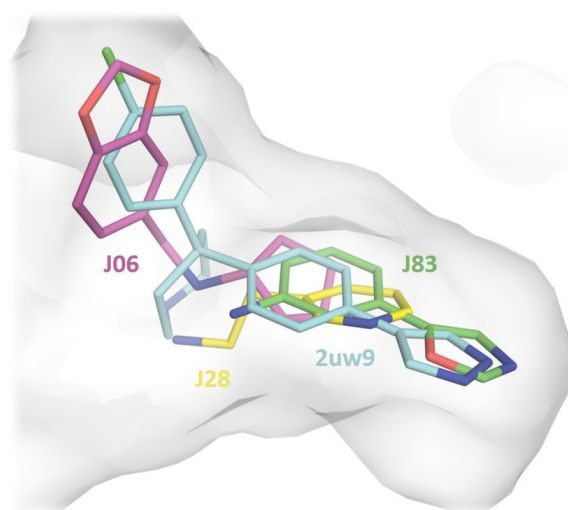


Figure 75: Structure alignment of 2uw4 with the complexes of J28, J06, and J83. The image shows the binding motifs in the hinge region of the ATP-binding pocket, the ribose, phosphate pocket and the beginning of the glycine rich loop. Bound fragments are displayed as sticks. The colours of carbon atoms correspond to the labels. The protein surface is shown in grey.

### 3.3.4. The new PKI-free PKA crystals: Characteristics and study effect

After several attempts of protein expression, purification, crystallisation, fragment soaking, crystal data collection, and data analysis, new PKA crystal structures without the bound peptide inhibitor PKI could be obtained. PKI has a nanomolar affinity to the peptide substrate pocket of PKA and stabilises crystallisation.<sup>3</sup> The presence of PKI accelerates the crystallisation process. Crystal growth is initiated by microseeding so that even after a few hours tiny crystals can be observed under the microscope. After one or two weeks, the crystals have grown to optimal size for data collection. In case of PKI-free crystals, an incubation time of three or four weeks is needed until first crystals are formed and ready for data collection. There is also a noticeable difference during manipulation of crystals in the soaking or mounting procedures. The crystals seem to possess higher density as they sink faster in crystallisation drops in contrast to PKI-containing crystals. This complicates the process of crystal fishing. Additionally, these crystals seem to be more robust against mechanical stress, e.g., intensive contacts with the cryo-loop or osmotic stress during soaking. The PKI-containing crystals are more fragile and suffer from cracks more easily. Furthermore, the PKI-free PKA crystals scatter better in the X-ray beam. On average, an improvement of 0.25 Å in mean resolution is achieved. The best resolution for a PKA dataset in the series was obtained for a PKI-free crystal at 1.07 Å, whereas for a PKI-containing crystal 1.32 Å was achieved. Both crystals were measured at the same synchrotron facilities and beamline.

After data collection, the data were analyzed, and space group and cell parameters are determined. Remarkably, the space group for the new crystals remains the same (P2<sub>1</sub>2<sub>1</sub>2<sub>1</sub>). However, cell parameters changed with respect to unit cell dimension. This is shown in Table 15. The unit cell axes of a and c are reduced by 7 Å and 11 Å respectively, which reduces the total volume of the unit cell by ca. 84800 Å<sup>3</sup>. Considering the packing arrangement of PKA in both crystal forms, a

	With PKI	PKI - free
<b>Space group</b>	P 2 <sub>1</sub> 2 <sub>1</sub> 2 <sub>1</sub>	P 2 <sub>1</sub> 2 <sub>1</sub> 2 <sub>1</sub>
<b>Unit cell parameters: a, b, c [Å]</b>	58 72 108	51 72 97
<b>α, β, γ [deg]</b>	90 90 90	90 90 90

Table 15: Symmetry and space group parameters of PKI-containing and PKI-free PKA crystals.

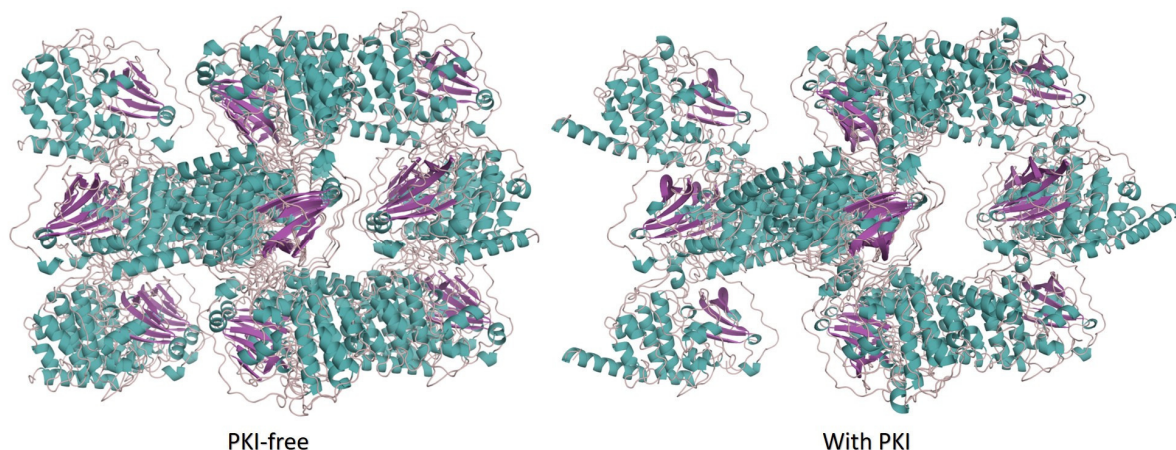


Figure 76: Structural arrangement of PKA molecules in PKI-containing (right) and PKI-free (left) crystal forms. Proteins are shown in cartoon mode with cyan  $\alpha$ -helices, magenta  $\beta$ -sheets, and loops in salmon. The two images are produced from the same point of view. This visual comparison shows directly the reduced space between the PKA molecules in the PKI-free form.

tighter packing in the PKI-free form is obvious. This comparison is visualised in Figure 76. The reduced solvent content (56% to 45%) and Matthews coefficient ( $2.8 \text{ \AA}^3/\text{Da}$  to  $2.2 \text{ \AA}^3/\text{Da}$ ) of PKI-free crystals also reflects the tighter packing of the latter form. Visual inspection suggests that PKA molecules are coming closer together in the PKI-free form than in the peptide-bound case, which is in accordance with the smaller unit cell. An analysis of both structures via LSQ Superimposition (*COOT*) showed this great shift in the crystal packing. The overall RMSD of both proteins is  $1.22 \text{ \AA}$ . For very small differences, a value between  $0.2 - 0.3 \text{ \AA}$  should result.<sup>113</sup> The maximal deviation between similar atoms in both proteins of the two crystal forms amounts to  $35.1 \text{ \AA}$ , which indicates locally major deviations. Closer inspection reveals that bound PKI shifts PKA. Whenever PKI (type SCP0064) binds to PKA, there is an N-terminal part that is not in

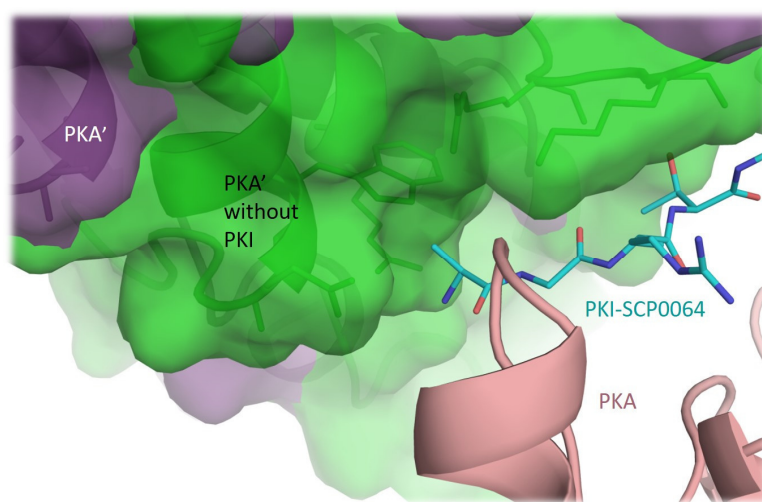
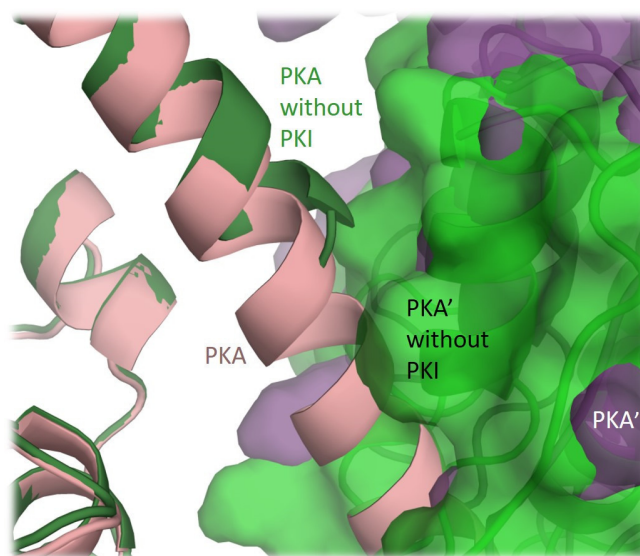


Figure 77: Blow-up of the protein interface between two PKA molecules. The original PKA molecule is shown in cartoon mode and coloured in salmon. The respective bound PKI molecule is shown as stick in cyan. The respective symmetry-related molecule of this structure is shown in cartoon and purple coloured surface. The green surface belongs to a symmetry related molecule of a PKI-free crystal.

contact with a neighbouring crystal mate and remains scattered over multiple arrangements. The space occupied by this scattered portion cannot be occupied by a symmetry-related PKA molecule in the crystal. This could explain why the neighbouring protein molecule is found at a larger distance (Figure 77). The bound peptide (cyan) would clash with the symmetry-related crystal mate in the PKI-free packing (green). It is worth mentioning that the PKI peptide is not completely assigned. Two residues of the peptide chain are missing and would penetrate even further into the region of the symmetry-related molecule. Another difference between both crystal forms is observed at the N-terminus of PKA, where the long  $\alpha$ -helix starts. This helix is fully defined in crystals with bound PKI. Even the cleaved residues remaining from the TEV protease cleavage site are visible in the electron density, which includes the amino acids up to Glu-2. In PKI-free crystals, this helix is only partly visible in the electron density. The first amino acid that could be assigned is Gln12. Obviously, 15 amino acids remain scattered and do not contribute to the diffraction pattern. The explanation for this disordered state is visualised in Figure 78. A symmetry-related crystal mate in PKI-free crystals would come too close to the first one so that it would collide with this helix if it would be completely folded as in the other crystal form. This is indicated by the salmon helix penetrating into the green surface of the adjacent PKA' molecule in the PKI-free form (green). The inspection of several other PDB entries of PKA showed that also PKI-bound structures exhibit incompletely folded  $\alpha$ -helices with a partial disorder. Overall, the released space, due to the absence of PKI, allows the protein molecules to arrange closer to each other resulting in a tighter crystal packing.



*Figure 78: Blow-up of the protein interface between two PKA crystal mates. The original PKA mate is shown in cartoon mode and coloured in salmon. The PKA mate without PKI to be compared is coloured in dark green. The respective symmetry-related molecule of the PKI-binding PKA is shown in cartoon mode and purple coloured surface. The green surface belongs to the symmetry-related molecule of a PKI-free crystal.*

Another change in the PKA structure, which is likely induced due to the absence of PKI (type SCP0064), can be seen in a small loop between amino acids 79 and 85. The aligned structures of PKI-free and PKI-containing crystals do not show large changes in the secondary structure. Nevertheless, a small shift of this loop can be observed. The detailed view in Figure 79 shows the altered backbone course and the different positions of the side chains. From Val80 to Gln84, the backbone of the PKI-bound structure (deep purple) is pushed upwards, and a side chain swap of Gln84 is observed in comparison to the PKI-free form (green). The side chain of His23 of PKI is located close to the loop. The gained space at this position in PKI-free structures is occupied by Gln84. This occupation by Gln84 is supported by a different backbone course compared to PKI-containing structures. This different course strongly affects the position of Leu82 (see Figure 79). Usually, the side chains of this loop are less well defined in PKI-containing structures. Also, the electron density of the His23 side chain of PKI is not well defined, which indicates a strongly disordered state. The inspection of other PDB entries with PKI-containing PKA structures revealed that the loop can also be better defined by the electron density. These cases include another type of PKI (P7739) with a shorter C-terminus. The long C-terminus of the PKI-type SCP0064 is usually unbound and therefore exhibits strong residual mobility, which also affects the nearby His23.

Furthermore, stability improvement is noticed for a special part of the loop following the N-terminal  $\alpha$ -helix. In all structures of this series with bound PKI inhibitor, the amino acids Ser34,

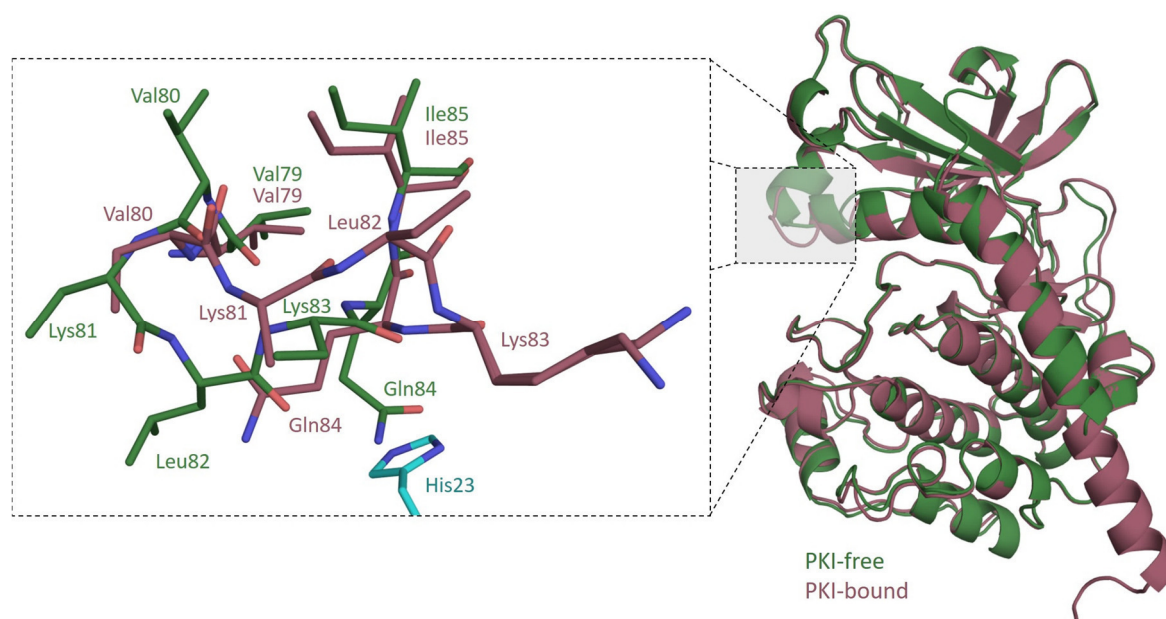
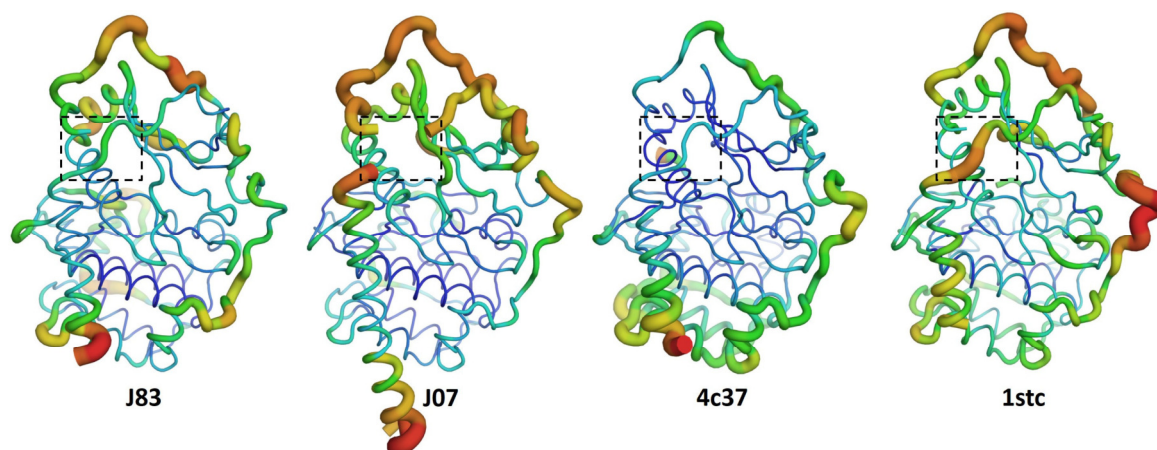


Figure 79: Aligned crystal structures of PKA with and without bound PKI. The right part shows the proteins in cartoon mode to compare the overall deviations in the secondary structure. The proteins are coloured corresponding to their labels. The left image displays a detail view of the framed part on the right. Protein residues are shown as sticks, whereas the colour code remains the same. The His23 side chain of PKI is represented in cyan.

Gln35, and Asn36 have ill-defined electron density, so that they either have relatively large B-values or cannot even be assigned to the electron density, as in the case of the PKA complex with **J07**. In contrast, all PKI-free crystals show a clear density and only a minor increase of the B-value in comparison to the neighbouring amino acids. An explanation for this stability-gain is not obvious, and direct influence of PKI can be excluded as it is too far remote. The comparison with other PDB entries did not give any further hints and even showed that PKI bound PKA crystals can show stability in this region (Figure 80). To provide an explanation for this effect further



*Figure 80: PKA protein structures displayed in B-factor-putty. Red areas exhibit the highest B-values of the structure and blue areas the lowest B-values. Aside from the general higher values in C- and N-terminal tail of the protein and the rather low values at the inner core, no clear pattern is recognizable at first glance. The framed loop can also be well ordered and stable as structure 4c37 shows.*

investigations would be required.

Upon analysis of the discovered fragments, it was recognised that three compounds bind in a hydrophobic pocket next to the  $\beta$ -sheet area (Figure 61). Furthermore, it was realised that this pocket is not present in all PKA structures. Only in the PKI-free crystals, this pocket was observed to be opened. Possibly, the new crystal form makes the formation of this pocket visible. Subsequently, inspection of published PKA entries in the PDB provided us with more information about the presence of this pocket. There are 16 of 47 randomly chosen entries with bound PKI showing the pocket in an accessible formation, whereas in the residual ones the pocket is blocked by Arg45. The latter ones also contain bound PKI. Therefore, it is clear that the position of Arg45 is independent of PKI binding, but this residue can adopt two positions (demonstrated in Figure 62), which are represented in the structure of PDB entry **5bx7**. In the structure, the occupancy distribution was refined to 50:50, which suggests no preferences of one orientation in this structure. However, this pocket is not present in every structure. Its formation seems to be favoured in the

new PKI-free form under the described conditions. Binding of low-affinity fragments is achieved more easily because Arg45 has not to be replaced by the ligand.

### 3.4. Summary

The crystallographic screening of the newly established fragment library with 96 compounds results in a remarkably high hit rate of 31.3% for cAMP-dependent protein kinase A. Among the 30 fragments deviating binding modes and positions are observed (ATP-binding pocket and protein surface). Fragments that bind in the ATP-binding pocket were sorted into groups depending upon their interaction motifs. The protein surface binders were categorised into 3 classes evaluating the surface buried and interaction pattern formed with surrounding protein molecules, to estimate the likelihood of a crystal-only binding mode. In line with the idea of FBDD, the presence of specific functional groups helped to establish a topological map to see where these functional groups are primarily accommodated. In comparison with other PDB entries of the cAMP-dependent protein kinase catalytic subunit alpha and previous studies in FBDD with kinases, it could be demonstrated that the detected fragments are suitable for a follow-up optimisation strategy using fragment merging. The comparison with other PDB entries also shows that the discovered fragments expand the scope of binding motifs to occupy the ATP-binding pocket. Furthermore, a new crystal form of PKA without the bound peptide inhibitor PKI was observed, which shows improved diffraction properties, leading to resolutions up to 1.07 Å. Differences between the two crystal forms were elucidated in detail.





**4. Identification of novel Pim1 kinase inhibitors using the SCUBIDOO database, fragment docking, and crystallographic screening**

Chapter 4 is a part of a cooperation project with AG Kolb and AG Diederich. I was responsible for the protein production, purification and crystallisation of Pim1 in complex with fragment 4012413, as well as for the TSA. Florent Chevillard handled the strategy, a ligand-based approach, performed the docking screening with OpenEye tools, the visual inspection and selection of promising fragments to optimise. Helena Rimmer synthesised the fragment 4012413. Lukas Heyder is currently working on follow-up products. Corey Taylor helped with the docking screening using DOCK (results not shown here), and evaluation of ligand poses obtained by the FRED screening.

## 4.1. Introduction

The relevance and role of the oncogenic protein kinase Pim1 (Proviral integration Maloney) and its two family members (Pim2 and Pim3) in tumour genesis with its functional position in cell proliferation and cell survival have been shown in several cases, for example pancreatic, prostate or colon melanomas.<sup>114 115 116 117 118 119 120 44</sup> The unregulated overexpression of Pim1 kinase in human hematopoietic cells is associated with leukaemia. Inspired by the importance of this highly interesting drug target<sup>42</sup>, we started a drug discovery project in the field of fragment-based drug design using a computational approach as an initial screening technique.

The idea to use low-molecular-weight binding fragments to grow them further into potential binding motifs within a protein target binding pocket has been shown multiple times by several research projects<sup>112 83</sup>. This is also the case for the Pim1 kinase<sup>121</sup>. In this study, two binding hot spots were highlighted where a small fragment-like molecule could interact. At one end of the binding site, the backbone carbonyl oxygen of Glu121 and the side chain amino group of Lys67 are located and at opposite side, the acidic side chains of Asp128 and Glu171 are found. The first goal of our project aimed at identifying fragment binders, which form compelling interactions with Glu121 and Lys67. As a starting point for the virtual hit identification, we used the database SCUBIDOO<sup>122</sup>, which contains 21 million computer-generated products constructed out of two fragment components. These fragments were combined into one putative compound using 58 robust chemical reactions (Hartenfeller et al. 2011)<sup>123</sup>. In case the virtual screening provides reasonable fragment hits, the identified hits will be optimised by growing the discovered fragments in the pocket toward Asp128 or Glu171 to hopefully improve their affinities.

Two core fragments were selected from the above-mentioned database via docking and one via a ligand-based similarity search in the “Chembridge building block library.” With these three fragments and corresponding compatible chemical reactions in SCUBIDOO, diverse compounds were suggested for synthesis. Our synthesis part is still in progress. Thus we will demonstrate here the first assay and the first crystallographic data we collected for the three aforementioned core fragments.

## 4.2. Materials and methods

### 4.2.1. Protein expression, purification, and crystallisation

The full-length human Pim1 (Isoform2), previously cloned into the pLIC-SGC Vector with an N-terminal His<sub>6</sub>-tag connected to a TEV cleavage site, was transferred into a BL21 (DE3)/pLysS *E. coli* host strain (Agilent Technologies). The protein expression was performed in ZYM 5025 medium, with an additionally 1 mM IPTG induced expression after 9 hours of cell growth at 310 K.

After 58 hours of further incubation at 293 K, the cells were harvested via centrifugation and after flash freezing resuspended in a buffer containing 50 mM HEPES, 500 mM NaCl and 5% (V/V) glycerol. The cells were lysed, and after centrifugation, the supernatant was purified using Ni<sup>2+</sup>-NTA chromatography (HisTrap HP, GE Healthcare). In the subsequent dialysis, the His<sub>6</sub>-tag was cleaved by TEV protease, and the phosphorylated Pim1 residues were dephosphorylated by λ protein phosphatase (Sigma Aldrich). The protein was further purified by a second Ni<sup>2+</sup>-NTA run and afterwards rebuffed in a 50 mM HEPES, 50 mM NaCl and 5 mM DTT solution (pH 7,0) for the anion-exchange chromatography column Mono Q (GE Healthcare). With a gradient to 150 mM NaCl, the protein was eluted. The collected protein fractions were pooled and concentrated in the relevant buffer for TSA or protein crystallisation.

Pim1 crystallisation was done as co-crystallisation. Therefore, the purified protein was concentrated to 7.0 mg/ml in a buffer containing 50 mM HEPES, 250 mM NaCl, 5% (V/V) glycerol and 5 mM DTT. After adding the consensus peptide PIMTIDE (ARKRRRHPSGPPTA-amide) at 1.0 mM concentration, a fragment DMSO stock solution (1M) was used to obtain a final compound concentration of 100 mM. The crystals grew on a sitting drop plate via vapour diffusion. One plate consisted of 24 diverse buffer conditions with variations of the kind of salt (Li<sub>2</sub>SO<sub>4</sub>, MgCl<sub>2</sub>, NaCl, LiCl, CaCl<sub>2</sub>, MgAc<sub>2</sub>) and the amount of precipitant PEG3350 (6%, 12%, 18%, 24%). Besides these ingredients, every condition contained Bis-tris propane 100 mM, 10% ethylene glycol and 0.3% DMSO at pH 7.0. The protein solution was mixed in a 1:1 ratio to a total drop volume of 4 µL. Depending on the co-crystallised fragment, first crystals were obtained three to seven days after sealing the plate. Crystals were grown for three to four weeks so that they were big enough for X-ray experiments. For the protection of the crystals during the data collection, they were transferred into a cryo buffer containing 25%(V/V) glycerol and 75%(V/V) crystallisation solution.

#### **4.2.2. Thermal shift assay**

The thermal shift assay was performed with a real-time PCR Thermo Cycler iQ5 (Biorad) using the fluorescence dye Sypro orange. After an initial test for obtaining the ideal assay buffer conditions, each compound was measured in triplicate on 96-well plates, so that the median is comparable to the value of the native protein. Each plate consisted of a triplicate of the native protein so that the measured effect of fragment binding was constantly compared to the native protein subjected to a similar measurement. In every well, the final amount of 40 µL was pipetted. This contains 38 µL mixture of basic buffer (50 mM HEPES at pH 7.0 and 200 mM NaCl) and Sypro Orange in a 500:1 ratio, 1 µL of a DMSO-compound-stock-solution (100mM) and 1µl of

protein solution. The concentration of protein solution was set to 7.0 mg/ml. For the measurement of the native protein triplet, we used pure DMSO.

#### 4.2.3. X-ray data collection, structure solution and refinement process

Pim1 crystals were previously mounted, flash frozen and tested on our in-house source to assess their diffraction quality. Those with the best quality were sent to a synchrotron facility to obtain data sets with higher resolution. The crystals of this series were measured at beamline (BL) 14.1 of Bessy II in Berlin<sup>62</sup>. Directly after data collection, the data sets were processed with the software *XDSAPP*<sup>68</sup>. After processing, the resulting structure factor file was used to determine each structure by molecular replacement using the software *Phaser*<sup>84</sup>. As reference search model the PDB entry **3WE8**<sup>86</sup> was used. For model building, the program *Coot* was applied<sup>73</sup>. The program *Phenix*<sup>72</sup> was used to refine the structures. The refinement included initial simulated annealing step. TLS refinement was carried out in further steps. Individual B-values were obtained by isotropic refinement. The occupancy of split orientations and multiple configurations of bound ligands was also refined. The crystallographic data for each sample are listed in the crystallographic tables found in the appendix. The tables also include Ramachandran data generated by the program *PROCHECK*<sup>74</sup>. The molecular graphic figures were made with the program *Pymol*<sup>87</sup>.

#### 4.3. Results and discussion

The identification of three core fragments for the fragment growing project by screening the SCUBIDOO database was performed as described in the thesis of Florent Chevillard of AG Kolb. The structures of these fragment-like molecules are displayed in Figure 81. Compound **4012414** was identified by the deconstruction of a docked virtual product (ID **3178025** in SCUBIDOO), which predicted an interaction with the amino group of Lys67 and the hinge at the backbone carbonyl oxygen of Glu121. A similarity search within SCUBIDOO targeting fragment **4012414** yielded **4012413**, a close analogue with an improved polar surface area (triazole replaced by

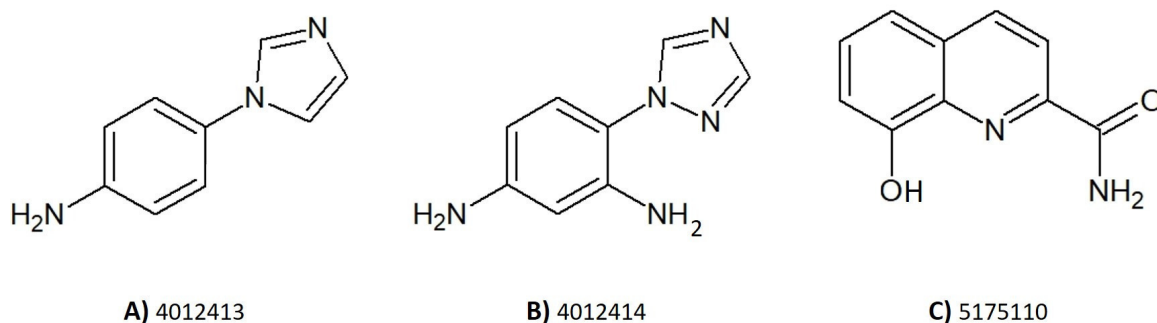


Figure 81: Chemical structure of the basic scaffolds, which could be identified via SCUBIDOO for the fragment growing strategy. Compound **A**) could be obtained via analogues research screens. Compound **B**) could be identified by docking screens. Compound **C**) was identified via a ligand based approach.

imidazole). Compound **5175110** could be identified as a useful fragment by screening the Chembridge fragment library against a library of crystallised ligands of Pim1 with FCFP4 (Feature-class fingerprint of diameter 4) fingerprints, a tool for similarity search. This fragment was previously crystallised in complex with Pim1 and deposited in the PDB as structure **3VBV**<sup>124</sup>. In order to validate our protein crystallisation protocol of Pim1, we tested the co-crystallisation of this fragment with our purified kinase. We were not able to grow large size Pim1 crystals with our technique, but the crystals diffracted well enough, resulting in a dataset with 1.73 Å resolution that was collected at synchrotron Bessy II in Berlin. Compared to the structure **3VBV** deposited in 2012, this is an improvement of 0.35 Å. The position of the fragment and its interactions were confirmed and underline the potential of this fragment as a starting point. Compound **4012413** was also successfully crystallised, and a data set collected. Unfortunately, the data quality was much poorer due to the occurrence of ice rings, so that the dataset was not suitable for detailed analysis or structure deposition. The complex with compound **4012413** shows binding to the ATP-binding pocket of Pim1. The obtained difference electron density map as found in the crystal structure is shown in Figure 82 along with the predicted binding pose of the triazole fragment by docking. The presence of electron density in the ATP-binding pocket indicates binding of compound **4012413**. Although the docking position does not match perfectly well with the experimental density, the agreement is convincing.

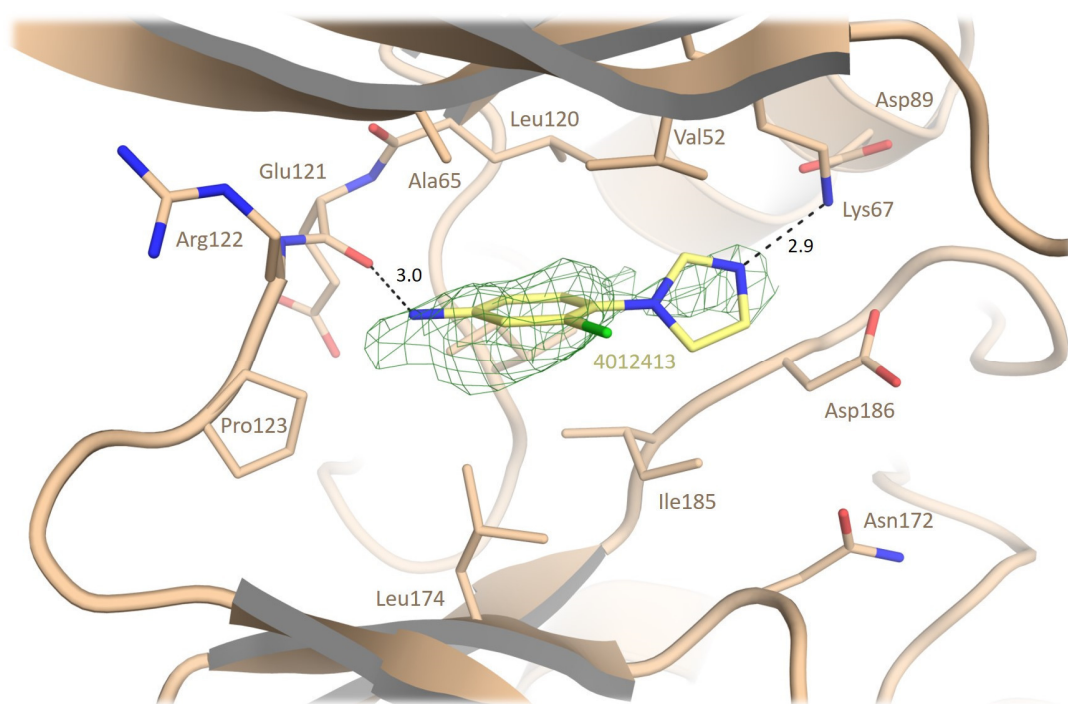


Figure 82: The observed difference electron density of the unbiased *mFo*-*DFc* (contoured at 3  $\sigma$ , green mesh) is shown together with the predicted binding mode of fragment **4012413** obtained by docking.

To investigate whether also the additional fragments could show binding to Pim1, we tested all compounds in a TSA. Our assay was set up with native Pim1, which showed an average melting point of 36.0 °C. All fragments showed a shift of this melting temperature to higher values, which suggests binding and a stabilizing effect of the protein. The fragment with the quinoline moiety resulted in the largest shift of 6.5 °C, whereas the imidazole-based fragment had a stabilizing effect of 1.8 °C. The standard deviation of these measurements amounts to  $\pm 0,2$  °C. We also tested the analogues of compound **4012413** and **4012414** exhibiting a nitro group substituent in order to evaluate the importance of the amino group for binding. Remarkably, these derivatives did not show any stabilizing or destabilizing effect on Pim1 (Figure 83). This fact underlines the relevance of the amino group since an H-bond donor must be present to interact with the backbone carbonyl of Glu121. The nitro group will be unable to form such an H-bond supposedly explaining the missing TSA shifting effect if a similar binding mode would be given. Nevertheless, compound **5175110** seems to be an even more promising fragment exhibiting a melting point shift of 6.5 °C.

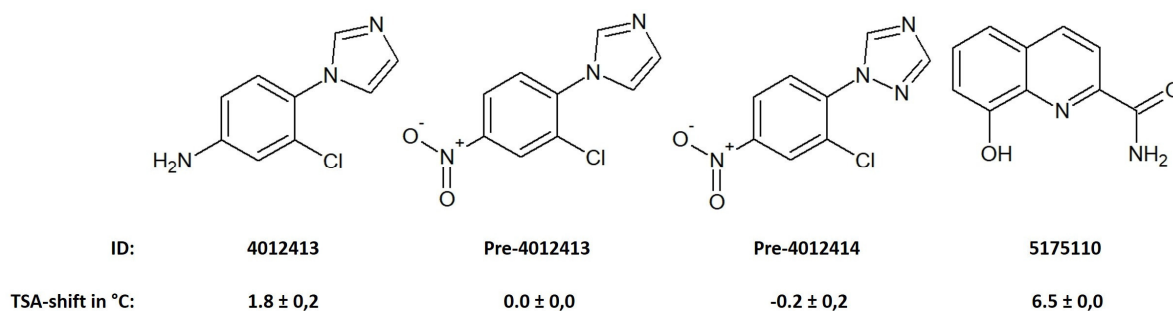


Figure 83: Results for several fragments tested by TSA. The respective temperature shifts are presented with standard deviations and the ID label of the test compounds.

#### 4.4. Status quo & perspective

The obtained results and the ongoing progress of this project demonstrate that with the aid of SCUBIDOO we were able to identify three potential fragments suitable as building blocks in subsequent synthesis by docking and ligand similarity searches. We were able to show the influence of these scaffolds on protein stability via TSA and therefore suggesting potential binding. Furthermore, we obtained a Pim1 crystal structure in complex with one of the suggested fragments, which confirmed the docking prediction.





## **5. Screening the ZINC database against Pim1 kinase via docking results in direct crystallographic hits**

Chapter 5 is a part of a co-operation project with AG Kolb. I was responsible for protein - production, purification and crystallisation in complex with compounds derived from the ZINC database, as well as for the thermal shift assay. The graduate student, Corey Taylor from AG Kolb, was responsible for compound docking and selection.

## 5.1. Introduction

In the field of structural biology and medicinal chemistry, the commercial availability of compounds or substrates for synthesis can be a challenge within the wide range of chemical space. The ZINC database provides more than 90 million commercially available compounds, freely accessible via SMILES notation, mol2, 3D SDF and DOCK flexibase format for subjecting the compounds to computational structure-based screening methods<sup>125 126</sup>. ZINC has been used to retrieve promising entries by docking against the first member of proviral integration Maloney kinase family, also known as Pim1. This protein is involved in many signalling pathways of cell-growth, cycle and survival<sup>42</sup> and the overexpression of Pim1 has been shown to correlate with the genesis of solid tumours. Starting from hematological malignancies, the list was elongated with Prostate adenocarcinoma, Pancreatic ductal carcinoma, and Gastric carcinoma, to provide a few examples.<sup>44</sup> Pim1, therefore, represents an ideal drug target to treat these forms of cancer.<sup>42</sup> The docking study resulted in the identification of six promising compounds, which, at first, were analyzed in a thermal shift assay to assess potential binding. Afterwards, data sets of co-crystals with Pim1 were collected. The subsequent analysis of crystallographic data revealed two hits, which will be presented and discussed in the following.

## 5.2. Material and Methods

### 5.2.1. Docking and ZINC compounds selection

Docking was performed with OpenEye's OEDocking suite after database parameterisation by Omega<sup>127</sup> and QUACPAC<sup>128</sup>. These tools were used to ensure correct protonation states and to find a meaningful balance between conformational space to be explored and computational tractability.

The cleaned lead-like subset of the ZINC database<sup>129</sup> was used comprising 4, 591, 276 molecules. It was chosen as this subset provides a reasonable balance of chemical novelty and compounds that are purchasable whilst removing chemical species unsuited for medicinal chemistry applications. The protein structure prepared for docking was downloaded from the Protein Data Bank (PDB: **3BGP**), incomplete and missing residues were added, and energy minimised using “CHARMM.”<sup>130</sup> “AM1BCC” was applied to attribute partial charges.<sup>128</sup>

Docking was performed with “FRED”<sup>131</sup> using default settings. The top-500 scores were retained and subjected to visual inspection. After evaluation, six compounds were purchased.

### 5.2.2. Protein expression, purification, and crystallisation

Protein expression, purification, and crystallisation were performed as described in chapter 4.2.1.

### 5.2.3. Thermal shift assay

The thermal shift assay was applied as previously described in chapter 4.2.2.

### 5.2.4. X-ray data collection, structure solution and refinement process

The crystallographic data collection, reduction and structure solution was performed as described in chapter 4.2.3

## 5.3. Results and discussion

The initial docking screen together with the further selection of promising candidates from the ZINC library finally resulted in six compounds, which are listed in Figure 84. The compounds were ordered and firstly subjected to a thermal shift assay, to assess their potential binding. The expected binding of these compounds was confirmed in five cases by the TSA. Five ligands exhibited a stabilizing effect on Pim1, indicated by a positive shift of the measured melting point of the protein. Only the sixth ligand **ZINC08880252** showed a small negative shift of  $-0.5\text{ }^{\circ}\text{C}$  ( $\pm 0,6$ ), minor in comparison to the highest shift of  $5.2\text{ }^{\circ}\text{C}$  ( $\pm 0,2$ ) obtained for the compound **ZINC13689545**. The TSA data of all compounds are listed in Table 16. With these promising pre-screening data, the

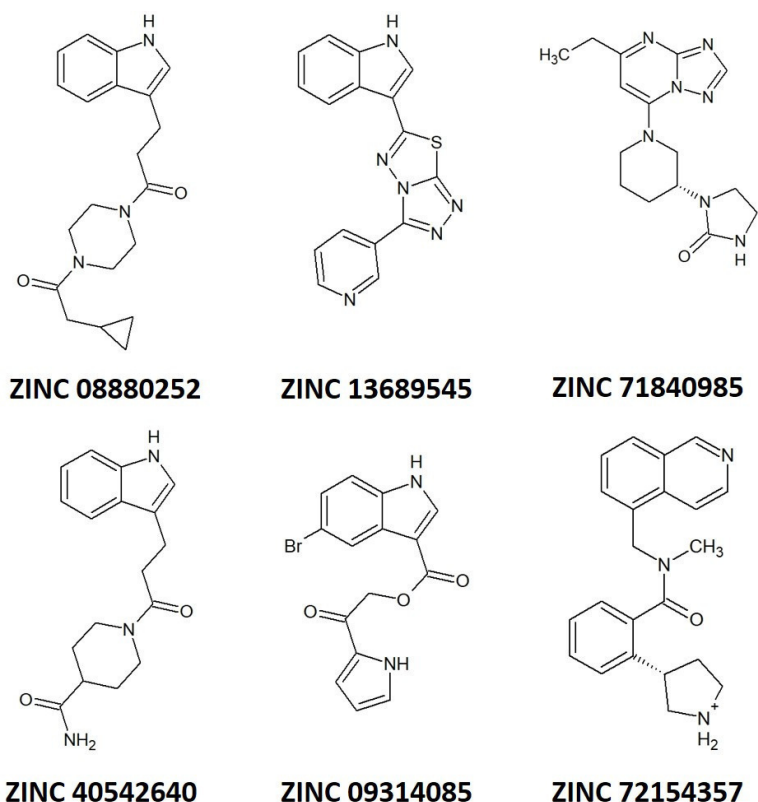


Figure 84: Chemical structure of selected ZINC compounds, which showed a prospective binding mode in the Pim1 docking screen. The compounds are labelled with their original ZINC ID number.

ZINC – ID	TSA – Shift [°C]	Standard deviation [°C]
ZINC08880252	-0.5	± 0,6
ZINC09314085	4.8	± 0,0
ZINC13689545	5.2	± 0,2
ZINC40542640	2.3	± 0,4
ZINC71840985	2.5	± 0,5
ZINC72154357	4.0	± 0,2

Table 16: TSA results of selected ZINC compounds on Pim1. The measured temperature shift and the standard deviation are represented in °C.

crystallographic analysis was subsequently commenced by the co-crystallisation trials of all six compounds. After an incubation time of four weeks, crystals were obtained with every compound. However, only in three cases, the crystals showed sufficient diffracting properties for data collection. Out of these three analyzed datasets two compounds were unambiguously identified as Pim1 ATP pocket binders. These compounds are **ZINC09314085** and **ZINC72154357**. The third ligand (**ZINC08880252**) could not be assigned to the difference electron density. This ligand experienced a negative temperature shift on Pim1 stability in TSA. Thus, the crystallographic data confirmed the binding potential, suggested by the TSA results. Whilst one of the identified compounds is completely defined (**ZINC72154357**), the second one is only partly visible in the difference electron density (**ZINC09314085**). The bromine atom of the compound is unambiguously localised by a strong anomalous signal. Here, the compound could be clearly assigned up to the atoms of the original carboxy ester group. A presentation of its binding mode is given in Figure 85. The fact that the density for the compound ruptures at the original ester

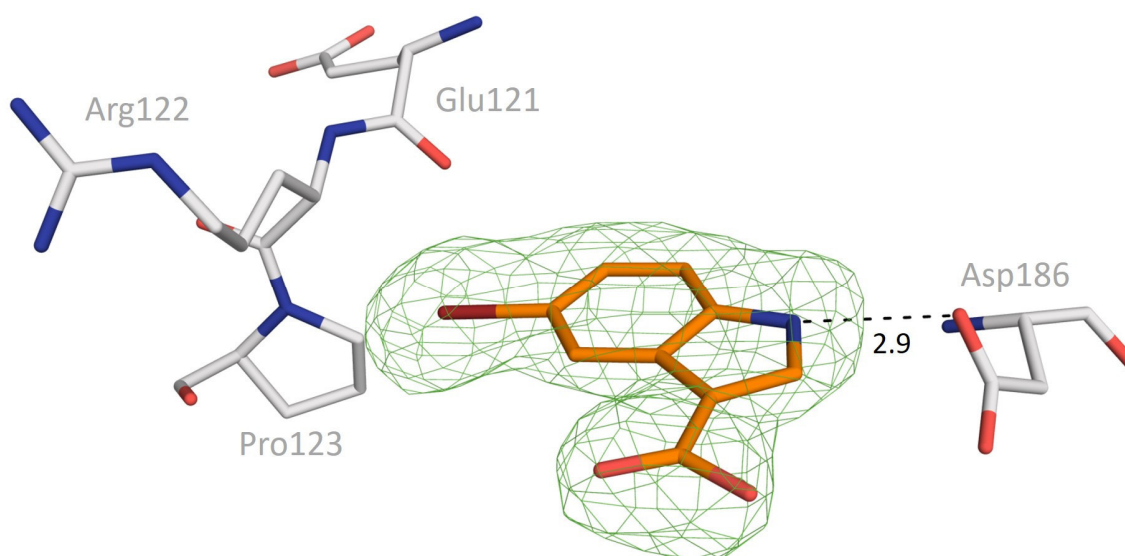


Figure 85: Binding mode of compound ZINC09314085 in a Pim1 crystal structure. Protein residues are shown as sticks in grey coloured carbon atoms. Carbon atoms of the partly placed ligand are coloured in orange. Oxygen atoms are coloured in red and nitrogen atoms in blue. Polar protein-ligand interactions are presented as black dashed lines. The unbiased  $mF_o - D F_c$  difference electron density for the ligand is shown in green and contoured at  $3\sigma$ .

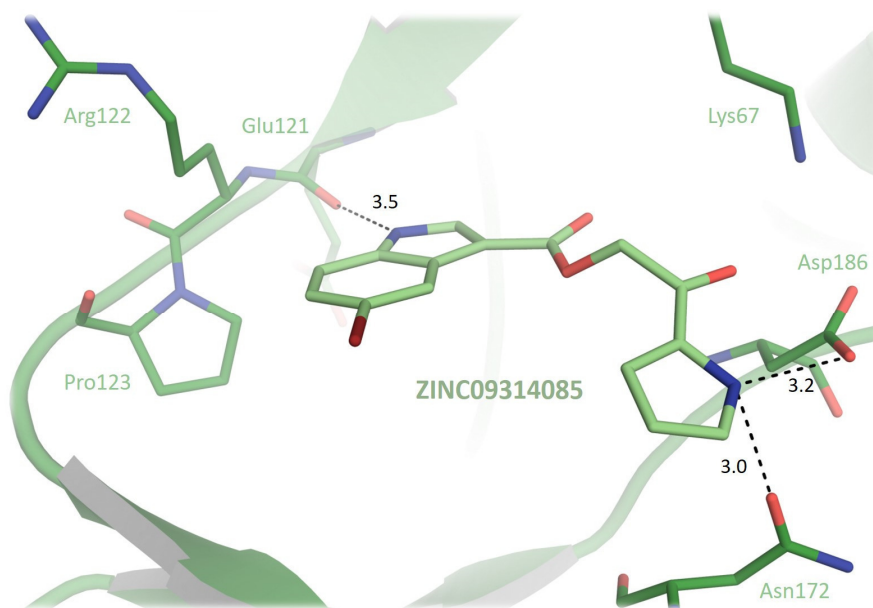


Figure 86: Docked binding mode of compound ZINC09314085. The presented Pim1 protein structure, used for the docking experiment comes from PDB entry 3bgp. The protein is shown in dark green and mainly as cartoon. Polar interaction motives like the hinge region or the DFG-Asp186 are presented as sticks, just like the docked compound but with light green carbon atoms. Distances between polar atoms are marked with black dashed lines.

function raises the question whether the compound is present as the portion resulting from ester hydrolysis or the missing portion is scattered over multiple orientations that do not contribute to a well-defined diffraction pattern. To assess putative ester hydrolysis, further investigations such as testing the isostructural amide derivate were initiated. As these investigations are still ongoing, the observed binding mode is compared to the previously calculated docking mode, which is presented

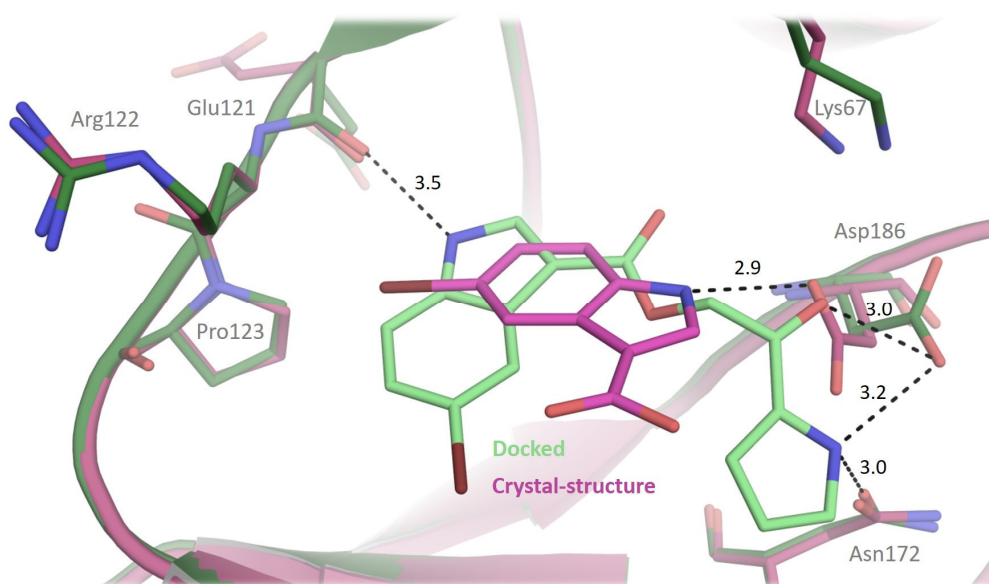


Figure 87: Docked binding mode in alignment with the experimental determined binding mode of compound ZINC09314085. Protein structures are represented in cartoon view. Relevant amino acids of the ATP-binding pocket are displayed as sticks. The obtained crystal structure is coloured in deep purple. The relevant bound ligand has purple carbon atoms. In green, the protein structure of 3bgp is shown and the relevant docked ligand in light green carbon atoms. Distances between polar atoms are marked with black dashed lines.

in Figure 86. In the docked binding pose of **ZINC09314085**, the ligand addresses multiple protein residues via polar interactions. First of all, the side chain of Asp186 is at a distance of 3.2 Å to the pyrrole moiety of the ligand, so that a hydrogen bond is formed. In addition, the carboxamide oxygen of Asn172 is close to this pyrrole nitrogen. The side chain nitrogen of Asn172 is interacting with the side chain of Asp167 thus the assignment of O and N of the carboxamide group appears well defined. As the pyrrole nitrogen bears only one proton, solely a single H-bond can be formed. Via  $\pi$ -conjugation, the nitrogen is adjacent to a keto group, so that it bears hardly any basic character. The oxygen atom of the keto group points in the direction of the side chain carboxylate oxygen of Asp186. An H-bond is also here rather unlikely since the carboxylate group would need to be protonated and the putative H-bond geometry would be quite unfavorable. A weak hydrogen bond (3.5 Å) is formed to the backbone carbonyl oxygen of Glu121 via the compound's indole moiety. The bromine, attached to the indole, points in the direction of the pocket opening, where it finds no polar interaction partner. Upon comparison of the docked and the crystallographically observed binding pose, it becomes apparent that the indole moiety in the experimentally observed binding mode is located close to the hinge, but clockwise rotated by approx. 90° (Figure 87). The indole nitrogen is not interacting with the hinge. Instead, it forms an H-bond with the side chain of Asp186. In comparison to the crystal structure of PDB entry **3bgs**, which was used for the docking procedure, the Asp186 side chain is flipped in the direction of the ligand, so that the distance between indole nitrogen and carboxylate side chain is reduced to 2.9 Å. As the protein is kept rigid during docking, the production of the experimental binding pose will never be possible. Furthermore, the question remains, whether the binding of the ligand results from the hydrolysis of the ester compound or whether pronounced residual mobility makes major parts of the ligand invisible in the density. Analysis of the properties of the compound under the applied crystallisation conditions is still ongoing.

Ligand **ZINC72154357** adopts a different binding pattern in its docking pose (Figure 88). Here, the interaction with Lys67 appears more determining for binding than to contact Asp186. The isoquinoline moiety operates as an acceptor for the H-bond donating side chain of Lys67, while the rest of this planar ring is clamped between the hydrophobic side chains of Leu174, Val52, and Ala65 (not shown). The hinge is not involved in any interaction with the ligand, and the ligand extends towards the pocket mouth, where the two carboxylate side chains of Asp131 and Asp128 are located close to the positively charged nitrogen atom of the pyrrolidine ring of the compound. Thus, salt bridges are formed to these two protein residues. The benzene ring and adjacent peptide bond function as linkers between isoquinoline and pyrrolidine moiety. The peptide bond is in no polar interaction with the protein. Only the benzene ring is in a hydrophobic contact range of 3.5

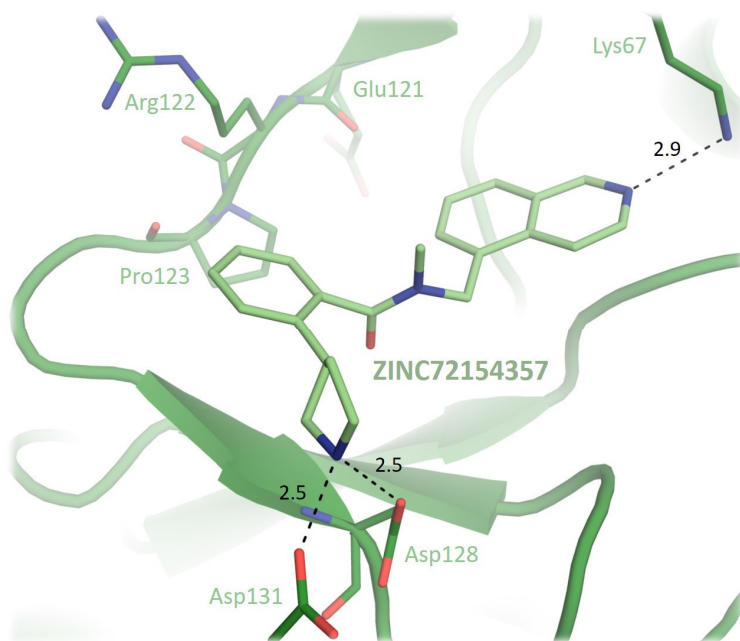


Figure 88: Docked binding mode of compound ZINC72154357. The presented Pim1 protein structure, used for the docking experiment originates from PDB entry 3bgp. The protein is shown in dark green and mainly as cartoon. Polar interaction motifs like the hinge region or the Lys67 are presented as sticks, just like the docked compound but with light green carbon atoms. Distances between polar atoms are marked with black dashed lines.

Å to the side chain of Leu44. The entire ligand **ZINC72154357** is visible in the crystal structure of Pim1 (Figure 89). In comparison with the docked structure, an entirely different mode is detected. The planar isoquinoline moiety is located in the adenosine binding site of the ATP-binding pocket, and its nitrogen atom is oriented towards the hinge region, however, without forming any H-bond interaction. The largest difference between both binding poses is observed for the pyrrolidine ring.

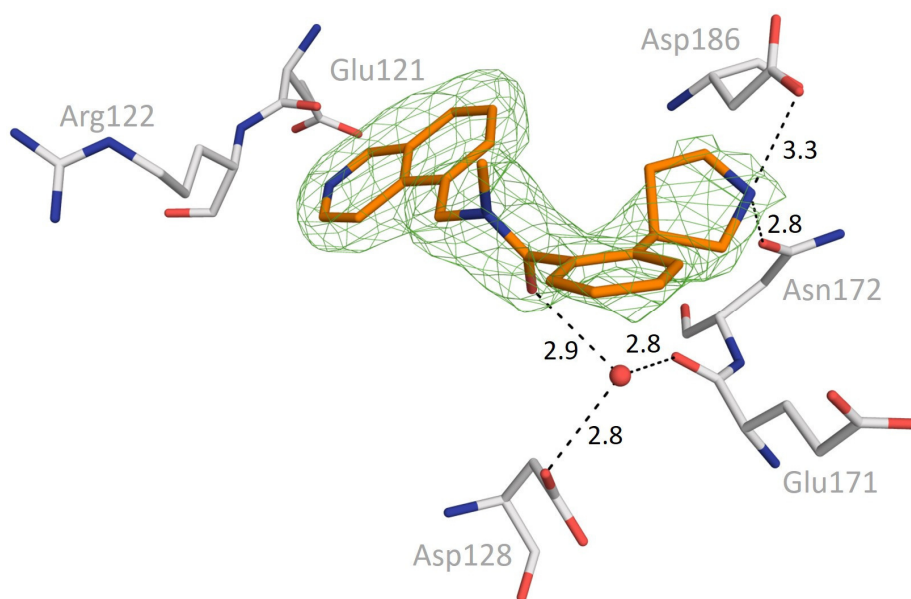


Figure 89: Binding mode of compound ZINC72154357 in a Pim1 crystal structure. Protein residues are shown as sticks in grey carbon atoms. The ligand placed in the electron density is coloured with orange carbon atoms. Polar protein-ligand interactions are presented as black dashed lines. The unbiased  $mF_o - DFC$  difference electron density for the ligand is contoured at  $3\sigma$ .



It is found to bind to the side chain residues of Asp186 and Asn172. The amino group is likely protonated so that a salt bridge to the side chain of Asp186 is possible. However, the distance of 3.3 Å suggests surprisingly only a weak interaction. Instead, the uncharged carboxamide oxygen of Asn172 is in 2.8 Å distance to the charged amino group forming an ideal H-bond. The linking central peptide bond of compound **ZINC72154357** is not involved in any direct interaction with the protein. Nevertheless, it orients the carbonyl oxygen in the direction of a water molecule, which mediates a contact to the side chain of Asp128 and the backbone carbonyl oxygen of Glu171. The alignment of docked and crystal structure illustrates the deviating binding, which is represented in Figure 90. This raises the question, why differences in the predicted docked structure and the crystal structure occur. One important fact results from the neglect of water molecules during docking. Consideration of water molecules during docking<sup>131</sup> was not applied during the retrieval of the six ZINC compounds. Water molecules will influence the binding and therefore also the binding properties of potential binders.<sup>132</sup> The inspection of other PDB entries revealed, that the water molecule between Asp128 and Glu171 is frequently observed. In the crystal structure, ligand **ZINC72154357** uses exactly this water molecule as a mediator for protein-ligand interaction. The second difference between docked and crystal structures is the presence/absence of the peptide PIMTIDE. This peptide was added to the crystallisation conditions to stabilise Pim1. PIMTIDE binding to the protein has a direct impact on the side chain of Asp128, which was otherwise

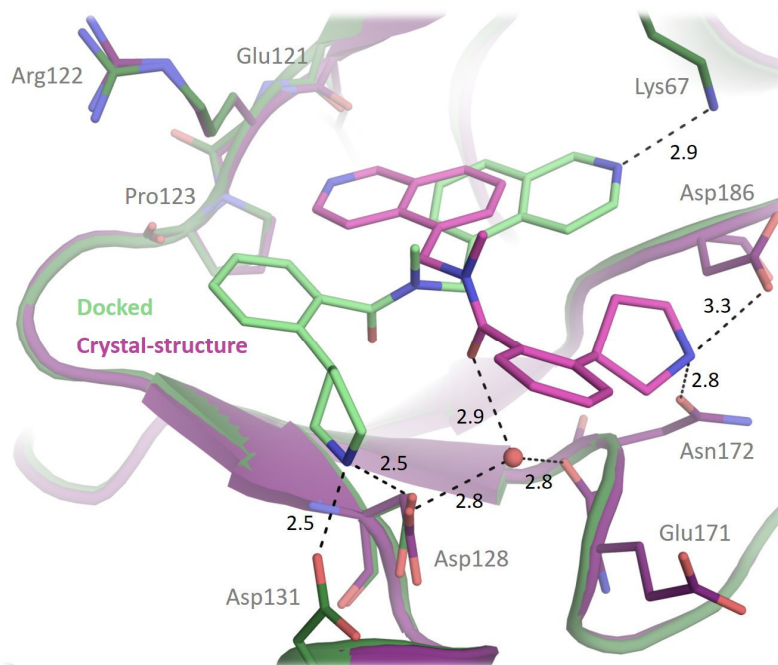


Figure 90: Docked binding mode in alignment to the experimentally observed binding mode of compound **ZINC72154357**. Protein structures are represented in cartoon view. Interesting amino acids of the ATP-binding pocket are displayed as sticks. The determined crystal structure is coloured in deep purple. The relevant bound ligand has purple carbon atoms. In green, the protein structure of 3bgp is shown and the relevant docked ligand in light green carbon atoms. Distances between polar atoms are marked with black dashed lines.

predicted to interact with the pyrrolidine amino group of **ZINC72154357**. The basic side chain of Arg6 of PIMTIDE extends to the carboxylate group of Asp128 so that a salt bridge is readily formed with this peptide residue. The structure used for docking (PDB entry **3bgp**) did not contain the bound peptide, which influences the properties of Asp128. The formation of a salt bridge to Arg6 will minimise the availability of Asp128 to form an additional salt bridge with the ligand. This effect is considered in the docking experiments. Despite the observed discrepancies between docking and crystallography, the project revealed two novel Pim1 binders in a short period of time.

#### **5.4. Status quo & perspective**

Out of the docking screen, six compounds were selected for further testing. The TSA resulted in five compounds with a stabilizing effect on Pim1, which confirmed their potential for Pim1 binding. Three of the compounds were successfully co-crystallised and analyzed by X-ray crystallography, and two allowed detecting of crystallographically confirmed binders. Interestingly, the compound showing no stabilizing effect is not well populated in the crystal structure suggested by the absence of a well-defined difference electron density. The two other compounds bind to the ATP-binding pocket of Pim1 and show deviating binding modes compared to the docking predictions. These deviations need in-depth analysis by further docking attempts and additional experimental investigations. The partly visible compound **ZINC09314085** needs mass spectrometric analysis to clarify whether any hydrolysis during crystallisation might have happened or whether the pronounced disorder is in operation. Another way to confirm binding would be to replace the ester by an amide bond so that the risk of hydrolysis is minimised. Additionally, the investigation of the compound's inhibitory effect is initiated (Eurofins Pharma Discovery Services UK Limited) to classify the selected ligands better. These further investigations will clarify the obtained results of this project.

## **6. Summary**

The primary aim of this thesis was the crystallographic analysis of PKA and Pim1 crystals in complex with small fragment-like molecules to identify potential fragment binders in the protein kinase binding pockets. In the first subproject of this thesis, the similarities and differences between both kinases are highlighted. The fragments used for this study were extracted as a part of an in-house library comprising 361 entries. These fragments were analyzed by TSA as a pre-screening method to evaluate their potential binding to both kinases. This pre-screening resulted in 31 putative binding candidates for the PKA, whereas 52 were identified for Pim1. The subsequent crystallographic analysis of these candidates revealed that 15 fragments had bound to PKA and 13 to Pim1. Referred to the number of collected datasets of each protein (31 PKA / 15 Pim1) this led to a hit rate of 48% for PKA and of 87% for Pim1. Due to the efficient pre-screening selection and the difficult crystallisation of Pim1 complexes, only three of the 361 fragments were commonly studied by protein crystallography with both kinases. Fragment F222 was the only one, which bound to PKA and Pim1. The binding mode of this fragment is similar in both proteins. Nevertheless, three striking differences were detected in the ATP-binding pocket, which influences protein-ligand interactions. Pim1 contains Pro123 in the hinge region, which reduces the number of H-bond donors in the ATP-binding pocket by one. PKA contains the hydrophilic side chain of Thr183 in the binding pocket, whereas Pim1 exposes the hydrophobic Ile185 at the same position. Additionally, PKA exhibits a long C-terminal loop, which is located close to the ATP-binding pocket. The side chain of Phe327 penetrates into the binding pocket of PKA and thus reduces the available space of the pocket and narrows the entrance. These differences in the binding pocket also affect the deviating binding modes of F222 in both kinases. As a pre-screening method, TSA had shown that enrichment of crystallographic hits could be achieved with both kinases, as an additional X-ray analysis of randomly picked test candidates outside the TSA hit list revealed a lower hit-rate of 20%. The overall results of the TSA analyses also provide some ideas about required selectivity features of the fragments between PKA and Pim1. In comparison with already published PKA and Pim1 binders, we could detect either known but also new structural scaffolds for the interactions with the protein.

In the second subproject of this thesis, complexes of PKA and fragments were analyzed by direct exposure of soaked crystal to X-ray analysis. A full library with 96 entries was tested. Of these 43 were soaked into a PKI containing crystal form and 53 into a PKI free one. There were 30 crystallographic hits found out of 96 collected data sets. This results in a hit-rate of 31%. The obtained hits were split into 15 PKI-containing and 15 PKI-free complex structures. There were 24 fragments detected to bind in the ATP-binding pocket. Since several fragments bound multiple times in one structure, 15 fragments were detected in a remote position leading overall to 39

different binding poses. The binders of the binding pocket were further classified in terms of their interaction motifs. They were sorted into groups such as direct hinge binders (12), water-mediated hinge binder (2), direct DFG-loop binders (16) and water-mediated DFG-loop binders (4). Remote binding fragments were analyzed in terms of the buried surface area with respect to the proximate PKA molecules to obtain some figures-of-merits, whether binding only occurs in the crystallographic packing and would turn out as ‘artefacts’ during an analysis by a method focussing on conditions in the solute phase. Five of these 15 fragments revealed a relatively high percentage of buried surface area with a neighbouring PKA molecule. Due to the high amount of ATP-pocket binders, a topological map of the pocket was drafted, giving some ideas where the detected structural motifs of the fragments assembled in the different sub-pockets. In comparison with another fragment-based study of the Saxty group with PKA/PKB, three fragments of the current study were conspicuous, which showed similarities in structure and binding mode to a nanomolar inhibitor found in their study. These three fragments indicate how a merged ligand could be formed. In the course of this sub-project, a new crystal form of PKA without the bound peptide inhibitor PKI was obtained (s. above). Growing these PKA crystals required a longer time span, but showed better diffraction properties. In relation to PKI-bound structures, mean improvement in resolution of 0.25 Å could be achieved. Additionally, these new crystals allowed the binding of fragments to the peptide binding site, which was successfully documented by the Arg-mimicking fragments **J72** and **J77**.

The third sub-project of this thesis is part of a cooperation project with AG Kolb and AG Diederich. Here, the first step to identify fragment molecules that interact with the amino acids Glu121 and Lys67 of the Pim1 kinase was accomplished. Suitable fragments will be combined with another component to achieve additional interactions with Asp128 and Glu171. We used the database tool SCUBIDOO to identify virtual screening hits. The search for suitable fragments resulted in three compounds, which were detected by docking, similarity search and an FCFP4 fingerprint analysis based on the “Chembridge building block library” (**4012413**, **4012414** and **5175110**). The latter fragment was already published in 2012 by Good et al. in complex with Pim1. We could simultaneously confirm the retrieval and subsequently the binding of this fragment by our procedure and the reliability of our strategy. The compound **4012413** was crystallised with Pim1. The electron density resulting from analysis of the dataset revealed that the ligand had presumably bound in the ATP-binding pocket. However, the observed difference electron density was too poorly defined to assign the ligand precisely into the structure. Testing all three fragments by TSA, suggested binding of all three fragments. Further crystallisation of fragment **4012413** and **4012414** is still pending.

The fourth subproject of this thesis was focused on compounds extracted from the ZINC databank. They were identified as potential Pim1 binders by docking experiments. A sample of six promising ligands was identified and selected showing a promising binding in the docking prediction. An analysis of these ligands by TSA revealed that all compounds, excluding one, had a stabilizing effect on Pim1, which indicates their binding. Three of these ligands were analyzed crystallographically. Two ligands showed a binding to the protein. The compound **ZINC08880252** could not be detected as a binder, and it was the only one lacking any stabilizing effect in TSA. Although the two ligands **ZINC72154357** and **ZINC09314085** showed a binding, their binding modes deviate from the docking prediction. The ligand **ZINC09314085** is only partly represented by the difference electron density. An explanation for this incompletely defined binding is still under investigation. Hydrolysis of its central ester group could be a possible reason or a pronounced partial disorder, or residual mobility is in operation. To investigate this, an exchange of the ester by an amide bond has been initiated, and a mass spectrometric analysis is currently performed.

## **7. Zusammenfassung**

Das primäre Ziel dieser Doktorarbeit war die kristallographische Untersuchung der beiden Kinasen Pim1 und PKA im Komplex mit kleinen Fragment-Molekülen, um ein mögliches Binden solcher Fragmente in den Proteinbindetaschen zu detektieren. In dem ersten größeren Teilprojekt dieser Arbeit wurden vor allem charakteristische Gemeinsamkeiten und Unterschiede zwischen den beiden Kinasen herausgestellt. Die Fragmente für diese Untersuchung stammten aus einer hauseigenen Bibliothek mit 361 Einträgen. Diese Fragmente wurde mittels einer Vorauswahl durch den Thermal Shift Assay auf ihre potentiellen Bindungseigenschaften an beide Kinasen untersucht. Diese Vorauswahl lieferte 31 potentielle Bindungs-Kandidaten für die PKA und in 52 für die Pim1. Die anschließende kristallographische Analyse dieser Treffer ergab, dass bei der PKA 15 Fragmente und bei der Pim1 13 gebunden hatten. Gemessen an den gesammelten Datensätzen für beide Proteine (31 PKA / 15 Pim1) ergab sich eine Trefferquote von 48% für die PKA und eine von 87% für die Pim1. Bedingt durch die Auswahl des Auswahlverfahrens und dem schwierigen Kristallisation-Verfahrens der Pim1-Kinase wurden lediglich drei der 361 Fragmente bei beiden Proteinen gemeinsam gefunden und dann kristallographisch untersucht. Lediglich das Fragment F222 wurde für beide Kinasen als Hit identifiziert. Der Bindungsmodus dieses Fragmentes ist bei beiden Proteinen sehr ähnlich. Dennoch verweist dieser Vergleich auf drei wesentliche Unterschiede in den ATP Bindetaschen, welche die Protein-Ligand-Interaktionen beeinflussen. Die Pim1 weist an der so genannten Hinge-Region Pro123 auf, wodurch ein Wasserstoffbrücken-Donor weniger in der Bindetasche zur Verfügung steht. Die PKA hat durch Thr183 eine weitere polare Seitenkette in der Bindetasche, wogegen die Pim1 dort ein hydrophobes Ile185 aufweist. Zusätzlich besitzt die PKA eine lange C-terminale Schleife, die an der Bindetasche entlang verläuft. Die Seitenkette des dort anliegenden Phe327 ragt aus dieser Schleife in die Bindetasche der PKA hinein, verringert dadurch das zur Verfügung stehende Volumen und verengt den Eingangsbereich. Diese markanten Unterschiede zeigen sich auch an einem leicht unterschiedlichem Bindemodus von F222 in beiden Kinasen. Der TSA hat als Vor-Testverfahren gezeigt, dass eine Anreicherung von kristallographischen Treffern bei den beiden Kinasen erreicht werden kann, da eine stichprobenartige kristallographische Analyse weiterer Kandidaten außerhalb der TSA-Trefferliste eine geringere Trefferquote von 20% aufzeigte. Ebenfalls deutet das Ergebnis der TSA-Analyse auf eine gewisse Selektivität der Fragmente zwischen PKA und Pim1 hin. Im Vergleich zu bereits publizierten PKA- und Pim1-Bindern konnten bekannte sowie neue Gruppierungen für die Proteininteraktionen detektiert werden.

In dem zweiten größeren Teilprojekt dieser Arbeit wurde die PKA einer ausschließlich direkten röntgenkristallographischen Durchsuchung mit Fragmenten unterzogen. Eine Bibliothek von 96 Fragment-Verbindungen wurde mittels „Soaking“ auf dieser Kinase getestet. Von 96 gesammelten



Datensätzen enthielten 30 einen kristallographisch bestätigten Binder. Dies entspricht einer Treffer-Quote von 31%. Dabei wurden 43 Fragmente einer PKI-gebundenen und 53 Fragmente einer PKI-freien Kristallform der PKA unterworfen. Die entdeckten 30 Treffer teilten sich hälftig in 15 Komplexe der PKI-haltigen und 15 Komplexe der PKI-freien Form auf. Es wurden 24 Fragmente gefunden, welche in der ATP Bindetasche gebunden hatten. Da einige Fragmente mehrfach aufgenommen wurden, konnten 15 Fragmente außerhalb dieser Tasche detektiert werden, sodass insgesamt 39 unterschiedliche Bindeposen detektiert wurden. Die Fragmente in der Bindetasche wurden je nach aufgetretenen Interaktionsmuster klassifiziert. Unterschieden wurde zwischen direkten (12) sowie Wasser-vermittelten (2) „Hinge“-Bindern bzw. direkten (16) oder Wasser-vermittelten (4) DFG-Schleifen-Bindern (4). Die außerhalb der ATP-Bindetasche bindenden Fragmente wurden hinsichtlich ihrer vergrabene Oberfläche mit weiteren in der Packung nahestehenden PKA Molekülen untersucht, um abzuklären, ob der beobachtete Bindungsmodus nur in der Festkörperpackung auftritt und unter Bedingungen in Lösung als Artefakt zu bezeichnen wäre. Insgesamt 5 dieser 15 Fragmente wiesen eine vergleichsweise hohe vergrabene Oberfläche mit Nachbar-Proteinmolekülen auf. Wegen der recht hohen Anzahl an Bindern in der ATP Bindetasche wurde eine topologische Auswertung dieser Tasche angefertigt, in der die detektierten Strukturelemente den verschiedenen Teilregionen dieser Tasche zugeordnet wurden. Im Vergleich mit einer anderen Fragment-basierten Studie aus der Saxty Gruppe an PKA/PKB fielen drei Fragmente aus der vorliegenden Untersuchung auf, die in Struktur und Bindungsmodus Ähnlichkeiten zu einem Inhibitor dieser Studie aufzeigten, der nM Binding aufweist. Diese drei Fragmente legen die Entwicklung eines „zusammengeführten-Liganden“ nahe. Im Laufe dieses Teilprojektes konnte eine neue Kristallform der PKA entwickelt werden, die ohne den Substratinhibitor PKI gewonnen wurde (s. oben). Diese PKA Kristalle zeichneten sich durch eine längere Wachstumsphase aber auch ein verbessertes Streuvermögen aus. Im Durchschnitt hatten die PKI-freien Strukturen eine verbesserte Auflösung von 0,25 Å. Zudem war bei diesen Kristallen die Peptid-Bindestelle zugänglich für Fragmente, was auch durch die Arg-ähnlichen Fragmente **J72** und **J77** genutzt wurde.

Das dritte Teilprojekt dieser Arbeit umfasst einen Teil eines Kooperationsprojektes mit der AG Kolb und der AG Diederich. Hierbei wurden im ersten Schritt Fragment-Moleküle gesucht, die mit den Aminosäuren Glu121 und Lys67 der Pim1 Kinase interagieren. Geeignete Fragmente sollen mit weiteren Synthesebausteinen kombiniert werden, um eine Interaktion mit Asp128 und Glu171 zu erhalten. Für die virtuelle Trefferidentifikation wurde die Datenbank SCUBIDOO verwendet. Die Suche nach geeigneten Fragmenten resultierte in drei Verbindungen, die durch Docking, Ähnlichkeit-Untersuchungen und einer „FCFP4 fingerprint“ - Untersuchung der

„Chembridge fragment library“ extrahiert wurden. Ein aufgefundenes Fragment wurde bereits 2012 von Good et. al. in Komplex mit Pim1 publiziert. Wir konnten mit unserem Verfahren dessen Auswahl und Bindung bestätigen und somit auch unser Verfahren auf dessen Funktionalität und Zuverlässigkeit überprüfen. Die Verbindung **4012413** wurde ebenfalls mit der Pim1 kristallisiert. Die resultierende Elektronendichte der vermessenen Kristallstruktur zeigte, dass die Verbindung vermutlich in der Bindetasche gebunden hatte. Allerdings war die Dichte aufgrund der schlechten Qualität des Datensatzes nicht ausreichend für eine zuverlässige Einpassung des Fragmentes. Durch die TSA-Analyse konnten ebenfalls Hinweise erhalten werden, die andeuten, dass die Fragmente an Pim1 binden. Eine erneute Kristallisation der Verbindungen **4012413** und **4012414** stehen in Aussicht.

Das vierte Teilprojekt dieser Arbeit beschäftigt sich mit Verbindungen aus der ZINC Datenbank, welche als potentielle Binder der Pim1 Kinase durch Docking identifiziert wurden. Eine Auswahl von 6 Verbindungen zeigten einen vielversprechenden Bindungsmodus im Docking. Eine Analyse der Liganden im TSA hinsichtlich Pim1 ergab, dass mit einer Ausnahme alle Verbindungen einen stabilisierenden Effekt auf Pim1 nehmen. Drei dieser Verbindungen wurden kristallographisch getestet. Zwei zeigten eine Bindung an das Protein. Die Verbindung **ZINC08880252** konnte nicht als Binder identifiziert werden und zeigte auch keinen stabilisierenden Effekt im TSA. Die beiden Verbindungen **ZINC72154357** und **ZINC09314085** ergaben kristallographisch einen anderen Bindungsmodus als in der Docking-Vorhersage. Die Verbindung **ZINC09314085** wurde nur teilweise in der Differenzelektronendichte entdeckt. Die Gründe für dieses Verhalten werden im weiteren Fortgang des Projektes geklärt. Die Hydrolyse der zentralen Carbonsäure-Ester Verknüpfung der Verbindung wäre eine mögliche Erklärung. Auch kann der nicht charakterisierte Teil des Liganden ungeordnet oder mit hoher Restmobilität vorliegen und sich daher nicht in der Differenzelektronendichte abzeichnen. Um diese Ansätze zu verfolgen wurde der Ersatz der Esterbindung durch eine Amid-Gruppe, sowie eine massenspektroskopische Analyse initiiert.

## **8. Appendix**

## 8.1. Thermal shift data results of the 361 library screen (PKA)

ID	$\Delta T_m$ [°C]	ID	$\Delta T_m$ [°C]	ID	$\Delta T_m$ [°C]	ID	$\Delta T_m$ [°C]	ID	$\Delta T_m$ [°C]
1	0.2 ± 0.0	40	0.0 ± 0.3	79	-0.7 ± 0.3	118	-1.6 ± 0.5	157	-0.5 ± 0.3
2	0.2 ± 0.3	41	1.8 ± 0.3	80	-0.3 ± 0.3	119	-4.5 ± 0.3	158	-1.7 ± 0.3
3	0.0 ± 0.3	42	0.3 ± 0.6	81	-0.2 ± 0.0	120	-1.0 ± 0.3	159	-0.5 ± 0.3
4	0.2 ± 0.0	43	-0.5 ± 0.6	82	-1.8 ± 0.0	121	-2.2 ± 0.6	160	0.7 ± 0.3
5	0.7 ± 0.3	44	0.0 ± 0.3	83	1.0 ± 0.3	122	-0.5 ± 0.3	161	-0.8 ± 0.3
6	-0.7 ± 0.3	45	-0.5 ± 0.5	84	-3.5 ± 0.0	123	-2.2 ± 0.3	162	0.0 ± 0.6
7	0.0 ± 0.3	46	0.5 ± 0.6	85	n.a.	124	-0.7 ± 0.6	163	1.8 ± 0.8
8	0.5 ± 0.3	47	1.7 ± 0.0	86	-1.0 ± 0.0	125	n.s	164	-3.3 ± 0.8
9	0.2 ± 0.3	48	-0.7 ± 0.5	87	-7.1 ± 0.3	126	-1.2 ± 0.3	165	-0.1 ± 0.8
10	-1.0 ± 0.3	49	-0.8 ± 0.3	88	-7.5 ± 0.0	127	-1.8 ± 0.0	166	-0.4 ± 0.3
11	-1.5 ± 0.3	50	1.7 ± 0.3	89	-0.7 ± 0.5	128	-2.0 ± 0.3	167	-1.7 ± 0.0
12	-1.2 ± 0.0	51	-7.5 ± 0.4	90	-1.0 ± 0.3	129	-1.0 ± 0.3	168	0.0 ± 0.0
13	-0.2 ± 0.0	52	0.7 ± 0.5	91	-1.3 ± 0.9	130	0.0 ± 0.3	169	-0.3 ± 0.3
14	-0.8 ± 0.3	53	n.a.	92	-6.0 ± 0.2	131	-1.0 ± 0.0	170	-1.2 ± 0.3
15	0.0 ± 0.3	54	-2.2 ± 0.8	93	0.2 ± 0.0	132	-3.0 ± 0.4	171	-0.3 ± 0.3
16	-0.2 ± 0.3	55	0.2 ± 0.3	94	-1.2 ± 0.0	133	0.5 ± 0.0	172	-0.7 ± 0.6
17	-0.2 ± 0.3	56	-0.7 ± 0.5	95	0.2 ± 0.3	134	-0.3 ± 0.0	173	-0.5 ± 0.0
18	-0.5 ± 0.0	57	0.6 ± 0.4	96	-1.2 ± 0.3	135	-3.0 ± 0.3	174	-2.0 ± 0.3
19	-0.2 ± 0.6	58	0.8 ± 0.3	97	n.s	136	-2.3 ± 0.0	175	-0.8 ± 0.0
20	0.8 ± 0.0	59	0.0 ± 0.3	98	-1.2 ± 0.0	137	-0.7 ± 0.5	176	-0.3 ± 0.3
21	-2.8 ± 0.3	60	-0.5 ± 0.3	99	-0.3 ± 0.3	138	-1.0 ± 0.3	177	0.0 ± 0.0
22	-0.5 ± 0.0	61	-0.5 ± 0.0	100	-0.5 ± 0.0	139	-5.8 ± 0.3	178	0.0 ± 0.5
23	-1.2 ± 0.0	62	-0.5 ± 0.3	101	-0.2 ± 0.3	140	-5.2 ± 0.3	179	-0.2 ± 0.8
24	-0.8 ± 0.5	63	6.0 ± 0.3	102	-2.8 ± 0.9	141	-5.5 ± 0.0	180	-1.3 ± 0.3
25	-0.2 ± 0.0	64	-0.1 ± 0.0	103	-0.3 ± 0.3	142	-2.0 ± 0.0	181	n.s
26	-1.3 ± 0.0	65	-0.2 ± 0.3	104	-0.5 ± 0.3	143	-1.0 ± 0.0	182	n.s
27	0.0 ± 0.3	66	0.7 ± 0.3	105	-0.8 ± 0.0	144	-1.0 ± 0.3	183	-1.2 ± 0.6
28	-0.2 ± 0.3	67	-1.2 ± 0.5	106	-1.5 ± 0.3	145	-1.2 ± 0.0	184	0.0 ± 0.3
29	-0.2 ± 0.0	68	-0.7 ± 0.0	107	-0.8 ± 0.3	146	-0.7 ± 0.0	185	0.0 ± 0.0
30	0.0 ± 0.0	69	0.2 ± 0.3	108	n.s	147	-0.3 ± 0.0	186	0.0 ± 0.3
31	-0.3 ± 0.0	70	1.3 ± 0.0	109	-1.3 ± 0.3	148	-2.0 ± 1.0	187	-0.3 ± 0.5
32	0.0 ± 0.2	71	-1.7 ± 0.3	110	0.5 ± 0.3	149	-0.2 ± 0.0	188	-1.2 ± 0.3
33	0.7 ± 0.3	72	-0.2 ± 0.3	111	-1.7 ± 0.3	150	-1.3 ± 0.0	189	-0.3 ± 0.0
34	n.s	73	-0.3 ± 0.3	112	0.7 ± 0.8	151	-3.0 ± 0.3	190	0.2 ± 0.3
35	0.5 ± 0.0	74	1.1 ± 0.0	113	-0.3 ± 0.3	152	-1.0 ± 0.3	191	0.2 ± 0.0
36	-0.7 ± 0.5	75	n.s	114	3.2 ± 0.3	153	-2.0 ± 0.8	192	0.2 ± 0.3
37	1.6 ± 0.0	76	-4.7 ± 0.3	115	-1.2 ± 0.2	154	-1.0 ± 0.6	193	-0.5 ± 0.3
38	1.7 ± 0.3	77	0.2 ± 0.2	116	-2.7 ± 0.3	155	-0.8 ± 0.6	194	-5.7 ± 0.0
39	0.7 ± 0.0	78	1.3 ± 0.0	117	-0.5 ± 0.5	156	n.s	195	0.2 ± 0.0

ID	$\Delta T_m$ [°C]	ID	$\Delta T_m$ [°C]	ID	$\Delta T_m$ [°C]	ID	$\Delta T_m$ [°C]	ID	$\Delta T_m$ [°C]
196	1.7 ± 0.6	232	-4.2 ± 0.5	268	-0.7 ± 0.3	304	1.2 ± 0.3	340	0.0 ± 0.3
197	-0.2 ± 0.0	233	-0.7 ± 0.6	269	-0.5 ± 0.3	305	0.1 ± 0.5	341	0.8 ± 0.6
198	-0.5 ± 0.0	234	-1.7 ± 0.0	270	0.0 ± 0.3	306	-0.2 ± 0.0	342	2.2 ± 0.5
199	0.3 ± 0.0	235	-1.0 ± 0.3	271	n.s	307	-1.0 ± 0.3	343	-0.2 ± 0.3
200	0.3 ± 0.0	236	0.5 ± 0.3	272	0.2 ± 0.0	308	-2.0 ± 0.0	344	0.8 ± 0.5
201	0.8 ± 0.4	237	1.2 ± 0.8	273	-1.5 ± 0.0	309	-2.0 ± 0.3	345	-1.2 ± 0.0
202	-0.3 ± 0.0	238	-0.7 ± 0.0	274	1.5 ± 0.0	310	n.s	346	0.0 ± 0.3
203	0.8 ± 0.0	239	-0.5 ± 0.0	275	0.0 ± 0.0	311	-2.2 ± 0.0	347	0.5 ± 0.3
204	1.5 ± 0.6	240	-0.2 ± 0.5	276	-0.3 ± 0.0	312	n.s	348	-0.7 ± 0.5
205	0.5 ± 0.3	241	-0.7 ± 0.3	277	-0.2 ± 0.4	313	-2.1 ± 0.5	349	-1.0 ± 0.3
206	0.0 ± 0.3	242	-1.8 ± 0.3	278	-0.5 ± 0.0	314	-4.8 ± 0.4	350	0.3 ± 0.0
207	0.5 ± 0.3	243	0.8 ± 0.3	279	-1.0 ± 0.9	315	0.0 ± 0.6	351	-0.5 ± 0.0
208	-0.3 ± 0.3	244	0.0 ± 0.4	280	-1.2 ± 0.8	316	-1.7 ± 0.5	352	-0.8 ± 0.6
209	-0.2 ± 0.0	245	-0.2 ± 0.0	281	0.0 ± 0.3	317	-3.5 ± 0.3	353	1.0 ± 0.0
210	n.s	246	0.0 ± 0.5	282	-0.5 ± 0.3	318	n.s	354	-1.3 ± 0.3
211	1.5 ± 0.6	247	-1.0 ± 0.3	283	-0.3 ± 0.4	319	0.0 ± 0.3	355	-0.5 ± 0.3
212	0.5 ± 0.0	248	-4.0 ± 0.3	284	-0.8 ± 0.0	320	0.5 ± 0.5	356	-0.5 ± 0.6
213	-2.0 ± 0.0	249	0.0 ± 0.5	285	0.5 ± 0.3	321	-0.2 ± 0.0	357	1.2 ± 0.5
214	-0.5 ± 0.6	250	0.0 ± 0.3	286	1.2 ± 0.0	322	-0.8 ± 0.3	358	1.3 ± 0.6
215	-0.3 ± 0.0	251	-1.0 ± 0.0	287	-1.0 ± 0.0	323	n.a.	359	0.2 ± 0.0
216	0.7 ± 0.3	252	-1.0 ± 0.6	288	-0.5 ± 0.3	324	0.5 ± 0.0	360	-1.0 ± 0.0
217	-0.8 ± 0.0	253	0.2 ± 0.3	289	-6.0 ± 0.0	325	1.3 ± 0.3	361	-0.8 ± 0.6
218	n.s	254	0.7 ± 0.0	290	1.5 ± 0.3	326	-0.3 ± 0.5	362	0.7 ± 0.3
219	-0.3 ± 0.0	255	-0.3 ± 0.3	291	-1.0 ± 0.8	327	0.3 ± 0.7	363	0.7 ± 0.0
220	-1.0 ± 0.0	256	0.0 ± 0.3	292	-2.0 ± 0.9	328	1.2 ± 0.4	364	-1.8 ± 0.6
221	0.5 ± 0.0	257	-0.5 ± 0.0	293	-0.2 ± 0.3	329	1.0 ± 0.9		
222	1.8 ± 0.3	258	-0.8 ± 0.0	294	-2.0 ± 0.2	330	0.3 ± 0.3		
223	-0.3 ± 0.3	259	-0.3 ± 0.3	295	-1.5 ± 0.0	331	-0.3 ± 0.6		
224	1.3 ± 0.0	260	-0.5 ± 0.0	296	-2.2 ± 0.3	332	0.3 ± 0.3		
225	0.3 ± 0.6	261	-0.3 ± 0.3	297	-2.3 ± 0.3	333	-6.8 ± 0.8		
226	0.0 ± 0.0	262	0.5 ± 0.3	298	-1.7 ± 0.5	334	0.0 ± 0.3		
227	-1.0 ± 0.3	263	0.2 ± 0.3	299	-0.8 ± 0.0	335	1.5 ± 0.3		
228	0.0 ± 0.3	264	-0.5 ± 0.3	300	-2.0 ± 0.3	336	0.7 ± 0.3		
229	n.s	265	n.s	301	-0.3 ± 0.3	337	0.3 ± 0.0		
230	-2.3 ± 0.3	266	0.2 ± 0.3	302	-1.0 ± 0.0	338	0.2 ± 0.3		
231	0.0 ± 0.0	267	1.3 ± 0.3	303	-0.9 ± 0.0	339	-0.3 ± 0.3		

## 8.2. Thermal shift data results of the 361 library screen (Pim1)

ID	$\Delta T_m$ [°C]	ID	$\Delta T_m$ [°C]	ID	$\Delta T_m$ [°C]	ID	$\Delta T_m$ [°C]	ID	$\Delta T_m$ [°C]
1	1.0 ± 0.2	40	-1.1 ± 0.2	79	3.0 ± 0.2	118	8.3 ± 0.5	157	0.3 ± 0.2
2	3.2 ± 0.2	41	1.8 ± 0.4	80	5.0 ± 0.2	119	-8.3 ± 1.1	158	0.0 ± 0.0
3	7.3 ± 0.0	42	-0.3 ± 0.1	81	1.5 ± 0.2	120	-1.2 ± 0.2	159	5.3 ± 0.0
4	1.5 ± 0.2	43	0.3 ± 0.0	82	-2.5 ± 0.2	121	-1.8 ± 0.0	160	-1.5 ± 0.2
5	2.3 ± 0.0	44	-0.3 ± 0.2	83	0.2 ± 0.0	122	-0.3 ± 0.0	161	-1.7 ± 0.4
6	1.8 ± 1.1	45	-0.3 ± 0.2	84	7.3 ± 0.2	123	2.3 ± 0.2	162	-0.8 ± 0.5
7	5.8 ± 0.0	46	-1.0 ± 0.5	85	-0.2 ± 0.2	124	-1.5 ± 0.2	163	1.0 ± 0.2
8	0.8 ± 0.0	47	-0.3 ± 0.2	86	3.2 ± 0.0	125	-1.5 ± 0.2	164	3.7 ± 0.2
9	0.0 ± 0.2	48	-0.7 ± 0.4	87	n.a.	126	n.s.	165	-0.3 ± 0.2
10	0.5 ± 0.2	49	-0.2 ± 0.0	88	-6.0 ± 0.2	127	3.0 ± 0.0	166	0.2 ± 0.2
11	-0.2 ± 0.0	50	0.0 ± 0.2	89	1.3 ± 0.2	128	-1.5 ± 0.0	167	6.2 ± 0.2
12	1.2 ± 0.2	51	-1.5 ± 0.2	90	0.2 ± 0.0	129	0.2 ± 0.2	168	4.5 ± 0.2
13	0.8 ± 0.0	52	-0.7 ± 0.0	91	6.6 ± 0.1	130	0.5 ± 0.4	169	-0.6 ± 0.3
14	2.3 ± 0.5	53	-5.2 ± 0.5	92	n.a.	131	-0.3 ± 0.2	170	-0.2 ± 0.0
15	2.3 ± 0.0	54	2.8 ± 0.0	93	0.0 ± 0.2	132	-1.8 ± 0.2	171	-1.6 ± 0.3
16	1.5 ± 0.2	55	1.5 ± 0.2	94	0.2 ± 0.0	133	4.8 ± 0.2	172	-0.2 ± 0.0
17	-1.0 ± 0.5	56	-0.8 ± 0.2	95	4.0 ± 0.2	134	3.2 ± 0.5	173	-0.7 ± 0.4
18	0.8 ± 0.0	57	n.a.	96	-1.5 ± 0.2	135	-2.8 ± 0.2	174	2.2 ± 0.2
19	2.7 ± 0.2	58	0.2 ± 0.2	97	n.s.	136	0.0 ± 0.0	175	1.2 ± 0.2
20	1.3 ± 0.0	59	6.0 ± 0.2	98	1.2 ± 0.4	137	-1.7 ± 0.2	176	-1.3 ± 0.2
21	-0.6 ± 0.1	60	3.2 ± 0.2	99	-0.8 ± 0.0	138	-1.0 ± 0.4	177	0.7 ± 0.2
22	-0.2 ± 0.0	61	3.5 ± 0.6	100	-1.8 ± 0.0	139	-4.3 ± 0.2	178	-0.3 ± 0.2
23	-1.0 ± 0.2	62	-1.0 ± 0.2	101	0.3 ± 0.2	140	-2.8 ± 0.2	179	0.2 ± 0.2
24	-0.2 ± 0.0	63	0.7 ± 0.0	102	2.2 ± 0.0	141	-2.2 ± 0.2	180	-1.7 ± 0.4
25	3.9 ± 0.1	64	-3.5 ± 0.2	103	-0.2 ± 0.2	142	-1.1 ± 0.2	181	n.s.
26	2.7 ± 0.2	65	-1.8 ± 0.3	104	-1.2 ± 0.2	143	-0.5 ± 0.0	182	n.s.
27	1.7 ± 0.2	66	2.0 ± 0.2	105	3.7 ± 0.4	144	0.8 ± 0.2	183	-8.4 ± 0.0
28	2.3 ± 0.0	67	-0.5 ± 0.2	106	3.2 ± 0.0	145	2.7 ± 0.2	184	5.2 ± 0.2
29	-0.5 ± 0.2	68	0.8 ± 0.5	107	-1.2 ± 0.2	146	1.8 ± 0.2	185	-4.4 ± 0.8
30	2.1 ± 0.3	69	0.2 ± 0.0	108	n.s.	147	2.8 ± 0.2	186	1.7 ± 0.2
31	2.0 ± 0.6	70	2.2 ± 0.0	109	-0.8 ± 0.0	148	-1.2 ± 0.2	187	-0.5 ± 1.0
32	2.3 ± 0.0	71	10.5 ± 0.2	110	0.0 ± 0.2	149	-0.8 ± 0.5	188	-2.5 ± 0.2
33	-0.2 ± 0.0	72	6.3 ± 0.3	111	-0.5 ± 0.2	150	-0.8 ± 0.2	189	0.5 ± 0.2
34	n.s.	73	2.3 ± 0.2	112	-0.5 ± 0.2	151	-10.2 ± 0.2	190	-1.2 ± 0.0
35	0.0 ± 0.2	74	0.0 ± 0.2	113	-1.2 ± 0.2	152	-1.2 ± 0.2	191	0.5 ± 0.2
36	-3.2 ± 0.0	75	n.s.	114	2.0 ± 0.2	153	-1.2 ± 0.2	192	2.3 ± 0.0
37	-4.3 ± 0.2	76	-10.2 ± 0.2	115	-0.3 ± 0.0	154	2.8 ± 0.4	193	1.4 ± 0.2
38	-1.8 ± 0.2	77	0.3 ± 0.2	116	-1.8 ± 0.0	155	2.0 ± 0.4	194	-23.1 ± 0.2
39	-0.9 ± 0.0	78	-0.2 ± 0.2	117	0.0 ± 0.2	156	n.s.	195	-0.1 ± 0.2

ID	$\Delta T_m$ [°C]	ID	$\Delta T_m$ [°C]	ID	$\Delta T_m$ [°C]	ID	$\Delta T_m$ [°C]	ID	$\Delta T_m$ [°C]
196	5.0 ± 0.0	232	-15.2 ± 0.2	268	-0.3 ± 0.3	304	9.3 ± 0.2	340	2.3 ± 0.0
197	3.6 ± 0.2	233	1.2 ± 0.4	269	0.0 ± 0.0	305	4.3 ± 0.2	341	2.3 ± 0.4
198	-0.4 ± 0.2	234	-0.7 ± 0.2	270	-0.1 ± 0.1	306	0.5 ± 0.0	342	2.3 ± 0.0
199	0.8 ± 0.0	235	-0.3 ± 0.2	271	n.s.	307	1.7 ± .2	343	-0.2 ± 0.0
200	7.6 ± 0.5	236	0.0 ± 0.0	272	0.0 ± 0.0	308	1.8 ± 0.2	344	4.0 ± 0.2
201	-0.6 ± 0.2	237	-2.2 ± 0.5	273	0.0 ± 0.0	309	2.0 ± 0.0	345	0.0 ± 0.2
202	-0.8 ± 0.0	238	3.3 ± 0.2	274	1.5 ± 0.0	310	n.s.	346	5.3 ± 0.4
203	0.4 ± 0.2	239	2.0 ± 0.0	275	0.0 ± 0.0	311	-5.3 ± 0.2	347	2.3 ± 0.0
204	1.8 ± 0.4	240	-1.2 ± 0.5	276	0.0 ± 0.0	312	n.s.	348	0.2 ± 0.2
205	-0.3 ± 0.0	241	4.2 ± 0.8	277	-0.5 ± 0.0	313	-3.2 ± 0.2	349	-2.3 ± 0.5
206	0.8 ± 0.0	242	-1.7 ± 0.2	278	-0.2 ± 0.2	314	-2.5 ± 0.0	350	3.7 ± 0.2
207	-0.8 ± 0.0	243	0.0 ± 0.0	279	-2.0 ± 0.0	315	1.0 ± 0.4	351	-0.2 ± 0.0
208	-0.8 ± 0.0	244	0.2 ± 0.2	280	4.5 ± 0.0	316	0.2 ± 0.5	352	0.0 ± 0.7
209	-0.8 ± 0.0	245	0.8 ± 0.2	281	-0.5 ± 0.0	317	-3.0 ± 0.0	353	0.0 ± 0.4
210	n.s.	246	-0.1 ± 0.1	282	-1.8 ± 0.2	318	n.s.	354	3.0 ± 0.2
211	0.8 ± 0.0	247	-0.3 ± 0.2	283	-0.1 ± 0.1	319	-3.0 ± 0.0	355	3.1 ± 0.0
212	-1.3 ± 0.0	248	-0.3 ± 0.2	284	-1.5 ± 0.0	320	-3.7 ± 0.2	356	2.1 ± 0.0
213	-1.3 ± 0.0	249	3.7 ± 0.2	285	1.2 ± 0.2	321	0.0 ± 0.2	357	-0.4 ± 0.0
214	-0.8 ± 0.0	250	2.5 ± 0.0	286	0.0 ± 0.0	322	0.0 ± 0.0	358	-0.4 ± 0.0
215	2.4 ± 0.2	251	-0.2 ± 0.2	287	0.0 ± 0.2	323	n.a.	359	-24.9 ± 0.7
216	0.8 ± 0.0	252	-1.5 ± 0.0	288	0.0 ± 0.2	324	-0.2 ± 0.0	360	0.1 ± 0.0
217	0.3 ± 0.0	253	0.5 ± 0.4	289	-25.0 ± 0.0	325	-0.3 ± 0.5	361	-0.4 ± 0.0
218	n.s.	254	5.0 ± 0.0	290	1.5 ± 0.7	326	2.8 ± 0.0	362	0.1 ± 0.0
219	-0.5 ± 0.0	255	-1.2 ± 0.2	291	-2.7 ± 0.2	327	-0.2 ± 0.0	363	0.6 ± 0.0
220	0.5 ± 0.0	256	-0.3 ± 0.2	292	-1.5 ± 0.0	328	3.3 ± 0.0	364	4.3 ± 0.2
221	3.0 ± 0.3	257	3.5 ± 0.0	293	-0.5 ± 0.0	329	-0.2 ± 0.0		
222	6.3 ± 0.0	258	-0.2 ± 0.2	294	-1.6 ± 0.4	330	-0.2 ± 0.4		
223	0.6 ± 0.2	259	1.3 ± 0.2	295	0.7 ± 0.2	331	6.3 ± 0.0		
224	2.6 ± 0.2	260	0.0 ± 0.0	296	0.3 ± 0.2	332	2.3 ± 0.0		
225	10.8 ± 0.2	261	1.3 ± 0.2	297	1.3 ± 0.2	333	-9.3 ± 0.5		
226	2.7 ± 0.2	262	1.2 ± 0.2	298	-1.5 ± 0.4	334	-0.2 ± 0.4		
227	-0.5 ± 0.0	263	1.0 ± 0.0	299	3.7 ± 0.2	335	0.2 ± 0.2		
228	-0.3 ± 0.2	264	0.0 ± 0.0	300	-2.0 ± 0.4	336	-0.2 ± 0.0		
229	n.s.	265	n.s.	301	6.3 ± 0.2	337	-0.3 ± 0.2		
230	6.5 ± 0.0	266	1.5 ± 0.0	302	1.2 ± 0.2	338	-0.5 ± 0.2		
231	-0.2 ± 0.2	267	4.3 ± 0.2	303	-1.2 ± 0.2	339	2.3 ± 0.0		

## 8.3. Crystallographic tables

	PKA J2 F5 (5N36)	PKA F37 (5N1G)	PKA J6 F39 (5N37)	PKA J7 F41 (5N1E)
<b>(A) Data collection and Processing</b>				
Space group	P 2 <sub>1</sub> 2 <sub>1</sub> 2 <sub>1</sub>	P 2 <sub>1</sub> 2 <sub>1</sub> 2 <sub>1</sub>	P 2 <sub>1</sub> 2 <sub>1</sub> 2 <sub>1</sub>	P 2 <sub>1</sub> 2 <sub>1</sub> 2 <sub>1</sub>
Unit cell parameters: a, b, c [Å]	58.6 72.6 109.1	51.5 71.3 98.0	58.8 72.6 108.3	58.6 72.5 108.4
α, β, γ [deg]	90.0 90.0 90.0	90.0 90.0 90.0	90.0 90.0 90.0	90.0 90.0 90.0
Matthews coefficient [Å <sup>3</sup> /Da]	2.9	2.2	2.9	2.8
Solvent content [%]	57	45	57	57
<b>(B) Diffraction data</b> <sup>[a]</sup>				
Resolution range [Å]	50-1.58 (1.67-1.58)	50-1.14 (1.21-1.14)	50-1.59 (1.69-1.59)	50-1.53 (1.62-1.53)
Unique reflections	64486 (10042)	128583 (21107)	63037 (9994)	70395 (11226)
R(I) <sub>sym</sub> [%] <sup>[b]</sup>	6.6 (52.3)	8.6 (39.4)	4.5 (53.5)	3.6 (54.7)
Completeness [%]	99.5 (97.2)	97.5 (91.0)	99.9 (99.5)	99.9 (99.7)
Redundancy (I/σ(I))	7.0 (7.1) 17.3 (6.1)	5.8 (5.4) 11.9 (3.6)	7.4 (7.2) 24.2 (3.8)	7.3 (7.4) 29.9 (3.7)
<b>(C) Refinement</b>				
Resolution range [Å]	45.60-1.58	48.98-1.14	45.68-1.59	45.56-1.53
Reflections used in refinement (work/free)	61261 / 3225	122153 / 6430	59885 / 3152	66875 / 3520
Final R value for all reflections (work/free) [%]	14.9 / 18.6	12.8 / 14.1	14.2 / 16.8	14.8 / 17.4
Protein residues	351	340	351	350
PKI-residues	14	-	13	13
Inhibitor atoms	10	33	34 / 6	31
Water molecules	238	363	276	262
<b>RMSD from ideality:</b>				
Bond length [Å]	0.012	0.010	0.011	0.011
Bond angles [deg]	1.08	1.20	1.12	1.06
<b>Ramachandran plot</b> <sup>[c]</sup> :				
Residues in most favoured regions [%]	92.2	92.4	91.9	93.4
Residues in additionally allowed regions [%]	7.8	7.6	7.8	6.3
Residues in generously allowed regions [%]	0	0	0	0.3
Residues in disallowed regions [%]	0	0	0.3	0
<b>Mean B factors [Å<sup>2</sup>]:</b>				
Protein non-hydrogen atoms	28.6	12.4	29.9	30.3
PKI atoms	33.0	-	30.5	31.3
Inhibitor	46.7	24.6	29.3 / 44.5	44.9
Water molecules	36.6	21.5	36.3	36.9

**[a]** Statistics for the highest-resolution shell are shown in parenthesis. **[b]**  $R(I)_{\text{sym}} = [\sum_h \sum_i |I_i(h) - \langle I(h) \rangle|] / [\sum_h \sum_i I_i(h)] \times 100$ , in which  $\langle I(h) \rangle$  is the mean of the  $I(h)$  observation of reflection  $h$ . **[c]** Statistics from PROCHECK <sup>74</sup>.



	PKA J14 F63 (5N1D)	PKA F74 (5N33)	PKA F83 (5N1O)	PKA J19 F112 (5N39)
<b>(A) Data collection and Processing</b>				
Space group	P 2 <sub>1</sub> 2 <sub>1</sub> 2 <sub>1</sub>	P 2 <sub>1</sub> 2 <sub>1</sub> 2 <sub>1</sub>	P 2 <sub>1</sub> 2 <sub>1</sub> 2 <sub>1</sub>	P 2 <sub>1</sub> 2 <sub>1</sub> 2 <sub>1</sub>
Unit cell parameters: a, b, c [Å]	58.6 73.5 108.7	58.2 72.6 108.8	59.1 71.9 108.9	58.3 72.4 108.7
α, β, γ [deg]	90.0 90.0 90.0	90.0 90.0 90.0	90.0 90.0 90.0	90.0 90.0 90.0
Matthews coefficient [Å <sup>3</sup> /Da]	2.9	2.8	2.9	2.8
Solvent content [%]	57	57	57	56
<b>(B) Diffraction data <sup>[a]</sup></b>				
Resolution range [Å]	50-1.61 (1.71-1.61)	50-1.43 (1.52-1.43)	50-1.80 (1.90-1.80)	50-1.45 (1.54-1.45)
Unique reflections	61272 (9718)	84316 (12943)	43882 (6860)	82204 (13122)
R(I) <sub>sym</sub> [%] <sup>[b]</sup>	6.3 (54.3)	6.6 (52.6)	4.9 (51.8)	3.5 (51.3)
Completeness [%]	99.4 (98.5)	99.2 (95.3)	99.6 (97.9)	99.9 (99.8)
Redundancy (I/σ(I))	4.8 (4.6) 17.2 (3.0)	6.3 (6.2) 14.9 (2.6)	7.2 (7.3) 23.0 (3.6)	6.7 (6.7) 27.2 (3.5)
<b>(C) Refinement</b>				
Resolution range [Å]	45.82-1.61	41.91-1.43	45.65-1.80	43.45-1.45
Reflections used in refinement (work/free)	58208 / 3064	80100 / 4216	41687 / 2195	78093 / 4111
Final R value for all reflections (work/free) [%]	15.6 / 18.6	15.0 / 17.4	17.1 / 19.1	14.5 / 16.9
Protein residues	353	351	340	351
PKI-residues	19	13	14	13
Inhibitor atoms	22	17	21	31
Water molecules	392	323	194	227
<b>RMSD from ideality:</b>				
Bond length [Å]	0.017	0.008	0.015	0.014
Bond angles [deg]	1.48	1.00	1.29	1.24
<b>Ramachandran plot <sup>[c]</sup>:</b>				
Residues in most favoured regions [%]	93.3	92.8	92.3	92.5
Residues in additionally allowed regions [%]	6.7	7.2	7.7	7.2
Residues in generously allowed regions [%]	0	0	0	0.3
Residues in disallowed regions [%]	0	0	0	0
<b>Mean B factors [Å<sup>2</sup>]:</b>				
Protein non-hydrogen atoms	23.7	24.5	38.7	29.9
PKI atoms	21.5	29.2	41.45	32.0
Inhibitor	27.8	20.1	37.8	48.8
Water molecules	32.4	33.7	40.3	33.5

	<b>PKA J20 F114 (5N7P)</b>	<b>PKA J26 F171 (5N3A)</b>	<b>PKA J28 F189 (5N3B)</b>	<b>PKA J29 F205 (5N3C)</b>
<b>(A) Data collection and Processing</b>				
Space group	P 2 <sub>1</sub> 2 <sub>1</sub> 2 <sub>1</sub>	P 2 <sub>1</sub> 2 <sub>1</sub> 2 <sub>1</sub>	P 2 <sub>1</sub> 2 <sub>1</sub> 2 <sub>1</sub>	P 2 <sub>1</sub> 2 <sub>1</sub> 2 <sub>1</sub>
Unit cell parameters: a, b, c [Å]	58.5 72.7 108.7	58.3 72.4 108.4	58.9 108.8 72.7	58.5 72.7 108.6
α, β, γ [deg]	90.0 90.0 90.0	90.0 90.0 90.0	90.0 90.0 90.0	90.0 90.0 90.0
Matthews coefficient [Å <sup>3</sup> /Da]	2.9	2.8	2.9	2.8
Solvent content [%]	57	56	57	57
<b>(B) Diffraction data <sup>[a]</sup></b>				
Resolution range [Å]	50-1.50 (1.59-1.50)	50-1.40 (1.49-1.40)	50-1.64 (1.74-1.64)	50-1.77 (1.88-1.77)
Unique reflections	73338 (11631)	90107 (14385)	57234 (8697)	45623 (7178)
R(I) <sub>sym</sub> [%] <sup>[b]</sup>	3.3 (59.2)	3.3 (52.2)	6.3 (57.4)	10.9 (59.5)
Completeness [%]	98.0 (97.4)	99.9 (99.8)	98.4 (96.8)	99.8 (98.9)
Redundancy (I/σ(I))	3.6 (3.6) 20.8 (2.1)	6.6 (6.4) 28.3 (3.4)	6.7 (6.8) 18.3 (3.3)	6.6 (6.4) 13.2 (3.1)
<b>(C) Refinement</b>				
Resolution range [Å]	45.59-1.50	39.71-1.40	45.74-1.64	45.59-1.77
Reflections used in refinement (work/free)	69671 / 3667	85601 / 4506	54372 / 2862	43341 / 2282
Final R value for all reflections (work/free) [%]	16.0 / 18.6	16.1 / 18.4	16.7 / 19.0	17.8 / 19.6
Protein residues	353	353	346	352
PKI-residues	13	13	13	13
Inhibitor atoms	24	10	20	15
Water molecules	214	255	222	235
<b>RMSD from ideality:</b>				
Bond length [Å]	0.006	0.007	0.009	0.007
Bond angles [deg]	0.78	0.91	0.96	0.89
<b>Ramachandran plot <sup>[c]</sup>:</b>				
Residues in most favoured regions [%]	92.3	92.6	92.4	92.2
Residues in additionally allowed regions [%]	7.7	7.4	7.6	7.8
Residues in generously allowed regions [%]	0	0	0	0
Residues in disallowed regions [%]	0	0	0	0
<b>Mean B factors [Å<sup>2</sup>]:</b>				
Protein non-hydrogen atoms	33.1	27.5	30.6	25.8
PKI atoms	36.4	28.1	35.3	31.3
Inhibitor	31.2	45.2	33.0	33.1
Water molecules	35.3	34.2	33.7	29.3

	<b>PKA J32 F211 (5N1H)</b>	<b>PKA F222 (5N1F)</b>	<b>PKA J33 F216 (5N3D)</b>	<b>PKA J41 F266 (5N3E)</b>
<b>(A) Data collection and Processing</b>				
Space group	P 2 <sub>1</sub> 2 <sub>1</sub> 2 <sub>1</sub>	P 2 <sub>1</sub> 2 <sub>1</sub> 2 <sub>1</sub>	P 2 <sub>1</sub> 2 <sub>1</sub> 2 <sub>1</sub>	P 2 <sub>1</sub> 2 <sub>1</sub> 2 <sub>1</sub>
Unit cell parameters: a, b, c [Å]	51.8 71.7 97.9	51.6 71.6 97.9	58.4 72.4 108.4	58.6 72.3 108.6
α, β, γ [deg]	90.0 90.0 90.0	90.0 90.0 90.0	90.0 90.0 90.0	90.0 90.0 90.0
Matthews coefficient [Å <sup>3</sup> /Da]	2.2	2.2	2.8	2.8
Solvent content [%]	45	45	56	57
<b>(B) Diffraction data <sup>[a]</sup></b>				
Resolution range [Å]	50-1.18 (1.25-1.18)	50-1.12 (1.19-1.12)	50-1.77 (1.88-1.77)	50-1.53 (1.62-1.53)
Unique reflections	119561 (18940)	137845 (20526)	44971 (7147)	69062 (10849)
R(I) <sub>sym</sub> [%] <sup>[b]</sup>	5.2 (55.3)	8.8 (58.4)	5.9 (53.4)	4.5 (64.7)
Completeness [%]	99.3 (98.5)	98.5 (91.7)	99.4 (99.0)	98.0 (96.3)
Redundancy (I/σ(I))	5.9 (5.9) 17.7 (3.4)	5.6 (4.4) 10.7 (2.3)	6.6 (6.8) 22.8 (3.7)	7.1 (7.3) 23.2 (3.5)
<b>(C) Refinement</b>				
Resolution range [Å]	45.77-1.18	48.97-1.12	45.46-1.77	45.54-1.53
Reflections used in refinement (work/free)	113583 / 5978	130952 / 6893	42722 / 2249	65608 / 3454
Final R value for all reflections (work/free) [%]	13.5 / 15.8	13.7 / 15.6	16.8 / 19.3	15.5 / 18.5
Protein residues	340	340	350	352
PKI-residues	-	-	13	14
Inhibitor atoms	48	30	21	21
Water molecules	372	359	223	241
<b>RMSD from ideality:</b>				
Bond length [Å]	0.009	0.010	0.007	0.006
Bond angles [deg]	1.13	1.17	0.87	0.82
<b>Ramachandran plot <sup>[c]</sup>:</b>				
Residues in most favoured regions [%]	93.1	93.1	93.4	92.6
Residues in additionally allowed regions [%]	6.9	6.9	6.6	7.1
Residues in generously allowed regions [%]	0	0	0	0.3
Residues in disallowed regions [%]	0	0	0	0
<b>Mean B factors [Å<sup>2</sup>]:</b>				
Protein non-hydrogen atoms	16.1	15.1	28.7	31.7
PKI atoms	-	-	32.2	34.0
Inhibitor	30.0	27.6	39.6	31.8
Water molecules	25.0	24.0	33.6	36.4

	PKA J42 F267 (5N1L)	PKA J45 F274 (5N1K)	PKA J46 F285 (5N3F)	PKA J47 F286 (5N1M)
<b>(A) Data collection and Processing</b>				
Space group	P 2 <sub>1</sub> 2 <sub>1</sub> 2 <sub>1</sub>	P 2 <sub>1</sub> 2 <sub>1</sub> 2 <sub>1</sub>	P 2 <sub>1</sub> 2 <sub>1</sub> 2 <sub>1</sub>	P 2 <sub>1</sub> 2 <sub>1</sub> 2 <sub>1</sub>
Unit cell parameters: a, b, c [Å]	58.3 72.4 108.7	58.2 71.5 107.6	58.8 72.2 108.8	58.4 72.6 108.7
α, β, γ [deg]	90.0 90.0 90.0	90.0 90.0 90.0	90.0 90.0 90.0	90.0 90.0 90.0
Matthews coefficient [Å <sup>3</sup> /Da]	2.8	2.8	2.8	2.8
Solvent content [%]	56	55	57	57
<b>(B) Diffraction data <sup>[a]</sup></b>				
Resolution range [Å]	50-1.49 (1.58-1.49)	50-1.80 (1.91-1.80)	50-1.68 (1.79-1.68)	50-1.44 (1.52-1.44)
Unique reflections	75725 (12049)	42190 (6642)	53011 (8418)	84440 (13073)
R(I) <sub>sym</sub> [%] <sup>[b]</sup>	4.4 (56.6)	7.2 (54.5)	4.7 (54.3)	6.3 (53.4)
Completeness [%]	99.9 (99.5)	99.2 (98.3)	99.9 (99.7)	99.3 (96.4)
Redundancy (I/σ(I))	6.6 (6.7) 21.7 (3.3)	5.3 (5.3) 14.6 (3.0)	6.6 (6.4) 25.0 (3.8)	6.4 (6.5) 12.0 (2.4)
<b>(C) Refinement</b>				
Resolution range [Å]	43.41-1.49	45.14-1.80	45.580-1.68	45.50-1.44
Reflections used in refinement (work/free)	71938 / 3787	40080 / 2110	50360 / 2651	80218 / 4222
Final R value for all reflections (work/free) [%]	14.3 / 17.5	17.5 / 20.7	17.2 / 19.3	15.2 / 17.0
Protein residues	351	344	321	351
PKI-residues	13	13	12	14
Inhibitor atoms	28	11 / 7 / 7	12 / 12	23
Water molecules	250	176	240	259
<b>RMSD from ideality:</b>				
Bond length [Å]	0.009	0.016	0.017	0.005
Bond angles [deg]	1.01	1.34	1.36	0.76
<b>Ramachandran plot <sup>[c]</sup>:</b>				
Residues in most favoured regions [%]	93.5	92.6	93.4	92.5
Residues in additionally allowed regions [%]	6.5	7.4	6.6	7.1
Residues in generously allowed regions [%]	0	0	0	0.3
Residues in disallowed regions [%]	0	0	0	0
<b>Mean B factors [Å<sup>2</sup>]:</b>				
Protein non-hydrogen atoms	27.6	32.0	30.2	28.9
PKI atoms	30.5	31.8	36.5	31.42
Inhibitor	27.3	38.2 / 42.8 / 44.7	43.1 / 42.6	47.0
Water molecules	32.9	37.5	36.1	35.0

	PKA F290 (5N32)	PKA F335 (5MHI)	PKA F342 (5N7U)	PKA F357 (5N1N)
<b>(A) Data collection and Processing</b>				
Space group	P 2 <sub>1</sub> 2 <sub>1</sub> 2 <sub>1</sub>	P 2 <sub>1</sub> 2 <sub>1</sub> 2 <sub>1</sub>	P 2 <sub>1</sub> 2 <sub>1</sub> 2 <sub>1</sub>	P 2 <sub>1</sub> 2 <sub>1</sub> 2 <sub>1</sub>
Unit cell parameters: a, b, c [Å]	58.7 72.3 108.5	58.3 72.6 108.6	58.4 72.6 108.7	58.3 72.5 108.5
α, β, γ [deg]	90.0 90.0 90.0	90.0 90.0 90.0	90.0 90.0 90.0	90.0 90.0 90.0
Matthews coefficient [Å <sup>3</sup> /Da]	2.8	2.8	2.8	2.8
Solvent content [%]	57	56	57	56
<b>(B) Diffraction data <sup>[a]</sup></b>				
Resolution range [Å]	50-1.83 (1.94-1.83)	50-1.49 (1.58-1.49)	50-1.37 (1.45-1.37)	50-1.41 (1.49-1.41)
Unique reflections	41140 (6515)	76141 (12124)	95068 (15377)	89447 (13809)
R(I) <sub>sym</sub> [%] <sup>[b]</sup>	4.7 (52.6)	3.8 (49.6)	2.3 (59.9)	5.9 (53.2)
Completeness [%]	99.8 (99.4)	99.8 (99.2)	97.4 (98.5)	99.2 (95.7)
Redundancy (I/σ(I))	6.5 (6.3) 27.3 (3.8)	7.3 (7.5) 26.1 (3.7)	3.7 (3.6) 27.6 (2.3)	6.4 (6.3) 16.1 (2.7)
<b>(C) Refinement</b>				
Resolution range [Å]	45.55-1.83	45.46-1.49	43.52-1.37	43.45-1.41
Reflections used in refinement (work/free)	39083 / 2057	72334 / 3807	90315 / 4753	84974 / 4473
Final R value for all reflections (work/free) [%]	18.8 / 21.4	14.7 / 16.5	16.1 / 17.7	15.3 / 17.9
Protein residues	348	353	353	352
PKI-residues	16	12	13	13
Inhibitor atoms	22 / 22	18	30	14
Water molecules	157	303	321	211
<b>RMSD from ideality:</b>				
Bond length [Å]	0.004	0.008	0.010	0.016
Bond angles [deg]	0.69	1.00	1.05	1.36
<b>Ramachandran plot <sup>[c]</sup>:</b>				
Residues in most favoured regions [%]	91.5	92.5	92.9	92.2
Residues in additionally allowed regions [%]	7.8	7.5	6.8	7.8
Residues in generously allowed regions [%]	0.3	0	0.3	0
Residues in disallowed regions [%]	0.3	0	0	0
<b>Mean B factors [Å<sup>2</sup>]:</b>				
Protein non-hydrogen atoms	36.2	27.6	28.4	28.6
PKI atoms	43.7	21.5	30.3	29.4
Inhibitor	78.4 / 74.9	48.6	45.1	41.5
Water molecules	37.1	35.7	35.8	31.5

	<b>PKA J56 (5N3G)</b>	<b>PKA J61 (5N3H)</b>	<b>PKA J62 (5N3I)</b>	<b>PKA J65 (5N3J)</b>
<b>(A) Data collection and Processing</b>				
Space group	P 2 <sub>1</sub> 2 <sub>1</sub> 2 <sub>1</sub>	P 2 <sub>1</sub> 2 <sub>1</sub> 2 <sub>1</sub>	P 2 <sub>1</sub> 2 <sub>1</sub> 2 <sub>1</sub>	P 2 <sub>1</sub> 2 <sub>1</sub> 2 <sub>1</sub>
Unit cell parameters: a, b, c [Å]	51.2 71.9 97.7	51.3 72.1 97.4	51.4 71.6 97.7	51.7 71.5 97.6
α, β, γ [deg]	90.0 90.0 90.0	90.0 90.0 90.0	90.0 90.0 90.0	90.0 90.0 90.0
Matthews coefficient [Å <sup>3</sup> /Da]	2.2	2.2	2.2	2.2
Solvent content [%]	45	45	45	45
<b>(B) Diffraction data <sup>[a]</sup></b>				
Resolution range [Å]	50-1.16 (1.23-1.16)	50-1.36 (1.44-1.36)	50-1.14 (1.21-1.14)	50-1.12 (1.19-1.12)
Unique reflections	124372 (19767)	77658 (12245)	129653 (20307)	138256 (22096)
R(I) <sub>sym</sub> [%] <sup>[b]</sup>	5.9 (56.6)	7.0 (60.6)	7.0 (56.1)	5.4 (57.2)
Completeness [%]	99.2 (98.7)	99.1 (98.0)	98.1 (96.0)	99.2 (99.0)
Redundancy (I/σ(I))	5.9 (5.7) 15.1 (2.8)	5.5 (5.3) 13.4 (2.4)	5.9 (5.7) 13.4 (2.9)	5.8 (5.6) 16.8 (3.0)
<b>(C) Refinement</b>				
Resolution range [Å]	45.37-1.16	48.71-1.36	48.85-1.14	45.66-1.12
Reflections used in refinement (work/free)	118153 / 6219	73775 / 3883	123170 / 6483	131343 / 6913
Final R value for all reflections (work/free) [%]	13.7 / 15.7	14.4 / 17.4	13.3 / 15.1	13.2 / 14.8
Protein residues	340	340	340	340
PKI-residues	-	-	-	-
Inhibitor atoms	19 / 19	15	27	16
Water molecules	364	302	395	367
<b>RMSD from ideality:</b>				
Bond length [Å]	0.011	0.007	0.010	0.010
Bond angles [deg]	1.17	0.92	1.12	1.11
<b>Ramachandran plot <sup>[c]</sup>:</b>				
Residues in most favoured regions [%]	93.4	92.4	91.4	91.8
Residues in additionally allowed regions [%]	6.6	7.6	8.6	8.2
Residues in generously allowed regions [%]	0	0	0	0
Residues in disallowed regions [%]	0	0	0	0
<b>Mean B factors [Å<sup>2</sup>]:</b>				
Protein non-hydrogen atoms	15.0	18.0	13.6	14.3
PKI atoms	-	-	-	-
Inhibitor	30.0 / 54.1	21.1	18.0	12.8
Water molecules	24.7	28.0	23.3	24.9

	PKA J72 (5N3K)	PKA J74 (5N3L)	PKA J77 (5N3M)	PKA J81 (5N3N)
<b>(A) Data collection and Processing</b>				
Space group	P 2 <sub>1</sub> 2 <sub>1</sub> 2 <sub>1</sub>	P 2 <sub>1</sub> 2 <sub>1</sub> 2 <sub>1</sub>	P 2 <sub>1</sub> 2 <sub>1</sub> 2 <sub>1</sub>	P 2 <sub>1</sub> 2 <sub>1</sub> 2 <sub>1</sub>
Unit cell parameters: a, b, c [Å]	51.4 72.1 97.5	52.1 71.2 97.2	52.0 71.0 97.6	51.2 72.0 97.7
α, β, γ [deg]	90.0 90.0 90.0	90.0 90.0 90.0	90.0 90.0 90.0	90.0 90.0 90.0
Matthews coefficient [Å <sup>3</sup> /Da]	2.2	2.2	2.2	2.2
Solvent content [%]	45	45	45	45
<b>(B) Diffraction data <sup>[a]</sup></b>				
Resolution range [Å]	50-1.33 (1.41-1.33)	50-1.38 (1.46-1.38)	50-1.23 (1.30-1.23)	50-1.22 (1.30-1.22)
Unique reflections	82006 (12994)	74698 (11766)	105001 (16697)	106846 (17018)
R(I) <sub>sym</sub> [%] <sup>[b]</sup>	3.8 (53.3)	10.4 (58.2)	5.2 (54.9)	4.7 (54.1)
Completeness [%]	98.3 (97.4)	99.3 (98.2)	99.5 (98.9)	99.9 (99.6)
Redundancy (I/σ(I))	5.9 (6.0) 22.6 (2.9)	5.7 (5.8) 12.7 (4.4)	5.8 (5.7) 17.6 (2.8)	13.0 (12.8) 32.8 (5.5)
<b>(C) Refinement</b>				
Resolution range [Å]	48.73-1.33	48.59-1.38	48.78-1.23	48.83-1.22
Reflections used in refinement (work/free)	77901 / 4100	70963 / 3735	99751 / 5250	101503 / 5343
Final R value for all reflections (work/free) [%]	14.5 / 17.2	13.0 / 16.0	13.9 / 16.4	13.5 / 15.3
Protein residues	340	340	340	340
PKI-residues	-	-	-	-
Inhibitor atoms	6	21	54	37
Water molecules	279	347	320	354
<b>RMSD from ideality:</b>				
Bond length [Å]	0.010	0.011	0.010	0.011
Bond angles [deg]	1.11	1.19	1.16	1.20
<b>Ramachandran plot <sup>[c]</sup>:</b>				
Residues in most favoured regions [%]	93.1	93.1	92.4	91.8
Residues in additionally allowed regions [%]	6.9	6.6	7.2	8.2
Residues in generously allowed regions [%]	0	0.3	0.3	0
Residues in disallowed regions [%]	0	0	0	0
<b>Mean B factors [Å<sup>2</sup>]:</b>				
Protein non-hydrogen atoms	21.6	13.2	17.0	13.3
PKI atoms	-	-	-	-
Inhibitor	24.9	11.1	19.8	20.3
Water molecules	29.7	24.7	26.4	24.9

	PKA J83 (5N3O)	PKA J84 (5N3P)	PKA J85 (5N3Q)	PKA J87 (5N3R)
<b>(A) Data collection and Processing</b>				
Space group	P 2 <sub>1</sub> 2 <sub>1</sub> 2 <sub>1</sub>	P 2 <sub>1</sub> 2 <sub>1</sub> 2 <sub>1</sub>	P 2 <sub>1</sub> 2 <sub>1</sub> 2 <sub>1</sub>	P 2 <sub>1</sub> 2 <sub>1</sub> 2 <sub>1</sub>
Unit cell parameters: a, b, c [Å]	51.5 72.3 97.3	51.8 71.7 97.7	51.6 72.0 97.6	51.4 71.3 97.9
α, β, γ [deg]	90.0 90.0 90.0	90.0 90.0 90.0	90.0 90.0 90.0	90.0 90.0 90.0
Matthews coefficient [Å <sup>3</sup> /Da]	2.2	2.2	2.2	2.2
Solvent content [%]	45	45	45	44
<b>(B) Diffraction data <sup>[a]</sup></b>				
Resolution range [Å]	50-1.32 (1.40-1.32)	50-1.58 (1.68-1.58)	50-1.31 (1.39-1.31)	50-1.36 (1.45-1.36)
Unique reflections	85946 (13641)	50422 (8033)	88063 (14042)	76370 (11569)
R(I) <sub>sym</sub> [%] <sup>[b]</sup>	9.6 (54.2)	11.2 (56.3)	7.6 (53.2)	8.5 (55.9)
Completeness [%]	99.7 (99.2)	99.6 (99.4)	99.9 (99.5)	98.7 (93.9)
Redundancy (I/σ(I))	6.2 (6.3) 13.2 (4.1)	6.3 (6.5) 11.9 (3.4)	6.5 (6.4) 17.4 (5.1)	5.6 (5.8) 16.4 (3.1)
<b>(C) Refinement</b>				
Resolution range [Å]	36.14-1.32	45.74-1.58	40.40-1.31	45.50-1.36
Reflections used in refinement (work/free)	81648 / 4298	47900 / 2522	83658 / 4404	72547 / 3819
Final R value for all reflections (work/free) [%]	13.4 / 15.8	15.8 / 18.1	13.5 / 15.5	15.9 / 19.3
Protein residues	338	339	339	339
PKI-residues	-	-	-	-
Inhibitor atoms	20 / 20 / 20	17	18 / 18	23
Water molecules	393	315	387	304
<b>RMSD from ideality:</b>				
Bond length [Å]	0.008	0.007	0.009	0.006
Bond angles [deg]	1.05	0.93	1.05	0.89
<b>Ramachandran plot <sup>[c]</sup>:</b>				
Residues in most favoured regions [%]	93.4	92.1	92.4	92.4
Residues in additionally allowed regions [%]	6.6	7.6	7.6	7.3
Residues in generously allowed regions [%]	0	0.3	0	0.3
Residues in disallowed regions [%]	0	0	0	0
<b>Mean B factors [Å<sup>2</sup>]:</b>				
Protein non-hydrogen atoms	11.5	15.8	13.6	14.0
PKI atoms	-	-	-	-
Inhibitor	17.3 / 11.8 / 20.6	12.5	12.6 / 16.2	21.0
Water molecules	22.37	25.3	24.2	22.8



	<b>PKA J89 (5N3S)</b>	<b>PKA J94 (5N3T)</b>
<b>(A) Data collection and Processing</b>		
Space group	P 2 <sub>1</sub> 2 <sub>1</sub> 2 <sub>1</sub>	P 2 <sub>1</sub> 2 <sub>1</sub> 2 <sub>1</sub>
Unit cell parameters: a, b, c [Å]	51.7 71.8 97.4	51.5 97.6 71.6
α, β, γ [deg]	90.0 90.0 90.0	90.0 90.0 90.0
Matthews coefficient [Å <sup>3</sup> /Da]	2.2	2.2
Solvent content [%]	45	45
<b>(B) Diffraction data <sup>[a]</sup></b>		
Resolution range [Å]	50-1.14 (1.21-1.14)	50-1.21 (1.28-1.21)
Unique reflections	131934 (20912)	108703 (17116)
R(I) <sub>sym</sub> [%] <sup>[b]</sup>	5.7 (56.6)	5.4 (56.3)
Completeness [%]	99.6 (98.6)	98.1 (96.5)
Redundancy (I/σ(I))	5.8 (5.6) 16.7 (3.5)	5.9 (6.0) 18.4 (3.7)
<b>(C) Refinement</b>		
Resolution range [Å]	48.69-1.14	45.580-1.21
Reflections used in refinement (work/free)	125337 / 6597	103267 / 5436
Final R value for all reflections (work/free) [%]	12.8 / 14.8	13.9 / 15.7
Protein residues	340	340
PKI-residues	-	-
Inhibitor atoms	34	14 / 14
Water molecules	383	306
<b>RMSD from ideality:</b>		
Bond length [Å]	0.010	0.008
Bond angles [deg]	1.14	1.02
<b>Ramachandran plot <sup>[c]</sup>:</b>		
Residues in most favoured regions [%]	92.4	92.8
Residues in additionally allowed regions [%]	7.3	7.2
Residues in generously allowed regions [%]	0.3	0
Residues in disallowed regions [%]	0	0
<b>Mean B factors [Å<sup>2</sup>]:</b>		
Protein non-hydrogen atoms	14.4	16.2
PKI atoms	-	-
Inhibitor	9.7	33.6 / 33.9
Water molecules	24.6	25.2

	Pim1 F3 (5N4Z)	Pim1 F72 (5N4N)	Pim1 F80 (5N50)	Pim1 F84 (5N4O)
<b>(A) Data collection and Processing</b>				
Space group	P6 <sub>5</sub>	P6 <sub>5</sub>	P6 <sub>5</sub>	P6 <sub>5</sub>
Unit cell parameters: a, b, c [Å]	98.6 98.6 80.9	98.5 98.5 80.3	98.3 98.3 80.5	97.9 97.9 80.3
α, β, γ [deg]	90.0 90.0 120.0	90.0 90.0 120.0	90.0 90.0 120.0	90.0 90.0 120.0
Matthews coefficient [Å <sup>3</sup> /Da]	3.2	3.2	3.2	3.1
Solvent content [%]	61	61	61	61
<b>(B) Diffraction data <sup>[a]</sup></b>				
Resolution range [Å]	50-2.26 (2.39-2.26)	50-2.09 (2.22-2.09)	50-1.92 (2.04-1.92)	50-2.22 (2.35-2.22)
Unique reflections	20497 (3298)	26155 (4178)	33834 (5425)	21715 (3450)
R(I) <sub>sym</sub> [%] <sup>[b]</sup>	7.8 (61.3)	5.3 (53.7)	8.6 (54.4)	6.4 (55.2)
Completeness [%]	97.1 (97.1)	99.8 (99.1)	99.9 (99.7)	99.7 (98.4)
Redundancy (I/σ(I))	3.2 (3.3) 13.4 (2.3)	8.5 (8.5) 27.5 (6.9)	8.0 (8.1) 15.0 (3.4)	8.6 (8.3) 23.1 (5.9)
<b>(C) Refinement</b>				
Resolution range [Å]	37.75-2.26	49.26-2.09	41.95-1.92	42.39-2.22
Reflections used in refinement (work/free)	19472 / 1025	24847 / 1308	32142 / 1692	20630 / 1085
Final R value for all reflections (work/free) [%]	17.9 / 20.8	15.9 / 18.8	15.8 / 18.0	18.2 / 19.6
Protein residues	272	273	273	271
PKI-residues	9	9	9	9
Inhibitor atoms	12	14	13	12
Water molecules	104	115	186	84
<b>RMSD from ideality:</b>				
Bond length [Å]	0.008	0.007	0.007	0.008
Bond angles [deg]	0.79	0.80	0.75	0.79
<b>Ramachandran plot <sup>[c]</sup>:</b>				
Residues in most favoured regions [%]	94.2	94.2	94.6	92.9
Residues in additionally allowed regions [%]	5.8	5.8	5.4	7.1
Residues in generously allowed regions [%]	0	0	0	0
Residues in disallowed regions [%]	0	0	0	0
<b>Mean B factors [Å<sup>2</sup>]:</b>				
Protein non-hydrogen atoms	40.6	43.7	39.6	51.4
PIMTIDE atoms	43.7	50.2	47.5	61.2
Inhibitor	39.1	51.0	48.1	51.7
Water molecules	38.9	43.8	43.9	47.9

	Pim1 F159 (5N4R)	Pim1 F167 (5N4U)	Pim1 F184 (5N4V)	Pim1 F200 (5NDT)
<b>(A) Data collection and Processing</b>				
Space group	P6 <sub>5</sub>	P6 <sub>5</sub>	P6 <sub>5</sub>	P6 <sub>5</sub>
Unit cell parameters: a, b, c [Å]	98.1 98.1 80.5	97.9 97.9 80.6	98.1 98.1 80.5	98.5 98.5 80.4
α, β, γ [deg]	90.0 90.0 120.0	90.0 90.0 120.0	90.0 90.0 120.0	90.0 90.0 120.0
Matthews coefficient [Å <sup>3</sup> /Da]	3.1	3.1	3.1	3.2
Solvent content [%]	61	61	61	61
<b>(B) Diffraction data <sup>[a]</sup></b>				
Resolution range [Å]	50-2.13 (2.26-2.13)	50-2.20 (2.33-2.20)	50-1.85 (1.96-1.85)	50-1.99 (2.11-1.99)
Unique reflections	24738 (3965)	22315 (3570)	37578 (5983)	30602 (4883)
R(I) <sub>sym</sub> [%] <sup>[b]</sup>	7.5 (54..2)	6.3 (54.1)	9.8 (52.4)	5.0 (56.1)
Completeness [%]	99.9 (99.6)	99.9 (99.5)	99.6 (98.5)	99.7 (99.4)
Redundancy (I/σ(I))	6.9 (7.0) 16.5 (3.5)	6.9 (7.0) 21.0 (3.9)	6.7 (6.8) 13.5 (2.7)	8.4 (8.4) 25.6 (5.5)
<b>(C) Refinement</b>				
Resolution range [Å]	49.06-2.13	42.39-2.20	41.87-1.85	42.66-1.99
Reflections used in refinement (work/free)	23501 / 1237	21199 / 1116	35699 / 1879	29071 / 1531
Final R value for all reflections (work/free) [%]	16.0 / 19.3	16.4 / 19.8	16.4 / 18.7	16.0 / 19.4
Protein residues	273	272	273	273
PKI-residues	9	9	9	9
Inhibitor atoms	12	16	17	12
Water molecules	132	91	152	122
<b>RMSD from ideality:</b>				
Bond length [Å]	0.007	0.011	0.007	0.006
Bond angles [deg]	0.79	0.92	0.76	0.76
<b>Ramachandran plot <sup>[c]</sup>:</b>				
Residues in most favoured regions [%]	93.0	91.3	93.4	94.6
Residues in additionally allowed regions [%]	7.0	8.7	6.6	5.0
Residues in generously allowed regions [%]	0	0	0	0.4
Residues in disallowed regions [%]	0	0	0	0
<b>Mean B factors [Å<sup>2</sup>]:</b>				
Protein non-hydrogen atoms	43.5	47.6	36.0	45.8
PIMTIDE atoms	50.9	54.8	46.2	58.0
Inhibitor	56.1	52.4	31.1	58.4
Water molecules	44.7	45.6	38.5	47.6

	Pim1 F222 (5MZL)	Pim1 F225 (5N4X)	Pim1 F230 (5N51)	Pim1 F301 (5N4Y)
<b>(A) Data collection and Processing</b>				
Space group	P6 <sub>5</sub>	P6 <sub>5</sub>	P6 <sub>5</sub>	P6 <sub>5</sub>
Unit cell parameters: a, b, c [Å]	97.9 97.9 80.2	98.0 98.0 80.9	98.0 98.0 80.3	98.3 98.3 80.7
α, β, γ [deg]	90.0 90.0 120.0	90.0 90.0 120.0	90.0 90.0 120.0	90.0 90.0 120.0
Matthews coefficient [Å <sup>3</sup> /Da]	3.1	3.1	3.1	3.2
Solvent content [%]	60	61	61	61
<b>(B) Diffraction data <sup>[a]</sup></b>				
Resolution range [Å]	50-1.96 (2.07-1.96)	50-2.20 (2.33-2.20)	50-2.12 (2.25-2.12)	50-2.56 (2.72-2.56)
Unique reflections	31579 (5033)	22535 (3603)	47470 (7565)	14330 (2300)
R(I) <sub>sym</sub> [%] <sup>[b]</sup>	4.6 (57.8)	9.9 (54.8)	7.3 (63.4)	8.8 (57.1)
Completeness [%]	99.6 (98.5)	99.9 (99.4)	96.8 (95.7)	99.8 (99.4)
Redundancy (I/σ(I))	6.2 (6.07) 24.4 (5.01)	7.0 (7.0) 13.8 (3.6)	2.7 (2.6) 11.9 (2.1)	6.9 (7.0) 20.2 (3.8)
<b>(C) Refinement</b>				
Resolution range [Å]	42.41-1.96	49.00-2.20	49.00-2.12	49.13-2.56
Reflections used in refinement (work/free)	29999 / 1578	21408 / 1127	45093 / 2377	13613 / 717
Final R value for all reflections (work/free) [%]	15.7 / 18.3	17.7 / 21.5	18.1 / 20.7	17.44 / 21.8
Protein residues	269	272	269	273
PKI-residues	8	8	8	8
Inhibitor atoms	30	11	20	14
Water molecules	120	107	107	56
<b>RMSD from ideality:</b>				
Bond length [Å]	0.003	0.008	0.008	0.007
Bond angles [deg]	0.59	0.83	0.77	0.83
<b>Ramachandran plot <sup>[c]</sup>:</b>				
Residues in most favoured regions [%]	93.3	93.7	91.6	91.7
Residues in additionally allowed regions [%]	6.7	5.9	8.0	8.3
Residues in generously allowed regions [%]	0	0.4	0.4	0
Residues in disallowed regions [%]	0	0	0	0
<b>Mean B factors [Å<sup>2</sup>]:</b>				
Protein non-hydrogen atoms	50.7	37.3	45.4	39.9
PIMTIDE atoms	56.7	53.4	55.4	44.3
Inhibitor	47.3	38.3	57.7	39.6
Water molecules	48.2	35.7	42.6	34.8

	<b>Pim1 F331 (5N52)</b>	<b>Pim1(5N5L) ZINC09314085</b>	<b>Pim1(5N5M) ZINC72154357</b>
<b>(A) Data collection and Processing</b>			
Space group	P6 <sub>5</sub>	P6 <sub>5</sub>	P6 <sub>5</sub>
Unit cell parameters: a, b, c [Å]	97.6 97.6 80.2	97.7 97.7 80.3	98.6 98.6 80.3
$\alpha$ , $\beta$ , $\gamma$ [deg]	90.0 90.0 120.0	90.0 90.0 120.0	90.0 90.0 120.0
Matthews coefficient [Å <sup>3</sup> /Da]	3.1	3.1	3.2
Solvent content [%]	60	60	61
<b>(B) Diffraction data <sup>[a]</sup></b>			
Resolution range [Å]	50-2.25 (2.39-2.25)	50-1.97 (2.09-1.97)	50-2.21 (2.35-2.21)
Unique reflections	20496 (3216)	30857 (4956)	22235 (3579)
R(I) <sub>sym</sub> [%] <sup>[b]</sup>	11.6 (52.7)	7.6 ( 57.0)	13.9 (57.3)
Completeness [%]	99.3 (97.1)	99.9 (99.4)	99.9 (99.8)
Redundancy (I/ $\sigma$ (I))	6.4 (6.1) 12.6 (5.1)	6.8 (6.6) 16.6 (3.2)	6.9 (6.9) 10.8 (3.2)
<b>(C) Refinement</b>			
Resolution range [Å]	48.80-2.25	48.84-1.97	49.30-2.21
Reflections used in refinement (work/free)	19471 / 1025	29314 / 1543	21123 / 1112
Final R value for all reflections (work/free) [%]	17.0 / 21.0	16.0 / 19.5	16.6 / 20.5
Protein residues	268	272	273
PKI-residues	7	9	9
Inhibitor atoms	15	13	26
Water molecules	84	166	135
<b>RMSD from ideality:</b>			
Bond length [Å]	0.008	0.007	0.008
Bond angles [deg]	0.81	0.77	0.76
<b>Ramachandran plot <sup>[c]</sup>:</b>			
Residues in most favoured regions [%]	92.8	93.3	94.2
Residues in additionally allowed regions [%]	7.2	6.7	5.8
Residues in generously allowed regions [%]	0	0	0
Residues in disallowed regions [%]	0	0	0
<b>Mean B factors [Å<sup>2</sup>]:</b>			
Protein non-hydrogen atoms	39.8	35.0	33.4
PIMTIDE atoms	46.7	41.6	42.0
Inhibitor	37.3	37.4	44.5
Water molecules	37.2	39.0	33.8

## 8.4. Binding mode dossiers

## PKA - J02 / F5 (PDB 5N36) – 1.58 Å

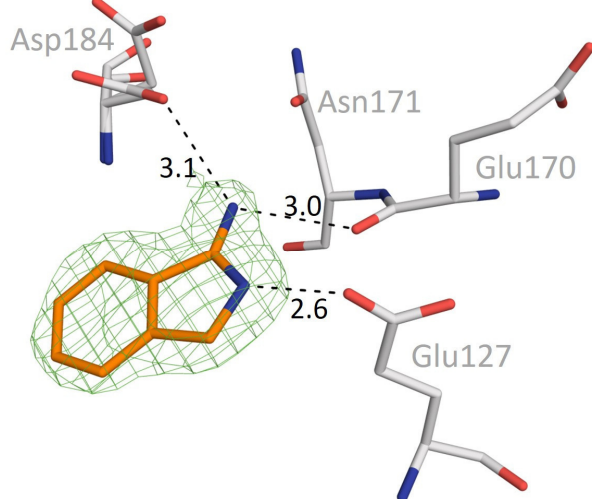


Figure 92 : Detailed-view of interaction pattern of fragment J02 with PKA. The green mesh represents the unbiased  $F_o-F_c$  electron density at  $3.0 \sigma$ .

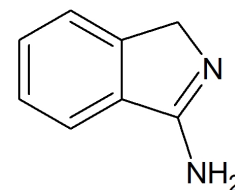


Figure 91: Chemical structure of fragment J02.

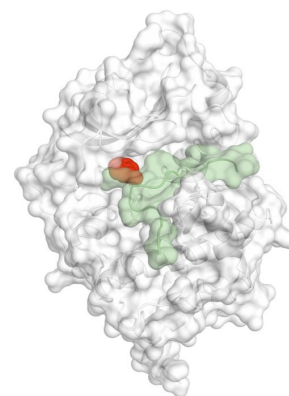


Figure 93: Fragment J02 is marked in red, PKI is marked in green.

## Binding keywords:

ATP-binding site, direct binding to Asp184, Glu127 and Glu170 interaction

## Detailed description of protein-ligand interaction:

The difference electron density ( $6.3 \sigma$ ) for fragment J02 is observed in the ATP-binding pocket close to the DFG motif. The fragment forms three direct interactions with the protein. As an H-bond donor the exocyclic nitrogen atom interacts with the carbonyl oxygen atom of the Glu170 backbone through a distance of  $3.0 \text{ \AA}$ . Additionally, the same nitrogen atom acts as an H-bond donor to form an H-bond to the carboxylate group of Asp184. The distance of one side chain orientation of Asp184 to the nitrogen atom of the fragment is  $3.1 \text{ \AA}$ . The refinement shows that 55% of this side chain is involved in this direct H-bond interaction. The endocyclic nitrogen atom also forms an H-bond as a donor in its protonated state to the carboxylate group of Glu127. The acceptor of this H-bond is at a distance of  $2.6 \text{ \AA}$  and therefore in very short distance for such an interaction. The benzene ring of J02 is pointing towards the hinge region without any direct interaction. The occupancy of the ligand refines to 100 %.

## PKA - F37 (PDB 5N1G) – 1.14 Å

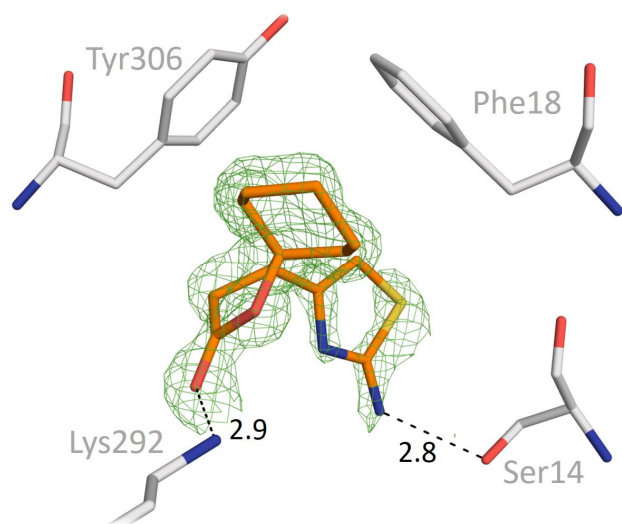


Figure 95: Detailed-view of interaction pattern of fragment F37 with PKA. The green mesh represents the unbiased  $F_o-F_c$  electron density at  $3.0 \sigma$ .

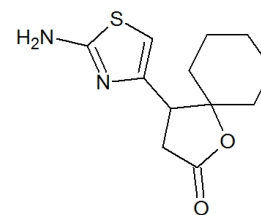


Figure 94: Chemical structure of fragment F37.

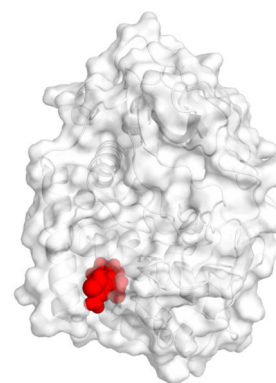


Figure 96: Overview of binding position of fragment F37 on PKA.

### Binding keywords:

Remote binding, direct interaction with Ser14 and Lys292

### Detailed description of protein-ligand interaction:

Fragment F37 binds in a pocket on the protein surface in proximity to the N-terminal  $\alpha$ -helix of PKA. The ligand could be completely assigned to the observed difference electron density ( $9.6 \sigma$ ). The point of view in Figure 95 shows the ligand seen from the inner of the protein so that the “bulk solvent” would be located behind the ligand if the crystal structure would correspond to the protein in solvent environment. Two polar protein-ligand interactions were observed in this complex. One H-bond is formed between the hydroxyl group of Ser14 and the exocyclic amino group attached to the thiazole ring of F37. The distance between both atoms is 2.8 Å. The thiazole ring is oriented towards the outside of the protein and shows more residual mobility in comparison to the cyclohexyl moiety, which is indicated by higher B-values ( $35.6 \text{ \AA}^2$  for the exocyclic nitrogen;  $17.4 \text{ \AA}^2$  for the carbon furthest away from the latter nitrogen). The second interaction partner of the protein is the carbonyl oxygen of the lactone ring. Here, the electron density is better defined, and the B-value of the oxygen atom is lower than those of the exocyclic amino group ( $18.1 \text{ \AA}^2$ ). The distance to the amino nitrogen of Lys292 is 2.9 Å, forming another H-bond between protein and ligand. The apolar cyclohexyl moiety is oriented towards a small pocket, which is mainly defined by apolar residues. Although the density of the ligand is clearly defined, no anomalous signal was obtained for the sulfur atom of the compound.

## PKA - J06 / F39 (PDB 5N37) – 1.59 Å

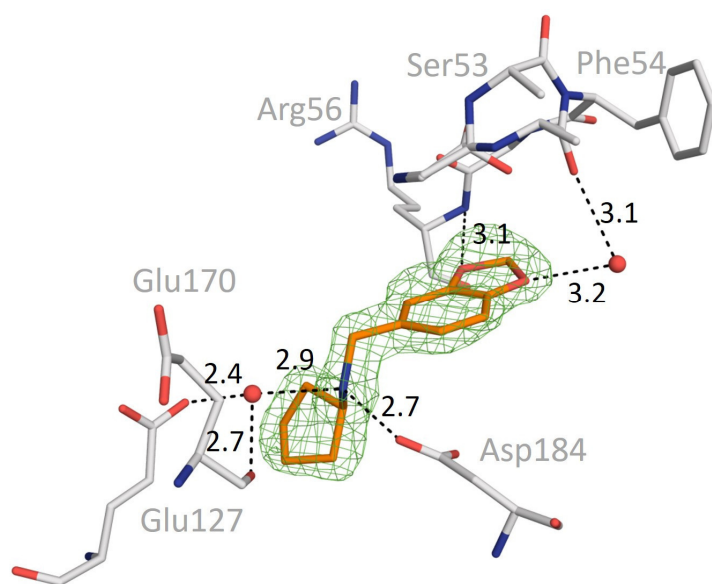


Figure 98: Detailed-view of interaction pattern of fragment J06 with PKA. The green mesh represents the unbiased Fo-Fc electron density at  $3.0 \sigma$ .

### Binding keywords:

G-loop region, direct interaction with Asp184, water bridge to Glu127 and Glu170

### Detailed description of protein-ligand interaction:

Fragment J06 is located close to the ATP-binding site. Although the difference electron density ( $8.5 \sigma$ ) is clearly defined, the occupancy refines to only 81%. The protonated amino group of this compound directly interacts via a salt bridge with the side chain of Asp184. A water molecule is positioned at a distance of 2.9 Å to the amino group, which accepts an H-bond from the ligand. This water molecule further interacts with the side chain of Glu127 and the backbone carbonyl oxygen of Glu170. The protonated amino group acts as a donor for both acceptors. With its benzo-dioxolane portion, J06 is the only fragment of this series that binds very close to the glycine-rich loop. One oxygen atom is at a distance of 3.1 Å to the amide nitrogen of Arg56, but the interaction geometry is not ideal for an H-bond. The second oxygen atom of J06 acts as an acceptor for a water molecule at a distance of 3.2 Å. This water molecule is also a donor for the carbonyl oxygen of Ser53 and consequently mediates a contact from ligand to the protein. As shown in Figure 98 the addressed serine is flexible and adopts two different orientations. The relevant orientation forming the water-mediated contact is slightly higher populated (51%).

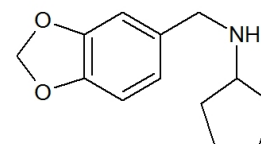


Figure 97: Chemical structure of fragment J06.

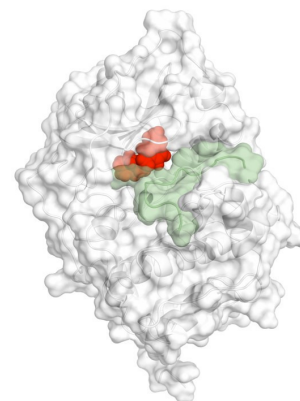


Figure 99: Fragment J06 is marked in red, PKI is marked in green.



## PKA - J06 / F39 (PDB 5N37) – 1.59 Å

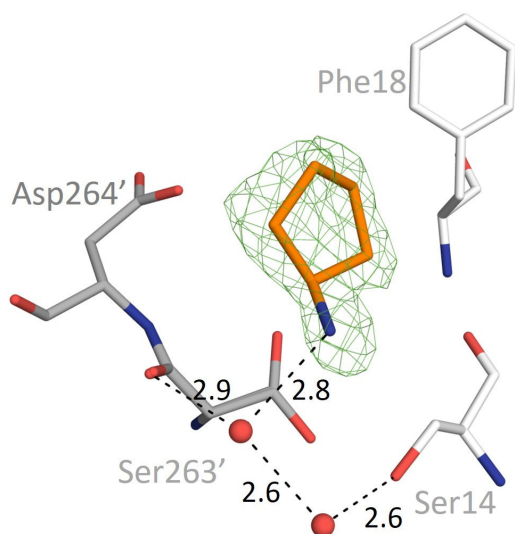


Figure 100: Detail-view of second interaction pattern of fragment J06 with PKA. The green mesh represents the unbiased  $F_o-F_c$  electron density at  $3.0 \sigma$ .

### Binding keywords:

Partly binding, Remote binding, between protein crystal mates

### Detailed description of protein-ligand interaction:

A second binding position of J06 was detected outside the ATP-binding pocket. As the electron density in this area, shown in Figure 100, is not equally well-defined as in the ATP site. The fragment is not entirely visible in the density, so only a part of the ligand could be assigned. The cyclopentyl moiety and the amino group are visible in the density. The amino group is  $2.8 \text{ \AA}$  apart from a nearby water molecule forming an H-bond interaction. This water molecule mediates a contact to Asp267' of a neighbouring symmetry-related PKA molecule, likely caused by the protein crystal packing. The surface area of this small fragment portion is buried to 54.9% by the one protein molecule and to 32.1% by the symmetry-related equivalent. Since the electron density of this fragment is not perfectly defined, the assigned part shows relatively high B-values (on average:  $44 \text{ \AA}^2$  in contrast to  $26 \text{ \AA}^2$  of the fragments bound to the ATP-binding pocket).

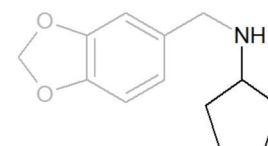


Figure 102: Chemical structure of fragment J06.

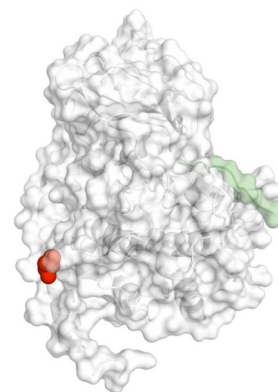


Figure 101: Fragment J06 is marked in red, PKI is marked in green.

## PKA - J07 / F41 (PDB 5N1E) – 1.53 Å

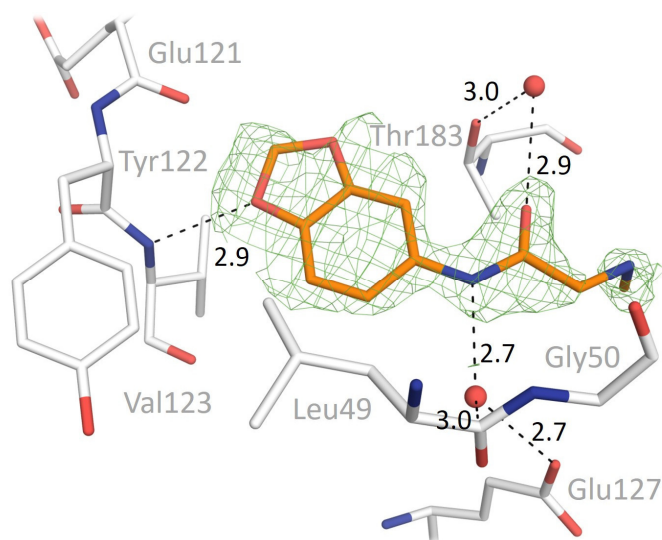


Figure 104: Detailed-view of interaction pattern of fragment J07 with PKA. The green mesh represents the unbiased  $F_o-F_c$  electron density at  $3.0 \sigma$ .

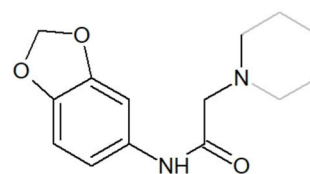


Figure 103: Chemical structure of fragment J07.

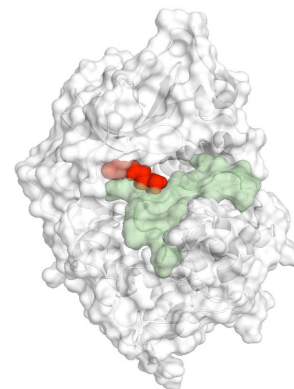


Figure 105: Fragment J07 is marked in red, PKI is marked in green.

### Binding keywords:

ATP-binding site, direct hinge interaction, water bridged interactions with Thr183 and Leu49

### Detailed description of protein-ligand interaction:

Most of the ligand fits in the observed difference electron density ( $9.9 \sigma$ ). The piperidine ring is only partly visible in the density so that only the nitrogen and an adjacent carbon atom could be assigned. The residual mobility in this region seems to be higher, which is also indicated by the B-values of the molecule. The B-value of the oxygen atom in the dioxolane ring,  $2.9 \text{ \AA}$  apart from the hinge region, is approx.  $38 \text{ \AA}^2$ . This oxygen atom shows the density maximum of the ligand. The assigned carbon atom of the piperidine ring shows the weakest density with a B-value of approx.  $55 \text{ \AA}^2$ . The fragment contains a peptide bond in its centre, which interacts in two directions with protein residues via water bridges. A water molecule is located at a distance of  $2.7 \text{ \AA}$  to the amide nitrogen. This water molecule acts as an H-bond acceptor for the nitrogen, but also as an H-bond donor addressing the backbone carbonyl oxygen of Leu49 and the carboxylate side chain of Glu127. On the other side of the peptide bond, the oxygen acts as an H-bond acceptor. Here, a water molecule mediates a contact to the carbonyl oxygen ( $2.9 \text{ \AA}$ ) and the hydroxy group of Thr183 ( $3.0 \text{ \AA}$ ). The fragment occupies this position by 93%.

## PKA - J14 / F63 (PDB 5N1D) – 1.61 Å

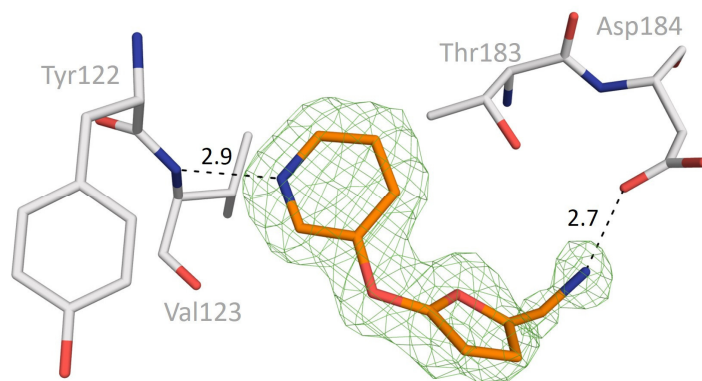


Figure 107: Detailed-view of interaction pattern of fragment J14 with PKA. The green mesh represents the unbiased  $F_o-F_c$  electron density at  $3.0 \sigma$ .

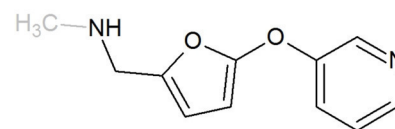


Figure 106: Chemical structure of fragment J14.

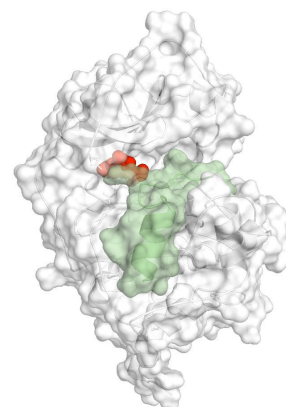


Figure 108: Fragment J14 is marked in red, PKI is marked in green.

### Binding keywords:

ATP-binding site, direct hinge interaction, direct DFG interaction

### Detailed description of protein-ligand interaction:

With the exception of the terminal methyl group attached to the secondary amino group, the difference electron density ( $8.7 \sigma$ ) of the entire fragment J14 is visible. The exocyclic nitrogen atom functions as an H-bond donor to the carboxylate of Asp184 of the DFG motif with a distance of  $2.7 \text{ \AA}$  to one oxygen atom. The pyridine-type nitrogen atom of the fragment is in H-bond contact to the backbone nitrogen atom of Val123 ( $2.9 \text{ \AA}$ ). The  $pK_a$  value for the protonated form of pyridine is approx. 5.2 and, therefore, should be deprotonated at the buffer conditions of pH of 6.9.<sup>97</sup> The oxygen substituent in meta position additionally decreases the  $pK_a$  value. The residual mobility of the bound compound increases from the pyridine ring via the furan ring to the secondary amino group. This is reflected by the respective B-values. The pyridine ring is located near the hinge region and has an average B-value of approx.  $16 \text{ \AA}^2$ . The furan ring is more mobile with an average B-value of approx.  $37 \text{ \AA}^2$ , whereas the secondary amino group has a B-value of  $41.2 \text{ \AA}^2$ . The concentration of the electron density ( $F_o-F_c$ ) in the respective regions underline this increasing mobility ( $4.5$  to  $3.4 \sigma$ ).

## PKA - F74 (PDB 5N33) – 1.43 Å

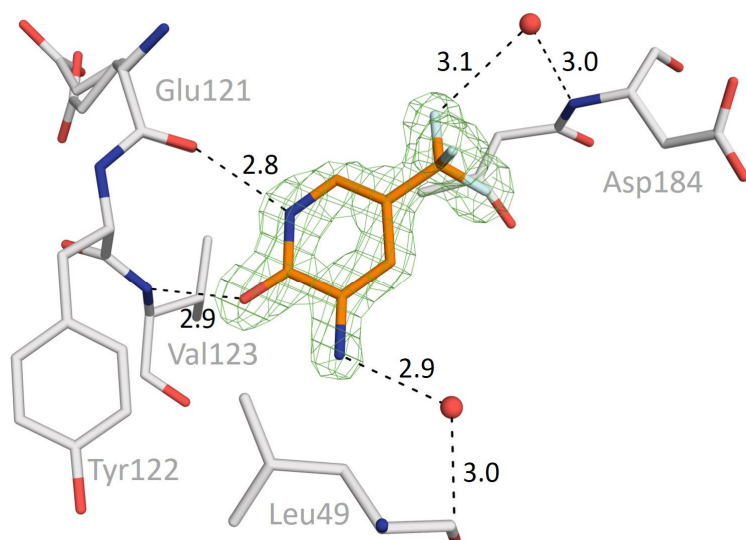


Figure 110: Detailed-view of interaction pattern of fragment F74 with PKA. The green mesh represents the unbiased  $F_o-F_c$  electron density at  $3.0 \text{ \AA}$ .

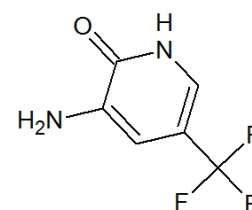


Figure 109: Chemical structure of fragment F74.

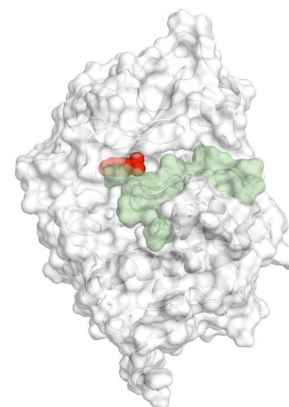


Figure 111: Fragment F74 is marked in red, PKI is marked in green.

### Binding keywords:

ATP-binding site, direct hinge interaction, water bridged to Leu49 and Asp184

### Detailed description of protein-ligand interaction:

The observed difference electron density ( $F_o-F_c$ ) of F74 is located inside the ATP-binding pocket of PKA. The ligand could be completely assigned to the density and is located close to the hinge region. The compound interacts via two H-bonds with the protein backbone: Oxygen and nitrogen atom of the lactam ring are in distances of  $2.9 \text{ \AA}$  and  $2.8 \text{ \AA}$  to the backbone nitrogen of Val123 and the backbone carbonyl oxygen of Glu121 respectively. The  $\text{CF}_3$  group is located in the proximity to the DFG loop. It is too far away for direct interaction with any of the DFG residues, but a water molecule, which is  $3.1 \text{ \AA}$  away from one fluorine atom, mediates a contact to the backbone nitrogen of Asp184. Here, the fluorine functions as weak H-bond acceptor.<sup>89</sup> Since fluorine atoms are weighted as weak H-bond acceptors, this water bridge has likely only a small contribution to affinity. Another water molecule mediates contact between the backbone carbonyl oxygen of Leu49 and the amino group of F74. The amino group can donate one polar hydrogen to the neighbouring water molecule ( $2.9 \text{ \AA}$ ), whereas, in turn, the water molecule is able to donate a hydrogen to the backbone carbonyl oxygen of Leu49 ( $3.0 \text{ \AA}$ ).

## PKA - F83 (PDB 5N1O) – 1.80 Å

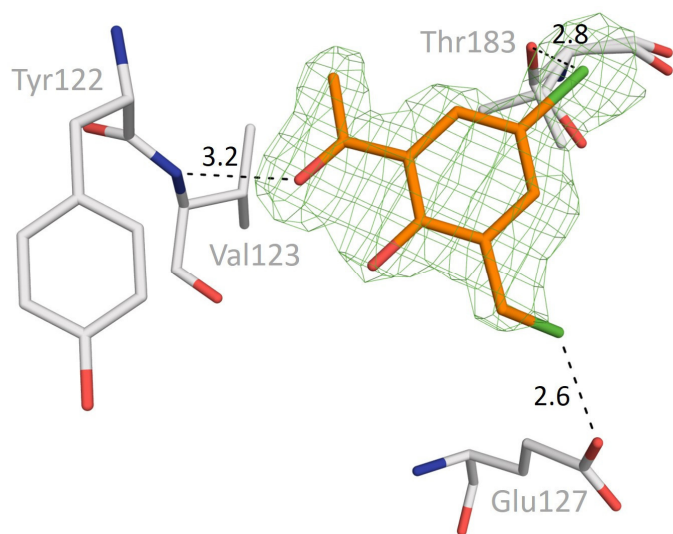


Figure 113: Detailed-view of interaction pattern of fragment F83 with PKA. The green mesh represents the unbiased  $F_o-F_c$  electron density at  $3.0 \sigma$ .

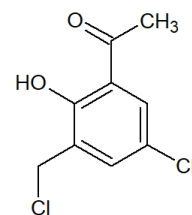


Figure 112: Chemical structure of fragment F83.

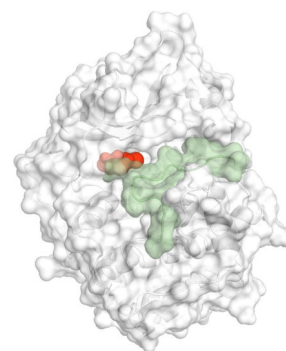


Figure 114: Fragment F83 is marked in red, PKI is marked in green.

### Binding keywords:

ATP-binding site, direct hinge interaction, interaction with Thr186 and Glu127

### Detailed description of protein-ligand interaction:

F83 binds in the ATP-binding pocket of PKA. The carbonyl oxygen of F83 is in 3.2 Å distance to the backbone nitrogen of Val123, so that an H-bond is formed with the hinge. Due to  $\pi$ -conjugation, the carbonyl group and the phenolic OH group are in a vinylogous position that affect the protonation state of both oxygen atoms. Here, the carbonyl oxygen atom acts as an H-bond acceptor. The compound contains two chlorine atoms. The first one is in para position to the phenolic hydroxyl group and exhibits the strongest electron density signal ( $5.2 \sigma$ ). With a distance of 2.8 Å, one conformer of the Thr183 hydroxyl group is in proximity to this chlorine atom. The second orientation of this side chain is oriented away from this chlorine atom. This rotamer shows an occupancy of 61%. The second chlorine is close to the carboxylate oxygen of Glu127. The distance between these atoms is 2.6 Å. Although chlorine is a strong scatterer for X-rays, this chlorine atom only shows the weakest signal of the entire ligand ( $2.4 \sigma$ ). Additionally, in refinement, the highest B-value of the compound ( $59.8 \text{ \AA}^2$ ) is assigned, which indicates enhanced mobility of the chloromethylene substituent. The other chlorine atom shows a B-value of  $39.4 \text{ \AA}^2$ . It seems that especially the second chlorine atom is not favorably positioned. Also, the first chlorine does not form an ideal halogen bond, indicated by a higher occupancy of the second orientation of Thr183 avoiding the O-Cl contact. Overall, the occupancy of 75% for this fragment indicates reduced population.

## PKA - J19 / F112 (PDB 5N39) – 1.45 Å

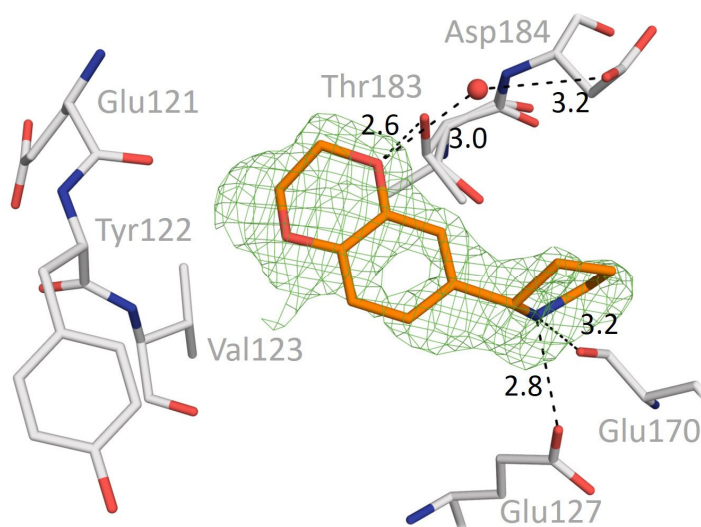


Figure 116: Detailed-view of interaction pattern of fragment J19 with PKA. The green mesh represents the unbiased  $F_o-F_c$  electron density at  $3.0 \sigma$ .

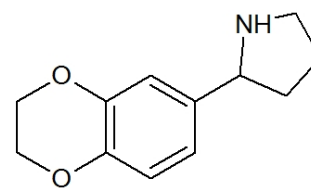


Figure 115: Chemical structure of fragment J19.

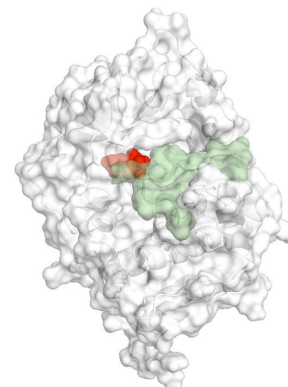


Figure 117: Fragment J19 is marked in red, PKI is marked in green.

### Binding keywords:

ATP-binding site, water bridged to Asp184, direct interaction with Thr183, Glu127, and Glu170

### Detailed description of protein-ligand interaction:

Although fragment J19 is detected in the ATP-binding site of PKA, it is too far remote to interact with the hinge region. There is also no water-mediated interaction to the hinge region. The only direct contacts of the fragment are formed to the side chain of Glu127 and backbone carbonyl oxygen of Glu170. Nevertheless, the two water molecules, which usually bind to the hinge in the absence of ATP pocket binders, are displaced by the ligand. The nitrogen of the pyrrolidine ring is likely protonated at a pH of 6.9. Therefore, it acts perfectly well as an H-bond donor to both mentioned protein residues. Thr183 is not fixed in one position and populates two alternative rotamers (A & B). Orientation A has an occ. of 38% and B an occ. of 62%. The hydroxy group in orientation A hydrogen-bonds to an oxygen atom of the fragment's dioxane ring. Full occupancy of the ligand is found, and since an H-bond to an ether oxygen is much weaker compared to a keto or ester oxygen atom, this fact can serve as an explanation why only a lower occupancy of orientation A is observed.<sup>133</sup> In orientation B the hydroxy group addresses the backbone carbonyl oxygen of Asn171 (not shown). The ether oxygen of the dioxane also forms a contact with a water molecule, which is 3.2 Å apart from Asp184 of the DFG motif. The difference density of the two carbon atoms of the pyrrolidine ring is not well defined and is only partly visible, but still significant enough to include them in the model.

## PKA - J20 / F114 (PDB 5N7P) – 1.50 Å

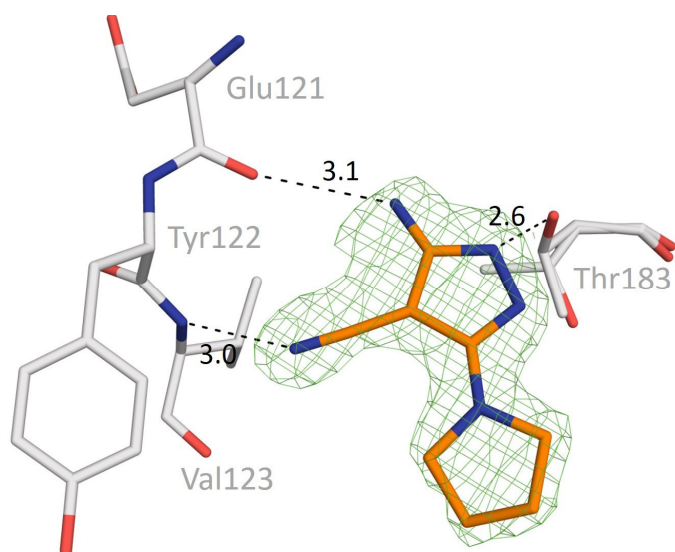


Figure 119: Detailed-view of interaction pattern of fragment J20 with PKA. The green mesh represents the unbiased  $F_o-F_c$  electron density at  $3.0 \sigma$ .

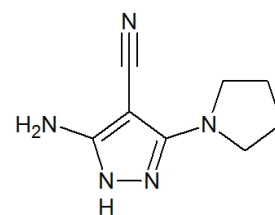


Figure 118: Chemical structure of fragment J20.

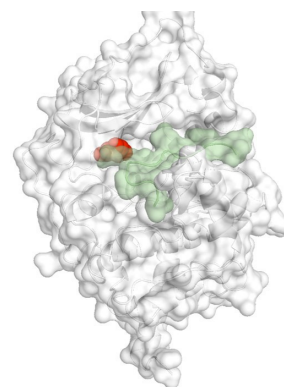


Figure 120: Fragment J20 is marked in red, PKI is marked in green.

### Binding keywords:

ATP-binding site, direct hinge interaction, no DFG interaction, direct interaction with Thr183

### Detailed description of protein-ligand interaction:

With a resolution of 1.50 Å a well-defined difference electron density ( $9.5 \sigma$ ) for the fragment J20 is obtained within the ATP-binding pocket. The fragment interacts directly with the backbone of the hinge region via two contacts. The primary amino group forms an H-bond (3.1 Å) to the backbone carbonyl oxygen of Glu121. The second interaction is established between the nitrile nitrogen of J20 and the backbone amide nitrogen of Tyr122 (3.0 Å). The pyrazole ring in the centre of the compound includes a nitrogen atom that addresses the hydroxy group of Thr183 (2.6 Å). The nitrogen atom orients its hydrogen in the direction of the hydroxy oxygen atom with an angle of approx.  $115^\circ$ . The Thr183 side chain adopts two orientation. Orientation B, which is forming the H-bond, has a higher occ. of 62%. The hydroxy group in orientation A addresses the backbone carbonyl oxygen of Asn171. The pyrrolidine ring is located in the ribose part of the ATP-binding pocket without forming any polar interaction to the protein; even though.

## PKA - J26 / F171 (PDB 5N3A) – 1.40 Å

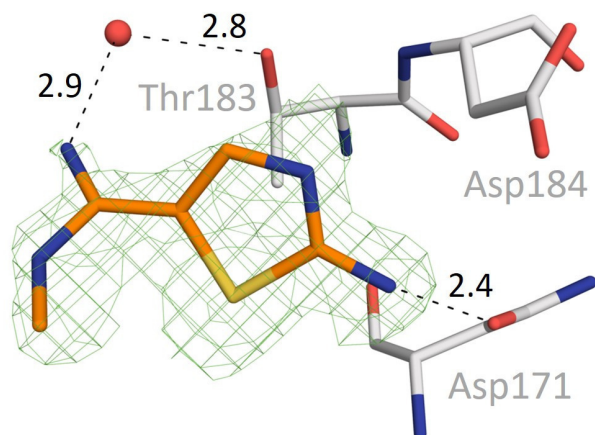


Figure 123: Detailed-view of interaction pattern of fragment J26 with PKA. The green mesh represents the unbiased  $F_o-F_c$  electron density at  $3.0 \sigma$ .

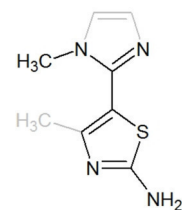


Figure 121: Chemical structure of fragment J26.

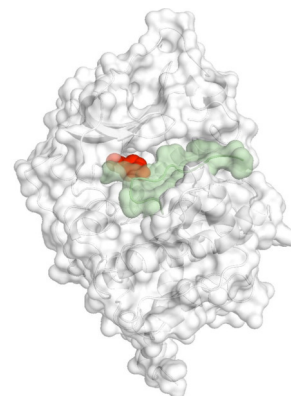


Figure 122: Fragment J26 is marked in red, PKI is marked in green.

### Binding keywords:

ATP-binding site, water bridged to Thr183, direct interaction with Asn171

### Detailed description of protein-ligand interaction:

The primary amino group of J26 forms the only direct interaction to the protein. With a distance of 2.4 Å, it is close enough to form a hydrogen bond to the side chain oxygen of Asn171, which acts as an acceptor. The ligand reaches deeper into the ATP-binding pocket. The non-methylated nitrogen of the imidazole ring addresses a water molecule at a distance of 2.9 Å. This water molecule is likewise in a close distance to the hydroxy group of Thr183 (2.8 Å). Thus, fragment J26 interacts via a water-mediated contact with the protein near the DFG motif. However, in a direction to the hinge region, the difference electron density for fragment J26 is too weak to model the remaining carbon atoms of the imidazole ring. Although the occupancy of J26 is 70%, the strongest density spot (10.5  $\sigma$  ( $F_o-F_c$ )) indicates the position of the sulfur atom. The RSCC value is at 0.85. The water molecule, which mediates the contact from ligand to the protein, is usually located at the hinge region (not shown). The second water molecule at the hinge, which interacts with the backbone nitrogen of Val123, is not influenced by the ligand.



## PKA - J28 / F189 (PDB 5N3B) – 1.64 Å

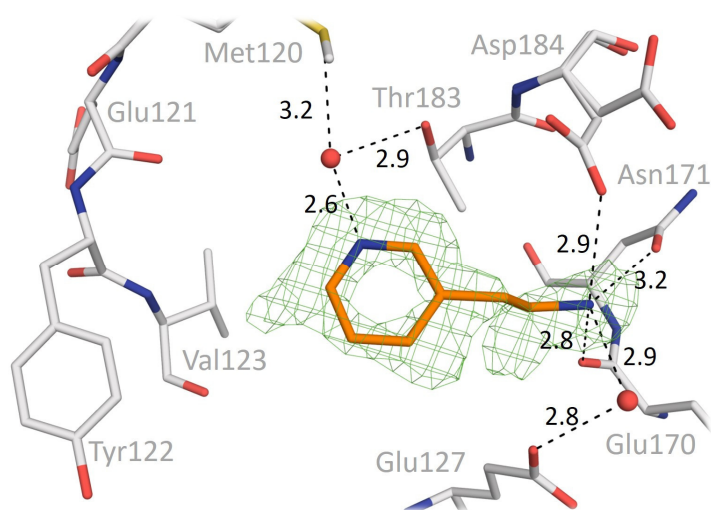


Figure 126: Detailed-view of interaction pattern of fragment J28 with PKA. The green mesh represents the unbiased  $F_o-F_c$  electron density at  $3.0 \sigma$ .

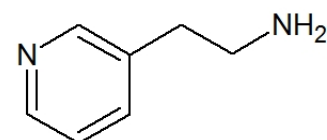


Figure 124: Chemical structure of fragment J28.

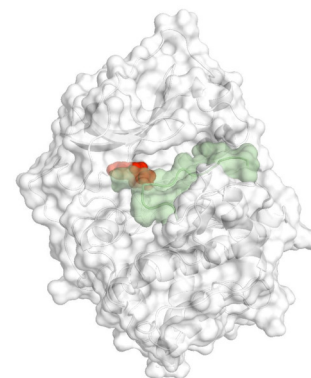


Figure 125: Fragment J28 is marked in red, PKI is marked in green.

### Binding keywords:

ATP-binding site, direct interaction with Asp184 Glu170 and Asn171, water bridged to Thr183 and Glu127.

### Detailed description of protein-ligand interaction:

The electron density for J28 is observed in the ATP-binding pocket of PKA. The only direct interactions with the protein are formed by the protonated primary amino group of the compound. Three residues are in hydrogen bonding distance: the backbone oxygen atom of Glu170, the side chain oxygen atoms of Asn171 and Asp184. The refinement of the assigned ligand results in an occupancy of 83%. However, the alternative position of Asp184 does not correlate with the ligand occupancy, although this side chain rearrangement of Asp184 seems to be influenced by the presence of the ligand. The primary ammonium group of J28 forms an additional hydrogen bond to a water molecule (2.9 Å). This water molecule mediates a contact to the carboxylate group of Glu127 (2.8 Å). The nitrogen atom of the pyridine ring also interacts with a water molecule in 2.6 Å distance. This water molecule contacts the hydroxy group of Thr183 (2.9 Å). Interestingly, this water molecule is also in close contact with the sulfur atom of the Met120 side chain (3.2 Å) in alternative orientation. Such rare interactions with methionine sulfur have been described previously.<sup>134</sup>

## PKA - J29 / F205 (PDB 5N3C) – 1.77 Å



Figure 127: Chemical structure of fragment J29.

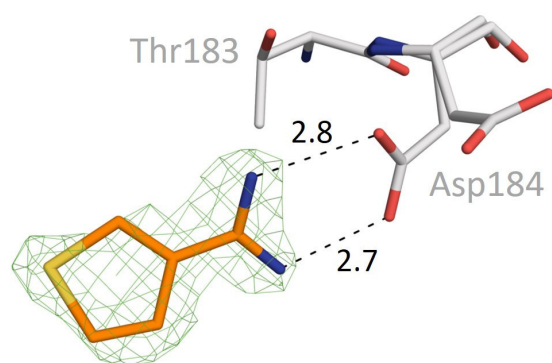


Figure 129: Detailed-view of interaction pattern of fragment J29 with PKA. The green mesh represents the unbiased  $F_o-F_c$  electron density at  $3.0 \sigma$ .

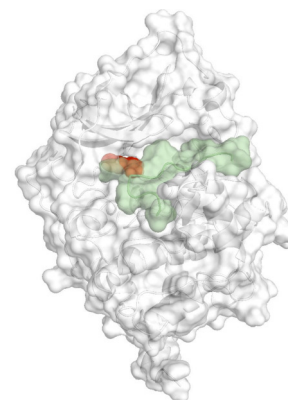


Figure 128: Fragment J29 is marked in red, PKI is marked in green.

### Binding keywords:

ATP-binding site, direct interaction with Asp184

### Detailed description of protein-ligand interaction:

Fragment J29 interacts directly with one amino acid side chain: Asp184 of the DFG motif. Its amidine group has a  $pK_a$  value of approx. 12.5. Therefore, the fragment is most likely protonated and interacts with the carboxylic acid group of Asp184 via a salt bridge. The distances between nitrogen and oxygen atoms are 2.8 and 2.7 Å, respectively. The occupancy of fragment J29 refines to 69%. The alternative orientation of Asp184 is correlated with ligand occupancy. The sulfur atom in the thiophene ring does not give the strongest electron density peak ( $3.9 \sigma$  ( $F_o-F_c$ )). The densest one comes from a carbon atom within the thiophene ring ( $5.2 \sigma$ ). The B-value of the sulfur atom is  $38 \text{ \AA}^2$  and highest within the ligand. The two amidine nitrogen atoms show the lowest B-value with approx.  $30 \text{ \AA}^2$ . The average B-value of the ligand is  $35 \text{ \AA}^2$ . The average B-values of the protein atoms surrounding the ligand are even lower with approx.  $22 \text{ \AA}^2$ .

## PKA - J32 / F211 (PDB 5N1H) – 1.18 Å

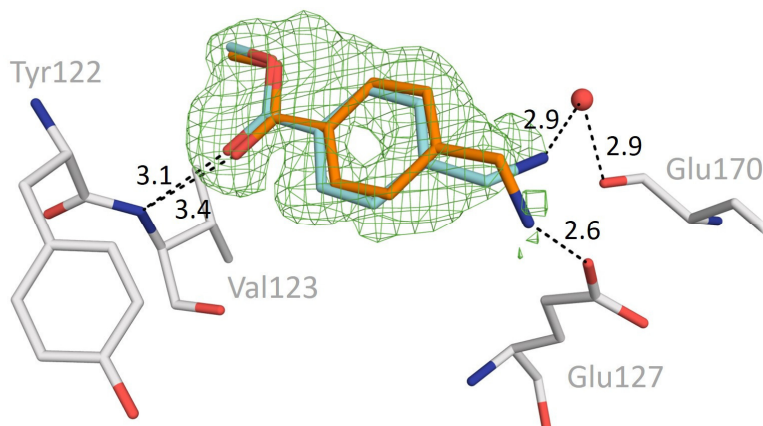


Figure 132: Detailed-view of interaction pattern of fragment J32 with PKA. The green mesh represents the unbiased  $F_o-F_c$  electron density at  $3.0 \text{ \AA}$ .

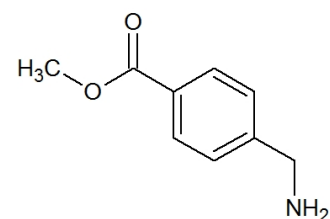


Figure 130: Chemical structure of fragment J32.

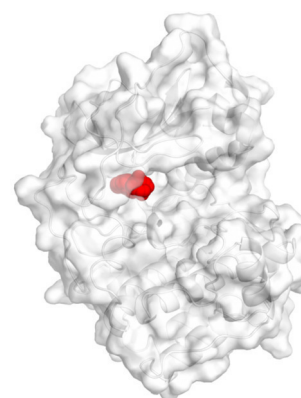


Figure 131: Overview of binding position of fragment J32 on PKA.

### Binding keywords:

ATP-binding site, direct interaction with Val123 and Glu127, water bridge to Glu170

### Detailed description of protein-ligand interaction:

The two orientations of fragment J32, shown in cyan and orange in Figure 132, differ in the orientation of the primary methylene amino side chain. The amino group is likely protonated at pH 6.9. The nitrogen atom of orientation A (orange) addresses the terminal carboxylate group of Glu127 with a distance of  $2.6 \text{ \AA}$ , thus, forming a salt bridge. The nitrogen atom of orientation B (cyan) is approaching a water molecule close to the backbone carbonyl oxygen of Glu170. This water molecule is  $2.9 \text{ \AA}$  apart from its two interaction partners. After refinement, the occupancy of orientation B is 73% and of orientation A 27%. At the hinge region, the ester carbonyl oxygen of both orientations is hydrogen bonded to the Val123 backbone nitrogen, with a distance of  $3.1 \text{ \AA}$  for orientation B and  $3.4 \text{ \AA}$  for orientation A. Interestingly, the terminal methyl group of the ester comes close to the backbone carbonyl oxygen of Glu121. The distances between protein and fragment are  $2.6 \text{ \AA}$  and  $2.7 \text{ \AA}$ , respectively. A search in the CSD (Query-parameters C - O distance ( $1.8 - 2.8 \text{ \AA}$ ), C - H - O angle ( $100 - 180^\circ$ ), C = O - H angle ( $70 - 180^\circ$ )) revealed that 129 out of 432 entries exhibit similar or lower C-O distances than  $2.6 \text{ \AA}$ .

## PKA - F222 (PDB 5N1F) – 1.12 Å

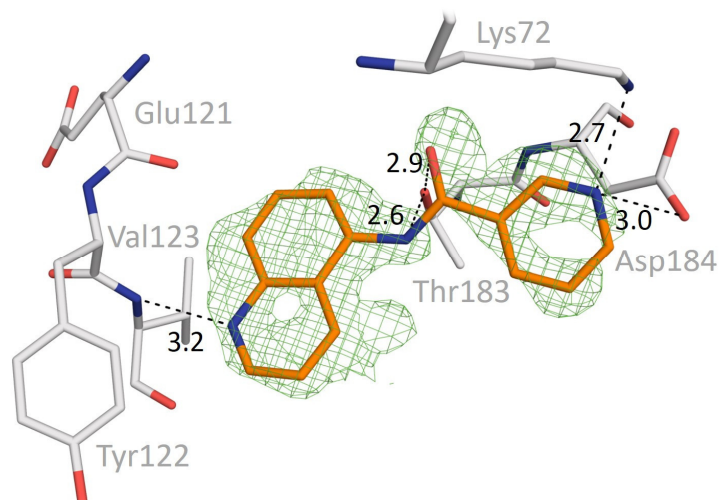


Figure 134: Detailed-view of interaction pattern of fragment F222 with PKA. The green mesh represents the unbiased  $F_o-F_c$  electron density at  $3.0 \sigma$ .

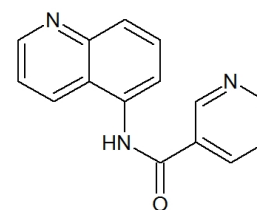


Figure 133: Chemical structure of fragment F222.

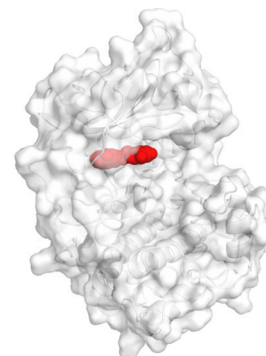


Figure 135: Overview of binding position of fragment F222 on PKA.

### Binding keywords:

ATP-binding site, direct hinge interaction, direct interaction with Thr183 and Asp184

### Detailed description of protein-ligand interaction:

At the high-resolution level of 1.12 Å, fragment F222 was detected to bind in the ATP-binding pocket of PKA. Nevertheless, the electron density is not well defined for every atom of the compound. The overall occupancy was refined to 85%. F222 interacts with the protein at the hinge region. The quinoline nitrogen of F222 accepts an H-bond from the backbone nitrogen of Val123 with a distance of 3.2 Å. Not every polar contact indicated in Figure 134 shows ideal geometry for H-bonds. The central amide bond of the fragment is in proximity to the hydroxy group of Thr183, with distances to the carbonyl oxygen of 2.9 Å and the amide nitrogen of 2.6 Å. Nevertheless, the hydroxy group spans an angle of 66° (O-O-C) with the amide group far off from ideal H-bond geometry. An angle below 90° is classified as unfavorable for H-bonding.<sup>98</sup> The poor electron density indicated for the amide bond supports the idea of an unfavorable placement. Similar to the nitrogen atom of the quinoline moiety, the nitrogen of the pyridine moiety is also likely deprotonated. Thus, it accepts an H-bond from the protonated Lys72. Asp184 is 3.0 Å apart from the quinoline nitrogen. Additionally, some indications for an alternative binding mode of F222 are present, however, too weak to assign an alternative orientation of the fragment.

## PKA - J33 / F216 (PDB 5N3D) – 1.77 Å

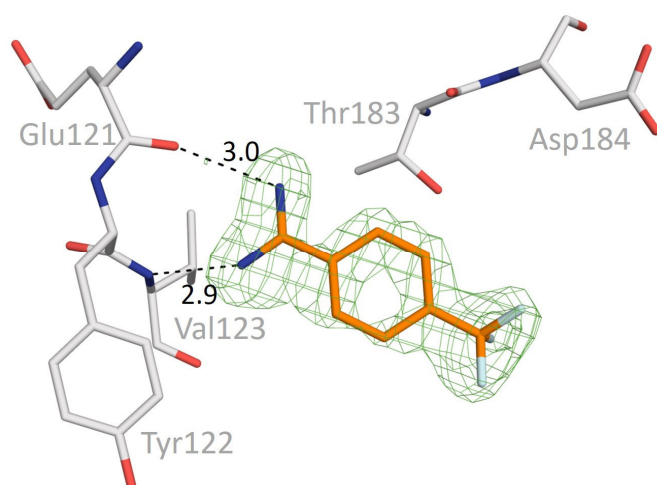


Figure 137: Detailed-view of interaction pattern of fragment J33 with PKA. The green mesh represents the unbiased  $F_o-F_c$  electron density at  $3.0 \sigma$ .

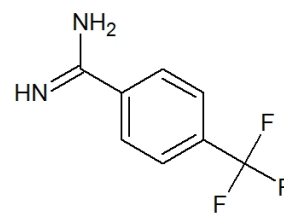


Figure 136: Chemical structure of fragment J33.

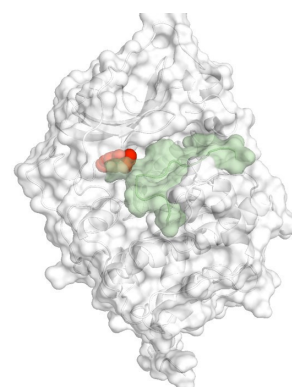


Figure 138: Fragment J33 is marked in red, PKI is marked in green.

### Binding keywords:

ATP-binding site, direct hinge interaction, direct interaction with Glu127 and Leu49

### Detailed description of protein-ligand interaction:

The fragment J33 is observed to bind in the ATP-binding pocket of PKA. Its amidine group binds to the hinge region of the protein via two H-bonds and the  $CF_3$ -group orients towards the pocket's entrance. One of the amidine nitrogen atoms interacts with the backbone nitrogen of Val123 as an H-bond acceptor and the second nitrogen acts as an H-bond donor with the backbone carbonyl oxygen of Glu121. These nitrogen atoms are at 2.9 Å and 3.0 Å distance, respectively. Amidines usually have a basic character with  $pK_a$  values of approx. 12.5. The  $CF_3$  group reduces the basic character via its -I effect. Most likely, this leads to an uncharged state of J33 in the binding pocket, so that the backbone N-H of Val123 can be accepted. Two of the fluorine atoms are close enough for interaction with the protein (not shown). The carboxylate group of Glu127 is in 2.8 Å distance to the first fluorine, and the other fluorine is at a distance of 3.0 Å to the backbone carbonyl oxygen of Leu49. The B-values are also higher for the  $CF_3$  moiety (average: approx. 49 Å<sup>2</sup>) in contrast to the remaining amidine portion (average: approx. 22 Å<sup>2</sup>). The nitrogen atom close to the backbone nitrogen of Val123 has the lowest B-value with 19.7 Å<sup>2</sup> and B-values increase in the direction of the  $CF_3$  group close to Glu127. Here the highest B-value with 50.5 Å<sup>2</sup> is found for a fluorine atom.

## PKA - J41 / F266 (PDB 5N3E) – 1.53 Å

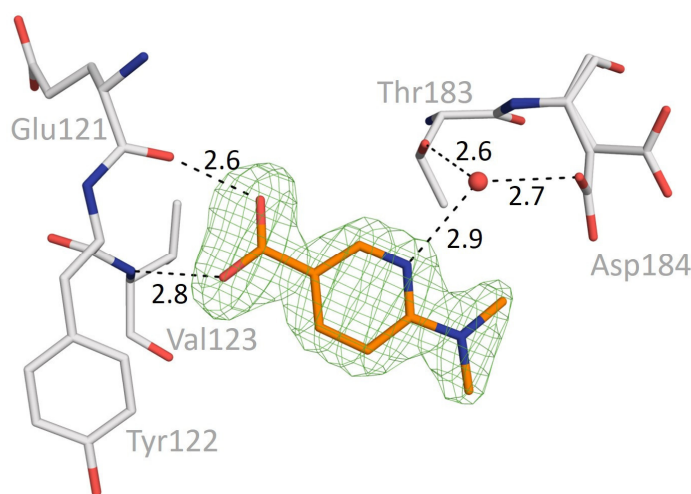


Figure 140: Detailed-view of interaction pattern of fragment J41 with PKA. The green mesh represents the unbiased  $F_o - F_c$  electron density at  $3.0 \sigma$ .

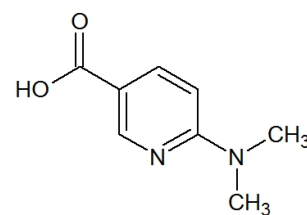


Figure 139: Chemical structure of fragment J41.

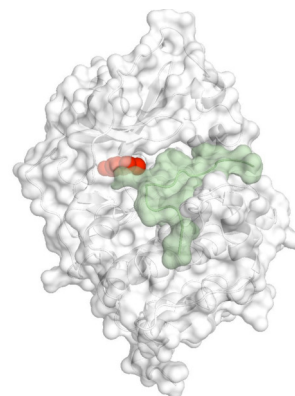


Figure 141: Fragment J41 is marked in red, PKI is marked in green.

### Binding keywords:

ATP-binding site, direct interaction with Val123 and Glu121, water bridge to Thr183

### Detailed description of protein-ligand interaction:

Complete electron density is observed for fragment J41 in the ATP-binding pocket of PKA, which allowed to assign the entire ligand to the difference electron density. According to the established interaction pattern, it is obvious that the carboxylate group of the compound must be oriented towards the hinge, whereas the tertiary amino group is placed toward the opening of the pocket. Hydrogen bonds are formed to the hinge backbone atoms with distances of 2.8 Å and 2.6 Å, respectively. This requires that the carboxylate group adopts the neutral protonated form, as the backbone carbonyl oxygen of Glu121 can only serve as H-bond acceptor. The positive mesomeric effect of the amino group in the para position to the carboxylate group reduces the acidity of J41 and therefore stabilises the protonated state. A third interaction with the protein is formed by the pyridine nitrogen. A water molecule is involved in an H-bond (2.9 Å) to this nitrogen atom. Furthermore, this water molecule forms hydrogen bonds to the side chain of Thr183 and to orientation A of the side chain of Asp184, which is to 44% occupied. In this geometry, J41 connects the hinge region with the DFG loop via H-bonds. The tertiary amine has no direct interaction partner and orients towards the opening of the binding pocket.

## PKA - J42 / F267 (PDB 5N1L) – 1.49 Å

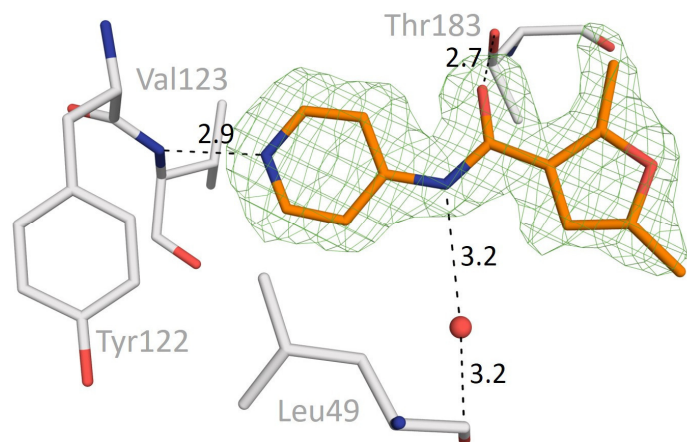


Figure 144: Detailed-view of interaction pattern of fragment J42 with PKA. The green mesh represents the unbiased  $F_o-F_c$  electron density at  $3.0 \sigma$ .

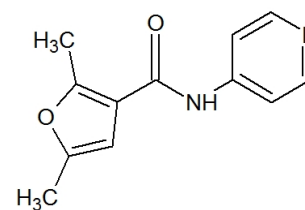


Figure 142: Chemical structure of fragment J42.

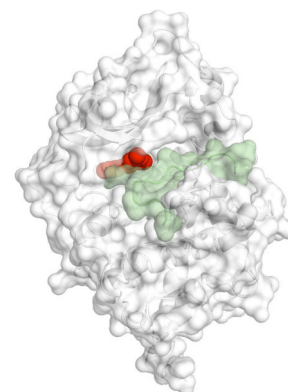


Figure 143: Fragment J42 is marked in red, PKI is marked in green.

### Binding keywords:

ATP-binding site, direct interaction with Val123 and Thr183, water bridge to Leu49

### Detailed description of protein-ligand interaction:

J42 binds with an overall planar geometry to the ATP-binding pocket of PKA. The highest concentration of electron density is found for the nitrogen atom of the pyridine ring near the hinge region ( $12.3 \sigma$  ( $F_o-F_c$ )). The methyl group with the longest distance to this nitrogen, attached to the furan ring of the fragment, displays the lowest density ( $2.7 \sigma$ ). The pyridine nitrogen acts as an H-bond acceptor ( $2.9 \text{ \AA}$ ) for the amide hydrogen of Val123. In the centre of the fragment, a peptide bond is present, which establishes interactions to two protein residues. The carbonyl oxygen of the peptide bond forms an H-bond to the hydroxy group of Thr183 ( $2.7 \text{ \AA}$ ). The nitrogen of the corresponding amide group forms an H-bond to a water molecule ( $3.2 \text{ \AA}$ ). The carbonyl oxygen of Leu49 is at a distance of  $3.2 \text{ \AA}$  to this water molecule. Accordingly, this water molecule mediates a contact between J42 and PKA. The methylated furan ring is pointing towards the pocket's opening without undergoing further interactions. The higher B-values for this moiety indicate enhanced residual mobility, compared to the remaining fragment moieties (approx.  $32 \text{ \AA}^2$  to  $23 \text{ \AA}^2$ ).

## PKA - J45 / F274 (PDB 5N1K) – 1.80 Å

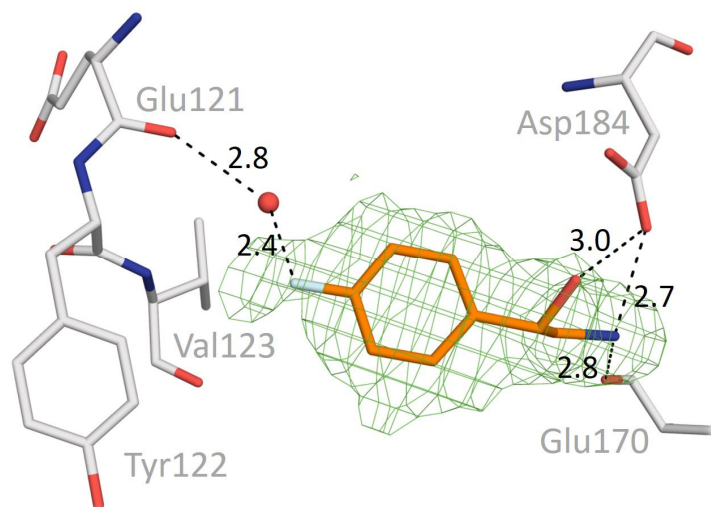


Figure 146: Detailed-view of interaction pattern of fragment J45 with PKA. The green mesh represents the unbiased  $F_o-F_c$  electron density at  $3.0 \sigma$ .

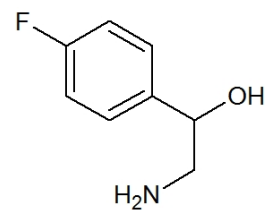


Figure 145: Chemical structure of fragment J45.

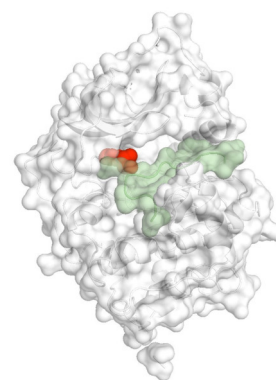


Figure 147: Fragment J45 is marked in red, PKI is marked in green.

### Binding keywords:

ATP-binding site, water bridge to Glu121, direct interaction with Asp184 and Glu170

### Detailed description of protein-ligand interaction:

Among the soaked PKA crystals, the data set with fragment J45 shows a resolution to only 1.8 Å. Nevertheless, the electron density is observed for this fragment at three different sites. The first and strongest density was found in the ATP-binding pocket. Two further density maxima were detected outside this pocket. In the binding pocket, the fluorine substituent at the benzene ring is pointing toward the hinge backbone without any direct interaction. A nearby water molecule (distance: 2.4 Å) is used to bridge the distance of 4.7 Å to the backbone carbonyl oxygen of Glu121. The fluorine must serve as H-bond acceptor<sup>89</sup>. Interestingly, only R - configuration of the racemically applied compound is apparent. The protonated amino group is favorably positioned between the backbone carbonyl oxygen of Glu170 and the carboxylic acid group of Asp184. Whereas the amino group is in 2.7 Å distance of to the carboxylate group, the hydroxy group of J45 forms an H-bond to the same atom (distance: 3.0 Å).



## PKA - J45 / F274 (PDB 5N1K) – 1.80 Å

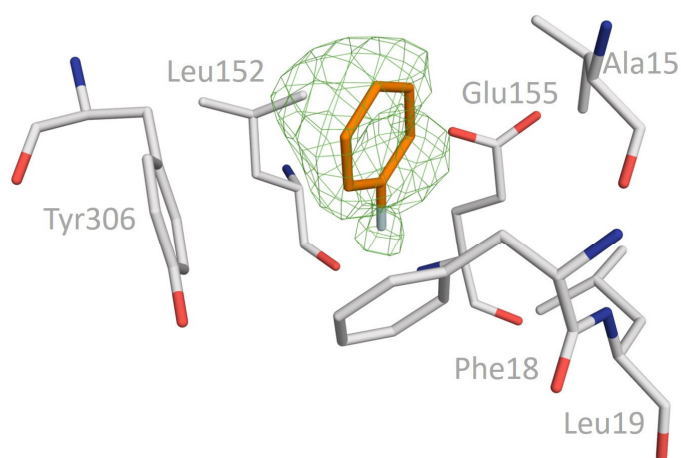


Figure 149: Detailed-view of interaction pattern of fragment J45 with PKA. The green mesh represents the unbiased  $F_o-F_c$  electron density at  $3.0 \sigma$ .

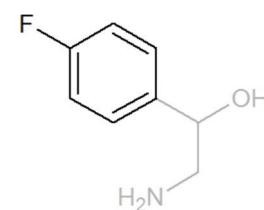


Figure 148: Chemical structure of fragment J45.

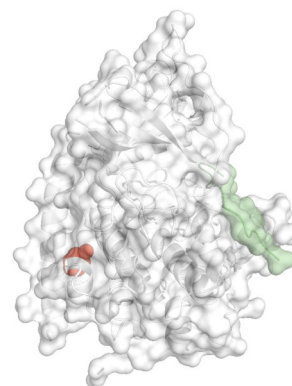


Figure 150: Fragment J45 is marked in red, PKI is marked in green.

### Binding keywords:

Remote binding, no polar interaction

### Detailed description of protein-ligand interaction:

The second copy of fragment J45 was detected in a small cleft, at the predominantly alpha-helical C-terminal part of the protein. This small pocket at the protein surface is primarily formed by hydrophobic amino acids. In Figure 149 it is shown how the ligand is surrounded by Ala15, Phe18, Leu152, Tyr306, and Glu155. The fluorine atom points into the pocket. Whereas the density for the benzene ring and the fluorine atom are still reasonable, the ethanolamine part is too far away from any protein residues to be fixed in place, resulting in a poorly defined electron density. The RSCC value is one of the worst with 0.71 and therefore belongs in the third (bad) category.

## PKA - J45 / F274 (PDB 5N1K) – 1.80 Å

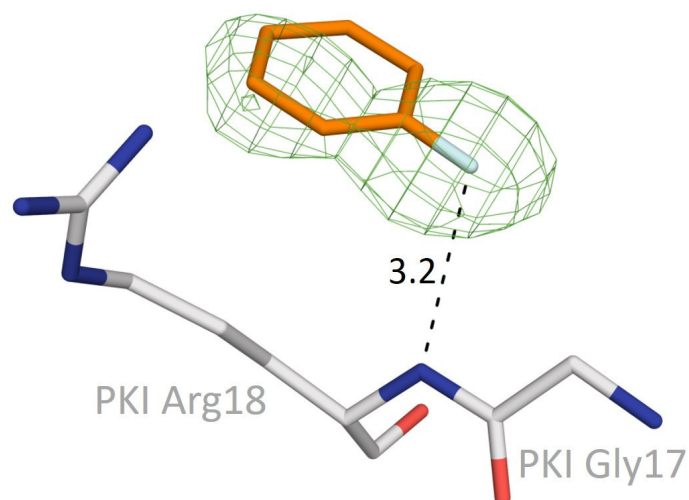


Figure 152: Detailed-view of interaction pattern of fragment J45 with PKA. The green mesh represents the unbiased  $F_o-F_c$  electron density at  $3.0 \sigma$ .

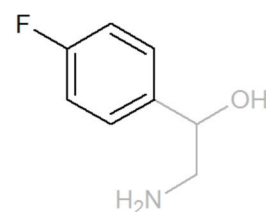


Figure 151: Chemical structure of fragment J45.



Figure 153: Fragment J45 is marked in red, PKI is marked in green.

### Binding keywords:

PKI-Arg18 interaction, close to ATP-binding pocket opening

### Detailed description of protein-ligand interaction:

Similarly, as for the second copy of fragment J45, there is also not sufficient difference electron density visible to assign the entire ligand in the third position near the ATP-binding site. Only a strong density signal for the fluorine and a slightly smaller one for the benzene ring is observed as shown in Figure 152. There is no density for the ethanolamine part, and the density of the benzene ring is also not completely visible. Because the fragment is binding at the protein surface and no further stabilizing interaction with a symmetry equivalent molecule is formed, only a part of J45 could be assigned to the density at this position. In contrast to all other bound fragments of the series, J45 interacts with the peptide inhibitor PKI. The used crystallisation peptide PKI binds close to the opening of the binding pocket. For a direct interaction with the fragment, Arg18 of the PKI peptide plays an important role. The backbone nitrogen is  $3.2 \text{ \AA}$  apart from the position of the compound's fluorine atom, which acts as a weak hydrogen bond acceptor. Here, the RSCC value of 0.90 is much better, when compared to the second copy of the fragment.

## PKA - J46 / F285 (PDB 5N3F) – 1.68 Å

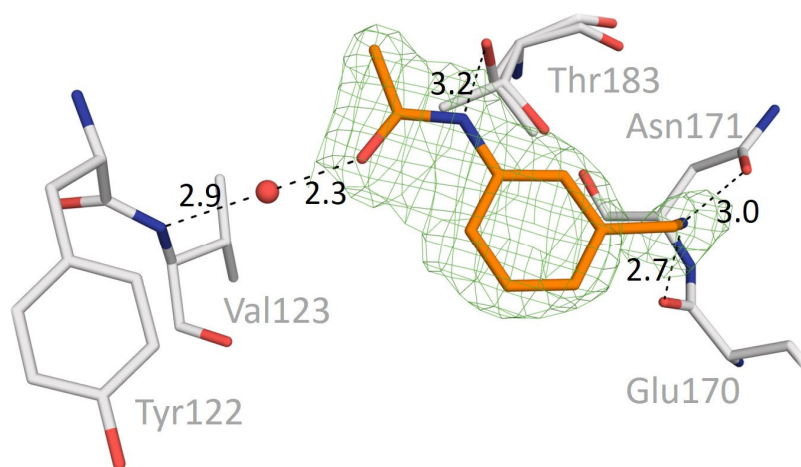


Figure 156: Detailed-view of interaction pattern of fragment J46 with PKA. The green mesh represents the unbiased Fo-Fc electron density at  $3.0 \sigma$ .

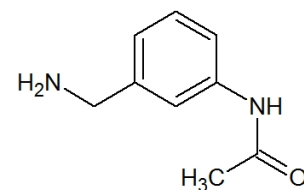


Figure 154: Chemical structure of fragment J46.

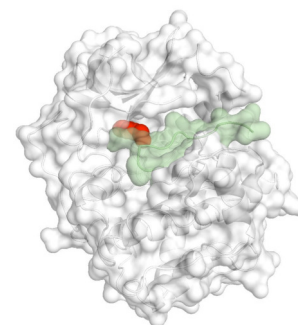


Figure 155: Fragment J46 is marked in red, PKI is marked in green.

### Binding keywords:

ATP-binding site, water bridge to Val123, direct interaction with Thr183, Asn171, and Glu170

### Detailed description of protein-ligand interaction:

Fragment J46 is detected in the ATP-binding pocket of PKA, but without forming a direct contact to the hinge backbone. There is an interstitial water molecule between the backbone nitrogen of Val123 and the amide carbonyl oxygen of J46. The water molecule is 2.9 Å apart from the backbone nitrogen and has a short distance of 2.3 Å to the oxygen of J46. The nitrogen atom of the amide group of J46 orients a hydrogen in the direction of the hydroxy group of orientation A of Thr183. This orientation shows the hydroxy group in a position, where such an H-bond can be formed via 3.2 Å. Nevertheless, the occupancy of orientation A is only at 40%. With a distance of 2.7 Å, the protonated amino group of fragment J46 interacts with the backbone carbonyl oxygen of Glu170 and the Asn171 side chain. Nevertheless, this part of the compound shows the highest residual mobility. In comparison to the amide nitrogen ( $36.9 \text{ \AA}^2$ ), the amino nitrogen has a much higher B-value of  $50.8 \text{ \AA}^2$ . Additionally, the Fo-Fc electron density is weaker in the region of the amino group ( $3.5 \sigma$  to  $6.0 \sigma$ ), which underlines this fact.

## PKA - J46 / F285 (PDB 5N3F) – 1.68 Å

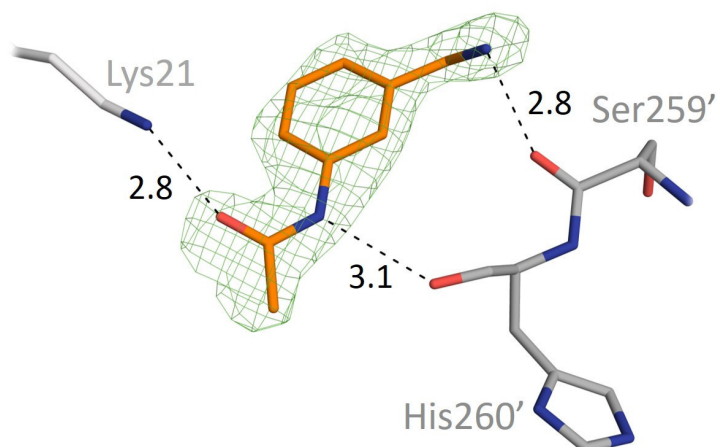


Figure 158: Detailed-view of interaction pattern of fragment J46 with PKA. The green mesh represents the unbiased  $F_o-F_c$  electron density at  $3.0 \sigma$ .

### Binding keywords:

Remote binding, direct interaction with Lys21, Ser259' and His260'

### Detailed description of protein-ligand interaction:

A second binding position of fragment J46 was observed outside the ATP-binding pocket. As shown in the overview of Figure 159, the compound is located on the protein surface. It binds close to an adjacent symmetry-related protein molecule, thereby forming interactions additionally. Lys21 is part of the long alpha-helix at the N-terminal end of PKA. Its side chain reaches to the amide oxygen of J46 to form an H-bond. The ammonium group of Lys21 is at a distance of  $2.8 \text{ \AA}$  to the carbonyl oxygen. Both nitrogen atoms of the compound interact with a backbone carbonyl oxygen of the neighbouring PKA molecule. The amide nitrogen forms an interaction with the backbone carbonyl oxygen of His260' ( $3.1 \text{ \AA}$ ). Also the amino group of the J46 acts as an H-bond donor. Here, it is  $2.8 \text{ \AA}$  apart from the backbone carbonyl oxygen of Ser259'. In contrast to the binding position within the ATP-binding-pocket, the amino nitrogen is positionally better fixed. This becomes obvious when comparing both B-values:  $50.8 \text{ \AA}^2$  in the ATP-binding site,  $37.9 \text{ \AA}^2$  near the symmetry-related protein molecule.

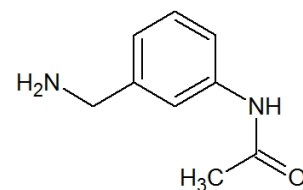


Figure 157: Chemical structure of fragment J46.

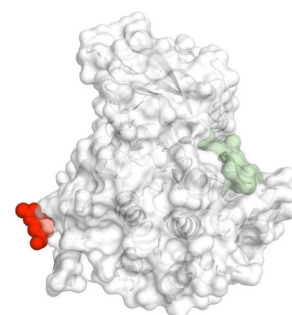


Figure 159: Fragment J46 is marked in red, PKI is marked in green.

## PKA - J47 / F286 (PDB 5N1M) – 1.44 Å

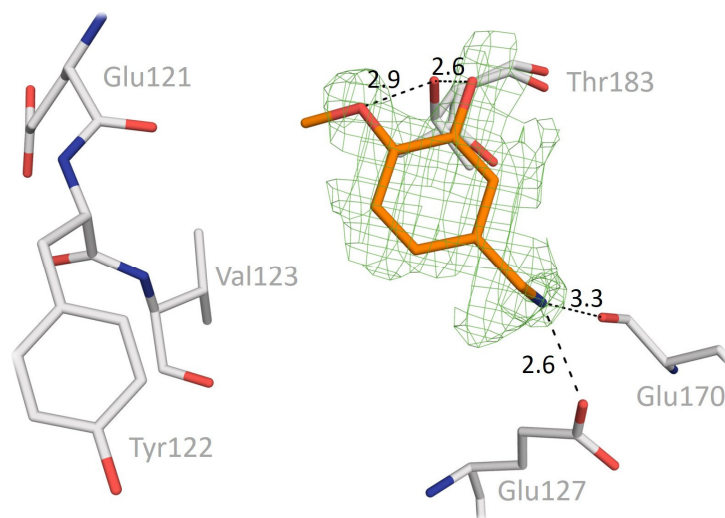


Figure 162: Detailed-view of interaction pattern of fragment J47 with PKA. The green mesh represents the unbiased  $F_o-F_c$  electron density at  $3.0 \sigma$ .

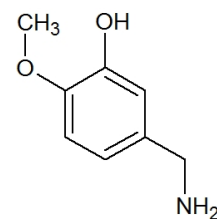


Figure 160: Chemical structure of fragment J47.

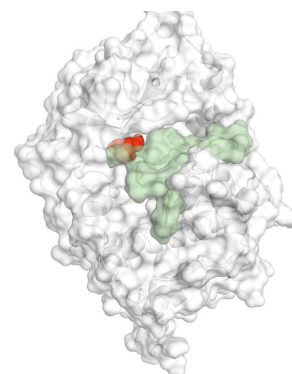


Figure 161: Fragment J47 is marked in red, PKI is marked in green.

### Binding keywords:

ATP-binding site, no hinge interaction, direct interaction with Thr183, Glu127, and Glu170

### Detailed description of protein-ligand interaction:

The density of fragment J47 is observed in the ATP-binding site. However, after placement of the fragment into the density, it is too remote from the hinge region to form an interaction. A water molecule interacts with the hinge, whereas a second one, which is usually observed in many crystal structures, is displaced by the methoxy group of J47. The refined occupancy of fragment J47 is 81%. Thr183 adopts two side chain orientations. Orientation A with 55% occupancy is in close contact with both oxygen atoms of J47. The hydroxy group of the side chain acts as an H-bond donor for the methoxy group oxygen, whereas the hydroxy group of J47 is presumably donating its hydrogen to the side chain oxygen of Thr183. After refinement, the occupancies of ligand and Thr183 A do not correlate, and the lower occupancy of the threonine side chain indicates that the hydrogen bonds are only partly accomplished. The carboxyl group of Glu127 is likely deprotonated in contrast to the protonated amino group of the fragment. The distance of 2.6 Å between nitrogen and oxygen atom indicates a salt bridge. The backbone carbonyl oxygen of Glu170 also interacts directly with the amino group of J47. However, compared to the salt bridge to Glu127, this oxygen is farther away (3.3 Å).

## PKA - F290 (PDB 5N32) – 1.83 Å

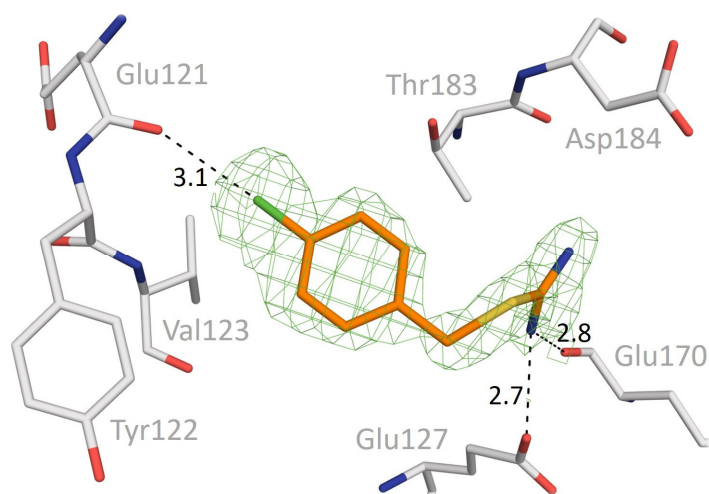


Figure 165: Detailed-view of interaction pattern of fragment F290 with PKA. The green mesh represents the unbiased  $F_o-F_c$  electron density at  $3.0 \sigma$ .

### Binding keywords:

ATP-binding site, direct hinge interaction, direct interaction with Glu127 and Glu170

### Detailed description of protein-ligand interaction:

The chlorine atom of F290 corresponds to a strong electron density signal ( $7.5 \sigma$  ( $F_o-F_c$ )) close to the hinge region of PKA. It is in 3.1 Å distance to the backbone carbonyl oxygen of Glu121. The angle from carbon to chlorine and oxygen is  $165.7^\circ$ , which indicates a halogen bond to the carbonyl oxygen of Glu121.<sup>89</sup> The basic amidino group of the ligand extends into the ribose pocket of PKA. It is likely protonated and therefore positively charged. Thus, it can form a salt bridge to the carboxylate side chain of Glu127 with a distance of 2.7 Å. Additionally, the backbone carbonyl oxygen of Glu170 is in proximity to the amidino moiety (2.8 Å) in H-bond distance. The mean B-value of F290 is relatively high with  $70.1 \text{ \AA}^2$  in contrast to the protein ( $36.2 \text{ \AA}^2$ ). The lowest values of the compound were found for the atoms directly interacting with protein residues. The chlorine atom has the lowest value with  $50.6 \text{ \AA}^2$ . The value of the amidino nitrogen increases to  $67.0 \text{ \AA}^2$ . The carbon atom between the benzene ring and the sulfur atom shows the highest residual mobility with a value of  $80.7 \text{ \AA}^2$ . An anomalous signal is detectable for the chlorine atom, whereas not for the sulfur atom. In contrast, other sulfur atoms of the protein are visible in the anomalous map. Likely the reduced density around the sulfur atom takes influence on the localisation of the anomalous scatterer. This is also supported by the second binding mode of F290 (next page), where the sulfur atom is better fixed in place, and the anomalous scattering signal is well visible, whereas the chlorine atom cannot be localised. The occupancy of this fragment molecule refines to 100 %.

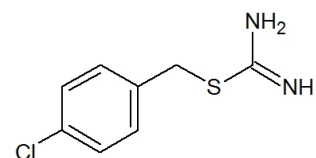


Figure 163: Chemical structure of fragment F290.

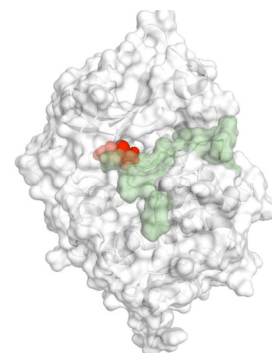


Figure 164: Fragment F290 is marked in red, PKI is marked in green.

## PKA - F290 (PDB 5N32) – 1.83 Å

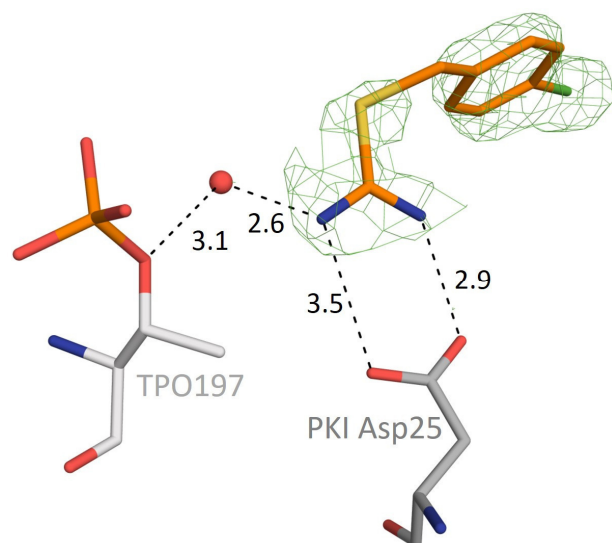


Figure 167: Detailed-view of interaction pattern of fragment F290 with PKA. The green mesh represents the unbiased  $F_o-F_c$  electron density at  $3.0 \sigma$ .

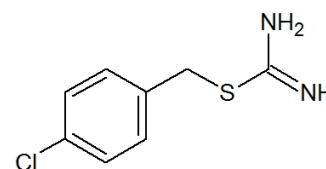


Figure 166: Chemical structure of fragment F290.

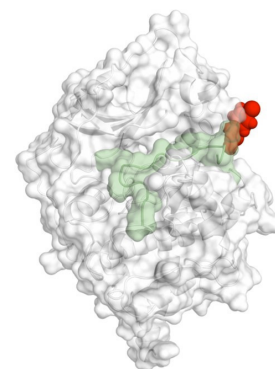


Figure 168: Fragment F290 is marked in red, PKI is marked in green.

### Binding keywords:

Remote binding, direct interaction with Asp25 (PKI), water bridge to TPO197

### Detailed description of protein-ligand interaction:

The second binding position of fragment F290 is detected outside the ATP-binding pocket. The ligand interacts with the peptide inhibitor PKI. Especially Asp25 of the latter peptide is important for this interaction. A salt bridge between the amidino group of F290 and the deprotonated carboxylate group of Asp25 is formed. The shortest distance between one oxygen and one nitrogen atom is 2.9 Å. The second oxygen atom is more remote than the first one (distance 3.5 Å). The compound also interacts with PKA mediated by a water molecule. Thus, interaction from the amidino group of F290 to the phosphorylated side chain of Thr197 (TPO197) is formed. The distance from the water molecule to the phosphate oxygen and to the amidino nitrogen amounts to 3.1 and 2.6 Å, respectively. The chloro-substituted benzene ring is neither interacting with the protein nor with the PKI peptide. It is exposed to the outside of the protein, and likely exhibits pronounced residual mobility. Hence, it is not surprising, that the B-values for this moiety are the highest for the entire molecule with 80.4 Å<sup>2</sup>. In contrast to the binding pose of F290 in the ATP-binding pocket, the current ligand placement shows an anomalous scattering signal for the sulfur atom but not for the chlorine.

## PKA - F335 (PDB 5MHI) – 1.49 Å

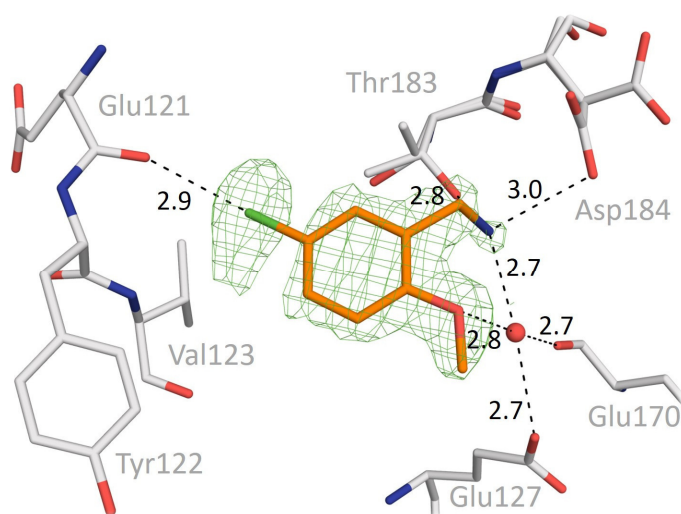


Figure 171: Detailed-view of interaction pattern of fragment F335 with PKA. The green mesh represents the unbiased  $F_o-F_c$  electron density at  $3.0 \sigma$ .

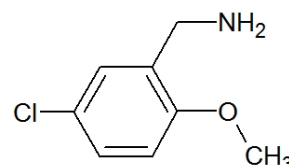


Figure 169: Chemical structure of fragment F335.

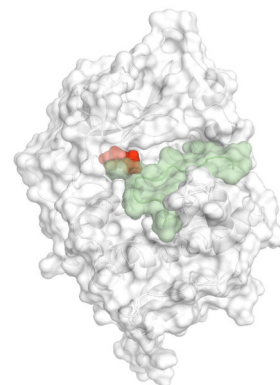


Figure 170: Fragment F335 is marked in red, PKI is marked in green.

### Binding keywords:

ATP-binding site, direct interaction with Glu121, Thr183, and Asp184, water bridge to Glu127 and Glu170

### Detailed description of protein-ligand interaction:

Fragment F335 binds in the ATP-binding pocket of PKA to the hinge region. The chlorine atom of F335 shows the strongest electron density peak of the compound ( $12.7 \sigma$  ( $F_o-F_c$ )). Additionally, an anomalous scattering signal can be observed for the chlorine atom. With an angle of approx.  $160^\circ$  from carbon via chlorine to the backbone carbonyl oxygen of Glu121 and a distance of  $2.9 \text{ \AA}$  a halogen bond is formed to the hinge.<sup>89</sup> The amino group of F335 binds close to the side chains of Thr183 and Asp184. With the hydroxy group of Thr183 it forms an H-bond ( $2.8 \text{ \AA}$ ) to the amino group of F335, and with the carboxylate group of Asp184, which adopts an alternative orientation, it interacts via a salt bridge ( $3.0 \text{ \AA}$ ). The amino group is likely protonated at pH 6.9. The occupancy of the ligand refines to 100%. A water molecule mediates a further contact to the side chain of Glu127 (distance:  $2.7 \text{ \AA}$ ) and to the backbone carbonyl oxygen of Glu170 (distance:  $2.7 \text{ \AA}$ ). The oxygen atom of the methoxy group is a rather weak H-bond acceptor (distance to water:  $2.8 \text{ \AA}$ ).



## PKA - F335 (PDB 5MHI) – 1.49 Å

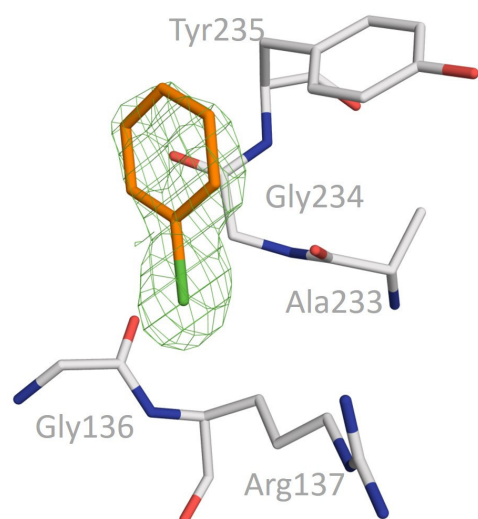


Figure 173: Detailed-view of interaction pattern of fragment F335 with PKA. The green mesh represents the unbiased  $F_o-F_c$  electron density at  $3.0 \sigma$ .

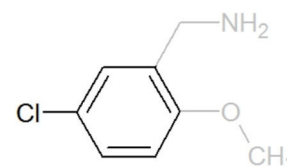


Figure 172: Chemical structure of fragment F335.

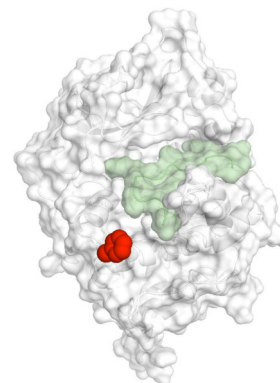


Figure 174: Fragment F335 is marked in red, PKI is marked in green.

### Binding keywords:

Remote binding, No polar protein interaction

### Detailed description of protein-ligand interaction:

A second binding pose of F335 is detected at the protein surface between two symmetry-related PKA molecules. In this orientation, the chloro-substituted benzene moiety of the ligand is located close to the amino acids Arg137 and Tyr235. This binding pose shows neither a direct nor a water-mediated polar interaction with the protein. The position of the chlorine atom and the benzene ring are assigned to the difference electron density with an RSCC value of 0.94, which indicates a good density fitting. The electron density for the methoxy and the methylene amino group are not visible in the density. The calculation of the buried solvent accessible surface area of the visible portion shows that 50.8% of the assigned ligand surface is buried by the closest protein molecule and 24.2% is covered by an adjacent PKA molecule in the crystal packing.

## PKA - F342 (PDB 5N7U) – 1.37 Å

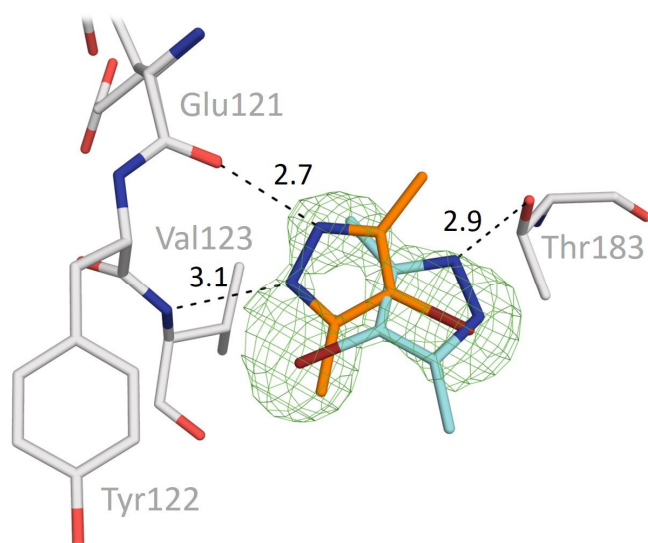


Figure 176: Detailed-view of interaction pattern of fragment F342 with PKA. The green mesh represents the unbiased  $F_o-F_c$  electron density at  $3.0 \sigma$ .

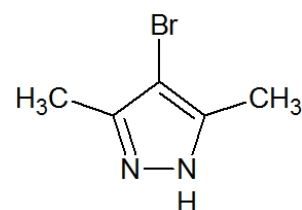


Figure 175: Chemical structure of fragment F342.

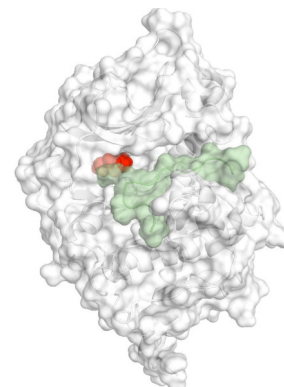


Figure 177: Fragment F342 is marked in red, PKI is marked in green.

### Binding keywords:

ATP-binding site, direct interaction with Glu121, Val123, and Thr183

### Detailed description of protein-ligand interaction:

Two large electron density blobs can be observed in the ATP-binding pocket of PKA in complex with F342 ( $17.1$  and  $10.8 \sigma$  ( $F_o-F_c$ )). Since the soaked fragment F342 comprises only one bromine atom, which could strongly contribute to scattering, the fragment has been assigned to a second orientation, which places the bromine atom in the second density maximum. The strongest density peak is located close to the hinge region and corresponds to the bromine of orientation A (cyan), which is higher populated ( $60\%$ ), whereas  $40\%$  occupancy are refined for B. The bromine in arrangement A adopts a distance of  $3.6 \text{ \AA}$  to the backbone nitrogen of Val123, which donates an H-bond in the direction of the bromine atom.<sup>89</sup> Simultaneously, one nitrogen atom of the pyrazole ring forms an H-bond to the hydroxy group of Thr183 ( $2.9 \text{ \AA}$ ). Thus, F324 bridges between hinge and DFG-loop. The pyrazole nitrogen atoms in orientation B fall close to the hinge. The backbone carbonyl oxygen of Glu121 interacts via a distance of  $2.7 \text{ \AA}$  with the protonated pyrazole nitrogen, whereas the unprotonated one forms an H-bond to the backbone nitrogen of Val123 ( $3.1 \text{ \AA}$ ). The bromine in this second arrangement B is oriented towards the entrance of the pocket without forming any interactions with the protein.

## PKA - F357 (PDB 5N1N) – 1.41 Å

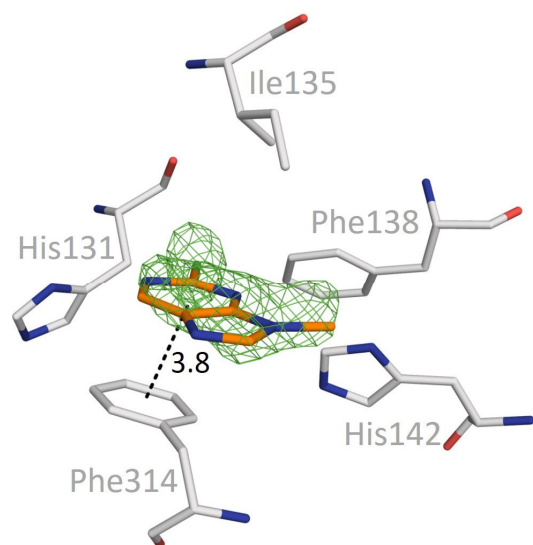


Figure 179: Detailed-view of interaction pattern of fragment F357 with PKA. The green mesh represents the unbiased  $F_o-F_c$  electron density at  $3.0 \sigma$ .

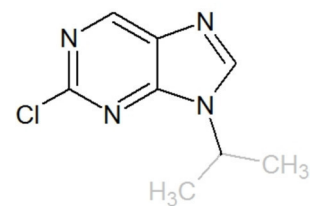


Figure 178: Chemical structure of fragment F357.

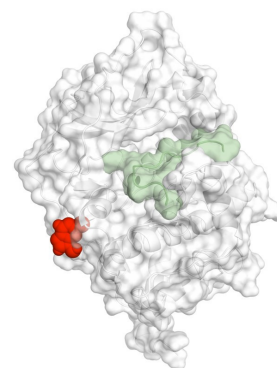


Figure 180: Fragment F357 is marked in red, PKI is marked in green.

### Binding keywords:

Remote binding,  $\pi - \pi$  – interaction with Phe314

### Detailed description of protein-ligand interaction:

The purine scaffold of F357 reminds of adenosine. Nevertheless, the observed density of this ligand is not found in the ATP-binding pocket. It is located in a small hydrophobic cleft on the protein surface. This pocket is surrounded by the protein residues His131, Ile135, Phe138, His142, and Phe314. The side chain of Phe314 interacts with the compound via its aromatic side chain. With its purine moiety the fragment stacks against the side chain of Phe314. The mean distance between both  $\pi$ -systems is 3.8 Å. No other protein-ligand interactions are experienced. The comparison with other fragment structures, which do not show a bound ligand at this position, reveals that F357 induces a slight shift of the side chain of Phe314. Interestingly, the B-values of the fragment and the side chain of Phe314 are similar. The mean B-value of ligand atoms is 41.5 Å<sup>2</sup>, and that of the contacting side chains is 38.9 Å<sup>2</sup>. The latter value is higher than for any other protein residues in this area (e.g., His131: 20.2 Å<sup>2</sup>). Although the electron density for this ligand was detected after several refinement cycles, it does not represent the entire ligand. Two terminal methyl carbon atoms of the isopropyl moiety are not visible in the density. The occupancy of the fragment was refined to 73%.

## PKA - J56 (PDB 5N3G) – 1.16 Å

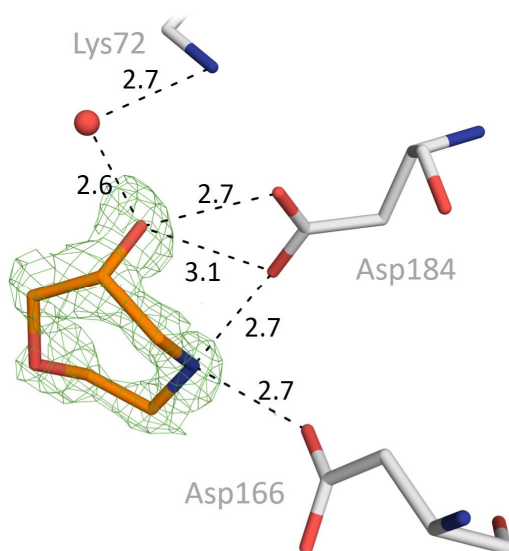


Figure 182: Detailed-view of interaction pattern of fragment J56 with PKA. The green mesh represents the unbiased  $F_o-F_c$  electron density at  $3.0\sigma$ .

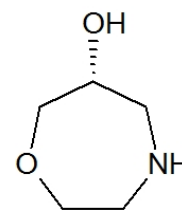


Figure 181: Chemical structure of fragment J56.

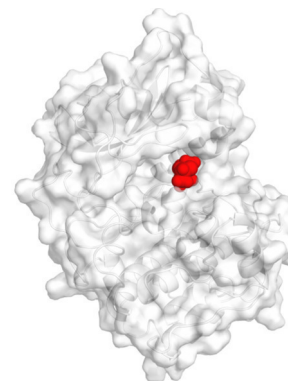


Figure 183: Overview of binding position of fragment J56 on PKA.

### Binding keywords:

ATP-binding site, direct interaction with Asp166 and Asp184, water bridge to Lys72

### Detailed description of protein-ligand interaction:

At a resolution of 1.16 Å, two well-defined density peaks are detected to assign fragment J56 in the PKA structure. The position of the strongest density peak is located close to the DFG motif, remote from the hinge. An R-configuration at the stereogenic centre of J56 can be assigned. The carboxylate group of Asp184 is at close distance to the amino and the hydroxyl group of the ligand (2.7 and 3.1 Å). The amino group is presumably protonated and forms a salt bridge to Asp184 and Asp166 in favoured position also indicated by the low B-value of 24.0 Å<sup>2</sup> for this atom compared to 31.7 Å<sup>2</sup> for the ether oxygen. The third contact to a protein residue is mediated by a water molecule to the ammonium group of Lys72 with distances of 2.7 Å and 2.6 Å respectively.

## PKA - J56 (PDB 5N3G) – 1.16 Å

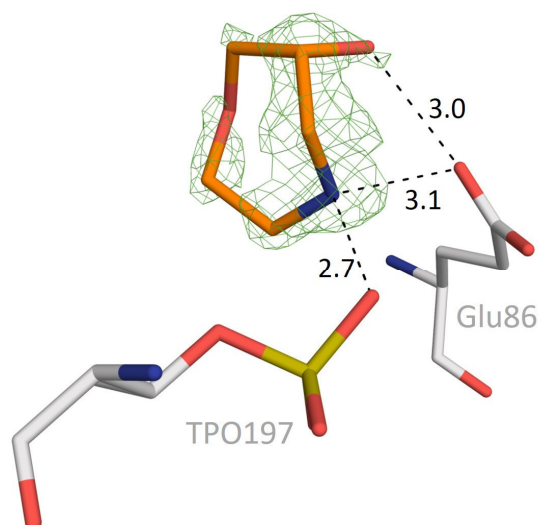


Figure 185: Detailed-view of interaction pattern of fragment J56 with PKA. The green mesh represents the unbiased  $F_o-F_c$  electron density at  $3.0 \sigma$ .

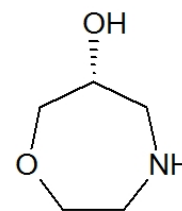


Figure 184: Chemical structure of fragment J56.

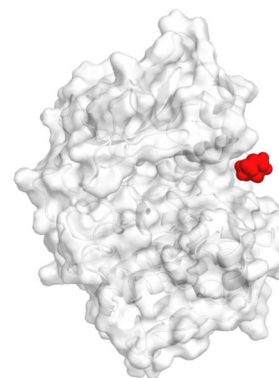


Figure 186: Overview of binding position of fragment J56 on PKA.

### Binding keywords:

Remote binding, direct interaction with TPO197 and Glu86

### Detailed description of protein-ligand interaction:

A second copy of fragment J56 is found outside the binding pocket on the protein surface. It is close to the peptide binding cleft, where the peptide inhibitor PKI could bind. In this structure no PKI is present. The auto-phosphorylation of PKA leads to a phosphorylated threonine at position 197 (TPO197). As shown in Figure 185 one oxygen of the phosphate group is close enough to interact with the protonated nitrogen of the ligand forming a salt bridge. It further attracts the negatively charged side chain of Glu86. Additionally, the hydroxy group of J56 forms an H-bond to the carboxylate oxygen of Glu86 ( $3.0 \text{ \AA}$ ). Next to the ether oxygen, J56 shows higher residual mobility also reflected by the B-values (nitrogen atom:  $46.6 \text{ \AA}^2$ , ester oxygen:  $50.6 \text{ \AA}^2$ ). The surface exposed position of J56 is close to an adjacent symmetry-related molecule. However, no polar interactions are experienced.

## PKA - J61 (PDB 5N3H) – 1.36 Å

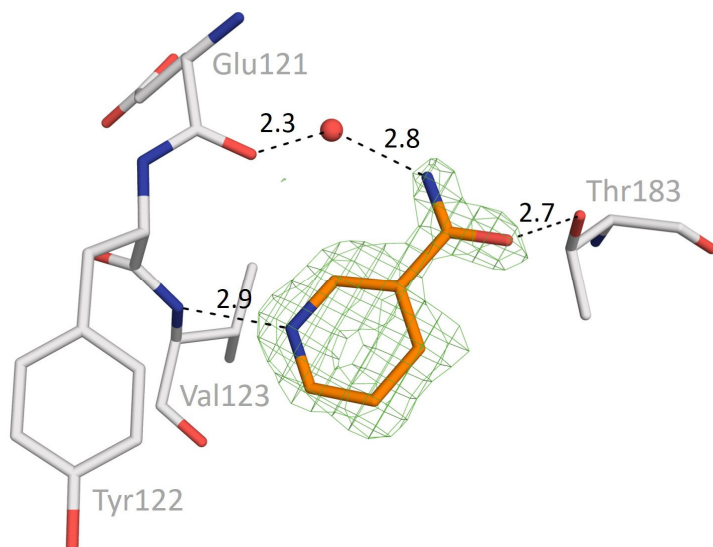


Figure 188: Detailed-view of interaction pattern of fragment J61 with PKA. The green mesh represents the unbiased  $F_o-F_c$  electron density at  $3.0 \sigma$ .

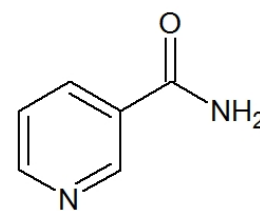


Figure 187: Chemical structure of fragment J61.

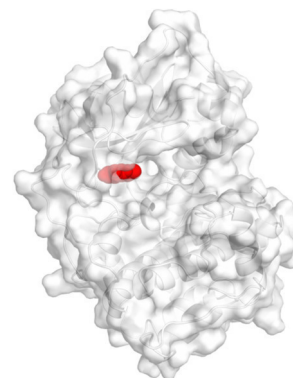


Figure 189: Overview of binding position of fragment J61 on PKA.

### Binding keywords:

ATP-binding site, direct interaction with Val123 and Thr183, water bridge to Glu121

### Detailed description of protein-ligand interaction:

Fragment J61, nicotinamide, is detected in the ATP-binding pocket of PKA. The ligand's pyridine nitrogen uses the backbone nitrogen of Val123 (2.9 Å) and the backbone carbonyl oxygen of Glu121 for a (water-mediated) H-bond interaction to the protein. The amide nitrogen of the ligand functions as an H-bond donor to the water molecule contacting the backbone carbonyl oxygen of Glu121 with its hydrogen. The amide nitrogen has two hydrogens with a  $pK_a$  value of approx. 3.2.<sup>135</sup> With direct contact with Thr183, the nicotinamide carbonyl oxygen links the hinge region and the DFG motif via 2.7 Å. Well-localised electron density and assigned B-values show that the residual mobility of the fragment is much lower on the pyridine than on the carboxamide part (pyridine-nitrogen: 15 Å<sup>2</sup> / carbonyl oxygen: 29 Å<sup>2</sup> / average: 21 Å<sup>2</sup>).

## PKA - J62 (PDB 5N3I) – 1.14 Å

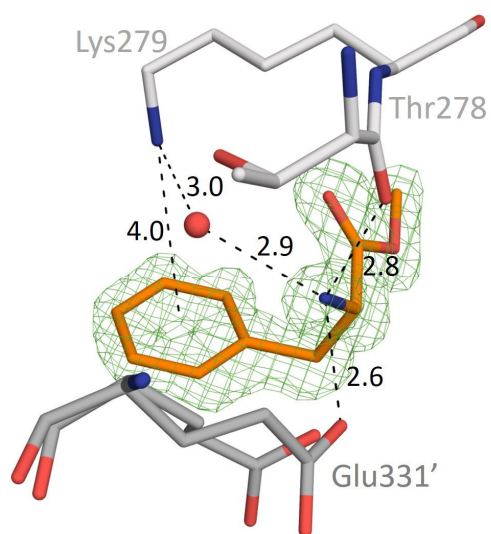


Figure 191: Detailed-view of interaction pattern of fragment J62 with PKA. The green mesh represents the unbiased  $F_o-F_c$  electron density at  $3.0 \sigma$ .

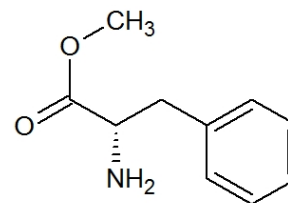


Figure 190: Chemical structure of fragment J62.

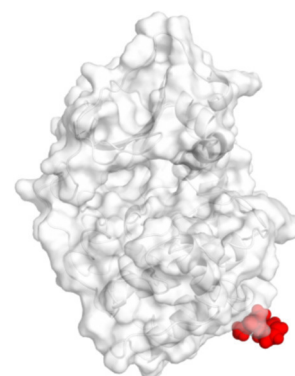


Figure 192: Overview of binding position of fragment J62 on PKA.

### Binding keywords:

Remote binding, direct interaction with Thr278 and Glu331', water bridge to Lys279

### Detailed description of protein-ligand interaction:

In contrast to most studied fragments, J62 is binding remotely from the ATP-binding pocket. Well-defined difference electron density was observed between three symmetry-related PKA molecules. Lys279 and Thr278 are close to the detected density. Whereas Thr278 forms an H-bond directly to the likely protonated amino group of the ligand, Lys279 uses an interstitial water molecule to contact the amino group. The ammonium group of Lys279 also forms a cation- $\pi$  interaction with J62. In the crystal packing Glu331' is positioned close to the fragment allowing an additional polar interaction. Both side chain conformers place the carboxylate group of Glu331' as H-bond acceptors towards the ligand's amino group. Orientation A, with 58% occupancy, is at a distance of 2.6 Å, while orientation B is at a distance of 2.8 Å. It is likely that the crystal packing facilitates the binding of the fragment, especially, since the buried surface areas of the symmetry-related molecules contribute 19.1% and 32.4% respectively, whereas the parent PKA molecule covers 31.7%.

## PKA - J65 (PDB 5N3J) – 1.12 Å

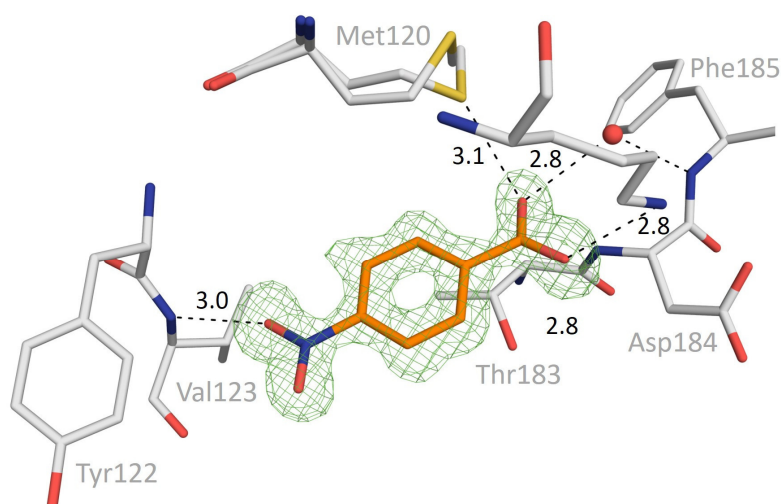


Figure 194: Detailed-view of interaction pattern of fragment J65 with PKA. The green mesh represents the unbiased  $F_o-F_c$  electron density at  $3.0 \sigma$ .

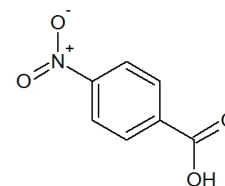


Figure 193: Chemical structure of fragment J65.

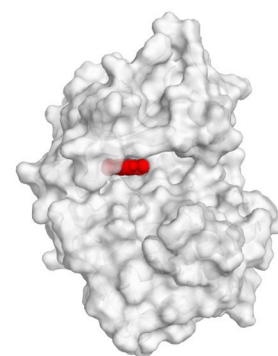


Figure 195: Overview of binding position of fragment J65 on PKA.

### Binding keywords:

ATP-binding site, direct hinge interaction, water bridge to DFG, direct Lys72 interaction

### Detailed description of protein-ligand interaction:

The position of fragment J65 is located in the ATP-binding site. To precisely place the ligand, the position of the nitrogen is indicated by higher electron density peak ( $17.6 \sigma$  ( $F_o-F_c$ )) compared to the carboxylate carbon atom ( $3.8 \sigma$ ). One oxygen atom of the nitro group directly interacts with the backbone nitrogen of Val123 ( $12.9 \text{ \AA}$ ). At the opposing side of the ligand, the carboxylic acid interacts with three different protein residues. The nitrogen atom of the side chain of Lys72 is  $2.8 \text{ \AA}$  apart forming a salt bridge. Mediated by a water molecule, the other carboxylate oxygen interacts with the backbone nitrogen of Phe185, which is part of the DFG motif. As third interaction partner, the backbone nitrogen of Asp184 forms an H-bond to the carboxylate group (distance  $2.8 \text{ \AA}$ , not shown). Additionally, the side chain of Met120 adopts an alternative orientation which places the sulfur atom close to the carboxylate oxygen with a distance of  $3.1 \text{ \AA}$ .<sup>134</sup> The central benzene ring overlaps with the planar adenosine moiety of the natural ATP ligand, showing the adenine located near to the hinge. The nitro group also overlaps with the adenine position. In contrast to compound J41, the carboxylate group is not interacting with the hinge. The nitro group increases the acidic character of J65. Therefore the carboxylate group is in its deprotonated state. This does not allow interaction with the backbone carbonyl oxygen of Glu121.



## PKA - J72 (PDB 5N3K) – 1.33 Å

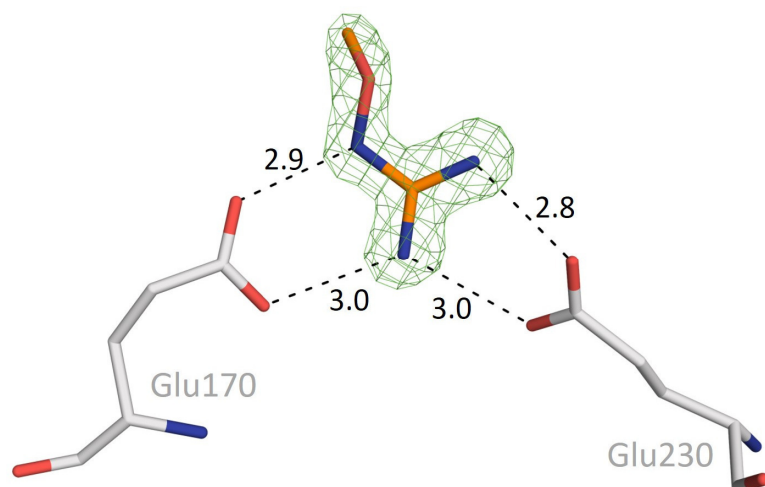


Figure 197: Detailed-view of interaction pattern of fragment J72 with PKA. The green mesh represents the unbiased  $F_o-F_c$  electron density at  $3.0 \sigma$ .

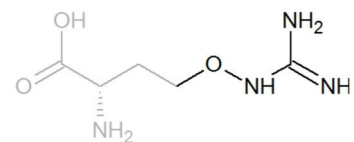


Figure 196: Chemical structure of fragment J72.

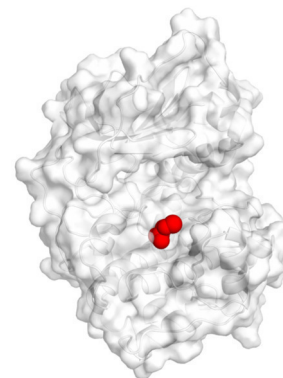


Figure 198: Overview of binding position of fragment J72 on PKA.

### Binding keywords:

Remote binding, PKI binding side, direct interaction with Glu170 and Glu230

### Detailed description of protein-ligand interaction:

Without bound PKI, PKA provides an empty binding site accessible for fragments. The guanidine part of J72 is located at the position where usually Arg19 of PKI (Type SCP0064) interacts with the kinase. Arginine differs from J72 only at the position next to the guanidino group, where an oxygen is found instead of a carbon atom in Arg. Therefore it is not surprising, that the binding mode mimics that of Arg19 in PKI. The triangular guanidine group fits perfectly well between Glu170 and Glu230. The oxygen atoms of their carboxylate groups interact with the guanidine part via salt bridges. All distances vary between 2.8 Å to 3.0 Å. Although the electron density next to both glutamic acids is well-defined, the complete ligand cannot be assigned. The missing part of the ligand sticks out of this pocket into the solvent, where it cannot find any interaction partner. This enhanced mobility is also reflected by the B-values. The nitrogen atom forming close contacts to both glutamic acids exhibits the lowest B-value (19.8 Å<sup>2</sup>), whereas the carbon atom following the oxygen atom has the highest value with 32.2 Å<sup>2</sup> (average: 22 Å<sup>2</sup>).

## PKA - J74 (PDB 5N3L) – 1.38 Å

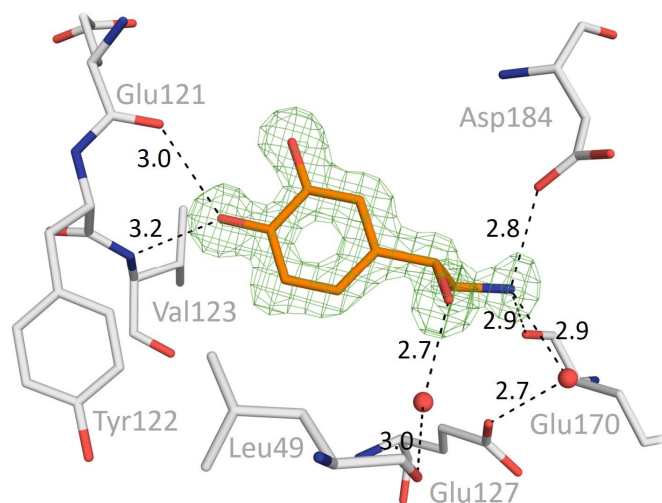


Figure 200: Detailed-view of interaction pattern of fragment J74 with PKA. The green mesh represents the unbiased  $F_o-F_c$  electron density at  $3.0 \text{ \AA}$ .

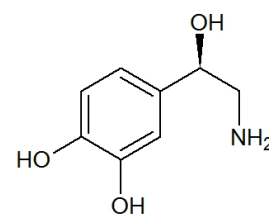


Figure 199: Chemical structure of fragment J74.

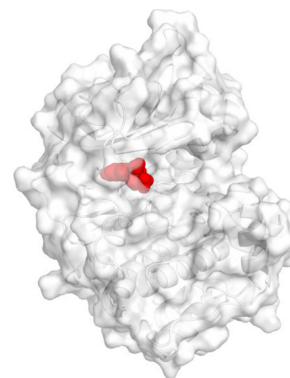


Figure 201: Overview of binding position of fragment J74 on PKA.

### Binding keywords:

ATP-binding site, direct interaction with Glu121, Val123, Glu170 and Asp184, water bridge to Leu49 and Glu127

### Detailed description of protein-ligand interaction:

Fragment J74 is noradrenaline. The binding position of J74 is located in the ATP-binding pocket. The compound satisfies multiple side chain interactions in the pocket. It extends from the hinge region, where the catechol is located, to Asp184 of the DFG motif, where the amino group of the ligand is positioned. As shown in Figure 200 the hydroxy group in para position interacts with the backbone nitrogen of Val123 and the backbone carbonyl oxygen of Glu121. The hydroxy group of J74 is  $3.2 \text{ \AA}$  apart from the backbone nitrogen of Val123 and  $3.0 \text{ \AA}$  apart from the backbone carbonyl oxygen of Glu121. The amino group of J74 is surrounded by potential interaction partners. A side chain oxygen of Asp184 is  $2.8 \text{ \AA}$  apart from the protonated amino group and forming a salt bridge. Another oxygen accepting an H-bond from the charged amino group is the carbonyl oxygen of the backbone of Glu170. With a distance of  $2.9 \text{ \AA}$ , it is also in ideal H-bond distance. The third contact is mediated by a water molecule to the backbone carbonyl oxygen of Glu127. Another water bridge is formed by the hydroxyl side chain of J74. The interstitial water molecule is located  $2.7 \text{ \AA}$  apart from the hydroxy group and  $3.0 \text{ \AA}$  from the backbone carbonyl oxygen of Glu127.

## PKA - J77 (PDB 5N3M) – 1.23 Å

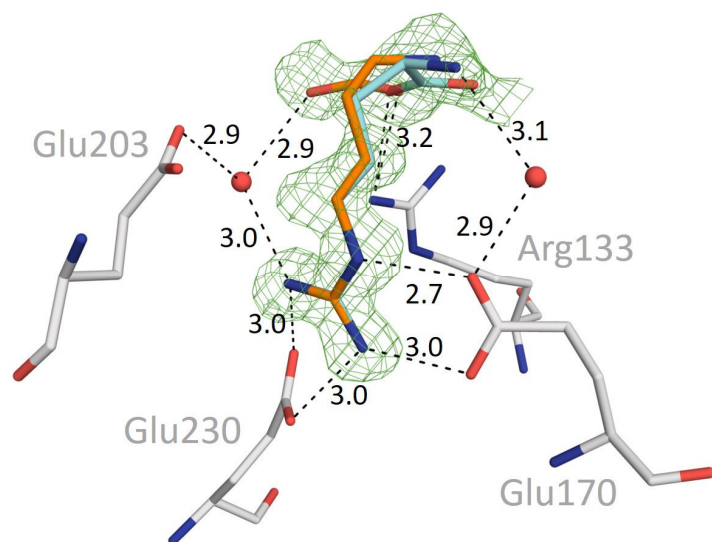


Figure 203: Detailed-view of interaction pattern of fragment J77 with PKA. The green mesh represents the unbiased  $F_o-F_c$  electron density at  $3.0 \sigma$ .

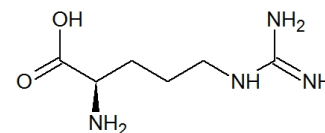


Figure 202: Chemical structure of fragment J77.

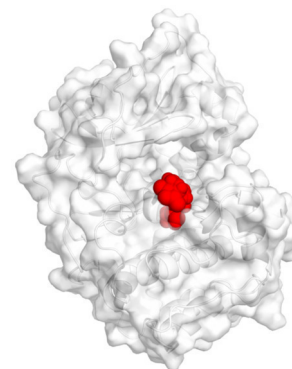


Figure 204: Overview of binding position of fragment J77 on PKA.

### Binding keywords:

PKI binding side, direct interaction with Arg133, Glu170 and Glu230, water bridge to Glu203

### Detailed description of protein-ligand interaction:

In contrast to J72, which binds at the same position, the entire ligand J77 is observed in the PKI binding cleft (structure obtained in a PKI-free form). Nevertheless, the higher residual mobility of the carboxylate and amino terminus is suggested by the occurrence of two orientations of the amino acid. The occupancy distributes to 65% (orientation A, orange) and 35% (orientation B, cyan). Due to the absence of PKI, J77 binds in the same position as Arg19 of PKI. The guanidino part of the ligand is most likely protonated and charged. Therefore it fits ideally between the two carboxylate groups of Glu230 and Glu170 of PKA forming salt bridges. The electron density is well-defined showing the fragment in a fixed position. The ligand forms another contact to the protein using a water molecule as mediator. The carboxylate group of Glu203 is  $2.9 \text{ \AA}$  apart from this water molecule, which is  $3.0 \text{ \AA}$  apart from the guanidino group of the ligand. In the more mobile part of the ligand, both conformers interact directly with Arg133 via their carboxylate oxygens. Both exhibit a similar distance (approx.  $3.2 \text{ \AA}$ ). Slightly shifted, orientation B forms an additional water bridge to the carboxylate group of Glu170 using its own terminal amino group. In contrast, orientation A forms a water bridge to Glu203 using its carboxylate group ( $2.9 \text{ \AA}$ ).

## PKA - J81 (PDB 5N3N) – 1.22 Å

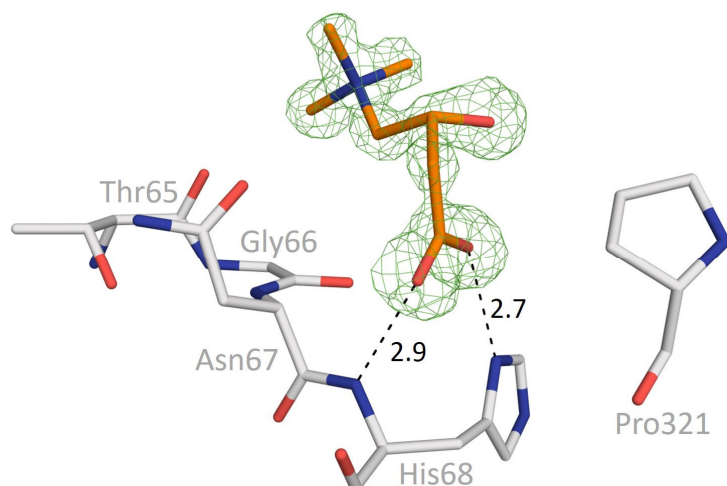


Figure 206: Detailed-view of interaction pattern of fragment J81 with PKA. The green mesh represents the unbiased  $F_o-F_c$  electron density at  $3.0 \sigma$ .

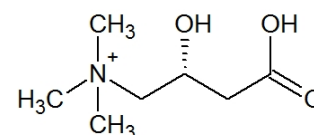


Figure 205: Chemical structure of fragment J81.

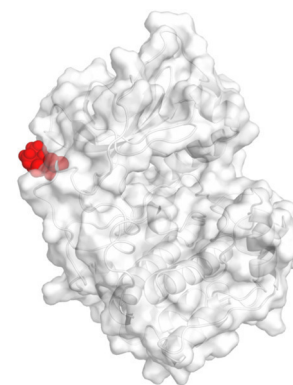


Figure 207: Overview of binding position of fragment J81 on PKA.

### Binding keywords:

Remote binding, Direct interaction with Asn67 and His68

### Detailed description of protein-ligand interaction:

In comparison to all other detected fragments of the series, fragment J81 has an alkylated ammonium group. This quaternary ammonium group is located near an electron-rich region on the protein surface. A major part of this surface area is formed by the backbone oxygen atoms of Asn67, Gly66, and Thr65. The electron density of the ammonium group is well defined, similar to the carboxylate group of the fragment. The latter group orients one of its oxygen atoms toward the backbone nitrogen of His68 to establish a 2.9 Å H-bond. Its second oxygen atom is at a distance of 2.7 Å to a nitrogen atom of the imidazole moiety of His68. J81 contains an R-configured stereogenic centre at the attached hydroxyl group. Although this group does not have any interaction partner, it is clearly defined in the electron density.

## PKA - J83 (PDB 5N3O) – 1.32 Å

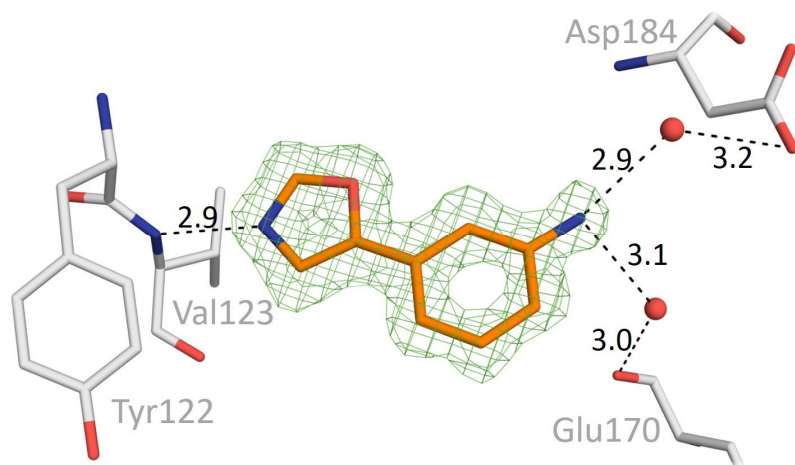


Figure 209: Detailed-view of interaction pattern of fragment J83 with PKA. The green mesh represents the unbiased Fo-Fc electron density at  $3.0 \sigma$ .

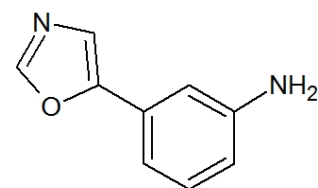


Figure 208: Chemical structure of fragment J83.

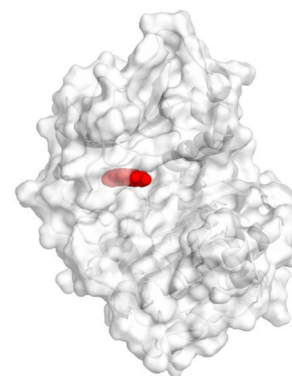


Figure 210: Overview of binding position of fragment J83 on PKA.

### Binding keywords:

ATP-binding site, direct interaction with Val123, water bridged interaction with Asp184 and Glu170

### Detailed description of protein-ligand interaction:

Three binding positions of fragment J83 were detected in this crystal structure. The first one is located in the ATP-binding site. An oxazole ring is attached to the benzene ring and orients towards the hinge region. There, the nitrogen H-bonds ( $2.9 \text{ \AA}$ ) to the backbone nitrogen of Val123. Two water molecules, usually bound to the hinge are replaced by the ligand. Close to the exocyclic amino group of the fragment, two water molecules are located (distance  $2.9$  and  $3.1 \text{ \AA}$ ). They mediate interaction with the carboxylate group of Asp184 and the backbone carbonyl oxygen of Glu170. The electron density of all atoms of the ligand is well-defined. Consistent with other fragments of the series, J83 shows increasing B-values from the hinge towards the pocket entrance. The oxazole nitrogen has a low value of  $7.6 \text{ \AA}^2$ , while the exocyclic nitrogen has an increased value of  $17.1 \text{ \AA}^2$  and is therefore above the mean B-value of the protein with  $11.5 \text{ \AA}^2$ . The occupancy of the ligand refines to 100%.

## PKA - J83 (PDB 5N3O) – 1.32 Å

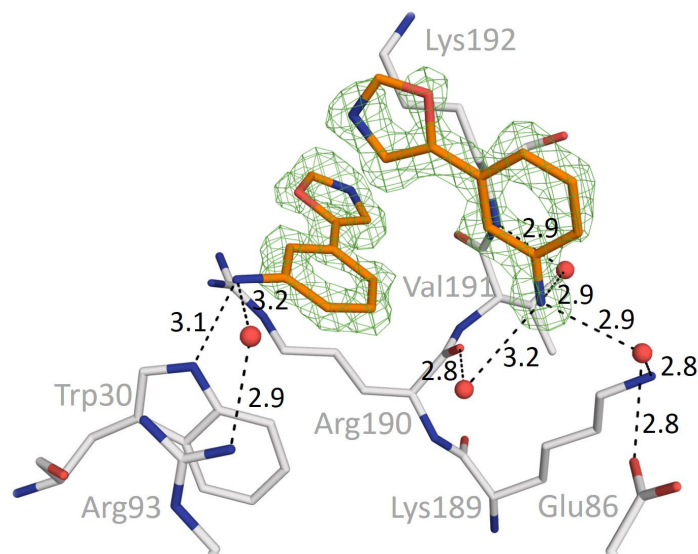


Figure 211: Detailed-view of interaction pattern of fragment J83 with PKA. The green mesh represents the unbiased  $F_o-F_c$  electron density at  $3.0 \sigma$ .

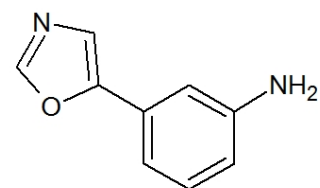


Figure 212: Chemical structure of fragment J83.

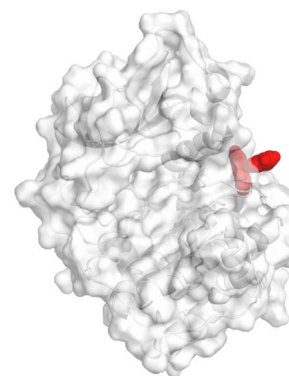


Figure 213: Overview of binding position of fragment J83 on PKA.

### Binding keywords:

Remote binding, direct interaction with Trp30, water bridge to Arg93, Glu86, Lys189, Val190 and Lys192

### Detailed description of protein-ligand interaction:

Two additional binding positions of fragment J83 are close to each other and displayed in Figure 211. There is no direct interaction between both molecules. The electron density is well-defined in both cases so that the ligand could be completely assigned to each position. The molecule with orange-colored carbon atoms interacts directly with the indole nitrogen of Trp30 via its exocyclic amino group. The amino group is presumably uncharged according to a  $pK_a$  value of 4.6.<sup>97</sup> The distance between the two nitrogen atoms is 3.1 Å. In addition, this amino group forms a water-mediated contact to one of the amidino nitrogens of Arg93. The oxazole ring and the guanidino group of Arg190 seem to establish a  $\pi$ - $\pi$ -stacking interaction (distance 3.9 Å not shown). The third copy of J83 is placed adjacently. The compound does not form any direct polar interactions with the protein. Instead, it recruits three water molecules, which surround its exocyclic amino group. Assuming an uncharged state, the amino group would bare two hydrogens, which are used to contact two water molecules, whereas the free electron pair interacts with a third water molecule. The water molecules are arranged in a triangular pattern around the amino group. They mediate contacts to Glu86, Lys189, Val191, and Lys192 (see Figure 211). Interestingly, the aniline-type ring seems to  $\pi$ - $\pi$ -stack with the amidino function of Arg133 of an adjacent crystal mate (distance of 4.0 Å not shown).

## PKA - J84 (PDB 5N3P) – 1.58 Å

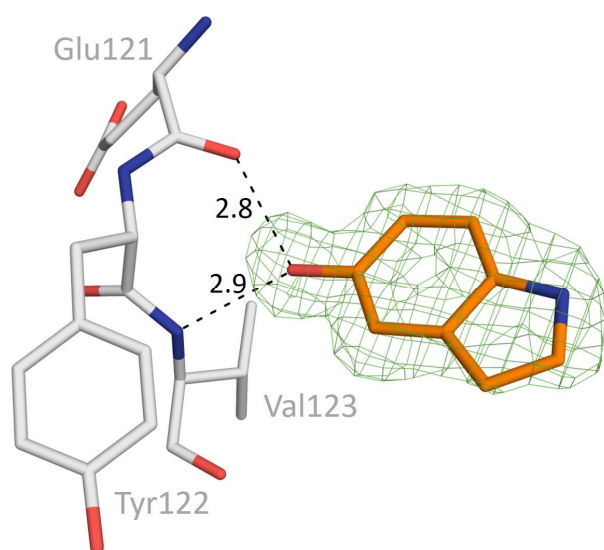


Figure 215: Detailed-view of interaction pattern of fragment J84 with PKA. The green mesh represents the unbiased  $F_o-F_c$  electron density at  $3.0 \sigma$ .

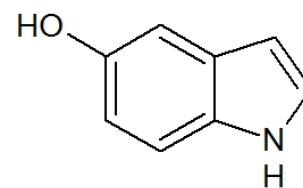


Figure 214: Chemical structure of fragment J84.

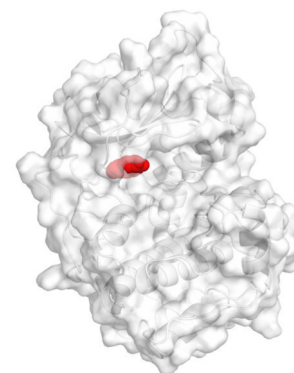


Figure 216: Overview of binding position of fragment J84 on PKA.

### Binding keywords:

ATP-binding site, direct interaction with Glu121 and Val123

### Detailed description of protein-ligand interaction:

Fragment J84 binds in the ATP-binding pocket of PKA. It is located close to the hinge region. The hydroxy group of the compound is placed between the backbone nitrogen of Val123 and the backbone carbonyl oxygen of Glu121, with distances of 2.9 Å and 2.8 Å respectively. From here the ligand extends towards the opening of the pocket without forming further directional interactions. Therefore, the B-values increase from hydroxyl oxygen ( $9.0 \text{ \AA}^2$ ) to indole nitrogen ( $15.4 \text{ \AA}^2$ ). The weaker electron density ( $F_o-F_c$ ) found for this part of the compound underlines this fact (oxygen:  $14.0 \sigma$ ; nitrogen:  $8.9 \sigma$ ).

## PKA - J85 (PDB 5N3Q) – 1.31 Å

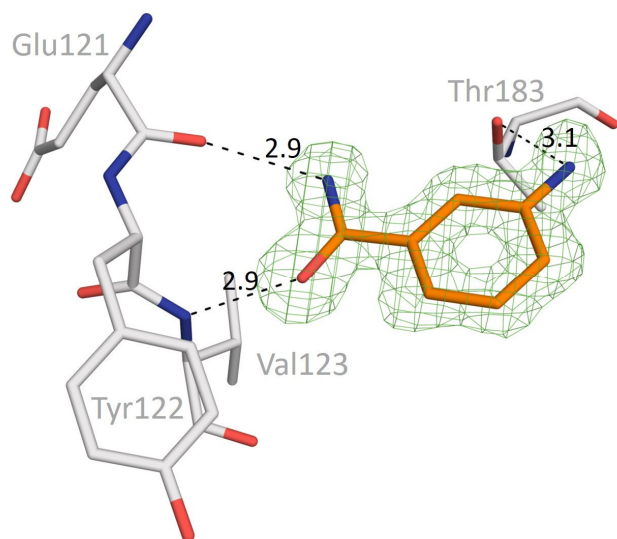


Figure 218: Detailed-view of interaction pattern of fragment J85 with PKA. The green mesh represents the unbiased  $F_o-F_c$  electron density at  $3.0 \sigma$ .

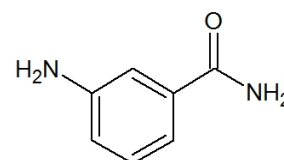


Figure 217: Chemical structure of fragment J85.

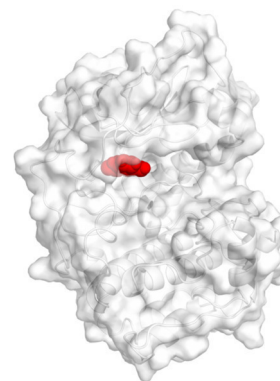


Figure 219: Overview of binding position of fragment J85 on PKA.

### Binding keywords:

ATP-binding site, direct interaction with Glu121, Val123, and Thr183

### Detailed description of protein-ligand interaction:

Fragment J85 binds in the ATP-binding pocket of PKA. It directly interacts with the protein at three positions via H-bonds. The amide group of the compound points towards the hinge region of PKA forming two parallel H-bonds with the backbone carbonyl oxygen of Glu121 and the backbone nitrogen of Val123. The distances are 2.9 Å for both H-bond. The exocyclic amino group of J85 is at a distance of 3.1 Å to the hydroxy group of Thr183 forming the third H-bond. The electron density of the fragment is clearly defined ( $15.6 \sigma$  ( $F_o-F_c$ )). The variation of the B-values across the compound is low, from 10.0 Å<sup>2</sup> (benzene carbon next to the amide group) to 14.0 Å<sup>2</sup> (amino group).



## PKA - J85 (PDB 5N3Q) – 1.31 Å

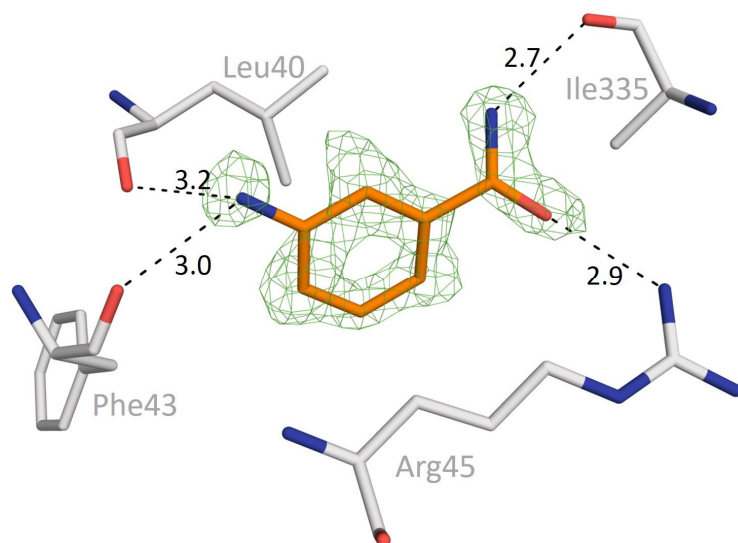


Figure 221: Detailed-view of interaction pattern of fragment J85 with PKA. The green mesh represents the unbiased  $F_o-F_c$  electron density at  $3.0 \sigma$ .

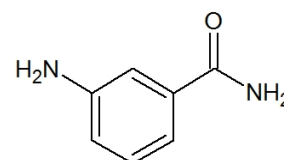


Figure 220: Chemical structure of fragment J85.

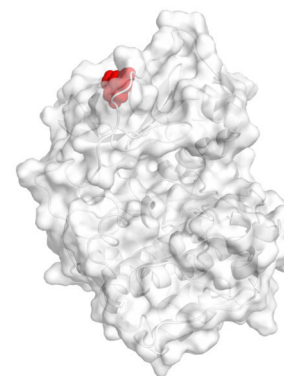


Figure 222: Overview of binding position of fragment J85 on PKA.

### Binding keywords:

Remote binding, direct interaction with Leu40, Phe43, Arg45, and Ile335

### Detailed description of protein-ligand interaction:

A second binding position of fragment J85 was observed on the protein surface in the  $\beta$ -sheet dominated region of PKA. The electron density defining this binding pose is weaker than the one in the ATP-binding pocket ( $5.9 \sigma$  ( $F_o-F_c$ )), nevertheless it is still sufficient to identify the fragment. A small binding pocket is formed by four surrounding amino acids that interact with the ligand. Leu40 and Phe43 are bordering the pocket with their backbone carbonyl oxygens, enabling H-bonds as acceptors with J85. The compound's exocyclic amino group addresses these oxygen atoms via H-bonds (distances: 3.2 and 3.0 Å). Arg45 and Ile335 interact with the carboxamide group of the compound. The nitrogen of this group acts as H-bond donor towards the backbone carbonyl oxygen of Ile335 (distance: 2.7 Å), and the oxygen atom interacts with the guanidino group of Arg45 (distance: 2.9 Å). The occupancy refines to 61% suggesting that binding to this pocket is less attractive than the ATP pocket. However, the RSCC value is 0.88, which is at the border of a very good density fit.

## PKA - J87 (PDB 5N3R) – 1.36 Å

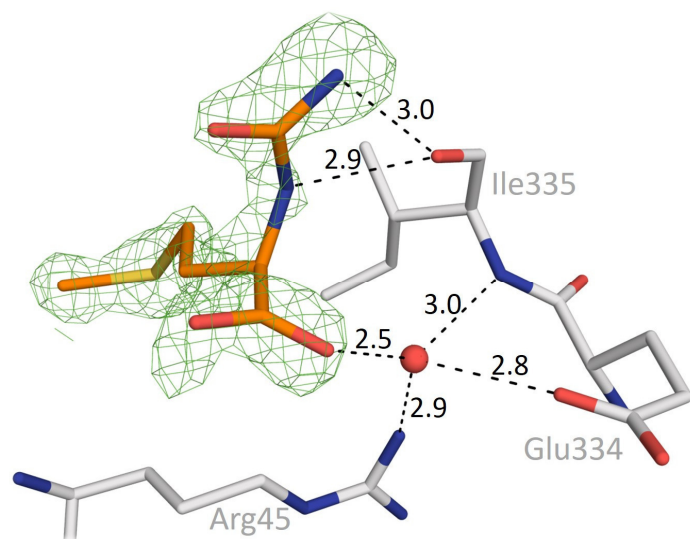


Figure 224: Detailed-view of interaction pattern of fragment J87 with PKA. The green mesh represents the unbiased  $F_o-F_c$  electron density at  $3.0 \sigma$ .

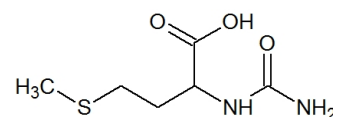


Figure 223: Chemical structure of fragment J87.

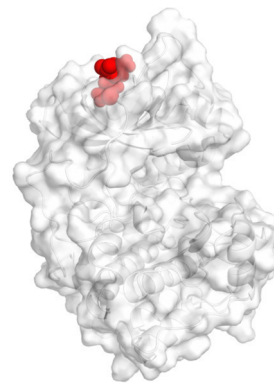


Figure 225: Overview of binding position of fragment J87 on PKA.

### Binding keywords:

Remote binding, direct interaction with Ile335, water bridge to Glu334 and Arg45

### Detailed description of protein-ligand interaction:

There is no density found for fragment J87 in the ATP-binding pocket of PKA. Instead, the ligand binds in a small pocket on the protein surface of the  $\beta$ -sheet dominated region. Both nitrogen atoms of the urea group are 3.0 Å and 2.9 Å close to the backbone carbonyl oxygen of Ile335 (Figure 224). The carboxylate group of fragment J87 directly interacts with a symmetry-related protein molecule in the packing. Arg144' and the phosphorylated Ser139' (SEP139') form polar interactions with the fragment (not shown). Furthermore, there is a water-mediated contact (2.5 Å) established by the carboxylate group of J87. The water molecule is located between two hydrogen bond acceptors (Glu334's and J87's carboxylate group) and two hydrogen bond donors (Arg45's guanidino group and Ile335's backbone nitrogen). The guanidino group of Arg45 is at a distance of 2.9 Å, whereas the backbone nitrogen of Ile335 has a distance of 3.0 Å. Although J87 was applied racemic during soaking, the density indicates that only the R-configured ligand is bound in this surface pocket.

## PKA - J89 (PDB 5N3S) – 1.14 Å

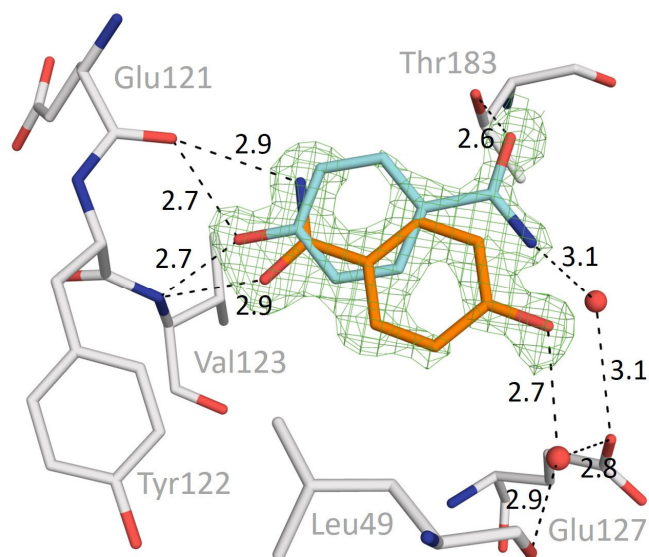


Figure 227: Detailed-view of interaction pattern of fragment J89 with PKA. The green mesh represents the unbiased  $F_o-F_c$  electron density at  $3.0 \sigma$ .

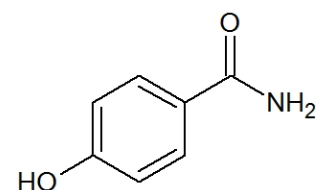


Figure 226: Chemical structure of fragment J89.

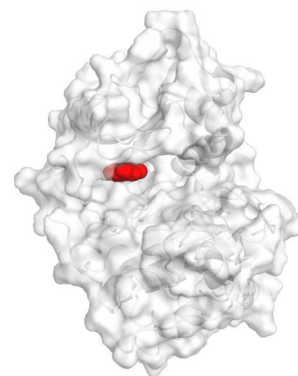


Figure 228: Overview of binding position of fragment J89 on PKA.

### Binding keywords:

ATP-binding site, direct interaction with Glu121, Val123, and Thr183, water bridge to Leu49 and Glu127

### Detailed description of protein-ligand interaction:

The fragment adopts two alternative orientation in the ATP-binding pocket (orientation A in orange and B in cyan). In both orientations, J89 binds to the hinge. Orientation A uses its carboxamide group, similar to J85, to form two parallel H-bonds with the backbone nitrogen of Val123 and the backbone carbonyl oxygen of Glu121. In orientation B the phenolic hydroxy group, similar to J84, serve simultaneously as H-bond partner for the backbone carbonyl oxygen of Glu121 and the backbone nitrogen of Val123. The hydroxy group adopts twice the distance of 2.7 Å to both backbone atoms whereas the heteroatoms of the carboxamide group show two distances of 2.9 Å. In orientation B, the carboxamide group contacts the DFG loop via Thr183 with an H-bond (2.6 Å) and water-mediated the carboxylate oxygen of Glu127. This water molecule is at a distance of 3.1 Å to both groups. In contrast, the phenolic hydroxyl group in orientation A penetrates into the ribose pocket and interacts via a water bridge with the carboxylate group of Glu127 and with the backbone carbonyl oxygen of Leu49. The refined occupancy suggests orientation A to be favoured by 60%. The RSCCs achieves convincing values of 0.98 both orientations.

## PKA - J94 (PDB 5N3T) – 1.21 Å

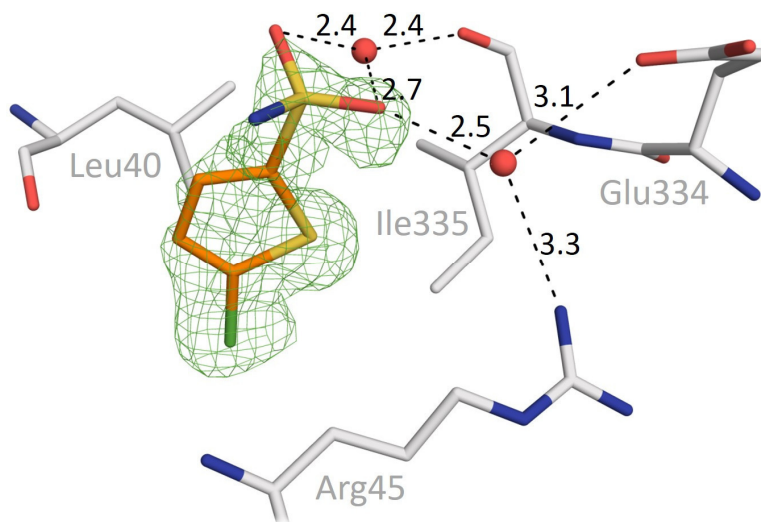


Figure 230: Detailed-view of interaction pattern of fragment J94 with PKA. The green mesh represents the unbiased  $F_o-F_c$  electron density at  $3.0 \sigma$ .

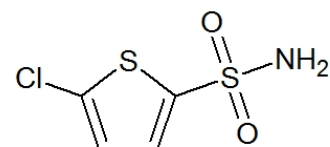


Figure 229: Chemical structure of fragment J94.



Figure 231: Overview of binding position of fragment J94 on PKA.

### Binding keywords:

Remote binding, water bridge to Ile335, Glu334, and Arg45

### Detailed description of protein-ligand interaction:

Similar to fragment J87, fragment J94 binds with the first copy to the small  $\beta$ -sheet pocket on the protein surface. Although the ligand uses only water molecules for polar interactions with the protein, the electron density is unblemished for the fragment. The fragment occupancy refines to 74%. In comparison to the chlorine ( $10.6 \sigma$ ) and the thiophene sulfur atom ( $10.7 \sigma$ ), the sulphonamide sulfur has a weaker ( $6.4 \sigma$ ) electron density ( $F_o-F_c$ ). The anomalous map shows only a signal for the thiophene sulfur atom. A water molecule in 2.4 and 2.7 Å distance to both sulphonamide oxygen atoms mediates a contact to the backbone carbonyl oxygen of Ile335. A further water bridge is established by one of the sulphonamide oxygens to the guanidino group of Arg45 and the carboxylate group of Glu334. With distances of 3.1 Å and 3.3 Å, the formed H-bonds are fairly weak. The distance of 2.5 Å between the water and the sulphonamide oxygen indicates a fairly strong H-bond to the polar sulphonamide group.

## PKA - J94 (PDB 5N3T) – 1.21 Å

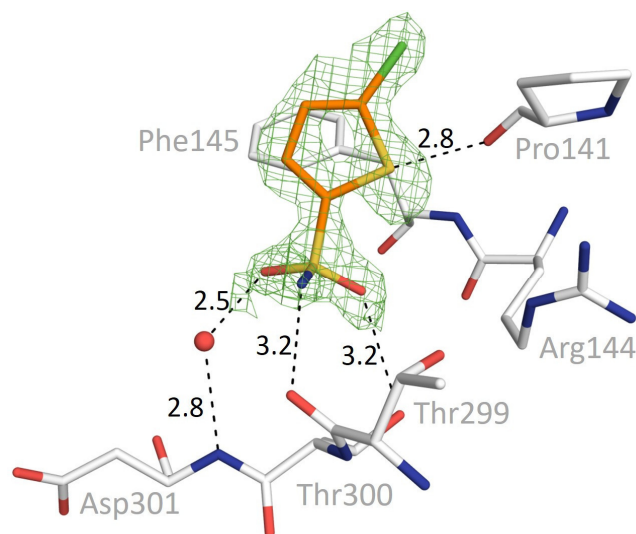


Figure 233: Detailed-view of interaction pattern of fragment J94 with PKA. The green mesh represents the unbiased  $F_o-F_c$  electron density at  $3.0 \sigma$ .

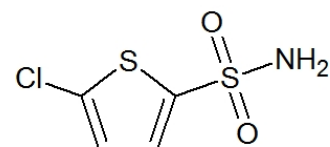


Figure 232: Chemical structure of fragment J94.

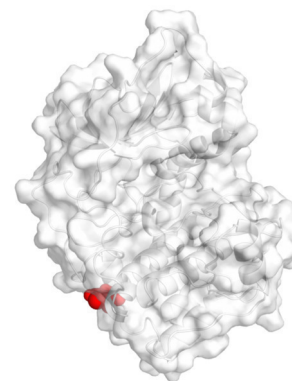


Figure 234: Overview of binding position of fragment J94 on PKA.

### Binding keywords:

Remote binding, direct interaction to Pro141 and Thr300, water bridge to Asp301

### Detailed description of protein-ligand interaction:

Pertaining the binding position of J94 in the  $\beta$ -sheet pocket, some similarities are apparent for the second binding pose. Also here, the occupancy refines to 74%. The fragment locates in a remote position between the hydrophobic F- $\alpha$ -helix and the long C-terminal loop. At this position, the sulphonamide group is better represented by the electron density whereas the chlorine is less well-defined. A direct H-bond is formed to the hydroxyl group of Thr300 via the sulphonamide oxygen, (3.2 Å). The second oxygen of this group uses a water-mediated contact to the backbone nitrogen of Asp301 (distances: 2.5 and 2.8 Å). The sulphonamide nitrogen forms an H-bond with the backbone carbonyl oxygen of Thr299. Further interaction with the protein is observed via the backbone carbonyl oxygen of Pro141 and the sulfur atom of the thiophene ring (2.8 Å).<sup>134</sup> The surface binding of J94 occurs in proximity to a neighbouring symmetry-related PKA molecule. The carboxylate group of Glu334', which is usually in contact with Arg144 in PKI-free PKA crystals, is also close to the ligand's nitrogen with a distance of 3.2 Å (not shown).

## Pim1 - F3 (PDB 5N4Z) – 2.26 Å

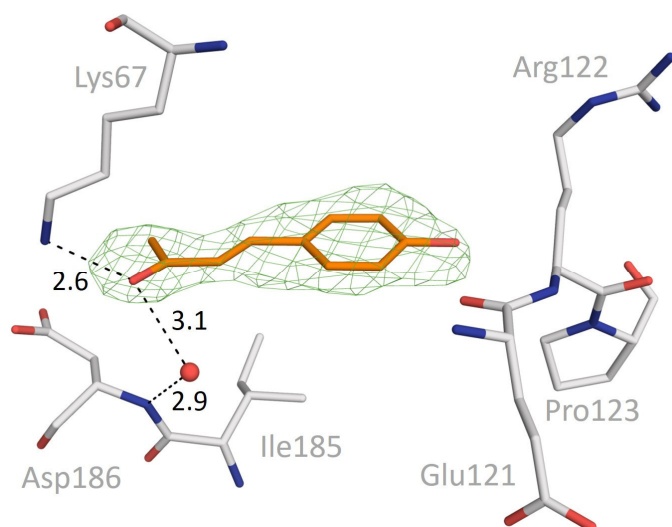


Figure 236: Detailed-view of interaction pattern of fragment F3 with Pim1. The green mesh represents the unbiased  $F_o-F_c$  electron density at  $3.0 \sigma$ .

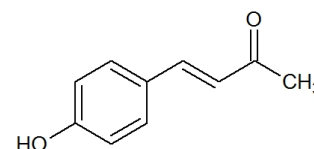


Figure 235: Chemical structure of fragment F3.

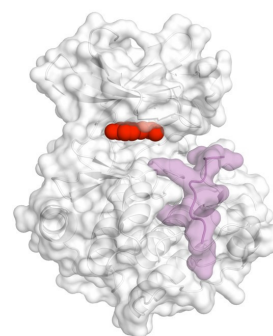


Figure 237: Fragment F3 is marked in red, PIMTIDE in violet.

### Binding keywords:

ATP-binding site, direct interaction with Lys67, water bridge to Asp186

### Detailed description of protein-ligand interaction:

Fragment F3 resembles a cinnamic acid derivative with a terminal methyl keto group at the place of the carboxylate group and a hydroxy group attached to the benzene ring. The ketone oxygen interacts through a short distance with the ammonium group of Lys67 (2.6 Å). A second polar interaction to the protein is mediated between the ketone oxygen and the backbone nitrogen of Asp186 by a water molecule. This water molecule is 3.1 Å apart from the ketone oxygen and 2.9 Å from the backbone nitrogen of Asp186. Although the ligand extends in the direction of the hinge, here, no polar interaction is formed to this motif. The distance of 3.8 Å between the phenolic oxygen and the adjacent backbone carbonyl oxygen is too long to establish an H-bond interaction.

## Pim1 - F72 (PDB 5N4N) – 2.09 Å

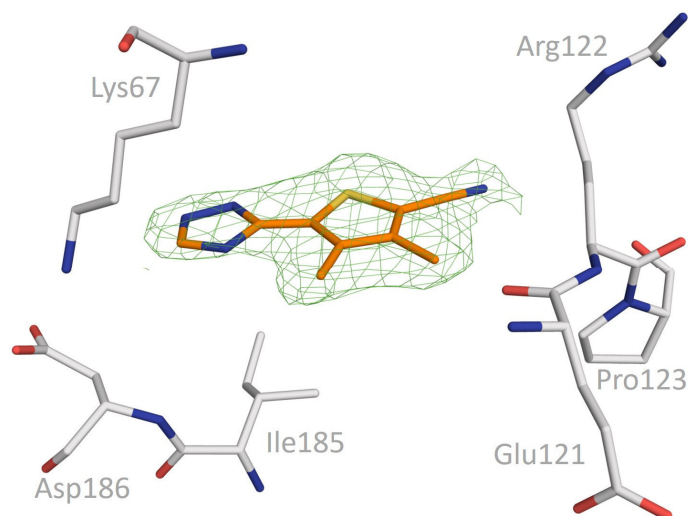


Figure 239: Detailed-view of interaction pattern of fragment F72 with Pim1. The green mesh represents the unbiased  $F_o-F_c$  electron density at  $3.0 \sigma$ .

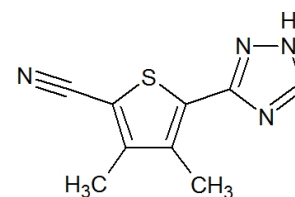


Figure 238: Chemical structure of fragment F72.

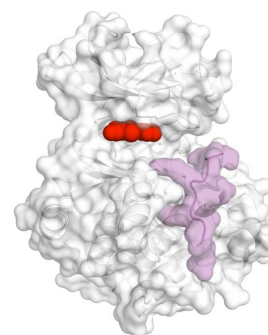


Figure 240: Fragment F72 is marked in red, PIMTIDE in violet.

### Binding keywords:

ATP-binding site, no polar contacts / interactions

### Detailed description of protein-ligand interaction:

For fragment F72 no polar interaction can be recognised. The planar compound fits ideal into the ATP-binding pocket of Pim1. The fragment is sandwiched between the hydrophobic side chain residues of the ATP-binding pocket (Leu44, Val52, Ala62, Leu174, and Ile185). The two methyl substituents at the thiophene ring expand towards the hinge region, whereas the spatially more demanding sulfur atom is closer to the pocket entrance, where the protein opens to the neighbourhood. The triazole moiety orients towards the catalytically important amino acids Lys67 and Asp186 without forming an H-bond interaction. The distance from the triazole moiety to Lys67 is  $4.3 \text{ \AA}$ , whereas the distance to Asp186 is  $5.2 \text{ \AA}$ . The nitrile moiety points in the direction of the prolonged part of the hinge region, where Pro125 and Glu124 are located. Although the relatively flexible side chain of Glu124 seems to be oriented towards the nitrile group, it is with  $4.3 \text{ \AA}$  too far away for direct interaction. Nevertheless, the ligand seems to be well-positioned in the ATP-binding pocket in the entirely defined electron density showing a good RSCC value of 0.92.

## Pim1 - F80 (PDB 5N50) – 1.92 Å

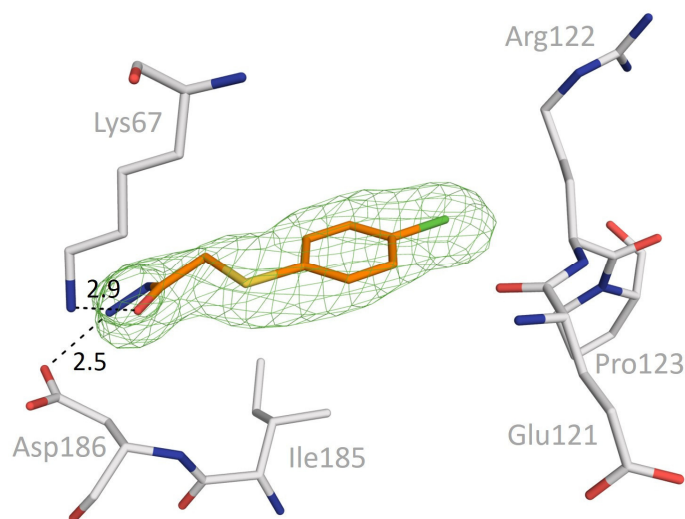


Figure 242: Detailed-view of interaction pattern of fragment F80 with Pim1. The green mesh represents the unbiased  $F_o-F_c$  electron density at  $3.0 \sigma$ .

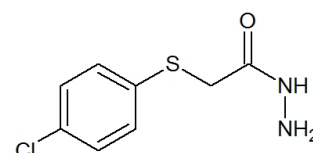


Figure 241: Chemical structure of fragment F80.

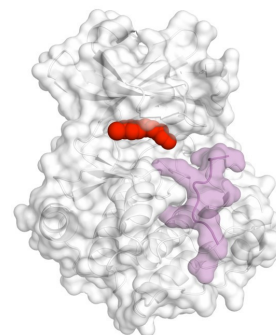


Figure 243: Fragment F80 is marked in red, PIMTIDE in violet.

### Binding keywords:

ATP-binding site, direct interaction with Lys67 and Asp186

### Detailed description of protein-ligand interaction:

The chloro-substituted benzene ring of F80 is sandwiched between two hydrophobic side chain residues of the ATP-binding pocket (Ala65 and Leu174). These residues are situated above and below the aromatic plane of the ring. The chlorine atom of F80 extends in the direction of Pro125, which is at the C-terminal end of the hinge. Nevertheless, no direct interaction with the hinge is observed. Instead, the hydrazide group of F80 interacts with two side chain residues of Pim1. The carbonyl oxygen of the hydrazide group forms an H-bond to the ammonium group of Lys67, which is at a distance of 2.9 Å. The terminal nitrogen of the hydrazide group is likely charged, thus, a salt bridge is experienced with the negatively charged carboxylate group of Asp186 via 2.5 Å distance. Although all polar interactions are located in the phosphate pocket, the lowest B-value is found for the benzene ring of the fragment ( $38.9 \text{ \AA}^2$ ), and the largest is assigned to the terminal hydrazide nitrogen ( $65.7 \text{ \AA}^2$ ).



## Pim1 - F84 (PDB 5N4O) – 2.22 Å

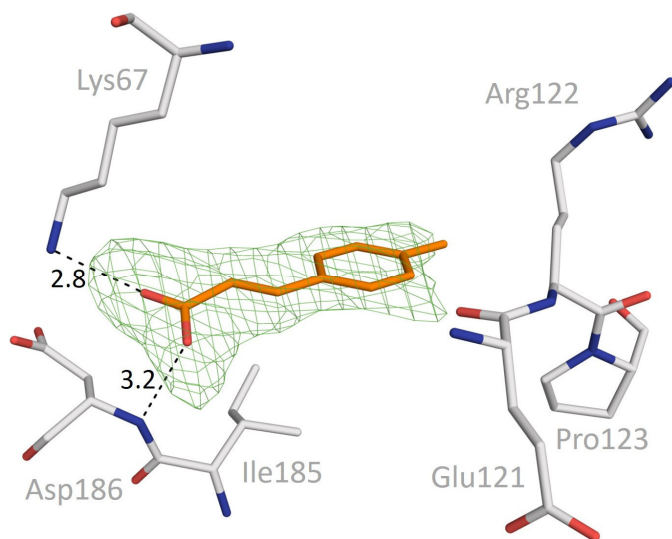


Figure 245: Detailed-view of interaction pattern of fragment F84 with Pim1. The green mesh represents the unbiased  $F_o-F_c$  electron density at  $3.0 \sigma$ .

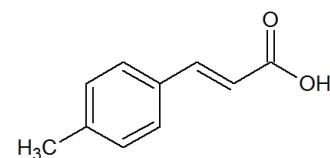


Figure 244: Chemical structure of fragment F84.

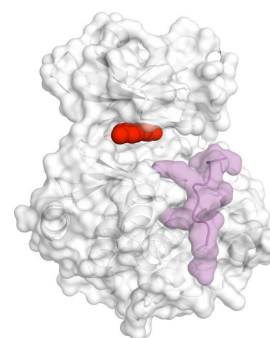


Figure 246: Fragment F84 is marked in red, PIMTIDE in violet.

### Binding keywords:

ATP-binding site, salt bridge to Lys67, direct interaction with Asp186 backbone

### Detailed description of protein-ligand interaction:

F84 is a cinnamic acid derivative and binds in the ATP-binding pocket of Pim1. All atoms of the compound adopt a planar arrangement. The benzene ring is placed between the two hydrophobic side chains of Ala65 and Leu174 in this pocket, which are located above and below the ring plane. The carboxylate group of the compound forms the polar interactions with protein residues. With a  $pK_a$  value of ca. 4.4<sup>97</sup> the carboxylate group will be deprotonated and negatively charged. The ammonium group of Lys67 is likely positively charged forming a salt bridge to the fragment (distance: 2.8 Å). Additionally, the carboxylate group acts as an H-bond acceptor for the backbone nitrogen of Asp186. (3.2 Å).

## Pim1 - F159 (PDB 5N4R) – 2.13 Å

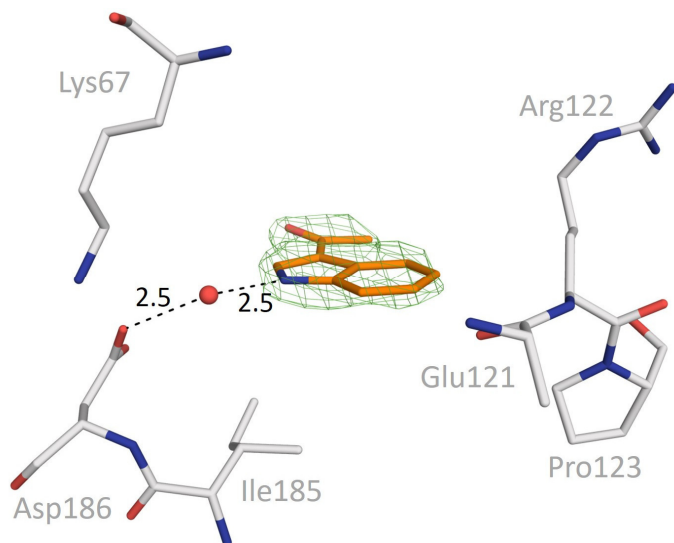


Figure 248: Detailed-view of interaction pattern of fragment F159 with Pim1. The green mesh represents the unbiased  $F_o-F_c$  electron density at  $3.0 \sigma$ .

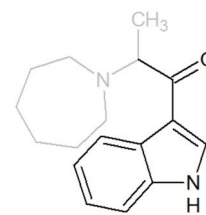


Figure 247: Chemical structure of fragment F159.

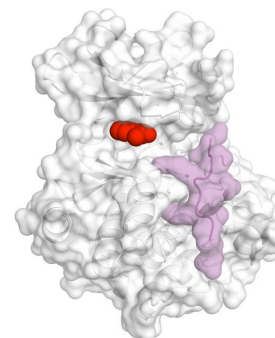


Figure 249: Fragment F159 is marked in red, PIMTIDE in violet.

### Binding keywords:

ATP-binding site, water bridge to Asp186 side chain

### Detailed description of protein-ligand interaction:

Although the difference electron density for F159 is visible in the ATP-binding pocket of Pim1, only a part of the fragment can be assigned to the density. The indole bicyclic system and the carbonyl group with the adjacent methylene carbon are indicated by the electron density ( $F_o-F_c$ ). The only polar protein-ligand interaction is a water-mediated contact between the indole nitrogen and the carboxylate group of Asp186. The water molecule is found in 2.5 Å distance to protein and ligand. The fragment does not form a direct interaction to the hinge region. The azepane ring with a most likely positively charged amino group is not visible in the density in the ribose pocket, where the pocket opens to the surrounding environment. Likely enhanced residual mobility of the ligand is given in this region. Asp128 is found in this area. However, its side chain is in contact with Arg6 of PIMTIDE, preventing interaction with the fragment.

## Pim1 - F167 (PDB 5N4U) 2.20 Å

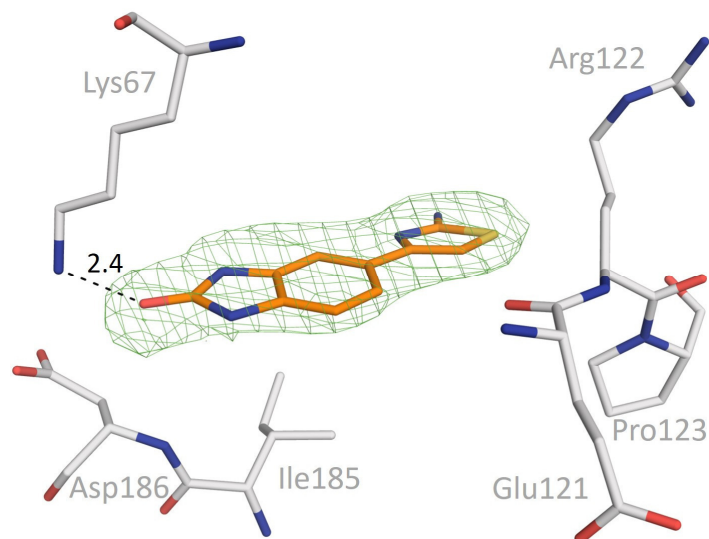


Figure 251: Detailed-view of interaction pattern of fragment F167 with Pim1. The green mesh represents the unbiased  $F_o-F_c$  electron density at  $3.0 \sigma$ .

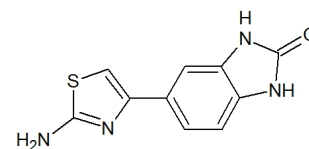


Figure 250: Chemical structure of fragment F167.

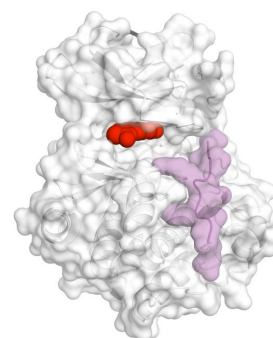


Figure 252: Fragment F167 is marked in red, PIMTIDE in violet.

### Binding keywords:

ATP-binding site, direct interaction with Lys67

### Detailed description of protein-ligand interaction:

F167 binds in the ATP-binding pocket of Pim1. Although there is no direct interaction with the hinge region observed, the fragment is fully defined by the difference electron density and extends from the phosphate binding pocket towards Pro125 (not shown). The occupancy refines to 100%. The fragment shows only one polar contact to the ammonium group of Lys67 using its carbonyl oxygen of the urea moiety. A short H-bond of 2.4 Å distance is formed. The water molecule that is usually found next to the backbone nitrogen of Asp186 is replaced in this complex by the ligand. The lowest B-value is assigned to one carbon atom of the benzene ring with 38.1 Å<sup>2</sup>, whereas the highest one is found for the exocyclic amino group of the thiazole moiety (65.4 Å<sup>2</sup>).

## Pim1 - F184 (PDB 5N4V) – 1.85 Å

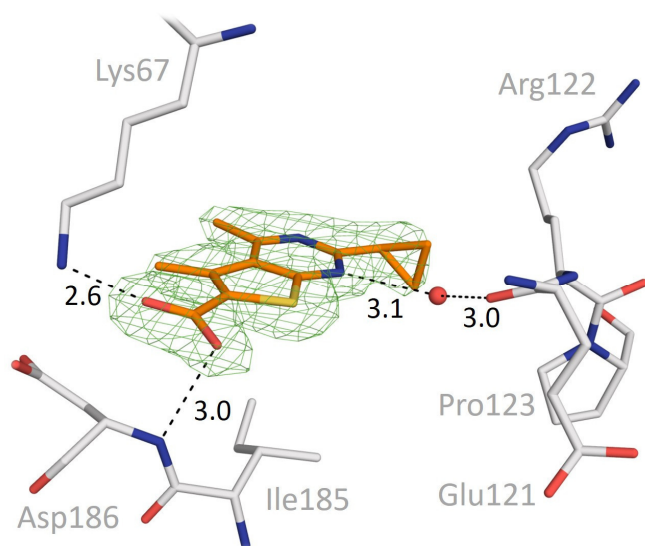


Figure 254: Detailed-view of interaction pattern of fragment F184 with Pim1. The green mesh represents the unbiased  $F_o-F_c$  electron density at  $3.0 \sigma$ .

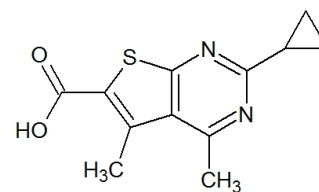


Figure 253: Chemical structure of fragment F184.

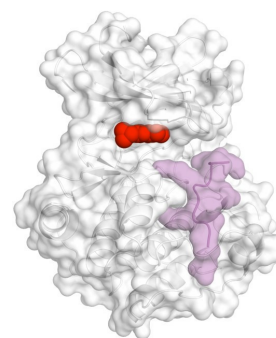


Figure 255: Fragment F184 is marked in red, PIMTIDE in violet.

### Binding keywords:

ATP-binding site, water bridge to Glu121, direct interaction with Lys67 and Asp186

### Detailed description of protein-ligand interaction:

Fragment F184 was detected in the ATP-binding pocket of Pim1. Mediated by a water molecule the compound interacts with the backbone carbonyl oxygen of Glu121. The water molecule is at a distance of  $3.0 \text{ \AA}$  to the latter and  $3.1 \text{ \AA}$  apart from the nitrogen of the pyrimidine moiety. Two further direct interactions to the protein are observed: To the ammonium group of Lys67 and to the backbone nitrogen of Asp186. The carboxylate group of F184 is most likely deprotonated with a  $pK_a$  value of  $4.8^{97}$  and Lys67 is likely charged. Thus, a salt bridge is formed with  $2.6 \text{ \AA}$  distance. The other carboxylate oxygen is in  $3.0 \text{ \AA}$  distance forming an H-bond to Asp186. Although an anomalous signal could not be observed for the sulfur atom of F184, its position is confirmed by the strong electron density peak ( $13.3 \sigma$ ;  $F_o-F_c$ ).

## Pim1 - F200 (PDB 5NDT) – 1.99 Å

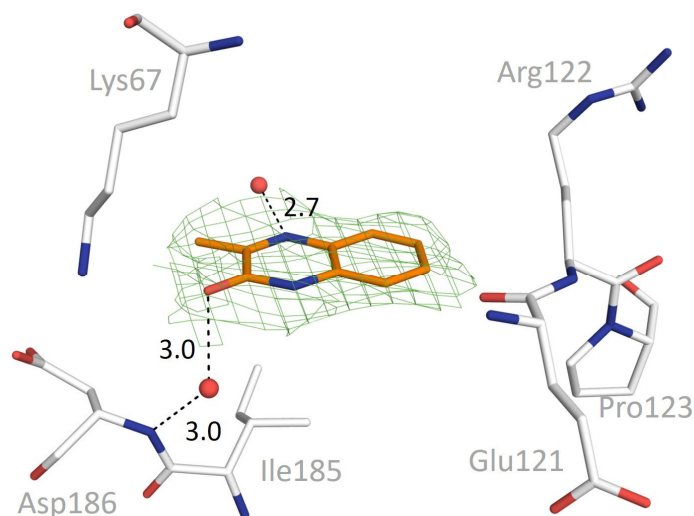


Figure 257: Detailed-view of interaction pattern of fragment F200 with Pim1. The green mesh represents the unbiased  $F_o-F_c$  electron density at  $3.0 \sigma$ .

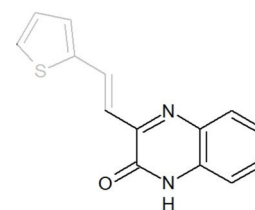


Figure 256: Chemical structure of fragment F200.

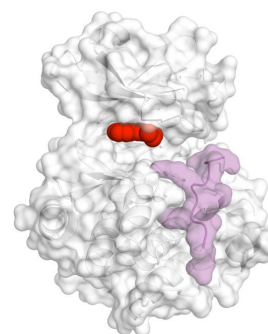


Figure 258: Fragment F200 is marked in red, PIMTIDE in violet.

### Binding keywords:

ATP-binding site, water bridge to Asp186

### Detailed description of protein-ligand interaction:

Fragment F200 contains a thiophene moiety attached by an ethene linker to the heterocycle of the compound. The observed electron density ( $F_o-F_c$ ) in the ATP-binding pocket suggests a putative placement of the latter heterocycle. It is likely that the side chain with the double bond and the terminal thiophene ring is scattered over multiple arrangements. However, modelling considerations do not support the attempted placement of the heterocycle. Possibly, it points towards the opening of the ATP pocket. The only direct polar interaction with the protein is mediated by a water molecule. The contact to the ligand could be performed by the lactam carbonyl group of F200 to the backbone nitrogen of Asp186 ( $3.0 \text{ \AA}$  for both H-bonds). The compound does not interact with the hinge nor with the Lys67 side chain. Nevertheless, the fragment fixes a water molecule at a distance of  $2.7 \text{ \AA}$  by the endocyclic nitrogen (B-value:  $61.2 \text{ \AA}^2$ ).

## Pim1 - F222 (PDB 5MZL) – 1.95 Å

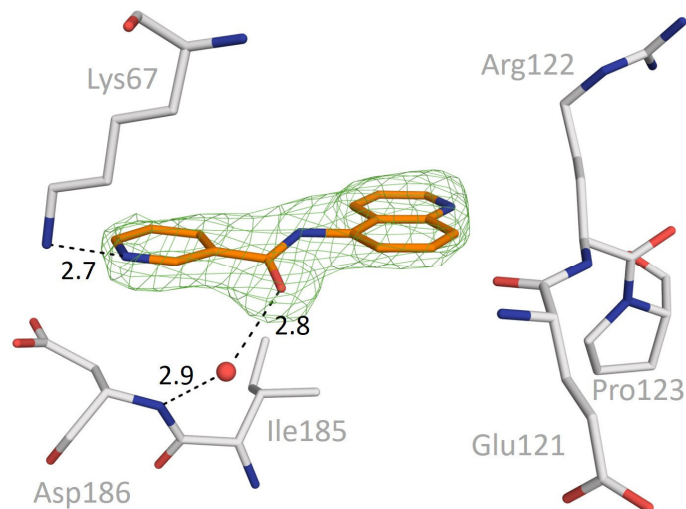


Figure 260: Detailed-view of interaction pattern of fragment F222 with Pim1. The green mesh represents the unbiased  $F_o-F_c$  electron density at  $3.0 \sigma$ .

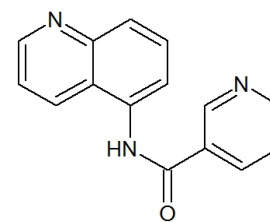


Figure 259: Chemical structure of fragment F222.

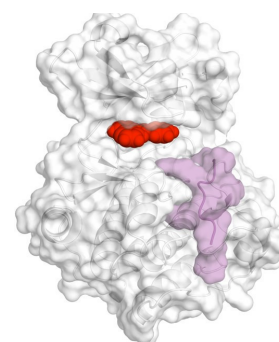


Figure 261: Fragment F222 is marked in red, PIMTIDE in violet.

### Binding keywords:

ATP-binding site, direct interaction with Lys67, water bridge to Asp186

### Detailed description of protein-ligand interaction:

Fragment F222 binds in the ATP-binding pocket of PKA and interacts with two protein residues. The pyridine ring of the compound forms an H-bond with the ammonium group of Lys67, which is 2.7 Å apart from it. The pyridine ring is likely deprotonated to undergo this interaction. With a mean  $pK_a$  value of ca. 5.2 for pyridine moieties<sup>97</sup> and a pH of 7.0 of the buffer, the deprotonated state seems reasonable. The second protein-ligand interaction is mediated by a water molecule. This water molecule is often found in Pim1 complexes and binds to the backbone nitrogen of Asp186. It is at a distance of 2.9 Å to this nitrogen atom and bridges the distance of 2.8 Å to the carbonyl oxygen of F222. Although the nitrogen atom of the quinoline ring is oriented towards the hinge region, no polar interaction with that part of the protein is observed.

## Pim1 - F225 (PDB 5N4X) – 2.20 Å

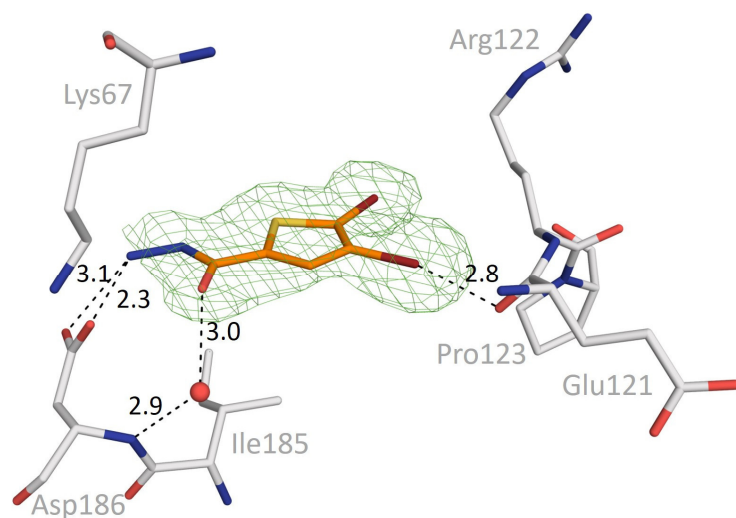


Figure 263: Detailed-view of interaction pattern of fragment F225 with Pim1. The green mesh represents the unbiased  $F_o-F_c$  electron density at  $3.0 \sigma$ .

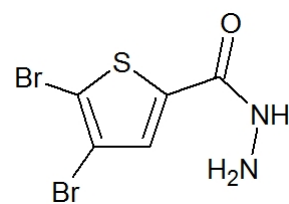


Figure 262: Chemical structure of fragment F225.

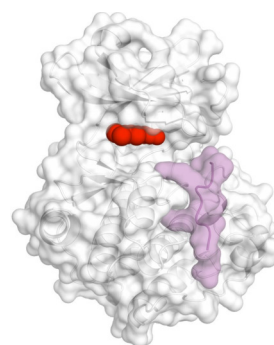


Figure 264: Fragment F225 is marked in red, PIMTIDE in violet.

### Binding keywords:

ATP-binding site, Halogen bond to Glu121, direct interaction with Asp186, water bridge to Asp186

### Detailed description of protein-ligand interaction:

The difference electron density of F225 is found in the ATP-binding pocket of Pim1. The two bromine atoms of F225 give rise to strong anomalous signals and confirm fragment binding. Similar to the binding of fragment F230, F225 forms a halogen bond to the backbone carbonyl oxygen of Glu121 with an angle of approx.  $159^\circ$  through a short distance of 2.8 Å. A query (distance 0.0 - 3.0 Å, C-Br - O angle  $140^\circ - 180^\circ$ , C=O - Br angle  $110^\circ - 180^\circ$ ) in the CSD revealed that even shorter distances than 2.8 Å are possible (167 entries). The likely protonated terminal nitrogen of the hydrazide group is in close contact (distance: 2.3 Å) with the side chain carboxylate group of Asp186. The carbonyl oxygen of the hydrazide moiety forms a water-mediated contact to the backbone nitrogen of Asp186. The water molecule is at a distance of 3.0 Å to the carbonyl oxygen and 2.9 Å to the backbone nitrogen of Asp186. In comparison to other fragments of the series, F225 induces a side chain flip of Asp186 in the direction of the ligand to establish the H-bond. By this, the fragment links the hinge region of Pim1 with the DFG loop.

## Pim1 - F230 (PDB 5N51) – 2.12 Å

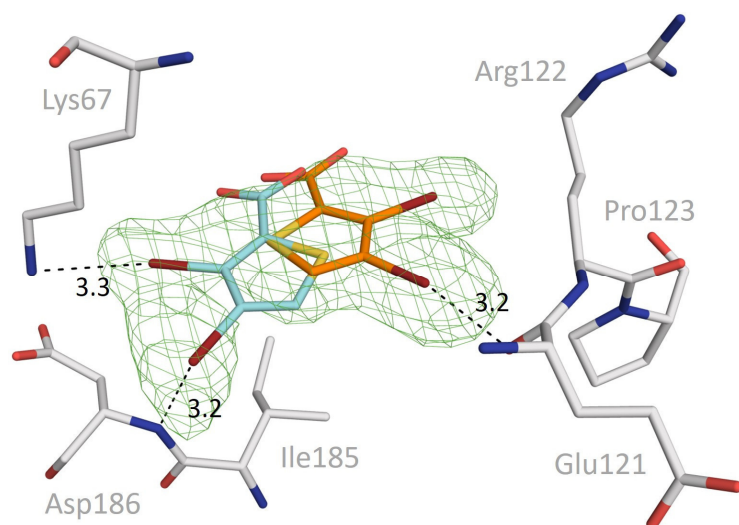


Figure 267: Detailed-view of interaction pattern of fragment F230 with Pim1. The green mesh represents the unbiased  $F_o - F_c$  electron density at  $3.0 \sigma$ .

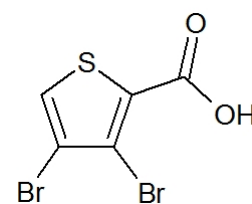


Figure 265: Chemical structure of fragment F230.

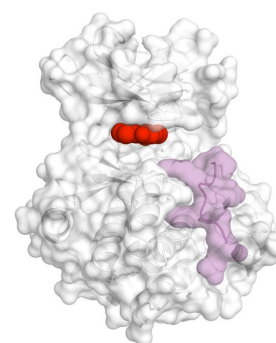


Figure 266: Fragment F230 is marked in red, PIMTIDE in violet.

### Binding keywords:

ATP-binding site, Halogen bond to hinge, Lys67 ammonium and Asp186 backbone

### Detailed description of protein-ligand interaction:

F230 binds in the ATP-binding pocket of Pim1. The two bromine atoms of the fragment give rise to anomalous signals, which are detected for the first orientation of the fragment (orange carbon atoms). The second orientation (cyan carbon atoms) does not show anomalous signals either for the two bromine or the sulfur atoms. This arrangement is less occupied (32%), whereas the first one results in 68% occupancy. One of the bromine atoms of the first orientation approaches the backbone carbonyl oxygen of Glu121 (distance: 3.2 Å), forming a halogen bond. The angle between carbon atom, bromine atom, and carbonyl oxygen is approx. 163°. These geometric dimensions match with other halogen bonds, where the so-called partially (electro)positive cap at the top of the bromine atom experiences an electrostatic attraction with the carbonyl oxygen of Glu121.<sup>90</sup> In the second (cyan) orientation one bromine atom forms an H-bond to the ammonium group of Lys67 and the second to the backbone nitrogen of Asp186 (distance of 3.3 Å and 3.2 Å respectively). Hydrogen bonds formed to halogens are rather weak, and obviously, the only polar interaction with the protein is formed by the fragment in the second arrangement. Possibly this explains the lower occupancy of the second orientation.



## Pim1 - F301 (PDB 5N4Y) – 2.56 Å

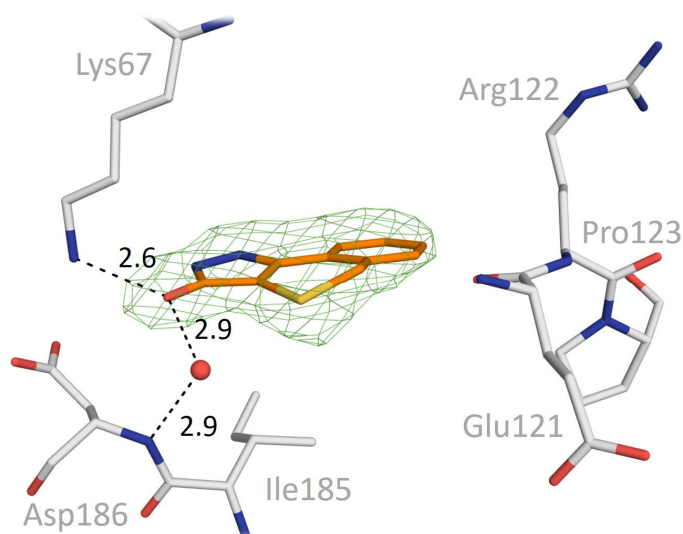


Figure 269: Detailed-view of interaction pattern of fragment F301 with Pim1. The green mesh represents the unbiased  $F_o-F_c$  electron density at  $3.0 \sigma$ .

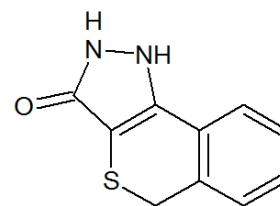


Figure 268: Chemical structure of fragment F301.

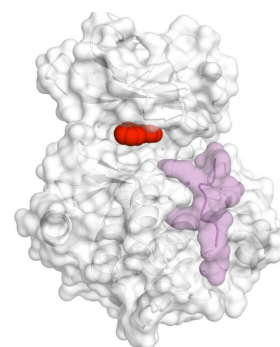


Figure 270: Fragment F301 is marked in red, PIMTIDE in violet.

### Binding keywords:

ATP-binding site, direct interaction with Lys67, water bridge to Asp184

### Detailed description of protein-ligand interaction:

Although the final resolution of this data set is only 2.56 Å, the electron density for F301 is well-defined. The fragment binds in the ATP-binding pocket of Pim1, but no direct polar interaction with the hinge region is detected. The carbonyl oxygen of the pyrazolone moiety is the only atom involved in polar interactions with the protein. One H-bond is formed to the ammonium group of Lys67 with a distance of 2.6 Å. The second contact to the protein is mediated by a water molecule to the backbone nitrogen of Asp186. The distance from this water molecule to the latter and to the carbonyl oxygen of F230 is 2.9 Å. The benzothiopyran is sandwiched by the hydrophobic side chains of Leu44, Val52, Ala62, Leu174 and Ile185 forming hydrophobic contacts to the protein. The sulfur atom of the ligand does not show an anomalous signal. However, despite the low structural resolution, the position of the sulfur atom is indicated by a higher electron density peak at  $6.9 \sigma$  ( $F_o-FC$ ).

## Pim1 - F331 (PDB 5N52) – 2.25 Å

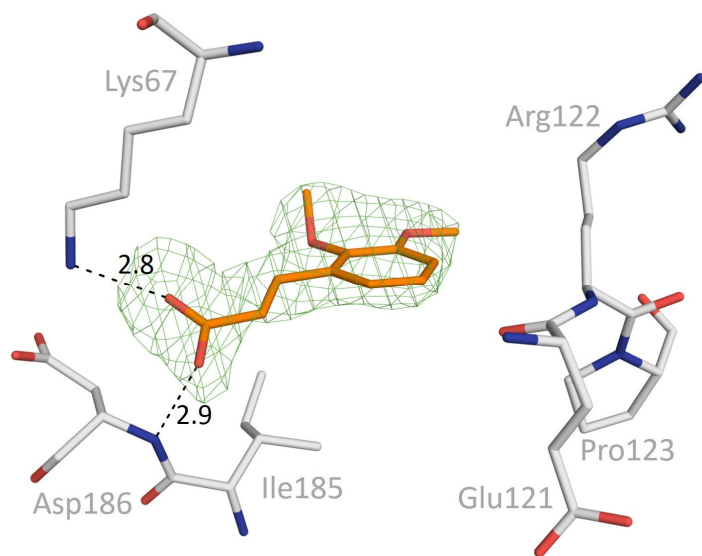


Figure 272: Detailed-view of interaction pattern of fragment F331 with Pim1. The green mesh represents the unbiased  $F_o-F_c$  electron density at  $3.0 \sigma$ .

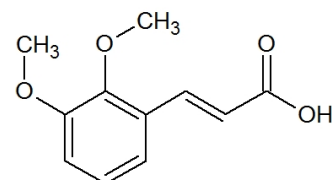


Figure 271: Chemical structure of fragment F331.

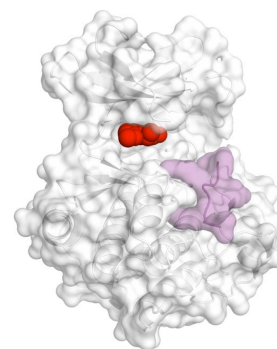


Figure 273: Fragment F331 is marked in red, PIMTIDE in violet.

### Binding keywords:

ATP-binding site, salt bridge to Lys67, direct interaction with Asp186's backbone

### Detailed description of protein-ligand interaction:

Fragment F331 is a cinnamic acid derivative with two methoxy groups in ortho- and meta-position to the attached ethylene linker. The ligand is most likely negatively charged. Thus, a salt bridge to the positively charged ammonium group of Lys67 is formed (2.8 Å). Cinnamic acid has a  $pK_a$  value of approx. 4.4<sup>97</sup>, which suggests full deprotonation at a pH of 7.0. In a similar distance (2.9 Å) to the second oxygen atom of this group interacts with the backbone nitrogen of Asp186, the latter donates a hydrogen for the H-bond. The electron density shows that the ethylene linker is in transoid geometry to the ortho methoxy group. Searches in the CSD reveal that this orientation is exclusively found for complexes with ortho substituents. The shape of the electron density distribution strongly supports the selected orientation of the benzene ring and the meta methoxy group is oriented outside the ring plane for steric reasons. No polar interaction with any hinge residues is observed.

## Pim1 - ZINC72154357 (PDB 5N5M) – 2.21 Å

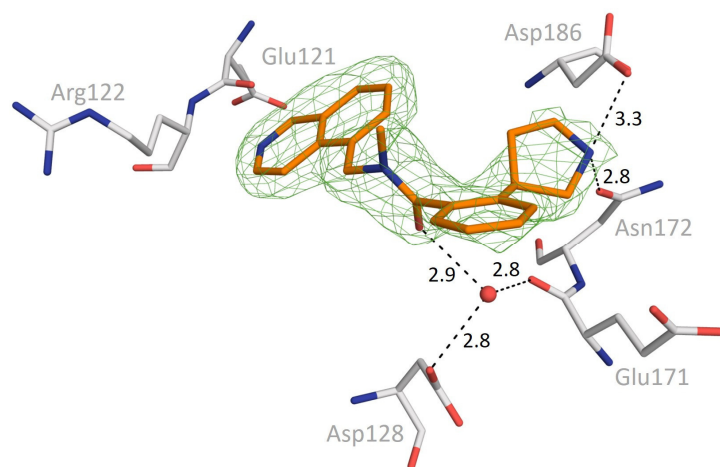


Figure 276: Detail-view of interaction pattern of ZINC72154357 with Pim1. The green mesh represents the unbiased  $F_o-F_c$  electron density at  $3.0 \text{ \AA}$ .

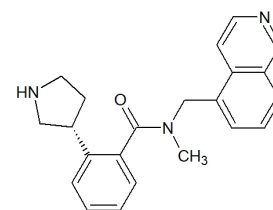


Figure 274: Chemical structure of ZINC72154357.

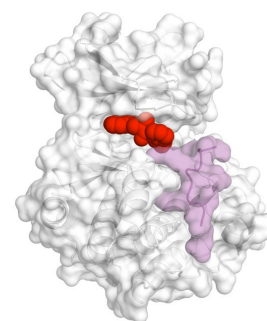


Figure 275: ZINC72154357 is marked in red, PIMTIDE in violet.

### Binding keywords:

ATP-binding site, direct interaction with Asn172 and Asp186, water bridge to Asp128 and Glu171

### Detailed description of protein-ligand interaction:

The compound ZINC72154357 binds close to the adenosine and phosphate pocket of Pim1. The planar isoquinoline ring binds in proximity to the hinge (distance:  $3.4 \text{ \AA}$ ), but without forming any direct polar interactions. The central peptide bond between isoquinoline and benzene moiety is arranged almost perpendicular to the isoquinoline plane. A water molecule, which is at a distance of  $2.9 \text{ \AA}$  to the carboxamide oxygen, bridges the distance to the side chain carboxylate group of Asp128 and to the backbone carbonyl oxygen of Glu171. A pyrrolidine ring is attached to the benzene ring in the ortho position with respect to the peptide bond. Its secondary amino group is most likely protonated and positively charged. Although this positive charge would make the ligand competent to form a salt bridge with the side chain of Asp186, for steric reasons it is  $3.3 \text{ \AA}$  apart, and no salt bridge with ideal geometry could be formed. The amino group is much closer to the carboxamide oxygen of the side chain of Asn172 (distance:  $2.8 \text{ \AA}$ ) forming a short H-bond.

## Pim1 - ZINC09314085 (PDB 5N5L) – 1.97 Å

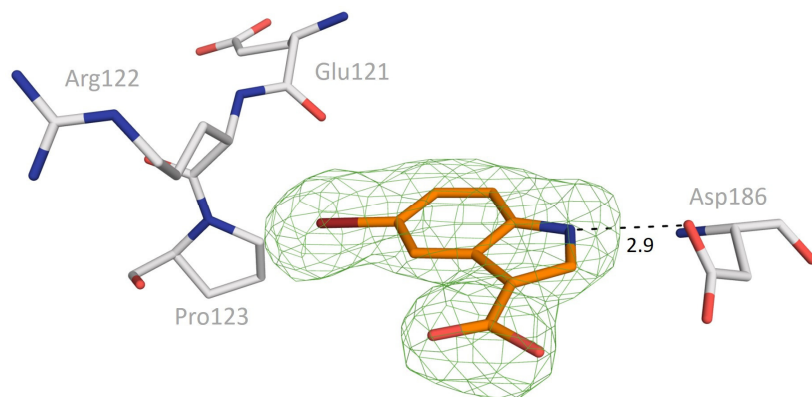


Figure 279: Detail-view of interaction pattern of ZINC09314085 with Pim1. The green mesh represents the unbiased  $F_o-F_c$  electron density at  $3.0 \sigma$ .

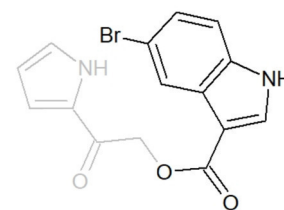


Figure 277: Chemical structure of ZINC09314085.

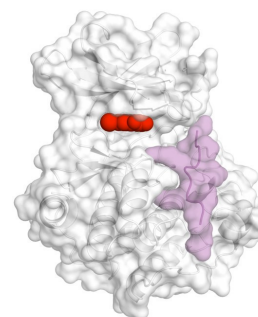


Figure 278: ZINC09314085 is marked in red, PIMTIDE in violet.

### Binding keywords:

ATP-binding site, direct interaction with Asp186

### Detailed description of protein-ligand interaction

Ligand ZINC09314085 could only be partly assigned to the difference electron density in the ATP-binding pocket of Pim1. From the bromine-substituted indole moiety and the attached carboxy ester group the ligand is well-defined. Consequently, the ketone and the terminal pyrrole moiety are not visible. The only polar contact of the ligand with a protein residue is observed via the indole nitrogen. It donates a hydrogen bond to the carboxylate side chain of Asp186 (2.9 Å). The position of the bromine is additionally confirmed by a strong anomalous signal. It is too far away (distance: 4.7 Å) to interact with the backbone carbonyl oxygen of Glu121. The bromine atom points in the direction of Glu124, which is also too far away for interactions. Thus, no direct interaction with the hinge is observed. The missing part of ZINC09314085 is either scattered over multiple orientations or the compound hydrolyzed during the co-crystallisation trials.

## 8.5. Expression, Aufreinigung und Kristallisation der PKA

### Protein Informationen

Name: cAMP-abhängige Protein Kinase katalytische Untereinheit Alpha (PKA)

Klassifikation: Transferase

Organismus: *Cricetulus griseus* (Chinesischer Hamster)

Mutation: Keine

Aminosäure Sequenz:

10	20	30	40	50
MGNAAA	AKKG	SEQESV	KEFL	AKAKEE
FLKK	WESPSQ	NTAQ	LDHFDRI	KTLL
60	70	80	90	100
GTGSFGR	VML	VKHKET	GNHY	AMKILD
KQKV	VKLKQIE	HTL	NEKRIL	QAVN
110	120	130	140	150
FPFLVK	LEFS	FKDNSN	LYMV	MEYVPG
GEMF	SHLRRIG	RFS	EPHARFY	AAQ
160	170	180	190	200
IVLTFEY	LHS	LDLIYR	DLKP	ENLLID
QGY	IQVTD	DFGFAK	RVKGR	TWTL
210	220	230	240	250
GTPEYL	APEI	ILSKGY	NKAV	DWWALG
VLIY	EMAAGY	PPFF	ADQPIQ	IYIEK
260	270	280	290	300
IVSGKVR	FPS	HFSSDL	KDLL	RNLLQV
DLTK	RFGNLK	NGVN	DIKNHK	WFAT
310	320	330	340	350
TDWIAI	YQRK	VEAPFI	PKFK	GPGDTS
SNFDD	YEEEEI	RVSI	NEKCGK	EFTE

F

### Expression - Klonen und Transformation

Die kodierende DNA Sequenz der PKA wurde in die NdeI/BamHI-Stelle eines pET16bTev Vektor (Novagen) mit einer Schnittstelle für eine TEV-Protease (tobacco etch virus) nahe des „His<sub>7</sub>-Tags“ geklont. Dieses Konstrukt wurde anschließend in einen BL21 (DE3)/pLysS *E. coli* Stamm von Agilent Technologies transformiert.

Nach der Transformation besaßen die *E. coli* Bakterien eine Ampicillin- und Chloramphenicol-Resistenz, die zur Selektion auf einer antibiotischen Agar-Agar-Platte genutzt wurde. Die isolierten Zellen wurden in 10 mL LB-medium transferiert. (Peptone aus CASEIN, Hefe, NaCl und Wasser), welches zusätzlich die beiden Antibiotika enthielt. Das Medium wurde über Nacht bei 37°C im Schüttler inkubiert. Die dadurch entstehende Suspension aus LB-Medium und *E. coli* Zellen wurde zur Erstellung von „Glycerol-Stocks“ oder direkt als Startpunkt für eine Expression genutzt.

## **Expression - Zell Vermehrung und Protein Expression**

Üblicherweise wurde mit einer Übernachtskultur (ÜNK) begonnen. Eine ÜNK besteht aus LB-Medium, den genannten Antibiotika und wurde jeweils am Tag vor der Hauptexpression aus einem Glycerol-Stock oder der Kultur nach der Transformation angeimpft. Eine ÜNK wurde über Nacht bei 37°C im Schüttler inkubiert. Pro Liter Hauptmedium (ZYM5025) wurden 10 mL ÜNK veranschlagt.

Das ZYM5025 Medium ist dafür bekannt die Expression des Proteins durch die beinhaltende Lactose selbst zu regulieren. Zusätzlich können die Zellen zu einer sehr hohen Zelldichte heranwachsen. Neben den vielen Inhaltsstoffen (siehe Puffer & Media) wurden ebenfalls die beiden Antibiotika hinzugegeben.

Nach dem Überführen der ÜNK in die Hauptkultur wurden die Bakterien für 9 Stunden bei 37°C und 190 rpm im Schüttler inkubiert. Die Temperatur wurde im Anschluss für 58 Stunden auf 20°C gesenkt. Durch die Zugabe von 1 mL Isopropyl-β-D-1-thiogalactopyranoside (IPTG - 1M) pro L Medium bei einer Absenkung auf 20°C konnte die finale Ausbeute an PKA gesteigert werden.

## **Expression – Ernte**

Die Zellen wurden durch Zentrifugation vom Medium getrennt (10.000 rpm für 10 Minuten). Das dabei entstehende Bakterien-Zell-Pellet wurde im Anschluss bei -80°C weggefroren oder direkt für einen Aufreinigungsprozess verwendet.

## **Aufreinigung – Resuspension**

Zum Resuspendieren der Zellpellets wurde der Puffer der ersten Säule verwendet (Puffer A). Die Menge an Zellen aus 2L ZYM-Medium wurden in 200-250 mL des Puffer A resuspendiert, in dem zuvor 1-2 Protease-Inhibitor-Tabletten (Complete™, EDTA-frei Protease Inhibitor Cocktail von Sigma-Aldrich) gelöst wurden. Mittels Fantaschale und Pistill kann die Suspension gut vorhomogenisiert werden, wurde aber in jedem Fall kurz vor dem Zellaufschluss mit einem ‚Dounce tissue grinder‘ sehr fein homogenisiert um Agglomerate zu vermeiden.

## **Aufreinigung – Zellaufschluss**

Hierfür wurde das Emulsiflex-System von Avestin verwendet. Dabei wurde die Suspension bei einem Gegendruck von 15.000 and 17.000 psi durch das System gepumpt. Nach zwei bis drei Durchläufen waren nahezu alle Zellen aufgeschlossen. Als In-Prozess-Kontrolle wurde auf eine Verdunkelung der Suspension geachtet. Hier musste besonders auf die Kühlung mit Eis geachtet werden, da sich die Suspension während des Druckaufschlusses erwärmt. Im Anschluss wurden

die Zelltrümmer von der Proteinlösung durch Zentrifugation separiert (1-1,5 Stunden bei 20.000 rpm und 4°C).

### **Aufreinigung – Erste Ni<sup>2+</sup> - Säule**

Das Zentrifugat wurde zum Abtrennen grober Partikel durch mehrere Membran-Filter (Porengröße 0,45 µm, Rotilabo<sup>®</sup> -Spritzenfilter) gespritzt. Dieser Reinigungsprozess beschleunigte auch das Beladen der ersten Ni<sup>2+</sup> - Säule (HisTrap HP 5ml, GE Healthcare Life Science).

Die Säule wurde vor dem Beladen mit dem 5-10 fachen Säulenvolumen (SV) mit dem Puffer A unter Einsatz einer Peristaltic pump P-1 (GE Healthcare Life Science) äquilibriert. In Anschluss wurde die Proteinlösung mit einer Flussrate von 3-4 mL / Minute auf die Säule getragen. Zur Kontrolle wurde eine Probe des Durchflusses genommen. Nach dem Beladen wurde die Säule noch mit ca. 5 SV Puffer A gewaschen. Eine Kühlung mit Eis begleitete den ganzen Prozess.

Weitergehend wurde die Säule an eine ÄKTA prime plus oder an das ÄKTA FPLC System angeschlossen, welche zuvor mit den Puffern A und B gespült wurden. Ein erster Waschschrift der Säule wurde mit 100-150 mL von Puffer A durchgeführt. Anschließend wurde der Gehalt an Puffer B auf 4 % angehoben. Bei diesen Schritt wurden unerwünschte Proteine mit geringer Affinität zur Säule von den übrigen getrennt. Nach dem Erreichen einer konstanten UV Absorption bei 4% Puffer B wurde mit dem nächsten Schritt begonnen.

Die Elution der PKA wurde durch das Anlegen eines Konzentrationsgradienten von 4% nach 100% Puffer B über 120 Minuten bei einer Flussrate von 4 mL/min initiiert. Die dabei eluierten Proteine wurden fraktioniert (7-10 mL / Fraktion) aufgefangen. Im Durchschnitt wurde die PKA bei einer Konzentration von 8-10% Puffer B eluiert. Nach der Elution der PKA schloss sich eine Reinigung der Säule mit 100% Puffer B an (5-10 SV).

Zur Kontrolle wurden Proben aus den Randbereichen des Elution-Peaks genommen und durch eine SDS-PAGE Analyse der Anteil an PKA verifiziert. Enthielt eine Fraktion im Verhältnis weniger PKA Protein als unerwünschte Proteine so wurde diese Fraktion verworfen. Für eine SDS-PAGE Analyse wurden zumeist folgende Proben genommen: Filtrat vor der Säule (Pre), Durchfluss der Säule (FT), Waschschrift an der ÄKTA, Fraktionen des Elution-Peaks und der Waschschrift mit 100% Puffer B. Jede Probe wurde im Verhältnis 4:1 mit SDS-Puffer gemischt. Die beiden ersten Proben wurden mit Wasser im Verhältnis 4:1 gemischt und somit die Proteinkonzentration gesenkt, da die Banden ohne diesen Schritt überladen gewesen wären (siehe Abbildung 280).

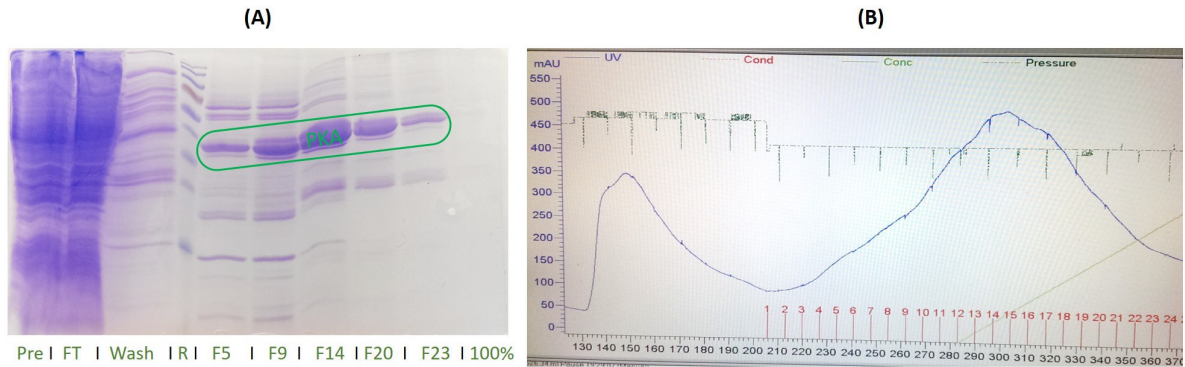


Abbildung 280: **(A)** SDS-gel der ersten  $\text{Ni}^{2+}$ -Säule. Die genommenen Proben sind wie folgt: Pre – Filtrat vor der Säule; FT – Durchfluss; Wash – Waschschrift and der ÄKTA; F5-F23 – Fraktionen des Elutions-Peak; 100% - 100%B Waschung. **(B)** Chromatogramm der ersten  $\text{Ni}^{2+}$ -Säule. Die Y-Achse zeigt die UV-Absorption in mAU und die X-Achse das Volumen in mL. Der erste Peak entsteht durch die Waschung mit 4% Puffer B. Der zweite Peak wird fraktioniert und enthält PKA.

## Aufreinigung – Dialyse I

Die kontrollierten Fraktionen wurden zusammengeführt und in einen Dialyseschlauch von SpectraPore mit einem cut-off von 12-14 kDa überführt. Rund 10 mg der TEV-Protease wurde anschließend hinzugegeben. Für die Dialyse wurden 5L der vorgekühlten Dialyse Puffer I Lösung (Natrium-di-hydrogen-phosphat, di-Natrium-hydrogen-phosphat, NaCl, Dithiothreitol (DTT), entsalztes Wasser (pH 8,0)) verwendet. Dialysiert wurde mindestens über einen Zeitraum von 24 Stunden bei 4°C. Nach 48 Stunden Dialyse wurde allerdings eine erhöhte Ausbeute erzielt, da mehr PKA durch TEV-Protease freigesetzt werden konnte. Der His<sub>7</sub>-Tag und das Imidazol diffundierten bei der Dialyse aus dem Schlauch.

## Aufreinigung – Zweite $\text{Ni}^{2+}$ -Säule

Nach der Dialyse wurde die Proteinlösung noch einmal über die  $\text{Ni}^{2+}$ -Säule geführt. Dafür wurde sie zuvor mit Puffer A2 (natrium-di-hydrogen-phosphat, di-Natrium-hydrogen-phosphat und NaCl) equilibriert. Nach dem Beladen der Proteinlösung erfolgte ein Waschschrift mit dem 5-10 fachen des SV mit Puffer A2. Aufgrund des Entfernens des „His<sub>7</sub>-Tags“ wies die PKA eine sehr geringe Affinität zum Säulenmaterial auf, so dass sie im Durchfluss zu finden war. Nicht freigesetztes Protein mit verbleibenden His<sub>7</sub>-tag band erneut am Säulenmaterial und wurden so von der freigesetzten PKA getrennt. Zur Kontrolle, ob die TEV Protease wirksam war bzw. PKA mit geringer Affinität auf der Säule gebunden hatte, wurde die Säule wiederholt an ein ÄKTA System angeschlossen und ein Konzentrationsgradient von Puffer A2 zu 100 % Puffer B über 50ml und einer Flussrate von 3-4 mL/Minute angelegt. Direkt nach dem Anschluss der Säule konnte eine kleine Menge an PKA mit 100% Puffer A2 eluiert werden. Das so erhaltene Protein wurde ebenfalls zu dem zuvor erhaltenen Durchfluss hinzugegeben. Da die TEV Protease ebenfalls einen His-Tag



besitzt, weist sie auch eine hohe Affinität zum Säulenmaterial auf. Zur Kontrolle boten sich folgende SDS-PAGE-Proben an: Ungeschnittene Proteinlösung (Pre), geschnittene Proteinlösung (Post), Durchfluss der Säule (FT), Waschschrift an der ÄKTA (A2-W.) und die Fraktionen des Gradienten (F2-F6) (siehe Abbildung 281). Auch hier wurde bei dem gesamten Prozess stets auf eine permanente Kühlung mit Eis geachtet. Die PKA enthaltenden Lösungen (FT & A2-W.) wurden für einen weiteren Dialyseschritt vereinigt.

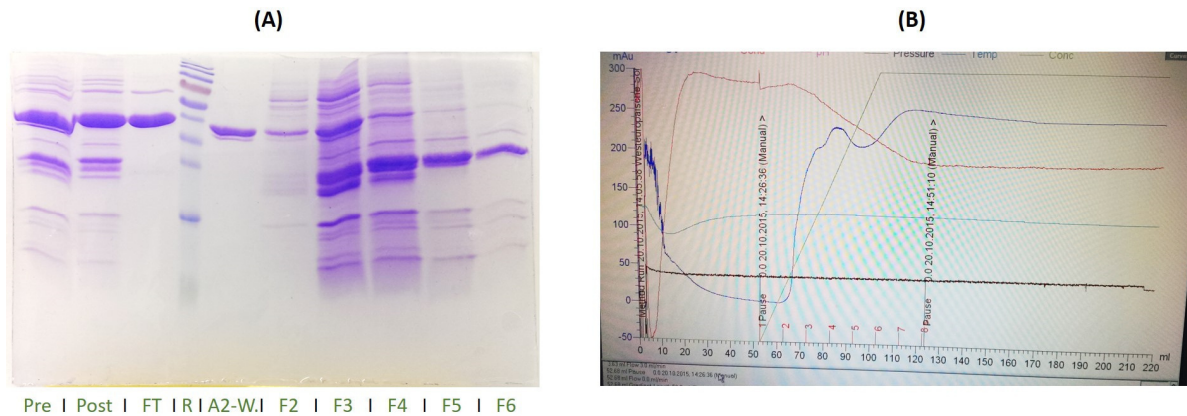


Abbildung 281: **(A)** SDS-Gel der zweiten Ni<sup>2+</sup>-Säule. Die gezeigten Proben sind: Pre – Vor der Dialyse; Post – Nach der Dialyse; FT – Durchfluss ; A2-W. – Waschschrift (Puffer A2); F2 -F6 – Fraktionen des Gradienten. **(B)** Chromatogramm der zweiten Ni<sup>2+</sup>-Säule. Die Y-Achse zeigt die UV-Absorption in mAU, die X-Achse das Volumen in mL.

## Aufreinigung – Dialyse II

Diese Dialyse diente der Vorbereitung für die “Mono S 10/100 GL” Kationen-Austauscher-Säule (GE Healthcare Life Science). Damit Proteine an die Säule binden konnten, wurde die NaCl Konzentration im Puffer durch eine Dialyse reduziert. Der verwendete Dialysepuffer beinhaltete HEPES, NaCl und DTT (pH 7,0). Die Dialyse wurde üblicherweise für 12-13 Stunden über Nacht bei 4 °C durchgeführt; mindestens aber über vier Stunden. Da die reduzierte NaCl-Konzentration auch die Stabilität der PKA verminderte, war eine schnelle Weiterverarbeitung ausschlaggebend für die finale Ausbeute.

## Aufreinigung - Mono S Säule

Die Aufreinigung mit der Mono S Säule erfolgte immer am ÄKTA-FPLC-System. Die dichte Packung des Säulenmaterials benötigte einen stärkeren Druck beim Beladen und Eluieren. Die Säule wurde vor dem Beladen mit Puffer C (HEPES, NaCl und DTT; pH 7,0) äquilibriert.

Gegebenenfalls auftretendes Präzipitat in der Dialyselösung wurde vor dem Beladen mittels Zentrifugation für 15 Min. bei 3500 rpm und 4°C von der Lösung getrennt. Über das Mehrwege-Ventil der ÄKTA und der Verwendung eines „Loops“ wurde die klare Proteinlösung auf die Säule geladen. Im Anschluss erfolgte ein Waschschrift mit rund 50 mL Puffer C.

Die Elution der PKA wurde durch Anlegen eines Konzentrationsgradienten nach 40% Puffer D über 200ml bei einer Flussrate von 2 mL/Minute initiiert. Puffer D beinhaltete 10 mal mehr NaCl als Puffer C. Die eluierten Protein-Peaks wurden in verschiedenen Fraktionen aufgefangen. Die Säule ermöglichte das Auftrennen der unterschiedlichen Phosphorylierungsstufen der PKA, wodurch diese separiert aufgefangen wurden. Die Fraktionen, die dem gleichen Peak entsprechen, wurden anschließend vereint und, nachdem sie in flüssigem Stickstoff schockgefroren waren, bei -80°C gelagert.

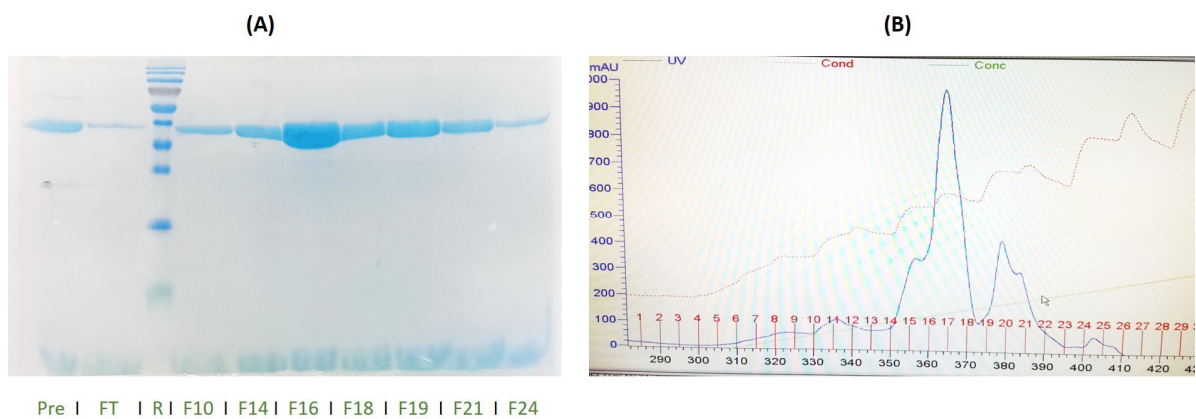


Abbildung 282: **(A)** SDS-Gel der Mono S Säule. Die entnommenen Proben sind wie folgt benannt: Pre – Vor dem Beladen; FT – Durchfluss; R – Protein Größenstandard; F10-F24 – Fraktionen des Gradienten. **(B)** Chromatogramm der Mono S-Säule. Die Y-Achse zeigt die UV-Absorption in mAU und die X-Achse das Volumen in mL.

## Aufreinigung – Ausbeute

Maßgeblich entscheidend für eine hohe Ausbeute war eine komplikationsfreie Protein-Expression und ein akkurates Arbeiten bei der Aufreinigung. Der höchste Wert, der nach einer Aufreinigung erreicht werden konnte, lag bei 67,0 mg PKA pro 1 L Expressionsmedium. Dieser Wert bezieht alle Phosphorylierungsstufen der PKA mit ein. Das Mengenverhältnis der einzelnen Phosphorylierungsstufen variierte je Expressionscharge. Der erst große Elutions-Peak (siehe Abbildung 282) machte aber in jedem Fall den größten Teil der Gesamtmenge aus (ca 60%).

## Kristallisation – Umpufferung

Der Kristallisationspuffer enthielt MES, BIS-TRIS, EDTA, DTT and LiCl bei pH 6,9. Für die Kristallisation wurde PKA entweder direkt aus der Aufreinigung oder aus dem weggefrorenen

Vorrat verwendet. Gegebenenfalls ausgefallenes Protein wurde zuerst abzentrifugiert. Die klare Proteinlösung wurde dann mittels Vivaspin 20 (Sartorius®, 10.000 Da cut off) bei 3500 rpm in der Zentrifuge dreimal aufkonzentriert und mit dem Kristallisationspuffer wieder verdünnt. Anschließend wurde die Lösung auf eine Konzentration zwischen 8-10 mg PKA/ml Puffer eingestellt. Die Konzentrationsbestimmung erfolgte mit einem NanoDrop™ 2000c (ThermoFisher Scientific®).

### Kristallisation – Kristallisation Mixtur

An dieser Stelle wurde entschieden, ob PKA Kristalle mit oder ohne den Peptid-Inhibitor PKI (cAMP dependent Protein Kinase Inhibitor PKI-tide von Sigma Aldrich) gezüchtet werden sollten. Die Zusammensetzung der jeweiligen Mixturen ist in Tabelle 17 aufgelistet. Auch hier war eine

<b>Inhalt</b>	<b>Mit PKI</b>	<b>Ohne PKI</b>
Protein im Kristallisationspuffer	88.1 %	88.1 %
MES-BIS-TRIS pH 6,9	2.4 %	9.5 %
Mega8-Lösung	2.4 %	2.4 %
PKI (10mM) im Kristallisationspuffer	7.1 %	0.0 %

*Tabelle 17: Zusammensetzung der Kristallisationsmixturen mit und ohne Peptidinhibitor PKI.*

Kühlung mit Eiswasser für die Stabilisierung der PKA notwendig. Eine fertige Mixtur wurde im Anschluss zum Pipettieren auf Kristallisationsplatten verwendet.

### Kristallisation – Bereitung der Kristallisationsplatte

Es wurde eine „24 well sitting drop“ Kristallisationsplatte von Hampton Research benutzt. Zusätzlich wurde das Podest des Kristallisationstropfens mit Baysilone-Paste von Bayer leicht benetzt. Die Reservoirs wurden mit ca. 500 µL einer Wasser-Methanol-Mixtur gefüllt. Der Anteil an Methanol variierte zwischen 19 and 26 %. Bei 23% Methanol wurden die besten Kristalle erhalten. Diese Platten wurden vor dem Aufbringen der Kristallisationstropfen (2-3 µL) bei 4°C vorgekühlt.

Üblicherweise wurden 3µl große Tropfen der Mixtur pipettiert. Um die Bildung der Kristalle zu initiieren, wurde „micro-seeding“ angewendet. Dieses erfolgte unter Verwendung von älteren PKA Kristallen mit Hilfe eines Pferdehaars. Bevor die Mikrokristalle in die Kristallisationstropfen überführt wurden, erfolgte ein Waschen des Pferdehaares mit Hilfe von 8 Wassertropfen (10µl). Danach wurde das Haar durch alle 24 Kristallisationstropfen auf der Platte gezogen. Die Kristallisationsplatte wurde abschließend mit Tape Shark™ (Duck Brand) versiegelt und bei 4°C gelagert.

## Kristallisation – Kristallwachstum

Je nachdem ob sich für die Züchtung von PKI-freie oder PKI-haltigen Kristallen entschieden wurde, variierte die Zeitdauer bis Kristalle einer Größe für Messungen bereit standen. Kristalle mit gebundenen PKI wuchsen schneller und waren teilweise bereits ein paar Stunden nach dem „Seeding“ unter dem Mikroskop zu erkennen. Nach zwei Wochen waren sie spätestens auf ausreichende Größe herangewachsen. Im Vergleich dazu benötigten die PKI-freien Kristalle vier Wochen bis sie ausreichende Qualität für eine kristallographische Analyse aufwiesen. Beide Kristallarten waren über Monate bei 4°C stabil.

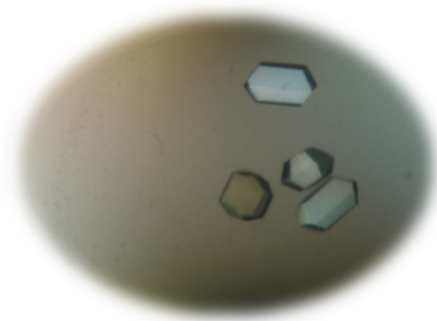


*Abbildung 283: PKA Kristalle mit gebunden PKI nach einer Wachstumsphase von einem Monat.*

**Material – Chemikalien**

- Ammonium persulfate (APS)
- Ammonium-chloride
- Aqua, demineralised
- BIS-TRIS (Bis(2-hydroxyethyl) amino-tris (hydroxymethyl) methane)
- Boric acid
- Bromophenol blue
- Calcium-chloride
- Cobalt-chloride hexahydrate
- cComplete™, EDTA-free Protease Inhibitor Cocktail
- Copper-chloride dihydrate
- Di-sodium-hydrogen-phosphate
- Dithiothreitol (DTT)
- Ethanol
- Glucose
- Glycerol
- HEPES (2-[4-(2-hydroxyethyl) piperazin-1-yl] ethane sulfonic acid)
- Hydrochloric acid
- Imidazole
- Iron-chloride hexahydrate
- Lactose
- Magnesium sulfate
- Manganese-chloride dihydrate
- Mega8 (Octanoyl-N-methylglucamide)
- Methanol
- Nickel-chloride hexahydrate
- Peptone from casein
- Potassium-di-hydrogen-phosphate
- Rotiphorese® 10x SDS-PAGE (Roth)
- Rotiphorese® Gel 30 (37 ,5:1) (Roth)
- Sodium sulfate decahydrate
- Sodium-chloride
- Sodium-di-hydrogen-phosphate
- Sodium-dodecyl-sulphate
- Sodium-hydroxide
- Sodium-molybdate dihydrate
- Sodium-selenite
- Tetramethylethylenediamine (TEMED)
- TRIS (2-Amino-2-(hydroxymethyl) propane-1,3-diol) hydrochloride
- Yeast extract
- Zinc-sulphate heptahydrate
- $\beta$ -D-1-thiogalactopyranoside (IPTG)
- $\beta$ -mercaptoethanol

## Equipment

- ÄKTA FPLC (GE Healthcare Life Science)
- ÄKTA prime plus (GE Healthcare Life Science)
- Avanti™ J-25 - Centrifuge (Beckmann Coulter)
- Emulsiflex C5 (Avestin)
- Fedegari Autoclavie (SPA)
- Min Incubator (Labnet International, Inc.)
- Mini-PROTEAN® Tetra System (Bio-RAD)
- Multifuge 3 S-R (Heraeus)
- NanoDrop™ 2000c (ThermoFisher)
- New Brunswick™ Innova® 43 (Eppendorf)
- Peristaltic pump P-1 (GE Healthcare Life Science)

## Puffer & Media – Protein Expression

### LB – Medium

Peptone aus Casein	10,0 g
Hefe Extrakt	5,0 g
Natrium-Chlorid	10,0 g
Demin. Wasser	<b>ad 1,0 L</b>

### ZYM5025 – Medium

Peptone aus Casein	40,0 g
Hefe Extrakt	20,0 g
Lactose	8,0 g
Glycerol	20,0 mL
Glucose	2,0 g
Di-Natrium-Hydrogen-Phosphat	17,80 g
Kalium-di-Hydrogen-Phosphat	13,61 g
Ammonium-Chlorid	10,70 g
Natrium-Sulfat Decahydrat	6,44 g
Magnesium-Sulfat	0,96 g
Trace metal stock solution	800 µL
Demin. Wasser	<b>ad 4,0 L</b>

### Trace metal stock solution

Eisen-Chlorid Hexahydrat	27,030 g
Calcium-Chlorid	4,440 g
Mangan-Chlorid Dihydrat	3,238 g
Zink-Sulfat Heptahydrat	5,751 g
Cobalt-Chlorid Hexahydrat	0,952 g
Kupfer-Chlorid Dihydrat	0,682 g
Nickel-Chlorid Hexahydrat	0,951 g
Natrium-Molybdat Dihydrat	0,968 g
Natrium-Selenit	0,692 g
Demin. Wasser	<b>ad 1,0 L</b>

**Puffer & Media – Protein Aufreinigung****Ni<sup>2+</sup>-Säule Puffer A (pH8,0)**

Di-Natrium-Hydrogen-Phosphat	13,84 g
Natrium-di-Hydrogen-Phosphat	0,30 g
Natrium-Chlorid	58,44 g
Imidazol	1,36 g
Demin. Wasser	<b>ad 2,0 L</b>

**Ni<sup>2+</sup>-Säule Puffer A2 (pH8,0)**

Di-Natrium-Hydrogen-Phosphat	13,84 g
Natrium-di-Hydrogen-Phosphat	0,30 g
Natrium-Chlorid	58,44 g
Demin. Wasser	<b>ad 2,0 L</b>

**Dialyse Puffer I (pH8,0)**

Di-Natrium-Hydrogen-Phosphat	34,60 g
Natrium-di-Hydrogen-Phosphat	0,74 g
Natrium-Chlorid	29,22 g
DTT	3,86 g
Demin. Wasser	<b>ad 5,0 L</b>

**Dialyse Puffer II (pH7,0)**

HEPES	59,97 g
Natrium-Chlorid	7,30 g
DTT	3,86 g
Demin. Wasser	<b>ad 5,0 L</b>

**Mono S Puffer C (pH7,0)**

HEPES	11,92 g
Natrium-Chlorid	2,92 g
DTT	0,77 g
Demin. Wasser	<b>ad 1,0 L</b>

**Mono S Puffer D (pH7,0)**

HEPES	11,92 g
Natrium-Chlorid	29,22 g
DTT	0,77 g
Demin. Wasser	<b>ad 1,0 L</b>

**Puffer & Media – Protein Kristallisation & Probenbearbeitung****SDS-gel Puffer**

TRIS-HC pH6.8	62,5 mM
Natrium dodecyl sulphat	2,5 %
Bromophenolblau	0,002%
β-mercaptoethanol	713,5 mM
Glycerol	10,0 %
Demin. Wasser	<b>Qs</b>

**Kristallisationspuffer pH 6.9**

MES-Bis-Tris	100 mM
DTT	1 mM
EDTA	0.1 mM
LiCl	75 mM
Demin. Wasser	<b>Qs</b>

## 8.6. Expression, Aufreinigung und Kristallisation der Pim1-Kinase

### Protein Informationen

Name: Pim1 Kinase (Isoform2)

Klassifikation: Transferase

Organismus: Homo sapiens

Mutationen: R250G

Aminosäure Sequenz:

```

      10      20      30      40      50
MLLSKINSLA HLRAAPCNDL HATKLAPGKE KEPLESQYQV GPLLGSGGFG
      60      70      80      90     100
SVYSGIRVSD NLPVAIKHVE KDRISDWGEL PNGTRVPMEV VLLKKVSSGF
      110     120     130     140     150
SGVIRLLDWF ERPDSFVLIL ERPEPVQDLF DFITERGALQ EELARSFFWQ
      160     170     180     190     200
VLEAVRHCHN CGVLHRDIKD ENILIDLNRG ELKLIDFGSG ALLKDTVYTD
      210     220     230     240     250
FDGTRVYSPP EWIRYHRYHG RSAAVWSLGI LLYDMVCGDI PFEHDEEIIIG
      260     270     280     290     300
GQVFFRQRVS SECQHLIRWC LALRPSDRPT FEEIQNHPWM QDVLLPQETA
      310
EIHLHLSLSPG PSK

```

### Expression – Klonen und Transformation

Die Sequenz der 36 kDa Isoform von Pim1 ( Sequenz-Identifikationsnummer: gi 33304198) mit der Mutation R250G wurde in einen pLIC-SGC Vektor mit einem N-terminalen „His<sub>6</sub>-Tag“ zusammen mit einer TEV-Protease-Schnittstelle geklont und weiter in einen BL21 (DE3)/pLysS *E. coli* Stamm von Agilent Technologies transformiert.

Das modifizierte Bakterium besaß so eine Resistenz gegenüber Ampicillin und Chloramphenicol, welche für die gezielte Selektion der modifizierten *E. coli* Kultur genutzt wurde. Eine isolierte Kultur wurde anschließend in 10 mL LB-Medium überführt (Peptone von CASEIN, Hefe, NaCl und Wasser), welches ebenfalls die beiden Antibiotika enthielt. Das Medium wurde über Nacht bei 37°C inkubiert. Die dadurch entstehende Suspension aus LB-Medium und *E. coli* Zellen wurde zur Erstellung von „Glycerol-Stocks“ oder direkt als Startpunkt für eine Expression genutzt.



## **Expression – Zell Vermehrung und Protein Expression**

Begonnen wurde mit einer Übernachtskultur (ÜNK). Diese bestand aus LB-Medium sowie den oben genannten Antibiotika und wurde mit der Bakterienkultur aus einem Glycerol-Stock oder direkt aus der Kultur nach der Transformation angeimpft. Pro Liter Hauptmedium (ZYM5025) wurden 10 mL ÜNK veranschlagt.

Am Folgetag wurden die ÜNKs in das Hauptmedium überführt. Das verwendete ZYM5025 Medium ist dafür bekannt, dass die Induktion der Expression durch die bereits enthaltene Laktose automatisch reguliert wird. Zusätzlich können die Bakterien in diesem Medium zu einer sehr hohen Zelldichte heranwachsen. Die genaue Zusammensetzung des Mediums ist tabellarisch unter dem Abschnitt ‚Puffer & Media‘ angegeben (s. S. 249 f.). Auch hier wurden die Antibiotika Ampicillin und Chloramphenicol hinzugegeben.

Das beimpfte Hauptmedium wurde für 9 Stunden, bei 37 °C und 190 rpm im Schüttler inkubiert. Anschließend wurde die Temperatur für 58 Stunden auf 20 °C herunter gefahren. Die Ausbeute an Pim1 wurde erhöht, wenn zusätzlich 1 mL Isopropyl  $\beta$ -D-1-thiogalactopyranosid (IPTG – 1M) pro Liter Hauptmedium ab dem Erreichen von 20 °C hinzugefügt wurde.

## **Expression – Ernte**

Über Zentrifugation wurden die Zellen vom Medium getrennt (10.000 rpm für 10 Minuten). Das dabei entstehende Pellet aus Bakterien wurde anschließend in flüssigem Stickstoff schockgefroren und bei -80 °C gelagert. Alternativ konnte das Pellet auch direkt weiter verarbeitet werden.

## **Aufreinigung – Resuspension**

Zuerst wurde das Bakterienpellet in dem ersten Puffer der Aufreinigung resuspendiert ( Puffer A, erste  $\text{Ni}^{2+}$  Säule (HEPES pH7,0, NaCl und Glycerol)). Die Menge Pellet aus 2 Litern ZYM-Medium wurde in 200-250 mL Puffer A resuspendiert. Zusätzlich wurden vorher 1-2 Protease-Inhibitor-Tabletten (Complete™, EDTA-freie Protease Inhibitor Cocktail von Sigma-Aldrich) im Puffer gelöst. Die Suspension wurde mit einer Fantaschale und einem Pistill vor-homogenisiert, sollte aber vor dem Zellaufschluss immer mit einem ‚Dounce tissue grinder‘ abschließend homogenisiert werden um Agglomerate zu verhindern.

## **Aufreinigung – Zellaufschluss**

Für den Zellaufschluss wurde das Emulsiflex-System von Avestin verwendet. Während die Suspension durch das System gepumpt wurde, legte man einen Gegendruck von ca. 15.000 bis 17.000 psi an, um die Zellen aufzuschließen. Nach zwei bis drei Durchläufen waren annähernd

alle Zellen bearbeitet. Bei erfolgreichem Aufschluss verdunkelt sich die Suspension. Eine permanente Kühlung mit Eis war bei diesem Schritt sehr wichtig, da sich die Suspension erwärmte. Durch erneute Zentrifugation wurden die Zelltrümmer von der Lösung separiert (1-1,5 Stunden bei 20.000 rpm und 4°C).

### **Aufreinigung – Erste Ni<sup>2+</sup> - Säule**

Das Zentrifugat wurde zum Abtrennen übriger Partikel durch Membran-Filter (Porengröße 0,45 µm, Rotilabo® -Spritzenfilter) gespritzt. Dies hatte nicht nur eine reinigende Funktion sondern beschleunigte auch das Beladen der ersten Ni<sup>2+</sup> - Säule (HisTrap HP 5ml, GE Healthcare Life Science).

Vor dem Beladen der Säule wurde sie mit dem 5-10fachen des Säulen Volumens (SV) Puffer A mittels *Peristaltic pump* P-1 (GE Healthcare Life Science) äquilibriert. Anschließend wurde die gefilterte Proteinlösung mit derselben Pumpe und einer Flussgeschwindigkeit von 3-4 mL pro Minute auf die Säule geladen. Zur Kontrolle wurde eine Probe vom Durchfluss genommen. Nach dem Beladen wurden auf die Säule 5 SV von Puffer A gegeben. Auch hier musste auf ständiges Kühlen mit Eis geachtet werden.

Nun wurde die beladene Säule an das ÄKTA-System (ÄKTA prime plus oder ÄKTA FPLC) angeschlossen, welche zuvor auf die Puffer A und B äquilibriert wurde. Einmal angeschlossen wurde die Säule zuerst mit 100-150 mL Puffer A gewaschen. Anschließend wurde der Anteil an Puffer B im Gemisch mit Puffer A auf 30% erhöht. Durch diesen Schritt wurden erste unerwünschte Proteine entfernt. Die Anteil an Puffer B wird nach diesem Elutionspeak noch für 5-10 SV weiter bei 30% gehalten.

Im Anschluss wurde der Anteil an Puffer B auf 80 % erhöht. Hierdurch wurde die Elution von Pim1 herbeigeführt. Mit Hilfe der Monitoring Software wurde die Elution von Pim1 überwacht. Je nach Erfolg in der Expression variiert die Menge des eluierten Proteins. Restliche, unerwünschte Proteine wurden mit einem Puffer B Anteil von 100% von der Säule gewaschen (ca. 5 SV).

Zur Kontrolle wurden Proben verschiedener Prozessschritte (siehe unten) für eine SDS-PAGE Analyse genommen. Für das Weiterarbeiten sollte die Menge an Pim1 Protein mindestens genau so groß sein, wie die Menge der restlichen Proteine im Gemisch. War dieser Anteil kleiner wurde die gesammelte Fraktion verworfen. Eine SDS-PAGE Analyse wurde für folgende Proben durchgeführt: Filtrat vor der Säule (*Pre*), Durchfluss der Säule (*FT*), Waschung an der ÄKTA mit Puffer A und 30% Puffer B, Elutions-Peak mit 80% Puffer B und der finale Waschschrift mit 100%igen Anteil an Puffer B. Jede Probe wurde im Verhältnis 4:1 mit SDS-Puffer gemischt. Die

beiden ersten Proben sollten allerdings zusätzlich im Verhältnis 1:4 mit Wasser verdünnt werden, da sonst die Banden überladen sind (siehe A).

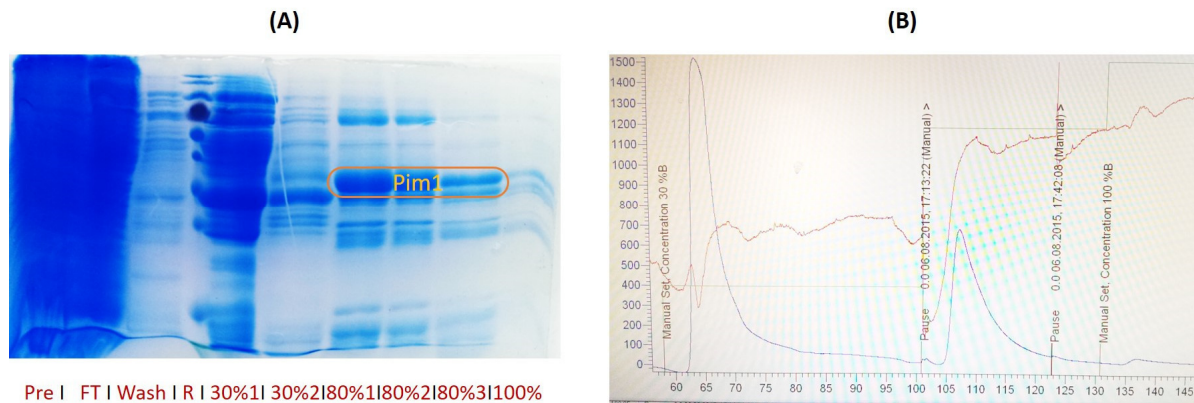


Abbildung 284: **(A)** SDS-Gel der ersten  $\text{Ni}^{2+}$ -Säule. Die verwendeten Proben sind wie folgt bezeichnet: Pre – Filtrat vor der Säule; FT – Durchfluss der Säule; R – Protein Größenstandard; Wash – ÄKTA Waschung (Puffer A); 30%1+2 – Fraktion ein und zwei des Peaks; 80%1+2 – Erster und zweiter Teil des Elutionspeaks; 100% – 100%B Waschung. **(B)** ÄKTA Chromatogramm der ersten  $\text{Ni}^{2+}$ -Säule. Die Y-Achse zeigt die UV-Absorption in mAU und die X-Achse das Volumen in mL. Der erste Peak enthält unerwünschtes Protein aus der 30% Puffer B Waschung. Der zweite Peak enthält Pim1-Protein bei 80% Puffer B.

## Aufreinigung – Dialyse I

Das eluierte Protein wurde in einen Dialyseschlauch von SpectraPore (12-14 kDa cut-off) überführt. Ca.10 mg der TEV-Protease wurde anschließend hinzugefügt, sowie 10  $\mu\text{L}$  einer in Lösung befindlichen Lambda Protein Phosphatase (Sigma Aldrich,  $\geq 400,000$  units/ml). Der Dialyseschlauch verbleibt dann mindestens 24 Stunden in 5L vorgekühltem Dialyse Puffer I (HEPES pH7,0, NaCl, Glycerol, Dithiothreitol (DTT) und Mangan(II)-Chlorid) bei 4 °C. Nach 48 Stunden war die Ausbeute allerdings höher. Während der Dialyse wurde der His<sub>6</sub>-tag abgespalten und Pim1 dephosphoryliert. Der His<sub>6</sub>-tag kann so wie das Imidazol den Dialyseschlauch passieren, wodurch sich die Konzentration verringerte.

## Aufreinigung – zweite Ni<sup>2+</sup>-Säule

Nach der Dialyse wurde die Lösung ein zweites Mal auf die Ni<sup>2+</sup>-Säule gegeben. Auch hier wurde sie vor der dem Vorgang mit Puffer A äquilibriert. Nach dem Auftragen der Dialyselösung wurden noch einmal mit dem 5-10fachen SV Puffer A gespült. Pim1 hatte immer noch eine leichte Affinität zum Säulenmaterial und war nicht im Durchfluss zu finden. Ein geringer Anteil (ca. 10%) an Puffer B sorgte schon zur Elution der Pim1 an der ÄKTA. Andere unspezifisch bindende Proteine behielten ihre Affinität zum Säulenmaterial und verblieben bei dem geringen (ca. 10%) Puffer B Anteil auf der Säule. Der Anteil an Puffer B wurde kontinuierlich auf 100% Puffer B über ein Durchflussvolumen von 120ml erhöht (3-4 mL/Minute). Wie in Abbildung 285 dargestellt, enthielt der Durchfluss (FT) und der Waschschritt mit Puffer A (A-W) kein Pim1. Im Vergleich mit dem Durchgang der ersten Ni<sup>2+</sup>-Säule wurde hier schon Pim1 bei ca. 10% Puffer B eluiert. Im späteren Verlauf des Gradienten wurde ebenfalls die TEV Protease eluiert und somit gelang auch hier wieder die Trennung von Pim1 (F 10-14). Die Proben auf dem SDS-Gel waren: FT, ÄKTA-A-wash und Fraktionen vom Gradienten. Auch bei diesem Aufreinigungsschritt war immer auf eine ausreichende Kühlung mit Eis zu achten. Die Fraktionen, die Pim1 enthalten wurden zusammen geführt und in eine weitere Dialyse gegeben.

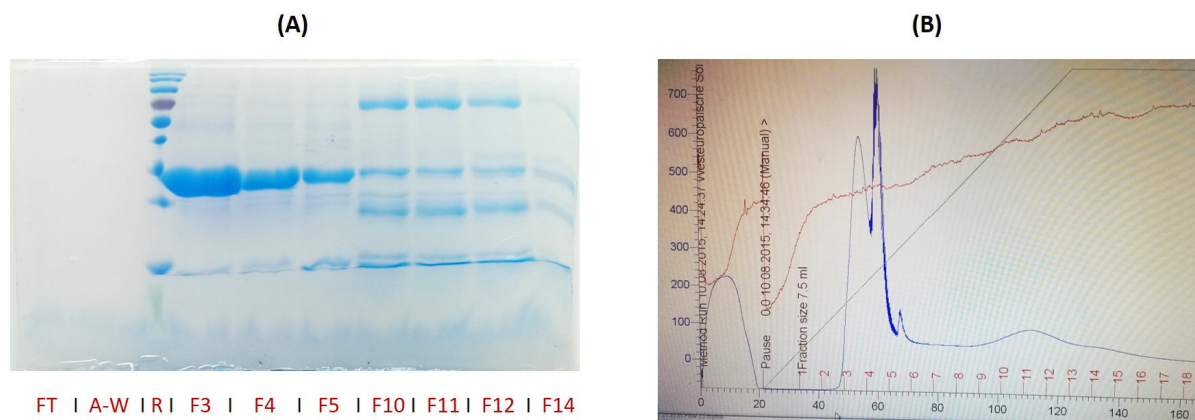


Abbildung 285: **(A)** SDS-Gel der zweiten Ni<sup>2+</sup>-Säule. Die genommenen Proben von links nach rechts: FT – Durchfluss ; A-W. – Waschung (Puffer A); R - Protein Größenstandard; F3-F14 – Fraktionen vom Gradienten **(B)** Chromatogramm der zweiten Ni<sup>2+</sup>-Säule. Die Y-Achse zeigt die UV-Absorption in mAU und die X-Achse das Volumen in mL. Die eluierten Proteine während dem Gradienten werden in Fraktionen gesammelt.

## Aufreinigung – Dialyse II

Diese Dialyse bereitet die Protein-Lösung für die “Mono Q 4.6/100 PE” Säule (GE Healthcare Life Science) vor. Diese Säule ist eine starke Anionen Austauscher-Säule. Damit das Protein an die Säule binden kann, wurde die Konzentration an NaCl durch die Dialyse reduziert. Der Dialyse-Puffer enthielt HEPES, NaCl (10% der Konzentration von Puffer B) und DTT bei einem pH-Wert von 7,0. Diese Dialyse wurde für mindestens 4 Stunden durchgeführt. Optimal waren aber

12-13 Stunden. Leider verursachte der geringe Anteil an NaCl, dass sich Agglomerate von Pim1 bildeten und das Protein ausfiel. Deswegen wurde die Dialyse nicht länger als 12 Stunden und bei 4 °C durchgeführt.

### Aufreinigung – Mono Q Säule

Die Mono Q Säule konnte nur am ÄKTA-FPLC-System verwendet werden. Durch die enge Packung des Säulenmaterials musste mit erhöhtem Druck die Lösung auf die Säule gepumpt werden. Äquilibriert wurde die Säule zuvor mit Puffer C (HEPES, NaCl und DTT; pH 7,0).

Durch Zentrifugation (15 min. bei 3500 rpm und 4°C) konnte gegebenenfalls vorliegendes Protein-Präzipitat aus der Lösung entfernt werden.

Über einen Loop konnte die Mono Q mit der klaren Protein-Lösung beladen werden. Anschließend wurde die Säule mit 50 mL Puffer C gewaschen.

Durch das Anlegen eines Gradienten zu einem finalen Anteil von 30% Puffer D über 90 mL (3 mL/Minute) wurde die Elution der Pim1 initiiert. Puffer D beinhaltet eine höhere NaCl Konzentration. Der Durchfluss wurde während des Gradienten in 5 mL Fraktionen gesammelt. Durch die Dephosphorylierung mittels Lambda Phosphatase in der ersten Dialyse sollte bestenfalls nur eine einheitlich zusammengesetzte Fraktion entstehen. Bei partieller Dephosphorylierung können auch mehrere Banden entstehen (Abbildung 286 (B)). Das Eluat, das dem ersten Peaks zugewiesen wurde, lässt sich weiter für die Proteinkristallisation verwendet. Das Protein wurde alsbald verwendet und nicht bei -80 °C gelagert um Verluste durch Denaturierung zu vermeiden.

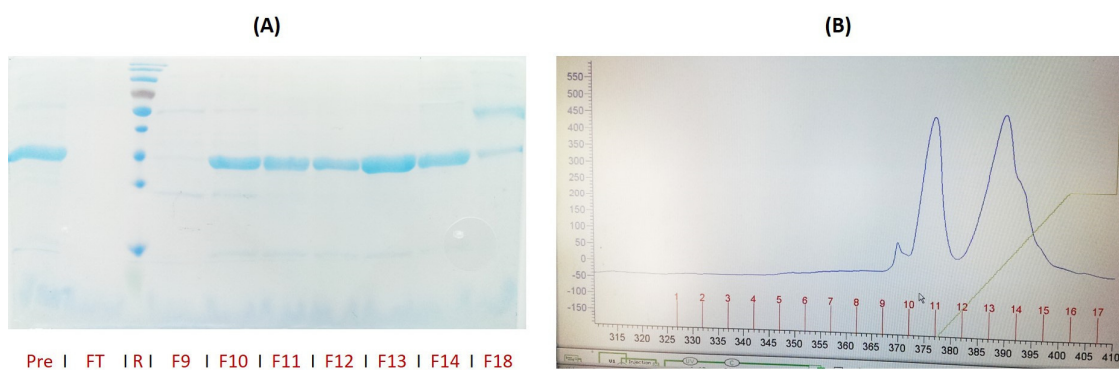


Abbildung 286: **(A)** SDS-Gel der Mono Q-Säule. Proben von links nach rechts: Pre – Lösung vor der Säule; FT – Durchfluss; R – Protein Größensstandard 9-18 – Fraktionen des Gradienten. **(B)** Chromatogramm der Mono Q-Säule. Die Y-Achse zeigt die UV-absorption in mAU und die X-Achse das Volumen in mL. Das eluierte Protein wurde in Fraktionen a 5 mL gesammelt.

## Aufreinigung – Ausbeute

Die finale Ausbeute an Pim1 hing maßgeblich von der Expressionrate des Proteins ab. Maximal konnte eine Menge von 17,0 mg Pim1 pro Liter Expressions-Medium erreicht werden.

## Kristallisation – Umpufferung

Vor der Kristallisation wurde Pim1 in den entsprechenden Kristallisationspuffer überführt. (HEPES, Natrium Chlorid, Glycerol und DTT bei pH 7,0). Da Protein Agglomerate die Kristallisation stören, wurden sie vor der Umpufferung durch Filtration abgetrennt. Für die Umpufferung wurde die Lösung in ein bis zwei Vivaspin 20 (Sartorius®) mit 10.000 Da cut off überführt und bei einer Drehzahl von 3500 rpm aufkonzentriert. Nachdem die Lösung 3 mal mit dem Kristallisationspuffer aufgefüllt worden war, wurde sie zu einer Protein-Konzentration von 6-8 mg Pim1 /mL Puffer aufkonzentriert. Die Messung der Konzentration erfolgte am NanoDrop™ 2000c (ThermoFisher Scientific®).

## Kristallisation – Kristallisationsmixture

Für die Co-Kristallisation der Pim1 wurden zusätzlich der Ligand und das Substratpeptid PIMTIDE hinzugegeben. Das Consensus Peptid PIMTIDE unterstützt den Kristallisationsprozess. Der Ligand war in DMSO gelöst. Je nach Affinität des Liganden variierte die Konzentration des Liganden. Für Liganden mit geringer Affinität wie Fragmente wurden 1M Lösungen (DMSO). Die genaue Zusammensetzung der Kristallisationsmixture ist in Tabelle 18 beschrieben:

Inhalt	Anteil
Protein in Kristallisationspuffer (6-8 mg/ml)	80.0 %
PIMTIDE in Kristallisationspuffer (10 mM)	10.0 %
Ligand in DMSO (1 M für Fragmente)	10.0 %

**Tabelle 18:** Zusammensetzung der Mixture zu r Co-Kristallisation der Pim1.

In einigen Fällen war der Ligand nicht zu 100% unter den Kristallisationsbedingungen löslich oder das Protein fiel bei der Zusammenführung aus. Daher wurde die finale Mixture noch einmal durch Zentrifugation gereinigt und Festsubstanz abgetrennt.

## Kristallisation – Vorbereitung der Kristallisationsplatte

Verwendet wurde eine 24-well „sitting-drop“ Kristallisationsplatte (Hampton Research). Das Podest für die Kristallisationslösung wurde zuvor mit Baysilone-Paste (Bayer) behandelt um ein Festwachsen der Kristalle zu verhindern. Die Reservoirs wurden mit 24 verschiedenen Kristallisationsbedingungen (siehe Seite 250) a 500 µL gefüllt. Die Bedingungen unterschieden sich

in Art der gelösten Salze und der Konzentration an PEG3350. Die variierenden Salze waren: Lithium-Sulfat, Magnesium-Chlorid, NaCl, Lithium-Chlorid, Calcium-Chlorid und Magnesium-Acetat.

Nach der Befüllung der Reservoirs wurde die Kristallisationsmischung auf die Podeste pipettiert. Bei einer üblichen Menge von 2  $\mu$ L pro Kristallisationstropfen wurde in der Regel 1  $\mu$ L Kristallisationsbedingung mit 1  $\mu$ L der Proteinlösung vermischt. Je schonender die Zusammenführung der beiden Tropfen war, desto weniger Komplikationen traten bei der Kristallisation auf. Abschließend wurde die Platte mit Tape Shark™ (Duck Brand) versiegelt und bei 4°C gelagert.

### Kristallisation – Kristallwachstum

Form und Wachstumszeit der Kristalle hing stark von dem Liganden ab, der co-kristallisiert wurde. Im besten Falle konnte ein Wachstum bereits nach 3-4 Tagen beobachtet werden. In manchen Fällen dauerte es allerdings auch Wochen. Solange nichts außer Präzipitat innerhalb der ersten 14 Tage beobachtet wurde, war davon auszugehen, dass kein Kristallwachstum stattfinden wird.

Es wurden verschiedene Formen von Pim1-Kristallen beobachtet. Alle endständigen Kristalle hatten einen hexagonalen und weitgehend isometrischen Habitus. Lediglich in Größe und Länge variierten sie. Große hexagonale Quader zeigten die besten Voraussetzungen für röntgenkristallographische Untersuchungen. Bis zu vier Wochen vergingen bis ein Kristall seine optimale Größe erreicht hatte.

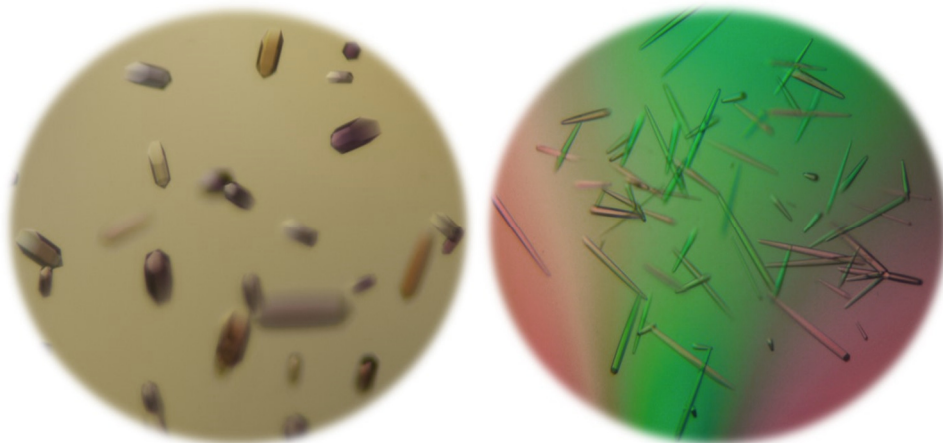


Abbildung 287: Co-kristallisierte Pim1 mit gebundenem PIMTIDE Peptid nach einer Wachstumszeitspanne von 4 Wochen.

---

**Material – Chemikalien**

- Ammonium persulfate (APS)
- Ammonium-chloride
- Ampicillin
- Aqua, demineralised
- BIS-TRIS (Bis(2-hydroxyethyl) amino-tris (hydroxymethyl) methane)
- Boric acid
- Bromophenol blue
- Calcium-chloride
- Chloramphenicol
- Cobalt-chloride hexahydrate
- cOmplete™, EDTA-free Protease Inhibitor Cocktail
- Copper-chloride dihydrate
- Di-sodium-hydrogen-phosphate
- Dithiothreitol (DTT)
- Ethanol
- Glucose
- Glycerol
- HEPES (2-[4-(2-hydroxyethyl) piperazin-1-yl] ethane sulfonic acid)
- Hydrochloric acid
- Imidazole
- Iron-chloride hexahydrate
- Lactose
- Magnesium sulfate
- Manganese-chloride dihydrate
- Mangan-chloride
- Methanol
- Nickel-chloride hexahydrate
- PageRuler™ Prestained Protein Ladder (Thermo Scientific)
- Peptone from casein
- Potassium-di-hydrogen-phosphate
- Rotiphorese® 10x SDS-PAGE (Roth)
- Rotiphorese® Gel 30 (37 ,5:1) (Roth)
- Sodium sulfate decahydrate
- Sodium-chloride
- Sodium-di-hydrogen-phosphate
- Sodium-dodecyl-sulphate
- Sodium-hydroxide
- Sodium-molybdate dihydrate
- Sodium-selenite
- Tetramethylethylenediamine (TEMED)
- TEV protease (Tobacco Etch Virus) (In-house expression and purification)
- TRIS (2-Amino-2-(hydroxymethyl) propane-1,3-diol) hydrochloride
- Yeast extract



- Zinc-sulphate heptahydrate
- $\beta$ -D-1-thiogalactopyranoside (IPTG)
- $\beta$ -mercaptoethanol
- $\lambda$  Protein Phosphatase (Sigma Aldrich)

## Equipment

- Avanti™ J-25 - Centrifuge (Beckmann Coulter)
- ÄKTA prime plus (GE Healthcare Life Science)
- ÄKTA FPLC (GE Healthcare Life Science)
- NanoDrop™ 2000c (ThermoFisher)
- Mini-PROTEAN® Tetra System (Bio-RAD)
- Multifuge 3 S-R (Heraeus)
- Emulsiflex C5 (Avestin)
- New Brunswick™ Innova® 43 (Eppendorf)
- Peristaltic pump P-1 (GE Healthcare Life Science)
- Min Incubator (Labnet International, Inc.)
- (Fedegari Autoclavie SPA)

**Puffer & Media – Protein Expression****ZYM5025 – Medium**

Peptone aus Casein	40,0 g
Hefe Extrakt	20,0 g
Lactose	8,0 g
Glycerol	20,0 mL
Glucose	2,0 g
Di-Natrium-Hydrogen-Phosphat	17,80 g
Kalium-di-Hydrogen-Phosphat	13,61 g
Ammonium-Chlorid	10,70 g
Natrium-Sulfat Decahydrat	6,44 g
Magnesium-Sulfat	0,96 g
Trace metal stock solution	800 µL
Demin. Wasser	<b>ad 4,0 L</b>

**LB – Medium**

Peptone aus Casein	10,0 g
Hefe Extrakt	5,0 g
Natrium-Chlorid	10,0 g
Demin. Wasser	<b>ad 1,0 L</b>

**Trace metal stock solution**

Eisen-Chlorid Hexahydrat	27,030 g
Calcium-Chlorid	4,440 g
Mangan-Chlorid Dihydrat	3,238 g
Zink-Sulfate Heptahydrat	5,751 g
Cobalt-Chlorid Hexahydrat	0,952 g
Kupfer-Chlorid Dihydrat	0,682 g
Nickel-Chlorid Hexahydrat	0,951 g
Natrium-Molybdat Dihydrat	0,968 g
Natrium-Selenit	0,692 g
Demin. Wasser	<b>ad 1,0 L</b>

**Puffer & Media – Aufreinigung****Ni<sup>2+</sup>-Säule Puffer A (pH7,0)**

HEPES	50 mM
Natrium-Chlorid	500 mM
Glycerol	50 mL
Demin. Wasser	<b>ad 1,0 L</b>

**Ni<sup>2+</sup>-Säule Puffer B (pH7,0)**

HEPES	50 mM
Natrium-Chlorid	500 mM
Glycerol	50 mL
Imidazol	150 mM
Demin. Wasser	<b>ad 1,0 L</b>

**Dialyse Puffer I (pH7,0)**

HEPES	50 mM
Natrium-Chlorid	500 mM
DTT	5 mM
Mangan (IV) Chlorid	50 µM
Demin. Wasser	<b>ad 5,0 L</b>

**Mono Q Puffer C (pH7,0)**

HEPES	50 mM
Natrium-Chlorid	50 mM
DTT	5 mM
Demin. Wasser	<b>ad 1,0 L</b>

**Mono Q Puffer D (pH7,0)**

HEPES	50 mM
Natrium-Chlorid	500 mM
DTT	5 mM
Demin. Wasser	<b>ad 1,0 L</b>

**Puffer & Media – Probenbearbeitung****SDS-Gel Puffer**

TRIS-HC pH6.8	62,5 mM
Natrium Dodecyl Sulfat	2,5 %
Bromphenolblau	0,002%
$\beta$ -mercaptoethanol	713,5 mM
Glycerol	10,0 %
Demin. Wasser	<b>Qs</b>

**Puffer & Media – Protein Kristallisation****Kristallisationspuffer (pH7,0)**

HEPES	50 mM
Natrium-Chlorid	250 mM
Glycerol	50 mL
DTT	5 mM
Demin. Wasser	<b>ad 1,0 L</b>

**Kristallisationsbedingungen (pH7,0)**

Bis-Tris-Propan	100 mM	100 mM	100 mM	100 mM	100 mM	100 mM
Salze [200mM]	LiSO <sub>4</sub>	MgCl <sub>2</sub>	NaCl	LiCl	CaCl <sub>2</sub>	MgOAc <sub>2</sub>
PEG 3350	6% , 12% , 18% oder 24%					
Ethylenglycol	10 %	10 %	10 %	10 %	10 %	10 %
DMSO	0.3 %	0.3 %	0.3 %	0.3 %	0.3 %	0.3 %



## **9. References**

- 
1. Berg, J.M., Tymoczko, J.L., Stryer, L. *Biochemistry*. Chapter 15 - An Introduction to Information Metabolism. (W H Freeman, New York, 2002).
  2. Manning, G., Whyte, D. B., Martinez, R., Hunter, T. & Sudarsanam, S. The protein kinase complement of the human genome. *Science* **298**, 1912–34 (2002).
  3. Knighton, D. *et al.* Crystal structure of the catalytic subunit of cyclic adenosine monophosphate-dependent protein kinase. *Science*. **253**, 407–414 (1991).
  4. Ubersax, J. A. & Ferrell, J. E. Mechanisms of specificity in protein phosphorylation. *Nat. Rev. Mol. Cell Biol.* **8**, 530–41 (2007).
  5. Madhusudan, M., Akamine, P., Xuong, N.-H. & Taylor, S. S. Crystal structure of a transition state mimic of the catalytic subunit of cAMP-dependent protein kinase. *Nat. Struct. Biol.* **9**, 273–277 (2002).
  6. Zhu, H. *et al.* Analysis of yeast protein kinases using protein chips. *Nat. Genet.* **26**, 283–9 (2000).
  7. Krebs, E. G., Graves, D. J. & Fischer, E. H. Factors affecting the activity of muscle phosphorylase b kinase. *J. Biol. Chem.* **234**, 2867–73 (1959).
  8. Kemp, B. E., Graves, D. J., Benjamini, E. & Krebs, E. G. Role of Multiple Basic Residues in Determining the Substrate Specificity of Cyclic AMP-dependent Protein Kinase\*. *J. Biol. Chem.* **252**, 4888–4894 (1977).
  9. Hunter, T. Synthetic peptide substrates for a tyrosine protein kinase. *J. Biol. Chem.* **257**, 4843–8 (1982).
  10. Foulkes, J. G., Chow, M., Gorka, C., Frackelton, A. R. J. and Baltimore, D. Purification and Characterization of a Protein-Tyrosine Kinase Encoded by the Abelson Murine Leukemia Virus\*. *J. Biol. Chem.* **260**, 8070–8077 (1985).
  11. Pinna, L. A. & Ruzzene, M. How do protein kinases recognize their substrates? *Biochim. Biophys. Acta - Mol. Cell Res.* **1314**, 191–225 (1996).
  12. Pearson, R. B. & Kemp, B. E. Protein kinase phosphorylation site sequences and consensus specificity motifs: tabulations. *Methods Enzymol.* **200**, 62–81 (1991).
  13. Ubersax, J. A. *et al.* Targets of the cyclin-dependent kinase Cdk1. *Nature* **425**, 859–864 (2003).
  14. Lee, T. *et al.* Docking motif interactions in Map kinases revealed by hydrogen exchange mass spectrometry. *Mol. Cell* **14**, 43–55 (2004).
  15. Heo, Y.-S. *et al.* Structural basis for the selective inhibition of JNK1 by the scaffolding protein JIP1 and SP600125. *EMBO J.* **23**, 2185–95 (2004).
  16. Noble, M. E. M. Protein Kinase Inhibitors: Insights into Drug Design from Structure. *Science (80-. )*. **303**, 1800–1805 (2004).
  17. Walsh, D. A., Perkins, J. P. & Krebs, E. G. An adenosine 3',5'-monophosphate-dependant protein kinase from rabbit skeletal muscle. *J. Biol. Chem.* **243**, 3763–3765 (1968).
  18. Gill, G. N. & Garren, L. D. A cyclic-3',5'-adenosine monophosphate dependent protein kinase from the adrenal cortex: Comparison with a cyclic AMP binding protein. *Biochem. Biophys. Res. Commun.* **39**, 335–343 (1970).

- 
19. Tao, M., Salas, M. L. & Lipmann, F. Mechanism of Activation by Adenosine 3':5'-Cyclic Monophosphate of a Protein Phosphokinase from Rabbit Reticulocytes. *Proc. Natl. Acad. Sci.* **67**, 408–414 (1970).
  20. Taylor, S. S., Ilouz, R., Zhang, P. & Kornev, A. P. Assembly of allosteric macromolecular switches: lessons from PKA. *Nat. Rev. Mol. Cell Biol.* **13**, 646–58 (2012).
  21. McConnachie, G., Langeberg, L. K. & Scott, J. D. AKAP signaling complexes: getting to the heart of the matter. *Trends Mol. Med.* **12**, 317–23 (2006).
  22. Walsh, D. A. & Van Patten, S. M. Multiple pathway signal transduction by the cAMP-dependent protein kinase. *FASEB J.* **8**, 1227–36 (1994).
  23. Taskén, K. & Aandahl, E. M. Localized effects of cAMP mediated by distinct routes of protein kinase A. *Physiol. Rev.* **84**, 137–167 (2004).
  24. Songyang, Z. *et al.* A structural basis for substrate specificities of protein Ser/Thr kinases: primary sequence preference of casein kinases I and II, NIMA, phosphorylase kinase, calmodulin-dependent kinase II, CDK5, and Erk1. *Mol. Cell. Biol.* **16**, 6486–93 (1996).
  25. Adams, J. A. & Taylor, S. S. Energetic limits of phosphotransfer in the catalytic subunit of cAMP-dependent protein kinase as measured by viscosity experiments. *Biochemistry* **31**, 8516–8522 (1992).
  26. Hanks, S. K., Quinn, A. M. & Hunter, T. The protein kinase family: conserved features and deduced phylogeny of the catalytic domains. *Science* **241**, 42–52 (1988).
  27. Schindler, T. *et al.* Structural mechanism for STI-571 inhibition of abelson tyrosine kinase. *Science* **289**, 1938–42 (2000).
  28. Taylor, S. S. & Kornev, A. P. Protein kinases: evolution of dynamic regulatory proteins. *Trends Biochem. Sci.* **36**, 65–77 (2011).
  29. Bachmann, M. & Möröy, T. The serine/threonine kinase Pim-1. *Int. J. Biochem. Cell Biol.* **37**, 726–730 (2005).
  30. Mikkers, H. *et al.* Mice deficient for all PIM kinases display reduced body size and impaired responses to hematopoietic growth factors. *Mol. Cell. Biol.* **24**, 6104–15 (2004).
  31. Levenson, J. D. *et al.* Pim-1 Kinase and p100 Cooperate to Enhance c-Myb Activity. *Mol. Cell* **2**, 417–425 (1998).
  32. Rainio, E.-M., Sandholm, J. & Koskinen, P. J. Cutting Edge: Transcriptional Activity of NFATc1 Is Enhanced by the Pim-1 Kinase. *J. Immunol.* **168**, 1524–1527 (2002).
  33. Losman, J. *et al.* IL-4 signaling is regulated through the recruitment of phosphatases, kinases, and SOCS proteins to the receptor complex. *Cold Spring Harb. Symp. Quant. Biol.* **64**, 405–16 (1999).
  34. Wang, Z. *et al.* Phosphorylation of the cell cycle inhibitor p21Cip1/WAF1 by Pim-1 kinase. *Biochim. Biophys. Acta - Mol. Cell Res.* **1593**, 45–55 (2002).
  35. Aho, T. L. T. *et al.* Pim-1 kinase promotes inactivation of the pro-apoptotic Bad protein by phosphorylating it on the Ser112 gatekeeper site. *FEBS Lett.* **571**, 43–49 (2004).
  36. Bhattacharya, N. *et al.* Pim-1 associates with protein complexes necessary for mitosis. *Chromosoma* **111**, 80–95 (2002).

- 
37. Bachmann, M., Hennemann, H., Pei, X. X., Hoffmann, I. & Möröy, T. The oncogenic serine/threonine kinase Pim-1 phosphorylates and inhibits the activity of Cdc25C-associated kinase 1 (C-TAK1): A Novel role for Pim-1 at the G2M cell cycle checkpoint. *J. Biol. Chem.* **279**, 48319–48328 (2004).
  38. Koike, N., Maita, H., Taira, T., Ariga, H. & Iguchi-Ariga, S. M. M. Identification of heterochromatin protein 1 (HP1) as a phosphorylation target by Pim-1 kinase and the effect of phosphorylation on the transcriptional repression function of HP1. *FEBS Lett.* **467**, 17–21 (2000).
  39. Ishibashi, Y. *et al.* Pim-1 translocates sorting nexin 6/TRAF4-associated factor 2 from cytoplasm to nucleus. *FEBS Lett.* **506**, 33–38 (2001).
  40. Peltola, K. J. *et al.* Pim-1 kinase inhibits STAT5-dependent transcription via its interactions with SOCS1 and SOCS3. *Blood* **103**, 3744–3750 (2004).
  41. Chen, X. P. *et al.* Pim serine/threonine kinases regulate the stability of Socs-1 protein. *Proc. Natl. Acad. Sci.* **99**, 2175–2180 (2002).
  42. Tursynbay, Y. *et al.* Pim-1 kinase as cancer drug target: An update. *Biomed. reports* **4**, 140–146 (2016).
  43. Mizuno, K. *et al.* Regulation of Pim-1 by Hsp90. *Biochem Biophys Res Commun* **281**, 663–669 (2001).
  44. Nawijn, M. C., Alendar, A. & Berns, A. For better or for worse: the role of Pim oncogenes in tumorigenesis. *Nat. Rev. Cancer* **11**, 23–34 (2011).
  45. Johnson, L. N., Noble, M. E. M. & Owen, D. J. Active and inactive protein kinases: Structural basis for regulation. *Cell* **85**, 149–158 (1996).
  46. Bullock, A. N., Debreczeni, J., Amos, A. L., Knapp, S. & Turk, B. E. Structure and substrate specificity of the Pim-1 kinase. *J. Biol. Chem.* **280**, 41675–41682 (2005).
  47. Friedmann, M., Nissen, M. S., Hoover, D. S., Reeves, R. & Magnuson, N. S. Characterization of the proto-oncogene Pim-1: Kinase activity and substrate recognition sequence. *Arch. Biochem. Biophys.* **298**, 594–601 (1992).
  48. Murray, C. W. & Rees, D. C. The rise of fragment-based drug discovery. *Nat. Chem.* **1**, 187–192 (2009).
  49. Lipinski, C.A., Lombardo, F., Dominy, B.W., Feeney, P. J. Experimental and computational approaches to estimate solubility and permeability in drug discovery and development setting. *Adv. Drug Deliv. Rev.* **23**, 3–25 (1997).
  50. Congreve, M., Carr, R., Murray, C. & Jhoti, H. A ‘Rule of Three’ for fragment-based lead discovery? *Drug Discovery Today* **8**, 876–877 (2003).
  51. Köster, H. *et al.* A Small Nonrule of 3 Compatible Fragment Library Provides High Hit Rate of Endothiapepsin Crystal Structures with Various Fragment Chemotypes. *J. Med. Chem.* **54**, 7784–7796 (2011).
  52. Hopkins, A. L., Groom, C. R. & Alex, A. Ligand efficiency: a useful metric for lead selection. *Drug Discovery Today* **9**, 430–431 (2004).
  53. Davis, B. J. & Erlanson, D. A. Learning from our mistakes: The ‘unknown knows’ in fragment screening. *Bioorg. Med. Chem. Lett.* **23**, 2844–2852 (2013).



- 
54. Palmer, N., Peakman, T. M., Norton, D. & Rees, D. C. Design and synthesis of dihydroisoquinolones for fragment-based drug discovery (FBDD). *Org. Biomol. Chem.* **14**, 1599–1610 (2016).
55. Keserű, G. M. *et al.* Design Principles for Fragment Libraries: Maximizing the Value of Learnings from Pharma Fragment-Based Drug Discovery (FBDD) Programs for Use in Academia. *J. Med. Chem.* **59**, 8189–8206 (2016).
56. Schiebel, J. *et al.* One Question, Multiple Answers: Biochemical and Biophysical Screening Methods Retrieve Deviating Fragment Hit Lists. *ChemMedChem* **10**, 1511–1521 (2015).
57. Huschmann, F. U. *et al.* Structures of endothiapsin–fragment complexes from crystallographic fragment screening using a novel, diverse and affordable 96-compound fragment library. *Acta Crystallogr. Sect. F Struct. Biol. Commun.* **72**, 346–355 (2016).
58. Swain, C. Fragment-Based Screening, What can we learn from published hits? Available at: [http://www.optibrium.com/downloads/Swain\\_Fragments.pdf](http://www.optibrium.com/downloads/Swain_Fragments.pdf). (Accessed: 27th April 2017)
59. Niesen, F. H., Berglund, H. & Vedadi, M. The use of differential scanning fluorimetry to detect ligand interactions that promote protein stability. *Nat. Protoc.* **2**, 2212–2221 (2007).
60. Layton, C. J. & Hellinga, H. W. Thermodynamic Analysis of Ligand-Induced Changes in Protein Thermal Unfolding Applied to High-Throughput Determination of Ligand Affinities with Extrinsic Fluorescent Dyes. *Biochemistry* **49**, 10831–10841 (2010).
61. Hajduk, P. J. & Greer, J. A decade of fragment-based drug design: strategic advances and lessons learned. *Nat. Rev. Drug Discov.* **6**, 211–219 (2007).
62. Mueller, U. *et al.* The macromolecular crystallography beamlines at BESSY II of the Helmholtz-Zentrum Berlin: Current status and perspectives. *Eur. Phys. J. Plus* **130**, 141 (2015).
63. The ESRF beamlines. Available at: [http://www.esrf.eu/UsersAndScience/Experiments/MX/About\\_our\\_beamlines](http://www.esrf.eu/UsersAndScience/Experiments/MX/About_our_beamlines). (Accessed: 14th May 2017)
64. Cicco, A. Di *et al.* Novel XAFS capabilities at ELETTRA synchrotron light source. *J. Phys. Conf. Ser.* **190**, 12043 (2009).
65. Otwinowski, Z. & Minor, W. in *Methods in enzymol.* **276**, 307–326 (1997).
66. Leslie, A. G. W. & Powell, H. R. in *Evolving methods for macromolecular Crystallography* 41–51 (Springer, Dordrecht, 2007). doi:10.1007/978-1-4020-6316-9\_4
67. Kabsch, W. XDS. *Acta Crystallogr. Sect. D Biol. Crystallogr.* **66**, 125–132 (2010).
68. Sparta, K. M., Krug, M., Heinemann, U., Mueller, U. & Weiss, M. S. XDSAPP2.0. *J. Appl. Crystallogr.* **49**, 1085–1092 (2016).
69. Hauptman, H. Phasing methods for protein crystallography. *Curr. Opin. Struct. Biol.* **7**, 672–680 (1997).
70. Murshudov, G. N. *et al.* REFMAC5 for the refinement of macromolecular crystal structures. *Acta Crystallogr. Sect. D Biol. Crystallogr.* **67**, 355–367 (2011).
71. Sheldrick, G. M. Crystal structure refinement with SHELXL. *Acta Crystallogr. Sect. C Struct. Chem.* **71**, 3–8 (2015).

- 
72. Adams, P. D. *et al.* PHENIX: A comprehensive Python-based system for macromolecular structure solution. *Acta Crystallogr. Sect. D Biol. Crystallogr.* **66**, 213–221 (2010).
  73. Emsley, P. & Cowtan, K. Coot: Model-building tools for molecular graphics. *Acta Crystallogr. Sect. D Biol. Crystallogr.* **60**, 2126–2132 (2004).
  74. Laskowski, R. A., MacArthur, M. W., Moss, D. S. & Thornton, J. M. PROCHECK: a program to check the stereochemical quality of protein structures. *J. Appl. Crystallogr.* **26**, 283–291 (1993).
  75. Davis, I. W., Murray, L. W., Richardson, J. S. & Richardson, D. C. MolProbity: Structure validation and all-atom contact analysis for nucleic acids and their complexes. *Nucleic Acids Res.* **32**, W615–W619 (2004).
  76. Berman, H. M. *et al.* The protein data bank. *Nucleic Acids Res.* **28**, 235–242 (2000).
  77. Bollag, G. *et al.* Vemurafenib: the first drug approved for BRAF-mutant cancer. *Nat. Rev. Drug Discov.* **11**, 873–886 (2012).
  78. Congreve, M., Chessari, G., Tisi, D. & Woodhead, A. J. Recent Developments in Fragment-Based Drug Discovery. *J. Med. Chem.* **51**, 3661–3680 (2008).
  79. Fabian, M. A. *et al.* A small molecule–kinase interaction map for clinical kinase inhibitors. *Nat. Biotechnol.* **23**, 329–336 (2005).
  80. Fedorov, O. *et al.* A systematic interaction map of validated kinase inhibitors with Ser/Thr kinases. *Proc. Natl. Acad. Sci.* **104**, 20523–20528 (2007).
  81. Langer, T. *et al.* NMR backbone assignment of a protein kinase catalytic domain by a combination of several approaches: application to the catalytic subunit of cAMP-dependent protein kinase. *Chembiochem* **5**, 1508–16 (2004).
  82. Studier, F. W. in *Methods in Molecular Biology* **1091**, 17–32 (2014).
  83. Schulz, M. N. *et al.* A crystallographic fragment screen identifies cinnamic acid derivatives as starting points for potent Pim-1 inhibitors. *Acta Crystallogr. Sect. D Biol. Crystallogr.* **67**, 156–166 (2011).
  84. McCoy, A. J. *et al.* Phaser crystallographic software. *J. Appl. Crystallogr.* **40**, 658–674 (2007).
  85. Kudlinzki, D. *et al.* High-resolution crystal structure of cAMP-dependent protein kinase from *Cricetulus griseus*. *Acta Crystallogr. Sect. F Struct. Biol. Commun.* **71**, 1088–1093 (2015).
  86. Wähler, K., Kräling, K., Steuber, H. & Meggers, E. Non-ATP-Mimetic Organometallic Protein Kinase Inhibitor. *ChemistryOpen* **2**, 180–185 (2013).
  87. Schrödinger. The PyMOL Molecular Graphics System.
  88. Warr, W. A. Fragment-based drug discovery. *J. Comput. Aided. Mol. Des.* **23**, 453–458 (2009).
  89. Politzer, P., Lane, P., Concha, M. C., Ma, Y. & Murray, J. S. An overview of halogen bonding. *J. Mol. Model.* **13**, 305–311 (2007).
  90. Lu, Y., Wang, Y. & Zhu, W. Nonbonding interactions of organic halogens in biological systems: implications for drug discovery and biomolecular design. *Phys. Chem. Chem. Phys.* **12**, 4543 (2010).
  91. Chilingaryan, Z., Yin, Z. & Oakley, A. J. Fragment-Based Screening by Protein Crystallography: Successes and Pitfalls. *Int. J. Mol. Sci.* **13**, 12857–12879 (2012).

- 
92. Krissinel, E. & Henrick, K. Inference of Macromolecular Assemblies from Crystalline State. *J. Mol. Biol.* **372**, 774–797 (2007).
  93. Jafari, R. *et al.* The cellular thermal shift assay for evaluating drug target interactions in cells. *Nat. Protoc.* **9**, 2100–2122 (2014).
  94. Qian, K. C. *et al.* Structural basis of constitutive activity and a unique nucleotide binding mode of human Pim-1 kinase. *J. Biol. Chem.* **280**, 6130–6137 (2005).
  95. Qian, K. *et al.* Hit to lead account of the discovery of a new class of inhibitors of pim kinases and crystallographic studies revealing an unusual kinase binding mode. *J. Med. Chem.* **52**, 1814–1827 (2009).
  96. Liu, L., Hudgins, W. R., Shack, S., Yin, M. Q. & Samid, D. Cinnamic acid: a natural product with potential use in cancer intervention. *Int. J. Cancer* **62**, 345–50 (1995).
  97. Lide, D. R. CRC Handbook of Chemistry and Physics, 2009–2010, 90th ed. CRC Handbook of Chemistry and Physics, 2009–2010, 90th ed. Edited by David R. Lide, Editor-in-Chief, and W. M. ‘Mickey’ Haynes, Associate Editor (National Institute of Standards and Technology, *J. Am. Chem. Soc.* **131**, 12862–12862 (2009).
  98. Torshin, I. Y., Weber, I. T. & Harrison, R. W. Geometric criteria of hydrogen bonds in proteins and identification of ‘bifurcated’ hydrogen bonds. *Protein Eng. Des. Sel.* **15**, 359–363 (2002).
  99. Bamborough, P., Drewry, D., Harper, G., Smith, G. K. & Schneider, K. Assessment of Chemical Coverage of Kinome Space and Its Implications for Kinase Drug Discovery. *J. Med. Chem.* **51**, 7898–7914 (2008).
  100. Erlanson, D. A., McDowell, R. S. & O’Brien, T. Fragment-Based Drug Discovery. *J. Med. Chem.* **47**, 3463–3482 (2004).
  101. Baker, M. Fragment-based lead discovery grows up. *Nat. Rev. Drug Discov.* **12**, 5–7 (2013).
  102. Erlanson, D. A., Wells, J. a & Braisted, a C. Tethering: Fragment-based drug discovery. *Annu. Rev. Biophys. Biomol. Struct.* **33**, 199–223 (2004).
  103. Liang, Z., Liu, F., Grundke-Iqbal, I., Iqbal, K. & Gong, C.-X. Down-regulation of cAMP-dependent protein kinase by over-activated calpain in Alzheimer disease brain. *J. Neurochem.* **103**, 2462–2470 (2007).
  104. Sapio, L. *et al.* Targeting protein kinase A in cancer therapy: an update. *EXCLI J.* **13**, 843–855 (2014).
  105. Hassell, A. M. *et al.* Crystallization of protein-ligand complexes. *Acta Crystallogr. D. Biol. Crystallogr.* **63**, 72–9 (2007).
  106. Deller, M. C. & Rupp, B. Models of protein-ligand crystal structures: trust, but verify. *J. Comput. Aided. Mol. Des.* **29**, 817–36 (2015).
  107. Glass, D. B., Cheng, H. C., Mende-Mueller, L., Reed, J. & Walsh, D. A. Primary structural determinants essential for potent inhibition of cAMP-dependent protein kinase by inhibitory peptides corresponding to the active portion of the heat-stable inhibitor protein. *J. Biol. Chem.* **264**, 8802–8810 (1989).
  108. Songyang, Z. *et al.* Use of an oriented peptide library to determine the optimal substrates of protein kinases. *Curr. Biol.* **4**, 973–982 (1994).

- 
109. Pflug, A. *et al.* Diversity of Bisubstrate Binding Modes of Adenosine Analogue-Oligoarginine Conjugates in Protein Kinase A and Implications for Protein Substrate Interactions. *J. Mol. Biol.* **403**, 66–77 (2010).
  110. Behnen, J. *et al.* Experimental and Computational Active Site Mapping as a Starting Point to Fragment-Based Lead Discovery. *ChemMedChem* **7**, 248–261 (2012).
  111. Klebe, G. *Drug Design - Methodology, Concepts, and Mode-of-Action*. Springer eBooks (2013).
  112. Saxty, G. *et al.* Identification of inhibitors of protein kinase B using fragment-based lead discovery. *J. Med. Chem.* **50**, 2293–2296 (2007).
  113. Vinet, L. & Zhedanov, A. A ‘missing’ family of classical orthogonal polynomials. *J. Phys. A Math. Theor.* **44**, 85201 (2011).
  114. Brault, L. *et al.* PIM serine/threonine kinases in the pathogenesis and therapy of hematologic malignancies and solid cancers. *Haematologica* **95**, 1004–1015 (2010).
  115. Bachmann, M. *et al.* The oncogenic serine/threonine kinase Pim-1 directly phosphorylates and activates the G2/M specific phosphatase Cdc25C. *Int. J. Biochem. Cell Biol.* **38**, 430–443 (2006).
  116. Amson, R. *et al.* The human protooncogene product p33pim is expressed during fetal hematopoiesis and in diverse leukemias. *Proc. Natl. Acad. Sci.* **86**, 8857–8861 (1989).
  117. Chen, W. W., Chan, D. C., Donald, C., Lilly, M. B. & Kraft, A. S. Pim Family Kinases Enhance Tumor Growth of Prostate Cancer Cells. *Mol. Cancer Res.* **3**, 443–451 (2005).
  118. Dai, H. *et al.* Pim-2 upregulation: Biological implications associated with disease progression and perineural invasion in prostate cancer. *Prostate* **65**, 276–286 (2005).
  119. Li, Y.-Y. *et al.* Pim-3, a Proto-Oncogene with Serine/Threonine Kinase Activity, Is Aberrantly Expressed in Human Pancreatic Cancer and Phosphorylates Bad to Block Bad-Mediated Apoptosis in Human Pancreatic Cancer Cell Lines. *Cancer Res.* **66**, 6741–6747 (2006).
  120. Popivanova, B. K. *et al.* Proto-oncogene, Pim-3 with serine/threonine kinase activity, is aberrantly expressed in human colon cancer cells and can prevent Bad-mediated apoptosis. *Cancer Sci.* **98**, 321–328 (2007).
  121. Ishchenko, A. *et al.* Structure-based design of low-nanomolar PIM kinase inhibitors. *Bioorganic Med. Chem. Lett.* **25**, 474–480 (2015).
  122. Chevillard, F. & Kolb, P. SCUBIDOO: A Large yet Screenable and Easily Searchable Database of Computationally Created Chemical Compounds Optimized toward High Likelihood of Synthetic Tractability. *J. Chem. Inf. Model.* **55**, 1824–1835 (2015).
  123. Hartenfeller, M. *et al.* Probing the Bioactivity-Relevant Chemical Space of Robust Reactions and Common Molecular Building Blocks. *J. Chem. Inf. Model.* **52**, 1167–1178 (2012).
  124. Good, A. C. *et al.* Implications of promiscuous Pim-1 kinase fragment inhibitor hydrophobic interactions for fragment-based drug design. *J. Med. Chem.* **55**, 2641–2648 (2012).
  125. Irwin, J. J. & Shoichet, B. K. ZINC - A free database of commercially available compounds for virtual screening. *J. Chem. Inf. Model.* **45**, 177–182 (2005).
  126. Cimmperman, P. *et al.* A Quantitative Model of Thermal Stabilization and Destabilization of Proteins by Ligands. *Biophys. J.* **95**, 3222–3231 (2008).

- 
127. Hawkins, P. C. D., Skillman, A. G., Warren, G. L., Ellingson, B. A. & Stahl, M. T. Conformer generation with OMEGA: Algorithm and validation using high quality structures from the protein databank and cambridge structural database. *J. Chem. Inf. Model.* **50**, 572–584 (2010).
128. Jakalian, A., Jack, D. B. & Bayly, C. I. Fast, efficient generation of high-quality atomic charges. AM1-BCC model: II. Parameterization and validation. *J. Comput. Chem.* **23**, 1623–1641 (2002).
129. Irwin, J. J., Sterling, T., Mysinger, M. M., Bolstad, E. S. & Coleman, R. G. ZINC: A Free Tool to Discover Chemistry for Biology. *J. Chem. Inf. Model.* **52**, 1757–1768 (2012).
130. Brooks, B. R. *et al.* CHARMM: The biomolecular simulation program. *J. Comput. Chem.* **30**, 1545–1614 (2009).
131. McGann, M. FRED and HYBRID docking performance on standardized datasets. *J. Comput. Aided. Mol. Des.* **26**, 897–906 (2012).
132. Klebe, G. Applying thermodynamic profiling in lead finding and optimization. *Nat. Rev. Drug Discov.* **14**, 95–110 (2015).
133. Lommerse, J. P. M., Price, S. L. & Taylor, R. Hydrogen bonding of carbonyl, ether, and ester oxygen atoms with alkanol hydroxyl groups. *J. Comput. Chem.* **18**, 757–774 (1997).
134. Pal, D. & Chakrabarti, P. Non-hydrogen Bond Interactions Involving the Methionine Sulfur Atom. *J. Biomol. Struct. Dyn.* **19**, 115–128 (2001).
135. Kim, S. *et al.* PubChem substance and compound databases. *Nucleic Acids Res.* **44**, D1202–D1213 (2016).
136. Protein Kinases: Human Protein Kinases Overview | CST. Available at: <https://www.cellsignal.com/common/content/content.jsp?id=kinases-human-protein>. (Accessed: 4th April 2017)
137. Thompson, E. E. *et al.* Comparative surface geometry of the protein kinase family. *Protein Sci.* **18**, 2016–2026 (2009).
138. Das, A. *et al.* Protein Kinase A Catalytic Subunit Primed for Action: Time-Lapse Crystallography of Michaelis Complex Formation. *Structure* **23**, 2331–2340 (2015).
139. Till, J. H., Chan, P. M. & Miller, W. T. Engineering the substrate specificity of the Abl tyrosine kinase. *J. Biol. Chem.* **274**, 4995–5003 (1999).
140. Flotow, H. *et al.* Phosphate groups as substrate determinants for casein kinase I action. *J. Biol. Chem.* **265**, 14264–9 (1990).
141. Meggio, F. & Pinna, L. A. One-thousand-and-one substrates of protein kinase CK2? *FASEB J.* **17**, 349–368 (2003).
142. Songyang, Z. *et al.* Catalytic specificity of protein-tyrosine kinases is critical for selective signalling. *Nature* **373**, 536–539 (1995).
143. Fiol, C. J., Wang, A., Roeske, R. W., Roach, P. J. & Hunter, T. Ordered multisite protein phosphorylation. Analysis of glycogen synthase kinase 3 action using model peptide substrates. *J. Biol. Chem.* **265**, 6061–5 (1990).
144. Hutti, J. E. *et al.* A rapid method for determining protein kinase phosphorylation specificity. *Nat. Methods* **1**, 27–29 (2004).

- 
145. Obata, T. *et al.* Peptide and protein library screening defines optimal substrate motifs for AKT/PKB. *J. Biol. Chem.* **275**, 36108–36115 (2000).
146. Shenolikar, S. & Cohen, P. The substrate specificity of cyclic AMP-dependent protein kinase: Amino acid sequences at the phosphorylation sites of herring protamine (clupeine). *FEBS Lett.* **86**, 92–98 (1978).

## 11. Acknowledgement

Zu allererst danke ich meinem Doktorvater Herrn *Prof. Dr. Gerhard Klebe* für meine Aufnahme in seine Arbeitsgruppe und die interessante und herausfordernde Aufgabenstellungen dieses Dissertationsthemas. Sein unverkennbarer Forschergeist hat sich in jeder unserer Besprechungen gezeigt und mir immer Positivität und Zuversicht vermittelt, wenn Experimente nicht planmäßig ausgingen. Seine konstruktiven Ansätze bei problematischen Fragestellungen haben wesentlich zu meinem Vorgehen und Problemlösungen beigetragen. Ebenfalls bedanke ich mich für seine Korrekturen des Manuskripts dieser Dissertation.

*Prof. Dr. Andreas Heine* danke ich für die detaillierte Einführung in die Proteinkristallographie, für die er sich nicht nur in Seminaren sondern auch in zahlreichen, stundenlangen Einzelgesprächen die Zeit zur Vermittlung der Materie genommen hat. Zudem Danke ich ihm für die Übernahme des Zweitgutachtens und für die Korrekturen des Manuskripts dieser Dissertation.

Prof. Dr. Klaus Reuter danke ich für alle Tipps und praktischen Ratschläge zur Arbeit im S1-Labor, sowie zur Proteinkristallisation und der Handhabung von Proteinkristallen.

*Dr. Alexander Metz* danke ich für die vielen Diskussionen über die experimentellen Ergebnisse und deren Auswertung. Bei Fragestellungen rund um Fragmente hat er immer ein offenes Ohr gehabt und ein nie enden wollenden Ideenreichtum an den Tag gelegt.

*Dr. Johannes Schiebel* danke ich für die etlichen Tipps zur Proteinkristallographie. Seine Ideen und Erfahrungen haben mir oft weiter geholfen. Ich bin dankbar, dass ich so viel von Ihm lernen konnte.

Der Arbeitsgruppe um *Prof. Dr. Eric Meggers* mochte ich für die Bereitstellung des Pim1 Plasmids sowie für die Einarbeitung in Expression, Aufreinigung und Kristallisation des Proteins danken. Der Einsatz von *Katja Kräling* und *Elisabeth Martin* sind hier besonders zu erwähnen.

Der AG Steinmetzer Danke ich für die Synthese und Bereitstellung des Pim1 Konsensus-peptids.

Während meiner Arbeit im S1-Labores habe ich mit vielen Kollegen eine anstrengende aber auch sehr schöne Zeit erlebt, in der man sich immer gegenseitig unterstützt hat. Besonderen Dank gilt hier *Steffanie Dörr*, die mich bei der technischen Einarbeitung des Themas tatkräftig unterstützt hat.

Weitere Dank gilt: *Dr. Manuel Kanitz*, *Phong Nguyen*, *Dr. Kan Fu*, *Dr. Nicole Bertoletti*, *Dr. Barbara Wienen*, *Dr. Jessika Jüngel*, *Dr. Janis Müller* und *Tanja Kwasi*.

Für das Korrekturlesen meines Dissertationskriptes mochte ich zusätzlich *Corey Taylor, Dr. Janis Müller, Lukas Heyder, Anne Diestel, Dr. Florent Chevillard* und *Dr. Manuel Kanitz* danken.

Meinen ehemaligen Vertiefungsstudenten *Ying Chen, Angela Marca Pizarroso, Refika Fidan, Maisa Alkheder Alahmad* und *Valentin Löbner* danke ich für ihren Einsatz und Engagement während ihrer Praktikumszeit.

*Lydia Hartleben* und *Christian Sohn* danke ich für etwaige Unterstützung und Hilfe bei administrativen Angelegenheiten. *Christian Sohn* auch noch einmal besonders für seine Einsatzbereitschaft bei technischen Fragestellungen und Problemen rund um das S1- und das Röntgenlabor.

Für ihre hohe Einsatzbereitschaft bei der Wartung und Instandhaltung des Computernetzwerkes danke ich den Administratoren der Arbeitsgruppe: *Michael Betz, Timo Krotzky, Denis Schmidt, Felix Terwesten, Phong Nguyen, Alexander Metz* und *Tobias Wulsdorf*.

Meinen Büropartnern *Dr. Michael Betz, Dr. Steffan Krimmer, Dr. Eggert Rühmann, Dr. Jonathan Cramer, Dr. Nicole Bertolotti* und *Francesca Magari* danke ich für die angenehme Arbeitsatmosphäre und die gegenseitige Unterstützung im Büro.

Der gesamten AG Klebe gebührt mein Dank für die angenehme Arbeitsatmosphäre. Es war für mich eine besondere Zeit, an die ich immer mit Freude zurückblicken werde. Ich schätze es meine Doktorandenzeit mit all diesen netten und lebensfrohen Menschen verbracht zu haben.

Der größte Dank gilt meiner Frau *Sandra*, die mir während der gesamten Zeit immer wieder Rückhalt gegeben und mich motiviert hat. Ohne Ihre Unterstützung wäre der zurück gelegte Weg um einiges härter und anstrengender gewesen. Ebenfalls großen Dank gebührt meinen Eltern *Bernhard Siefker* und *Gisela Siefker-Nagel*, die es mir immer möglich gemacht haben meinen Weg zu gehen.



## 12. Eidesstattliche Erklärung

Ich versichere, dass ich meine Dissertation

“Characterisation and differentiation of kinase binding pockets in PKA and Pim1 by small molecule fragments using protein crystallography.”

selbständig ohne unerlaubte Hilfe angefertigt habe und mich dabei keiner anderen als der von mir ausdrücklich bezeichneten Quellen bedient habe. Alle vollständig oder sinngemäß übernommenen Zitate sind als solche gekennzeichnet.

Die Dissertation wurde in der jetzigen oder einer ähnlichen Form noch bei keiner anderen Hochschule eingereicht und hat noch keinen sonstigen Prüfungszwecken gedient.

Marburg, den

.....

(Christof Siefker)

## **13. Curriculum Vitae**

**Zum Schutz personenbezogener Daten ist der Lebenslauf  
nicht in der elektronisch publizierten Version der  
Dissertation enthalten.**